Nanoanalysis by 4D-STEM of poorly crystallized materials : developments and application to astromaterials

Bahae-Eddine Mouloud

École doctorale n°104: Sciences de la Matière, du rayonnement et de l'environnement

— Thèse de doctorat —

Nanoanalysis by 4D-STEM of poorly crystallized materials: Developments and application to astromaterials

---

Nanoanalyse par 4D-STEM de matériaux faiblement cristallisés: Développements et application aux astromatériaux

---

présentée par

Bahae-eddine MOULOUD

Thèse préparée et soutenue publiquement le 19 juin 2024

En vue de l'obtention du grade de:

Docteur de l'université de Lille

Spécialité: **Milieux Denses, Matériaux et Composants**

Présentée devant la comission d'examen composée de :

Pr.	Muriel Veron	*Présidente (Examinatrice)*	Université de Grenoble
Pr.	Bertrand Devouard	*Rapporteur*	Université d'Aix Marseille
Dr. HDR.	Christophe Gatel	*Rapporteur*	Université de Toulouse
Dr. MCF.	Francisco De la Peña	*Co-encadrant de thèse*	Université de Lille
Pr.	Damien Jacob	*Directeur de thèse*	Université de Lille

Unité Matériaux et Transformation (UMET)

— UMR 8207 Université de Lille, 59655 Villeneuve d'Ascq —

Acknowledgements/Remerciements

Je tiens à exprimer ma profonde gratitude envers l'Université de Lille, la région Hauts-de-France, l'I-SITE, l'école doctorale SMRE, ainsi que l'Unité Matériaux et Transformations pour leur soutien financier dans le cadre de ces travaux de thèse et pour m'avoir accueilli au sein de l'Université de Lille et du laboratoire au cours de ces quatre dernières années.

Mes sincères remerciements vont également aux membres de mon jury pour leur lecture et évaluation de ma thèse. Un merci particulier à **Christophe Gatel** et **Bertrand Devouard**, rapporteurs de ces travaux, et à **Muriel Veron**, examinatrice, pour l'intérêt soutenu qu'ils ont porté à mon travail. Leurs commentaires élogieux et questions pertinentes lors de la soutenance ont été particulièrement appréciés. Leur grand intérêt et enthousiasme pour mes recherches m'ont profondément impressionné et je les en remercie chaleureusement.

Je tiens à exprimer ma profonde gratitude à tous ceux qui m'ont accompagné et soutenu tout au long de ma thèse. Votre présence et votre aide ont été inestimables et je suis reconnaissant pour chaque moment partagé avec vous. **Julien Lam** et **Jean**, vous avez été non seulement des collègues exceptionnels, mais aussi des amis précieux. **Tomasso**, **Konstantinos**, et **Jeff**, votre accueil chaleureux et votre bonne humeur ont enrichi mon expérience au laboratoire.
Je n'oublie pas **Dan** et nos séances de rédaction autour d'une tasse de café, ni **Thibaut**, **Van Hau**, **Maxime**, et mes compagnons du bureau 210, pour leur excellente compagnie durant mes derniers mois au laboratoire. Vous avez su apporter de la joie et des moments mémorables au bureau.
J'ai été honoré de collaborer avec **Gaelle**, **Patrice** et **Pauline** que je remercie sincèrement pour leur confiance et leur précieuse ouverture scientifique. À tous, je souhaite un avenir brillant. Cette expérience a non seulement enrichi ma vie professionnelle mais ont aussi contribué d'une manière positive à la personne que je suis maintenant.

Gang Ji, je te remercie pour les moments très agréables que nous avons partagés avec Ahmed et les discussions enrichissantes sur divers sujets. Je suis reconnaissant pour ta confiance en moi dans l'analyse de certaines de tes données 4D-STEM, qui présentaient de réels défis. Cette

expérience a été enrichissante et m'a permis d'apprendre énormément.

Alexandre Mussi, tu es tout simplement une personne très agréable. Merci pour l'intérêt vif que tu as toujours porté à mes travaux. Ton soutien inestimable lors de nos échanges, que ce soit au laboratoire ou ailleurs, ainsi que tes mots d'encouragement, ont été d'une grande importance pour moi.

Enfin, **Patrick Cordier**, une personne exceptionnelle et un chercheur de haut niveau. Les précieux moments d'échanges que nous avons eus ensemble ont été extrêmement enrichissants pour moi. Je te remercie sincèrement pour tous tes conseils qui ont eu un impact énorme sur ma recherche et mon développement personnel.

Je tiens à exprimer ma gratitude envers **Ahmed** pour les nombreux moments agréables que nous avons passés ensemble, tant au laboratoire qu'en dehors. Ton amitié et ton soutien ont été inestimables durant ces années. Un grand merci également à ta famille, et tout particulièrement à ta mère pour ses supplications. Son soutien à distance a été d'un grand réconfort. Un remerciement spécial à ta fille, **Zélie**, qui apportait toujours une touche de joie et de gaieté chaque fois que tu l'amenais au laboratoire. Sa présence lumineuse égayait nos journées et ajoutait une dimension chaleureuse à notre environnement de travail.

Les derniers remerciements que j'adresse aux membres du laboratoire vont bien évidemment à l'exceptionnelle équipe avec laquelle j'ai travaillé.

Damien, dès mon arrivée à l'UMET, tu as su voir au-delà de mon inexpérience et m'accorder ta confiance, faisant de toi un directeur de thèse idéal. Ton soutien indéfectible et ta compréhension tout au long de ces quatre dernières années ont été d'une valeur inestimable. Tu as été à mes côtés lors de moments particulièrement difficiles. Ton soutien, ta patience, et ta confiance durant ces périodes ont été inestimables. Merci pour toutes les discussions que nous avons eues, elles ont souvent été une source de motivation et d'inspiration. Grâce à toi, ces années ont été marquées par un apprentissage riche et des expériences inoubliables. Je ne te remercierai probablement jamais assez pour tout cela.

Francisco, dès le début, tu m'as accordé une confiance inébranlable, et cela a fait toute la différence. Ta confiance et ton soutien constants m'ont permis de traverser cette période avec assurance. Nos discussions ont toujours été des moments précieux, me poussant sans cesse à faire mieux et à me remettre en question chaque jour. Merci pour tout cela, et sache que je ne te remercierai aussi probablement jamais assez pour ton rôle essentiel dans cette aventure.

Hugues, tu as été un directeur d'équipe très admirable. Dès le début, tu m'as fait confiance

en m'intégrant à l'équipe et tu m'as accueilli chaleureusement. Je te remercie également pour toutes les discussions que nous avons eues sur les météorites, et pour ton rôle très crucial dans cette thèse.

Corentin, les discussions avec toi m'ont souvent incité à me remettre en question et à voir les choses sous un nouvel angle. Je te remercie également pour tous les précieux conseils que tu m'as apportés et pour ton rôle essentiel tout au long de cette aventure et ton dynamisme qui a été toujours une réelle inspiration pour moi.

Maya, je te remercier sincèrement pour toutes les heures que nous avons passées au microscope. Les superbes données 4D-STEM que tu as acquises ont été essentielles pour faire avancer ma thèse. Ton rôle crucial au sein de l'équipe, ta gentillesse et ta patience ont été d'une inspiration inestimable. Merci également pour le très beau gâteau le jour de ma soutenance et lors du pot de départ d'Adrien et moi-même, ce fut des moments mémorables.

Adrien, si cette thèse a connu un tel succès, c'est en grande partie grâce à toi. Dès ton arrivée à Lille, tu t'es investi pleinement dans les aspects détecteurs sans lesquels ce travail n'aurait jamais abouti. Grâce à ta bonne humeur et à ton esprit jovial, tu as toujours été un compagnon incomparable. Merci pour les journées passés à QEM2022, j'ai vraiement découvert dans ces jours la personne exceptionelle que tu es. Bon voyage à Toulouse et très bonne continuation.

Jean-Christophe, une très grande partie de ce succès te revient. C'est grâce à toi que ce projet a pu grandement avancer, et je ne serai jamais en capacité de te remercier suffisamment pour tout ce que tu as fait, même avant ton arrivée à Lille. Ta motivation et ton esprit ont été une source d'inspiration constante pour moi. Merci de m'avoir torturé avec des papiers et discussions sur des phyllosilicates ! Tu étais toujours tel un troisième encadrant pour moi, tu as toujours trouvé du temps pour m'aider, même dans les moments les plus difficiles et chargés pour toi. Tu es quelqu'un de vraiment génial et je te souhaite un très bel avenir.

Sylvain, ton arrivée à l'UMET a apporté un autre dynamisme à notre équipe. Je tiens à te remercier pour les jours formidables que nous avons passés ensemble à QEM2022 ! QEM2022 a été sans doute une révélation pour nous deux, et j'ai découvert de plus près la personne unique et exceptionnelle que tu es ! Je suis heureux d'avoir partagé tous ces moments avec toi, surtout les matinées de la deuxième semaine de QEM ;).

Adrien, **Jean-Christophe** et **Sylvain**, je suis si content d'avoir eu la chance de faire votre connaissance et de vous côtoyer dans la plus grande partie de ces quatre dernières années. Votre arrivée au laboratoire a complètement changé mon quotidien pour le meilleur, et pour cela je ne vous remercierai jamais assez ! Je vous remercie vous et Maya pour le beau caillou que vous

m'avez offert et pour les poussières de saponite, je les garderai précieusement.

Mes derniers remerciements vont à tous ceux qui ont enrichi ma vie de leur présence et leur soutien.

Mes parents et mes frères, votre contribution significative à ma personnalité depuis mon enfance est inestimable. Vous m'avez toujours encouragé à suivre mes propres aspirations et à poursuivre mes rêves avec détermination. Vos conseils, votre soutien inconditionnel et votre amour ont été les piliers sur lesquels j'ai construit ma vie et ma carrière. Je vous en suis infiniment reconnaissant.

Pour **Nouh** et son épouse **Malika**, je dirai que je n'oublierai jamais votre soutien inestimable lors des moments les plus difficiles pour moi. Vous avez toujours été ma petite famille loin de ma famille. Merci pour les moments précieux que nous avons passés ensemble. Vous êtes le noyau d'une future belle famille, un modèle de famille, et je vous souhaite un très bel avenir !

Mon cher ami **Ayoub**, je n'oublierai jamais ton soutien précieux durant notre première année en France. Les moments passés ensemble, les nuits de rigolade et de complicité resteront gravés dans ma mémoire.

Le plus grand remerciement que je puisse exprimer, c'est à toi, **Chaimae**, ma compagne fidèle et mon pilier durant cette période de thèse. Tu as été à mes côtés, sans jamais faillir, dans les moments les plus intenses et les plus difficiles. Nous avons traversé ensemble des épreuves où l'incertitude et la fatigue nous pesaient, mais à chaque fois, tu as su apporter de la lumière dans les ténèbres. Même lorsque tout semblait compliqué, nous avons trouvé la force de nous soutenir mutuellement et, à travers ces épreuves, nous avons toujours su retrouver la joie et la complicité qui nous unissent. Ton écoute, ta patience et ton amour m'ont permis de traverser chaque obstacle avec sérénité et de persévérer. Grâce à toi, j'ai trouvé la force d'aller de l'avant et d'accomplir ce parcours avec confiance. Je te remercie du fond du cœur pour tout ce que tu as fait pour moi et pour notre avenir commun.

Merci à vous tous !

Abstract

The primary scientific aim of this thesis is to explore the microstructure of meteorite and asteroid fragments. Specifically, it focuses on samples of the C-type asteroid Ryugu, collected by JAXA's Hayabusa2 space mission, and the closely related, CI-type, carbonaceous chondrite Orgueil. The nanostructure of these samples provides invaluable insights into the composition and evolutionary history of the early Solar System. However, traditional characterization methods are limited in their ability to effectively map mineralogical phases and fully comprehend their intricate structure at the nanoscale. Therefore, it becomes necessary to go beyond the current state-of-the-art methods for studying these samples. This imperative is met through the utilization of four-dimensional scanning transmission electron microscopy (4D-STEM), which, owing to remarkable advancements in electron detection technologies, has become a powerful tool for capturing both spatial and diffraction information of nanoscale structures in materials, opening new avenues for exploration across multiple disciplines. By leveraging the unique advantages of 4D-STEM and data processing techniques, this study aims to provide a comprehensive analysis of the samples' microstructures and mineral phases, with a particular emphasis on phyllosilicates, thereby advancing our understanding of the formation and evolution of asteroids and meteorites and paving the way for further explorations in this fascinating field of study.

Two distinct and successful 4D-STEM methods allowing unambiguous identification and mapping of mineralogical phases in Ryugu and Orgueil meteoritic samples are developed. The first being a direct approach based mainly on indexing an overall diffraction profile to map the different mineral phases which will be extensively used throughout this thesis, while the second in an unsupervised learning based method. Both methods are found to yield comparable results. The insights gained from these developments laid the groundwork for subsequent explorations of Ryugu and Orgueil samples. The identification of lizardite as the primary serpentine polymorph in Ryugu samples, was indicative of aqueous alteration occurring at low temperatures, while the observation of variations in smectite interlayer spacing revealing sub-microscale heterogeneity, provided valuable insights into the close association of organics with smectite-type clay minerals. Despite challenges with beam damage in Orgueil samples, 4D-STEM accurately identifies present minerals, and correctly maps the different mineral constituents in the phyllosilicate matrix. Also, our results suggest that Calcium sulfates in the matrix of Orgueil are most likely present in the form of anhydrite or bassanite.

The progress made here is expected to lay the groundwork for further investigations into extraterrestrial objects requiring structural characterization, with 4D-STEM anticipated to make significant contributions in these endeavors.

Résumé

L'objectif scientifique principal de cette thèse est d'explorer la microstructure des fragments de météorites et d'astéroïdes. Plus précisément, elle se concentre sur des échantillons de l'astéroïde de type C Ryugu, collectés par la mission spatiale Hayabusa2 de l'agence spatiale japonaise JAXA, ainsi que sur la chondrite carbonée d'Orgueil, présentant des similarités avec Ryugu. La nanostructure de ces échantillons offre un aperçu précieux sur la composition et l'histoire évolutive du système solaire précoce. Cependant, les méthodes de caractérisation traditionnelles sont limitées dans leur capacité à cartographier efficacement les phases minéralogiques et à comprendre pleinement leur structure complexe à l'échelle nanométrique.

Par conséquent, il devient nécessaire de surpasser les méthodes actuelles de caractérisation pour étudier ces échantillons. Cet impératif est satisfait grâce à l'utilisation de la microscopie électronique en transmission à balayage en quatre dimensions (4D-STEM), qui, grâce à des avancées remarquables dans les technologies de détection des électrons, est devenue un outil puissant pour capturer dans le même temps des informations spatiales et structurales des assemblages nanométriques dans les matériaux. En tirant parti des avantages uniques du 4D-STEM et des techniques de traitement des données, cette étude vise à fournir une analyse complète des microstructures et des phases minérales des échantillons, en mettant particulièrement l'accent sur les phyllosilicates.

Deux méthodes distinctes à base de 4D-STEM permettant l'identification et la cartographie des phases minéralogiques dans les échantillons météoritiques de Ryugu et d'Orgueil ont été développées. La première est une approche directe basée sur l'indexation d'un profil de diffraction global pour cartographier les différentes phases minérales, et qui sera largement utilisée dans cette thèse, tandis que la seconde est basée sur une méthode numérique d'apprentissage non supervisé. Les deux méthodes produisent des résultats comparables. Ces développements ont posé les bases pour des explorations plus fines des échantillons de Ryugu et d'Orgueil. L'identification de la lizardite comme le principal polymorphe de serpentine dans les échantillons de Ryugu indiquait une altération aqueuse se produisant à basse température, tandis que l'observation de variations dans l'espacement interfoliaire des smectites révélant une hétérogénéité submicrométrique, a fourni des perspectives précieuses sur l'association étroite des organiques avec les minéraux argileux de type smectite dans Ryugu. En outre, malgré les défis liés aux dommages causés par le faisceau électronique dans les échantillons d'Orgueil, on identifie et cartographie correctement les minéraux présents dans sa matrice phyllosilicatée. Nos résultats sur Orgueil suggèrent que les sulfates de calcium dans la matrice sont très probablement présents sous forme d'anhydrite ou de bassanite.

Les progrès réalisés ici devraient poser les bases pour de futures investigations sur les objets extraterrestres nécessitant une caractérisation structurale fine, le 4D-STEM étant prévu de faire des contributions significatives dans ces efforts.

Contents

List of Figures

Introduction

The solar system, a marvel of cosmic evolution, has fascinated humanity for thousands of years. From the very early observations of celestial bodies to the modern-day exploration of distant planets, our understanding of the solar system has evolved through a mosaic of scientific inquiry and technological advancement. The motivation to study meteorites and asteroids specifically emerges from a desire to unravel the mysteries of the solar system's formation and evolution. These celestial bodies, remnants of the primordial nebula from which our solar system emerged, offer invaluable insights into the processes that shaped our cosmic neighborhood over billions of years. By studying meteorites and asteroids, scientists seek to decipher the chemical compositions, mineralogical structures, and isotopic signatures preserved within these ancient relics.

In these endeavors, transmission electron microscopy (TEM) plays a central role. TEM is indeed an analytical technique that enables the determination of the composition, the structure and the organization of the matter with an atomic spatial resolution suiting well to the very fine scale complexity of minerals constitutive of meteorites and asteroids samples. TEM is furthermore a rapidly changing method, as advanced instruments and detection technologies are in continuous development. Recent innovations allow considerable progress in materials characterization, empowering scientists with unprecedented capabilities to probe the atomic and nanoscale organization of matter. Among these cutting-edge techniques is Four Dimensional Scanning Transmission Electron Microscopy (4D-STEM). The technique is based on the 2D scanning of the sample combined with the acquisition on a 2D numerical detector of a diffraction pattern at each scan location. It offers new possibilities to fully explore the structural information embedded in the diffraction signal in order to reconstruct on demand selective maps of the scanned area.

This thesis embarks on a journey to bridge advanced electron microscopy and planetary exploration. Leveraging the capabilities of 4DSTEM, never before applied to the study of meteorites and asteroids samples, this work seeks to unlock new insights from these extraterrestrial objects

and provide further pathways to be explored for a deeper understanding of their history and evolution. The work is fortunately concomitant with the return of asteroids samples from the Hayabusa2 space mission, a unique endeavor led by the Japan Aerospace Exploration Agency (JAXA). Our laboratory, alongside other selected research facilities across the globe, has been entrusted with the first-round analyses of samples retrieved from the Ryugu asteroid target of the Hayabusa2 spacecraft. Within the "Fine-Grain" analysis team, the focus was on utilizing advanced analytical electron microscopy techniques to investigate the samples at the nanoscale. The pristine nature of the samples and the beam-sensitivity of some of their constituents, namely organic matter and hydrated silicates, present significant challenges. The TEM-ASTER project led by Professor Hugues Leroux, within which this work has been made possible, aimed to address these challenges by employing advanced detector technology and leveraging developments in big data processing to enhance the resolution and potentially mitigate damage caused by the electron beam. As part of this project, two direct electron detectors, Timepix3 and Medipix3, have been installed on the last generation TEM available at the electron microscopy platform of the University of Lille.

As will be outlined in the first chapter of this thesis, Ryugu asteroid samples composition closely resembles that of a specific type of meteorites called carbonaceous Ivuna-type (CI) chondrites. This specific type of chondrites is widely used as a proxy for primitive material in the solar system because of its good alignment with the elemental abundances as measured in the solar photosphere. The mineralogy of CI chondrites is dominated by a fine-grained matrix, rich in phyllosilicates (mainly serpentine and smectite) hosting other accessory minerals. These phyllosilicates are indicative of aqueous alteration processes in the parent body of the chondrite. The degree of this alteration may vary from a meteorite sample to another revealing distinct geological evolution. Understanding the formation pathway of phyllosilicates, including the crystallization sequence of their constituents (such as serpentine and smectite), their interrelationships and their individual crystallographic properties at a nanoscale level, provides valuable insights into the pivotal processes shaping the history of these phyllosilicates in meteorites. Furthermore, a fine-scale analysis of these chondrites' phyllosilicates might bring additional constraints on the alteration history of their parent bodies.

While numerous experimental techniques allow for tackling these different aspects, 4D-STEM has its unique advantage of offering both high spatial representativity and local structural information at the nanoscale level, crucial for a full characterization of these chondritic samples. This technique might thus bring a complementary crystallographic perspective to further constrain the evolution of phyllosilicate formation within chondritic materials. In this frame,

the work achieved in this thesis provides a first 4D-STEM exploratory analysis of Hayabusa2 Ryugu samples. It also deals, in an initial comparison purpose, with the analysis of Orgueil CI chondrite samples, which is another emblematic specimen of the carbonaceous Ivuna-type (CI) chondrites widely studied in the past.

The opening chapter of this thesis will establish context by revisiting the key stages in the formation of the solar system. It will then delve into significant findings derived from meteorite studies, and provides the main findings of the Phase 1 analysis of Ryugu samples. Chapter 2 discusses the experimental methods and data analysis techniques employed in the thesis, with a specific emphasis on 4D-STEM. Chapter 3 focuses on the 4D-STEM characterization of the phyllosilicates in Ryugu asteroid samples. This chapter is actually the extended version of a paper published in the frame of the first-round analyses results in a dedicated volume of the Meteoritics and Planetary Science journal. Chapter 4 presents the 4D-STEM study of specific areas in the Orgueil CI chondrite sample discussing the findings and their implications as well as the challenges faced in this particular analysis. Finally, considering the various limitations that have been encountered in the data treatment of previous analyses, chapter 5 deals with the application of unsupervised learning approaches, namely a non-negative matrix factorization (NNMF) based strategy, for accurate phase mapping of meteorite samples 4D-STEM data. We resume the main results of this work and the perspectives it offers for the nanoscale analysis of astrominerals in the last chapter.

Chapter 1

Asteroids and Meteorites

1 Meteorites and the Formation of the Solar System

The Solar System contains multiple celestial bodies with varying compositions. These celestial bodies can be categorized through a diameter versus density diagram as illustrated in Figure 1.1. As summarized thereon, the sun and gas giants are primarily composed of Hydrogen and Helium. The sun, being a star, is a massive, luminous sphere of hot plasma dominated by these two elements. Similarly, gas giants like Jupiter and Saturn are large planets with thick atmospheres rich in hydrogen and helium. Terrestrial planets and moons, including Earth, Venus, Mars, and Mercury, are characterized by solid, rocky surfaces. Their composition is significantly different from that of gas giants, being denser and smaller. Ice giants and moons are composed of water in solid state, silicate rocks, and iron. This category includes planets like Uranus and Neptune, as well as various moons within the Solar System. These bodies are distinct from both terrestrial planets and gas giants, with a composition that includes significant amounts of frozen water along with rock and metal. However, there are also other celestial bodies like comets and asteroids and other smaller entities mostly composed of rock and metal. These are primarily found in the asteroid belt between Mars and Jupiter and share a close composition with terrestrial planets. When the orbits of comets intersect with Earth's path, they can venture into our planet's atmosphere. During this journey, the intense heat generated causes the comet's outer layers to vaporize, resulting in the creation of a dazzling streak known as a meteor. Those fragments that endure this fiery descent and reach the Earth's surface are **meteorites**. Meteorites can be broadly categorized into two main groups:

- **Chondrites (also known as undifferentiated meteorites):** This category encompasses meteorites that have not undergone significant differentiation processes, maintaining a more primitive composition.

- **Differentiated Meteorites:** This category is further subdivided into three classes:

  - ✔ *Achondrites:* A group of meteorites that have undergone partial to complete differentiation. They include various subtypes such as basaltic achondrites, lunar achondrites, martian achondrites, and HED[1] meteorites (from the asteroid Vesta).

  - ✔ *Iron Meteorites:* They are primarily composed of metallic iron and nickel, thus exhibiting characteristics indicative of partial melting and differentiation and representative of the cores of differentiated asteroids or protoplanets.

  - ✔ *Stony-Iron Meteorites:* These meteorites contain roughly equal amounts of metal and silicate material. Pallasites and mesosiderites are the two main subtypes.

[1] **H**owardites-**E**ucrites-**D**iogénites

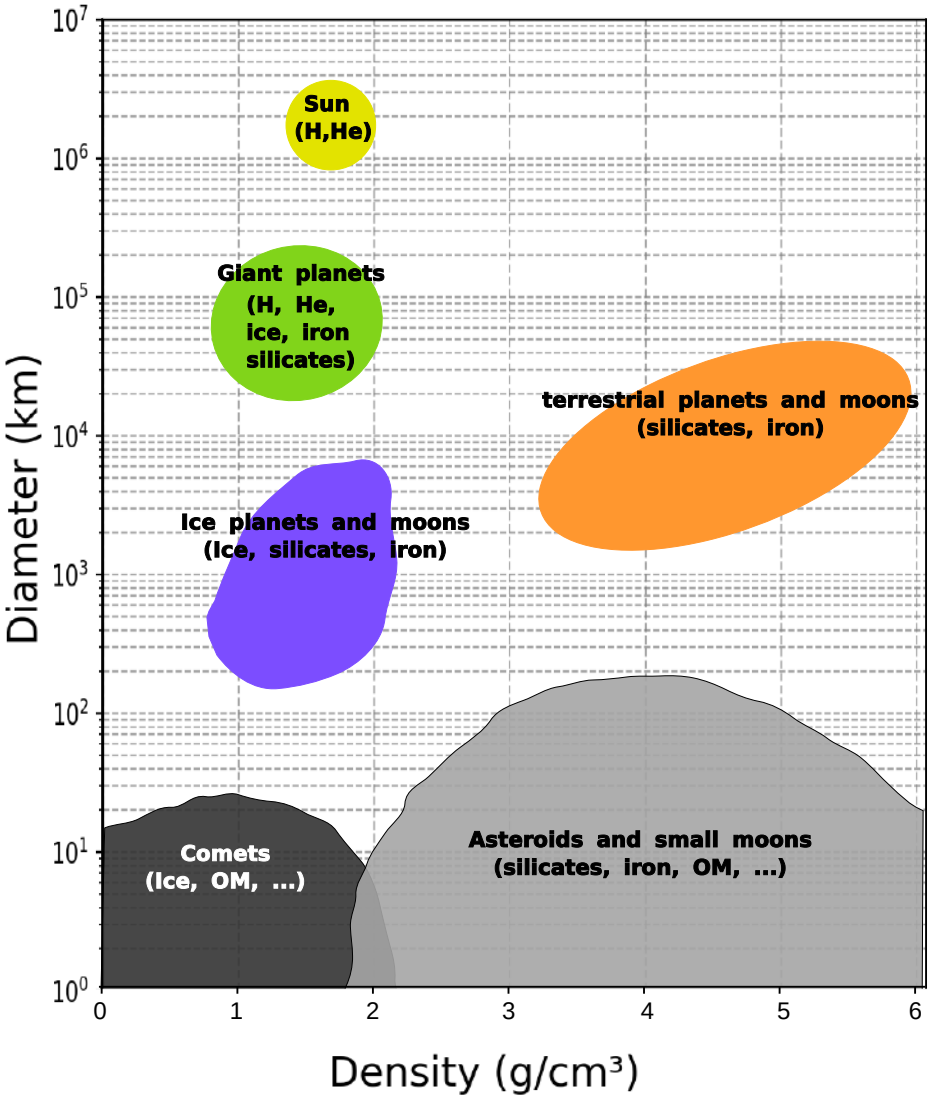

Figure 1.1: Diameter vs Density classification of celestial bodies: Diagram depicting the diameter (in km) versus the density (in g/cm³) of various astronomical objects, including asteroids, comets, planets, and their moons. OM refers to organic matter (Adapted from Caroli (2000)).

1.1 Chondrites

The term *chondrite* is derived from the Greek term *chondros*, meaning "grain" or "granule", describing the small, rounded mineral grains known as chondrules that are typically found in these objects. Chondrites predominantly consist of silicate minerals, chiefly olivine and pyroxene. They also exhibit varying degrees of metallic iron-nickel content, typically constituting approximately 10-20% of their volume. Notably, some chondrites contain hydrated minerals, such as phyllosilicates, indicative of aqueous alteration processes. Additionally, chondrites may feature trace amounts of various sulfides, carbonates, and rare accessory minerals like spinel (Brearley and R. Jones 1998). Figure 1.2 graphically represents the average elemental compo-

sition of chondrites in comparison to Earth's chemical composition.

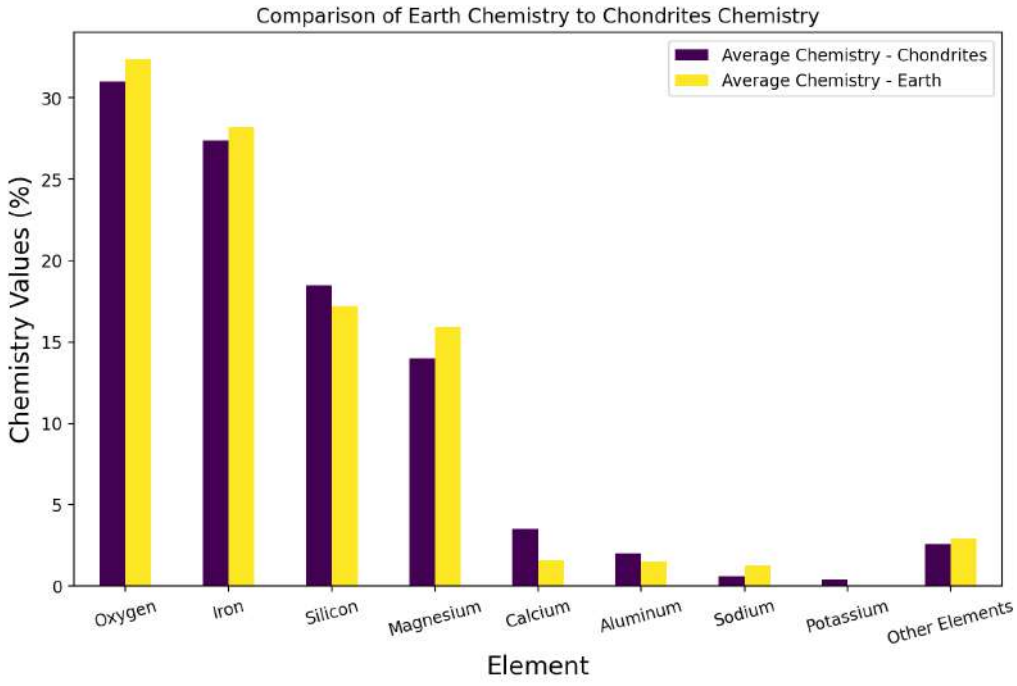

Figure 1.2: Comparison of elemental chemistry between Earth and Chondrites: Bar plot illustrating the average chemical composition of key elements in Earth's composition compared to that of chondrites (Caroli 2000).

It is observed that chondrites and Earth share a close chemical composition, leading to the hypothesis that Earth may have formed from chondritic material. However, in contrast to chondrites, the Earth exhibits chemical differentiation into concentric layers (core, mantle and crust), making it chemically heterogeneous.

1.2 Differentiated Meteorites

The chemical differentiation of Earth can be explained by examining differentiated meteorites. Interestingly, achondrites and iron meteorites present a chemistry that is similar to the different layers of Earth. Achondrites and iron meteorites are thought to originate from the fragmentation of a larger parent body, which itself had distinct layers such as a crust, mantle, and core, similar to Earth. It is possible to estimate the average chemical composition of these parent bodies by combining the compositions of the three layers given the knowledge of the sizes of the parent body and of the diverse layers.

Similarly to Earth, it is estimated that the bulk composition of other differentiated and unfragmented asteroids is found to closely resemble that of chondrites. Subsequently, these parent

bodies undergo chemical differentiation during a fusion stage, where the denser elements migrate towards the center of the protoplanet. This is why these meteorites are referred to as "differentiated" meteorites in contrast to chondrites, which are believed not to have undergone fusion and differentiation processes, thus the name "undifferentiated" meteorites.

Following these observations, a model for terrestrial planets formation has been established.

1.3 From the Solar Nebula to Planetary Formation

1.3.1 Formation of the Solar System and Planetary Bodies

The process of planetary formation is believed to have begun with the collapse of a massive cloud of gas and dust (Fig. 1.3) referred to as the solar nebula, under the influence of its own gravitation. This collapse resulted in the creation of a spinning, flattened disk of material referred to as the **protoplanetary disk**. At the disk's center, a substantial core emerged, while surrounding dust and gas gradually moved inward. As matter continued to accumulate, it produced higher temperatures and greater mass, ultimately drawing in additional dust leading to the birth of what is referred to as the "protosun".

As the disk gradually cooled, the dust particles within it began to clump together, thus beginning the accretion mechanism. The majority of these grains aggregates underwent further agglomeration, resulting in the accretion of objects measuring several kilometers across, which we refer to as planetesimals. These planetesimals, in turn, continued to collide and merge, eventually evolving into the celestial bodies we recognize nowadays as planets. Notably, remnants of these planetesimals exist in the form of asteroids, primarily located in the asteroid belt between Mars and Jupiter, which might not have successfully merged into planets, potentially due to the gravitational influence exerted by Jupiter.

1.3.2 Meteorites and Asteroids Formation

Within the protoplanetary disk, there were notable fluctuations in both pressure and temperature, which diminished as accretion occurred (Wood 2000). Chondrites, the most primordial rocks ever examined by scientists (Anders 1968), have been dated through radioisotope methods to over 4.5 billion years ago, a period predating the formation of planets. It is thought that their formation resulted from the accumulation of both mineral and organic components

(Patterson 1956).

The initial chemical processes within the nebula led to several key developments. Firstly, there was the formation of refractory inclusions and chondrules. Secondly, a distinct separation occurred between metal, sulfides, and silicate phases. Thirdly, there was a notable depletion of volatile elements within the inner regions of the solar nebula. The formation of chondritic components took place at various locations within the solar nebula and over a few million years. According to Wood (2000), refractory inclusions have formed in proximity to the sun during the peak activity phase of the disk. In contrast, chondrules emerged several million years after the refractory inclusions formation, originating during heating events in the vicinity of their accretion location (Krot et al. 2009).

In the progressively cooling nebula, the earliest minerals to condense are Aluminum and calcium-rich. These condensations occured at temperatures approximately between 1800 **K** and 1450 **K**. This process led to the formation of Calcium-Aluminum-rich Inclusions (CAIs). CAIs are believed to have formed in an oxygen-rich environment and are enriched in ^{16}O (Guan et al. 2000). Following this, there was a condensation of silicon, oxygen, iron, and nickel. The combination of silicon, oxygen, and iron resulted in the formation of forsterite, whereas iron and nickel together led to the creation of metallic iron, particularly around 1400 **K**. Additionally, sulfur combined with iron, crystallizing to form troilite (FeS), a process that could have occurred either through a heating episode or direct condensation from the nebula (Campbell et al. 2005; Scott and Krot 2007).

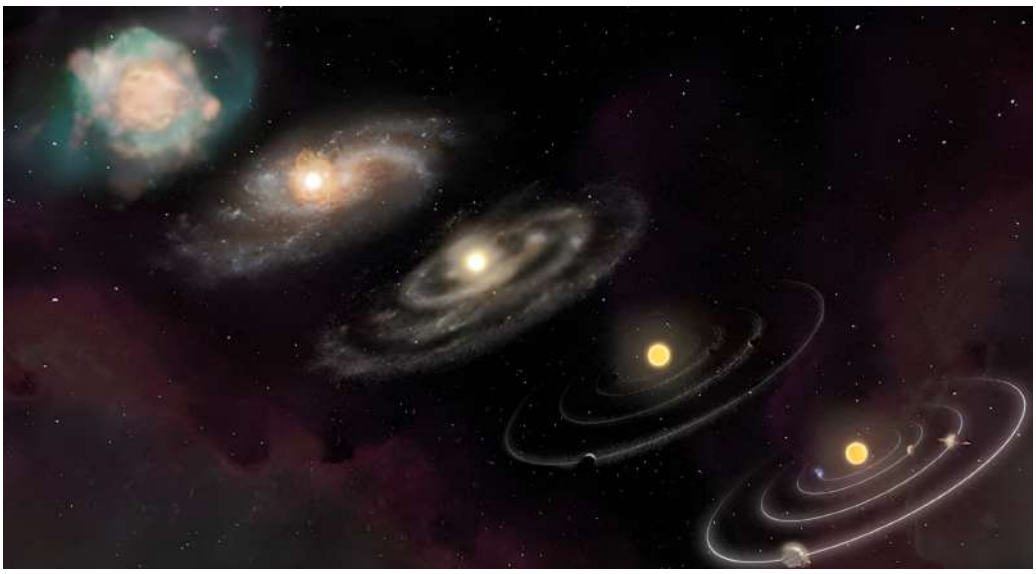

Figure 1.3: Conceptual representation of the Solar System's evolution, from the primordial solar nebula to the present-day arrangement of planets and orbits

1.3.3 The Particular Case of CI Chondrites

For a better understanding of chondrites' chemical composition and their significance in elucidating the formation and evolution of the Solar System, we begin by comparing their chemistry to the solar chemical composition. Lodders (2019) conducted a comparative analysis specifically between the CI-chondrites' and the photosphere element abundances which is summarized in Figure 1.4. CI-chondrites, specifically referring to the Carbonaceous Ivuna-type chondrites, are a specific group of meteorites that is the most volatile element-rich among any known chondritic meteorite groups (Mason 1960). The good alignment of CI chondrites with elemental abundances as measured in the solar photosphere (cf. Figure 1.4), including those of volatile elements (excluding highly volatile elements like H, C, N, O, and noble gases), along with their consistent continuity in elemental and isotopic abundance trends with mass number, made them ideal proxies among all chondritic material present on Earth for primordial Solar System studies. Other chondrite groups, such as carbonaceous chondrites (other than CI-chondrites), ordinary chondrites, and enstatite chondrites, exhibit notable discrepancies in their elemental compositions when compared to the solar photosphere. These discrepancies arise from volatility-related fractionations for certain elements, in addition to non-solar proportions of metal and silicate phases within these chondrites. The *Si/Fe* or *Mg/Fe* concentration ratios in these chondrites deviate from the solar values (Asplund et al. 2009), reflecting their distinct formation histories and compositions. Thus, they may not provide close representations of the early Solar System's

history. As of today, there exist only nine CI chondrites, with Ivuna, Orgueil, and Alais being the most prevalent among the nine.

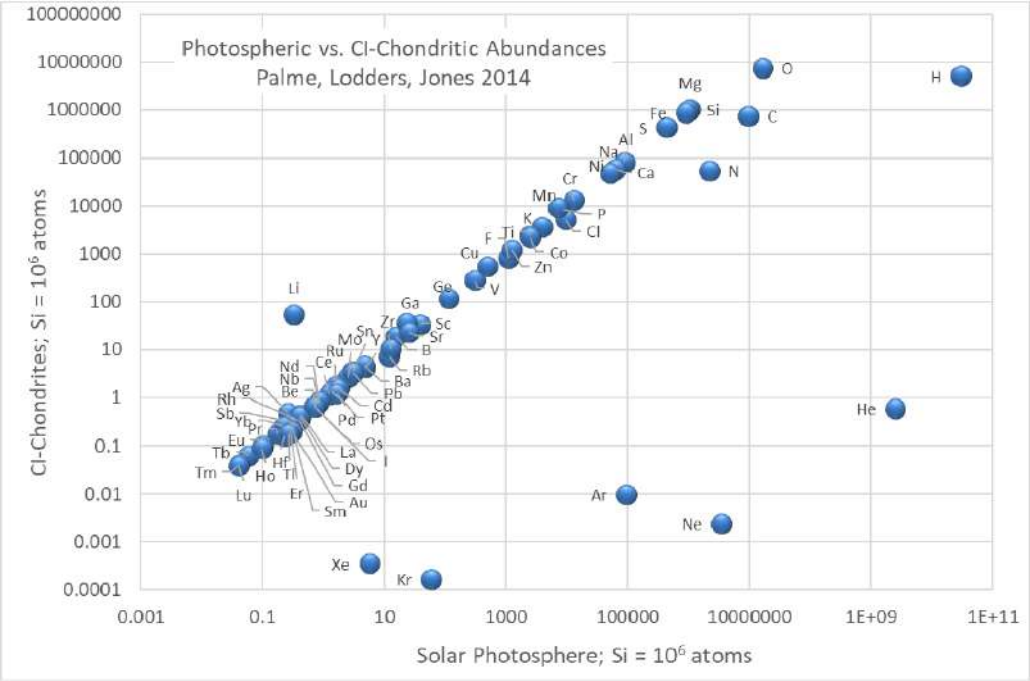

Figure 1.4: CI-chondrites versus sun's photosphere atomic abundances. Data normalized to 10^6 silicon atoms. Most elements closely align with a 1 : 1 line, showing impressive correspondence over 13 orders of magnitude. Exceptions include Lithium (lost to the sun) and volatile gases (H, C, N, O). Data from Lodders 2019

2 Secondary Processes on Parent Bodies

Throughout the 20th century, following the initial categorization of meteorites into differentiated and undifferentiated types, subsequent refinements in classification have been made possible through advancements in chemical and isotopic analytical techniques (Anders 1968; Clayton, Grossman, et al. 1973; Clayton, Mayeda, et al. 1991; Clayton and Mayeda 1996; Clayton and Mayeda 1999; Warren 2011). These unfolded in the classification shown in Figure 1.5.

In parallel, significant attention has been devoted to comprehending the transformative processes that meteorites and asteroids undergo. The majority of chondrites, for example, have undergone substantial physico-chemical alterations. These alterations hold great importance in the quest to decipher the original composition of the solar nebula, shed light on the formation of asteroids, and contribute to our understanding of the broader evolution of the Solar System. These alterations have been categorized into aqueous alteration phenomena and thermal metamorphism phenomena.

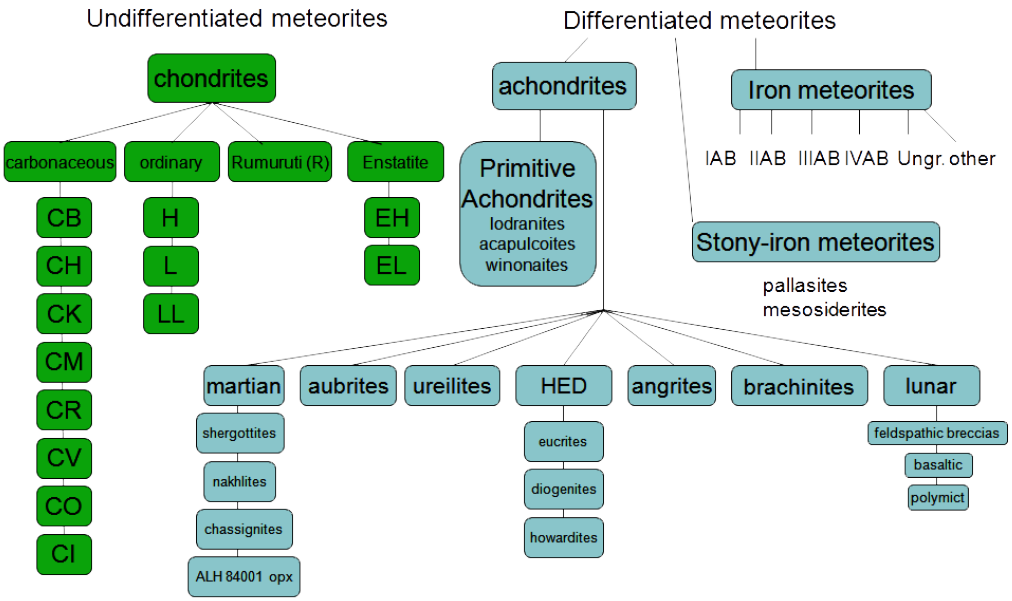

Figure 1.5: Meteorite classification chart. Adapted from: NASA website for meteorite collections

The intensity of these secondary alteration processes in meteorites was first introduced by Schmus and Wood (1967), who created a scale ranging from type 1 to 6 to represent the type and intensity of these secondary processes and has been later improved by Sears and Dodd (1988). Types 1 and 2 are indicative of aqueous alteration, with type 1 representing the most extensive level of the latter. Meteorites of type 3 are considered to closely resemble the initial mineralogy at the time of the asteroid accretion. Types 4 and 5 correspond to various levels of thermal metamorphism, with type 6 being the most extreme level of the latter, involving higher temperatures and metamorphic changes. Figure 1.6 provides a summary of the petrographic types in chondrites and the approximate temperatures of secondary processes.

Carbonaceous chondrites, for instance, often exhibit more pronounced aqueous alteration but may also exhibit traces of thermal metamorphism. These alterations manifest in various ways, including mineral transformations as well as textural, chemical and structural modifications.

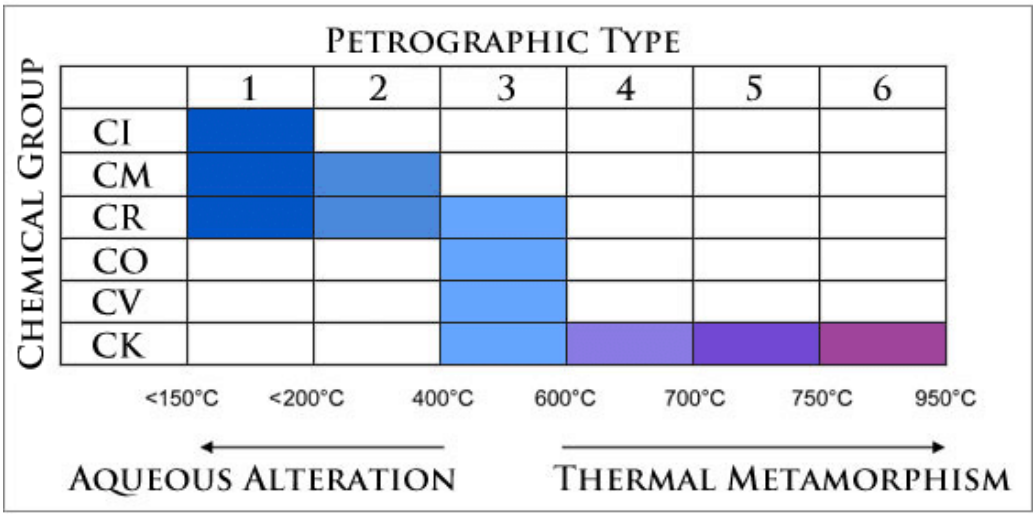

Figure 1.6: Summary of the petrographic types in chondrites and the approximate temperatures of secondary processes (I: Ivuna, M: Mighei, R: Renazzo, O:Ornans, V: Vigarano, K: Karoonda). Adapted from: Sephton (2002)

2.1 Thermal Metamorphism

Thermal metamorphism, in a general context, refers to the geological process that involves the alteration and transformation of rocks and minerals due to elevated temperatures, typically deep within the Earth's crust or in extraterrestrial bodies like asteroids. This process leads to changes in mineral composition, texture, and structure (E. Scott et al. 1992; Endress and Bischoff 1993; Keil et al. 1997; J. McSween H. Y. et al. 1988; Quirico et al. 2013). For the scope of this thesis, which primarily focuses on CI chondrites with petrographic types close to 3, thermal metamorphism is not a central concern as aqueous alteration is the most prevalent secondary process.

2.2 Aqueous Alteration

Aqueous alteration refers to the geochemical and mineralogical changes in asteroidal bodies caused by interaction with water. This process is integral in understanding the evolution of certain meteorites, impacting their mineralogy and chemistry significantly. The origin of this water can be traced back to ice grains that condensed in the outer parts of the solar system. These ice grains, upon being accreted within chondrites and subsequently heated, melt and react with anhydrous phases, initiating the process of aqueous alteration.

The extent of aqueous alteration in carbonaceous chondrites has been thoroughly assessed

through various analytical techniques. These include X-ray diffraction, which estimates total phyllosilicate abundances (e.g., Howard et al. 2009; Howard et al. 2011; Howard et al. 2015; King et al. 2015), light element analysis (e.g., C. M. O. Alexander et al. 2012; C. M. Alexander et al. 2013), IR spectral features corresponding to aqueous alteration products (e.g., Beck et al. 2014), and electron microscopy (e.g., Tomeoka and Buseck 1985; Tomeoka and Buseck 1988). A comprehensive review of this topic is available in Brearley (2006).

The effects of aqueous alteration can vary significantly across different types of carbonaceous chondrites. For example, alteration in CM chondrites typically leads to homogeneous bulk compositions, indicative of isochemical alteration processes. This type of alteration involves the exchange of elements, such as Ca, between the fine-grained matrix and chondrules (around 50-50% proportions). Notably, soluble Ca is leached from chondrules and calcium-aluminum-rich inclusions (CAIs) and then precipitated in the matrix as calcium carbonate (Suttle et al. 2021; Brearley 2006).

CR chondrites also show evidence of aqueous alteration in their matrices as noted by Weisberg et al. (1993). The CR chondrites' matrices are less fractionated and display depletions in Ca due to mobilization to form calcite during aqueous alteration (Brearley 2006).

In CI chondrites, aqueous alteration leads to the significant redistribution of soluble elements such as calcium (Ca), manganese (Mn), sodium (Na), potassium (K), and sulfur (S) at a scale of approximately 100 micrometers. These elements are mobilized and precipitated as sulfates and carbonates. This process has been extensively studied and is well documented in numerous works (H. Y. McSween and Richardson 1977; M. Zolensky et al. 1993; Adrian Brearley 1992).

A complex mineralogy unfolds from these aqueous alteration processes showing a complex mixture of various minerals. This complex assemblage is characterized by the presence of abundant phyllosilicate minerals (Eg. $\sim 95\%$ *vol.* of Orgueil constitutes the matrix), such as serpentine and smectite clays, which are the main indicators of aqueous alteration processes. These meteorites also contain small grains of metal, sulfides, and refractory minerals embedded within the matrix. A summarizing table of the different minerals found in CI, CM, and CR chondrites is shown in Figure 1.7.

CI Chondrites	CM Chondrites	CR Chondrites
Silicates	**Silicates**	**Silicates**
Fe-Mg serpentines	Fe-Mg serpentines	Fe-Mg serpentines
Saponite (smectite)	cronsteditite	saponite
Carbonates	*chlorite*	**Carbonates**
calcite	*saponite*	*calcite*
dolomite	*vermiculite*	
breunnerite		**Oxides**
siderite	**Tochilinite**	magnetite
	tochilinite	
Sulfates		**Sulfides**
gypsum	**Carbonates**	pyrrhotite
epsomite	calcite	pentlandite
bloedite	dolomite	
Ni bloedite	*aragonite*	
Sulfides	**Sulfates**	
pyrrhotite	*gypsum*	
pentlandite	*hemihydrate*	
cubanite	*anhydrite*	
	thenardite	
Oxides		
magnetite	**Oxides**	
ferrihydrite	*magnetite*	
Native elements	**Hydroxides**	
sulfur	*brucite*	
	Sulfides	
	pyrrhotite	
	pentlandite	
	Halides	
	halite	
	sylvite	

Figure 1.7: Comparative table of the different alteration phases found in CI, CM, and CR chondrites. Adapted from Brearley (2006)

3 Overview of the Mineralogy and Chemistry of a Typical Fine-grained Matrix in CI Chondrites

Phyllosilicates

Phyllosilicates, or sheet silicates, are a type of silicate minerals characterized by the stacking of tetrahedral layers, where tetrahedra ("**T**") share three out of four corners (the "basal" oxygens), while the fourth corner (the "apical" oxygen) is connected to an octahedral layer ("**O**") occupied by various cations such as aluminum (Al), magnesium (Mg), iron (Fe), and others. Within a CI chondrite sample matrix, the distribution of phyllosilicates is typically widespread and forms a significant portion of the matrix material. These phyllosilicates are found as fine-grained minerals or coarse grained "nodules" dispersed throughout the matrix (cf. Figure 1.9 and 1.10), suggesting that aqueous alteration processes have affected the entire meteorite as these are mainly formed by the alteration of primary minerals such as olivine and pyroxene. The transition between these different phyllosilicate arrangements is often relevant as shown in Figure 1.10.

In this manuscript, only two groups of phyllosilicates will be frequently encountered; the serpentine group and the smectite group. These are commonly seen in CI-chondrites and can intricately intertwine at extremely small scales within the phyllosilicate matrix, presenting challenges in accurately distinguishing these mineral phases and their spatial distribution.

- ***Serpentines:*** The most common species (polymorphs) of serpentine are all Mg-dominant: Lizardite, Chrysotile and Antigorite. Their crystal structure consists of **TO** layers where an octahedral sheet (**O**) is attached to a silica tetrahedral sheet (**T**) made of di-trigonal rings formed by SiO_4 tetrahedra units through sharing one oxygen atom ("apical" oxygen O_a) as shown in Figure 1.8. What makes the structure of serpentines so peculiar is the bending flexibility of their layers. These can be flat in the case of Lizardite, modulated in the case of Antigorite and curled in the case of Chrysotile.

- ***Smectites:*** Smectite minerals are a type of clay minerals that belong to the phyllosilicate family and have a *2:1* (**T-O-T**) layer structure consisting of an octahedral sheet (with Al^{3+}, Mg^{2+}, Fe^{2+}, Fe^{3+}, and Li^{+}, among others) sandwiched between two opposing tetrahe-

dral sheets (with Si^{4+}, Al^{3+}, and Fe^{3+}) as outlined in Brigatti et al. (2013). This structural arrangement forms the template for the silicate clay minerals (Fig. 1.8). However, the composition varies frequently due to substitution of ions within the mineral structure. For instance, weathering allows for the substitution of Si^{4+}, Al^{3+}, and Mg^{2+} with cations with comparable ionic radii in their respective tetrahedral and octahedral sheets. Consequently, Al^{3+}, may replace Si^{4+} in the center of the tetrahedron without changing the basic structure of the crystal. Moreover, cations such as $Fe^{3+|2+}$ and Zn^{2+} may replace Al^{3+} and Mg^{2+} in the octahedra (Barton and Karathanasis 2002). The process of replacing one structural cation for another of comparable size is referred to as isomorphic substitution. The particularity of smectites' structure is their ability to expand upon hydration, low porosity, high surface area, and high cation exchange capacity (Di Maio and Scaringi 2016). Indeed, isomorphic substitutions involving lower charge cations in tetrahedral and/or octahedral sheets create negatively charged *2:1* layers, known as "permanent charge". These negatively charged layers are balanced by hydrated exchangeable cations in the interlayer space, affecting the layer-to-layer distance. In a tri-hydrated state for instance, with three water molecules between the layers, the interlayer distance can reach up to $\sim\ 19 - 21$ Å, while a dehydrated state reduces it to around ~ 9.3 Å (Ferrage 2016; Colten-Bradley et al. 1987; Moyano et al. 2012; Sayers and Boer 2016).

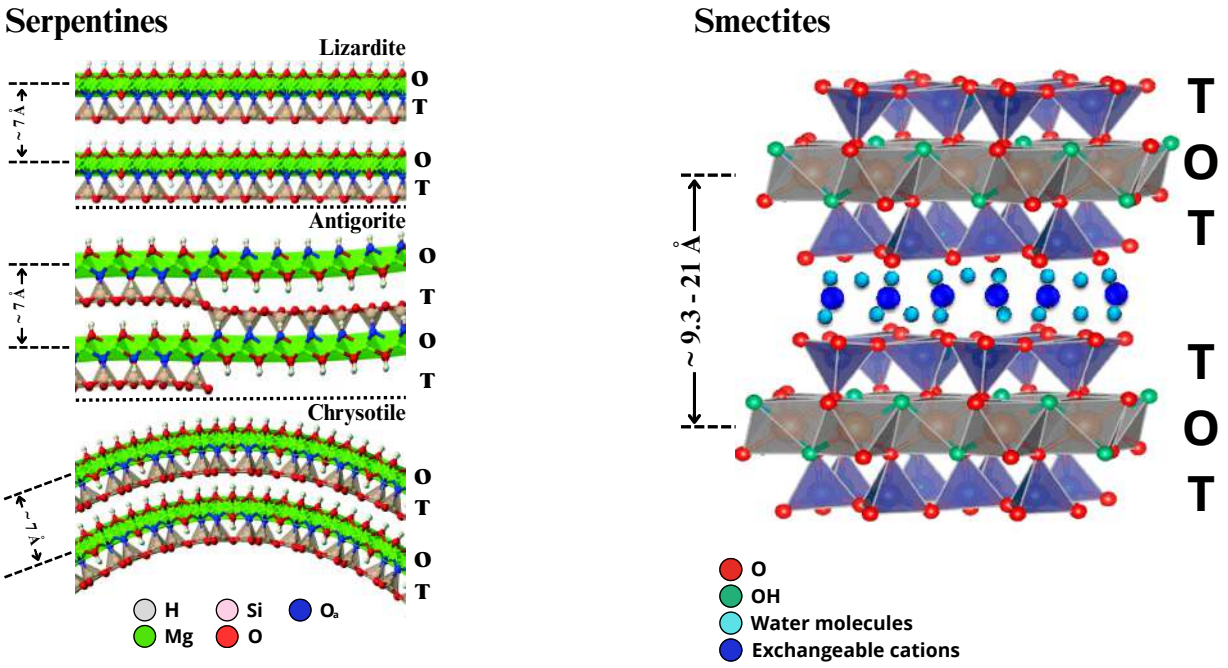

Figure 1.8: Schematic illustrating the arrangement of layers in the three main serpentine polymorphs (**T** refers to tetrahedral and **O** correspond to octahedral layers) and the typical arrangement of layers in smectite (right). O_a refers to "apical" Oxygen. The typical layer to layer distance in serpentines is $\sim$ 7 Å while in smectites, it can vary from $\sim$ 9.3 Å to $\sim$ 21 Å, depending on the arrangement of the material occupying their interlayer spacing. Adapted from Demichelis et al. (2016) and X. Wang and H. Wang (2021).

Amorphous silicates

Amorphous silicates, although significant in the study of extraterrestrial materials, are not notably abundant in CI chondrites. While crystalline silicates are prevalent in dying star environments, the interstellar medium primarily contains amorphous silicate dust grains. Some of this interstellar dust retains its isotopic signature from formation around other stars, and a fraction of it survives in recognizable form in meteorites. The exact amount of the so-called presolar amorphous silicates in meteorites remains uncertain, as these grains are vulnerable to alteration before and after their incorporation into meteorites. Nonetheless, some amorphous silicate-dominated grains with nonsolar oxygen isotopic compositions have been identified as presolar in origin (C. Alexander et al. 2017; Ishii et al. 2018; Nguyen et al. 2007; Messenger et al. 2003; A. Jones et al. 2013; Zhukovska et al. 2008; Hoppe et al. 2017; Kemper, Vriend, et al. 2004; Molster and Waters 2003; Kemper, Waters, et al. 2001).

Anhydrous silicates

Anhydrous silicates can be found in various proportions in many meteorite samples. The main two species being olivine and pyroxene. Grains of anhydrous silicates larger than five microns frequently exhibit irregular shapes and are believed to arise from the fragmentation of chondrules (eg. Simon et al. 2018). Other sub-micrometric sized grains are also present. Their chemical compositions is variable but Mg-rich compositions are the most common (eg. H. Leroux et al. 2015).

Sulfides and Oxides

The major sulfides within CI chondrites consist primarily of troilite, pyrrhotite, and pentlandite sulfides. Troilite and pyrrhotite are generally found as pure iron sulfides, whereas pentlandite comprises both iron and nickel. These sulfides span in size from approximately ten nanometers when intertwined with silicate material to more substantial grains measuring around one hundred microns in diameter (Schrader et al. 2021; Visser et al. 2019).

Iron oxides, like magnetite, are usually less abundant than sulfides in CI-chondrites. These iron oxides occasionally form alteration rims encircling metallic grains, and they may also be encountered in isolated sub-micrometric grains dispersed throughout the matrix. The formation of oxides in chondritic parent bodies, which lack a substantial atmosphere, requires the presence of an aqueous fluid that facilitates the oxidation of initially present iron within the matrix.

Ferric hydroxides (eg. Ferrihydrite) were also identified in some CI chondrites like Orgueil (Tomeoka and Buseck 1988) which are believed to originate from terrestrial weathering.

Carbonates and sulfates

Carbonates and sulfates are believed to be weathering products. These are less abundant than silicates in CI chondrites for instance. Carbonates are often found in the form of Calcite ($CaCO_3$) and Dolomite ($CaMg(CO_3)_2$). Sulfates presence in the form of Gypsum ($CaSO_4.2H_2O$) is also often reported (Fredriksson and Kerridge 1988; Gounelle and M. Zolensky 2001).

Organic matter

Carbonaceous chondrites can contain a significant amount of carbon, primarily in the form of sub-micrometric organic matter associated with clays or amorphous silicates. Recent advancements in microscopy and analytical techniques have allowed for the association of organic matter with surrounding phases to be directly observed. Various organic compounds have been

identified, such as amino acids, carboxylic acids, and hydrocarbons, indicating diverse origins and formation mechanisms. Furthermore, organic matter is sensitive to hydrothermal processes and metamorphism, which can alter its molecular nature (LeGuillou et al. 2011; Remusat et al. 2010; Pizzarello et al. 2006; Herd et al. 2011)

Figure 1.9 summarizes through low-voltage scanning electron microscopy (LVSEM) images the typical matrix mineralogy of Ryugu, which closely resembles that of CI chondrites. Meanwhile, Figure 1.10 provides an overview of High-Angle Annular Dark Field (HAADF) matrix images typical of Orgueil, which is a CI chondrite, emphasizing the diverse textures and compositions found within these chondrite types.

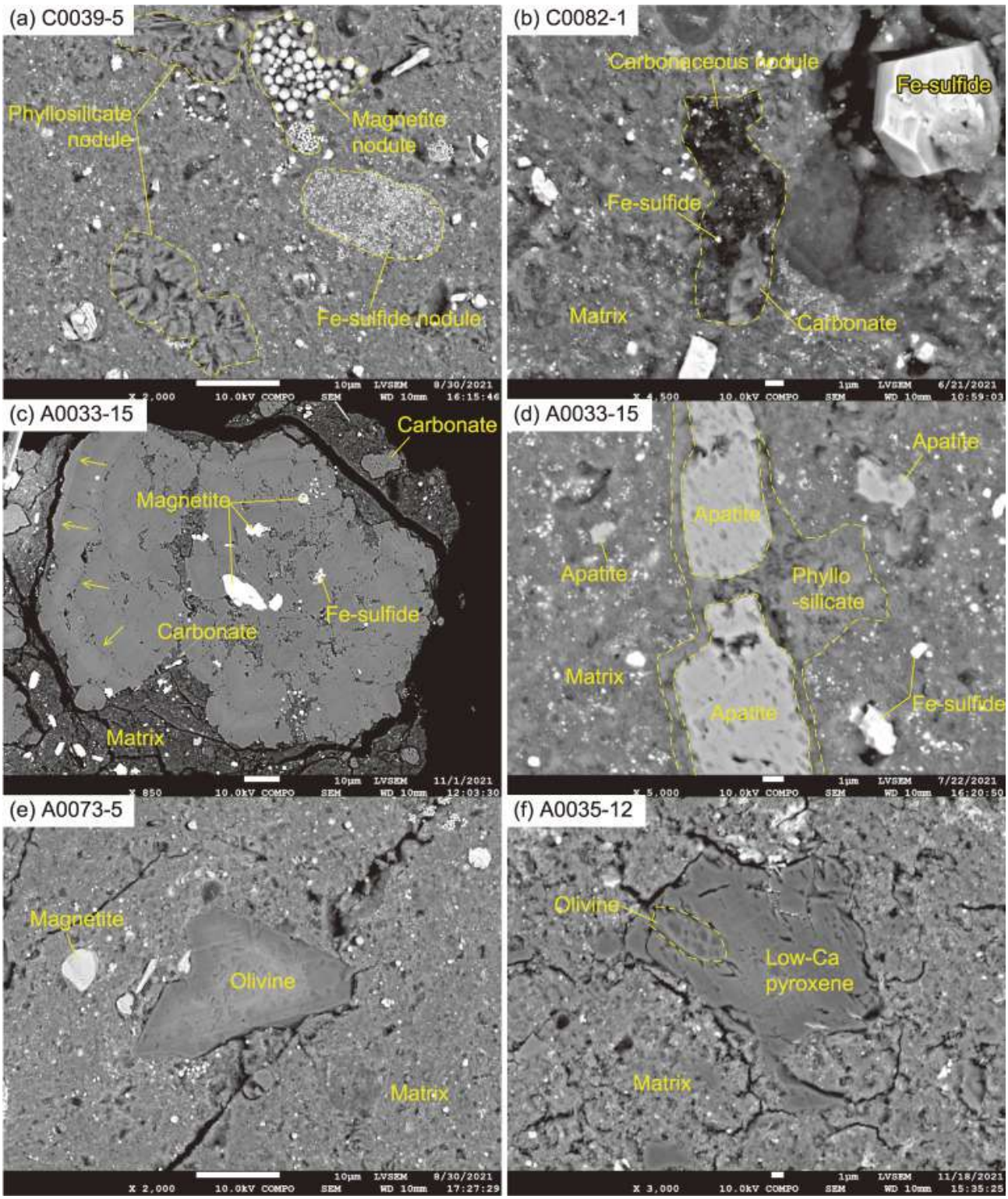

Figure 1.9: Low voltage scanning electron microscope (LVSEM) images showing the matrix mineralogy of Ryugu, similar to CI chondrite, includes various coarse-grained components such as phyllosilicate, carbonaceous, and carbonate nodules, magnetite, Fe-sulfide inclusions, apatite crystals, altered olivine fragments, and composite grains of low-Ca pyroxene and olivine. From E. Nakamura et al. (2022)

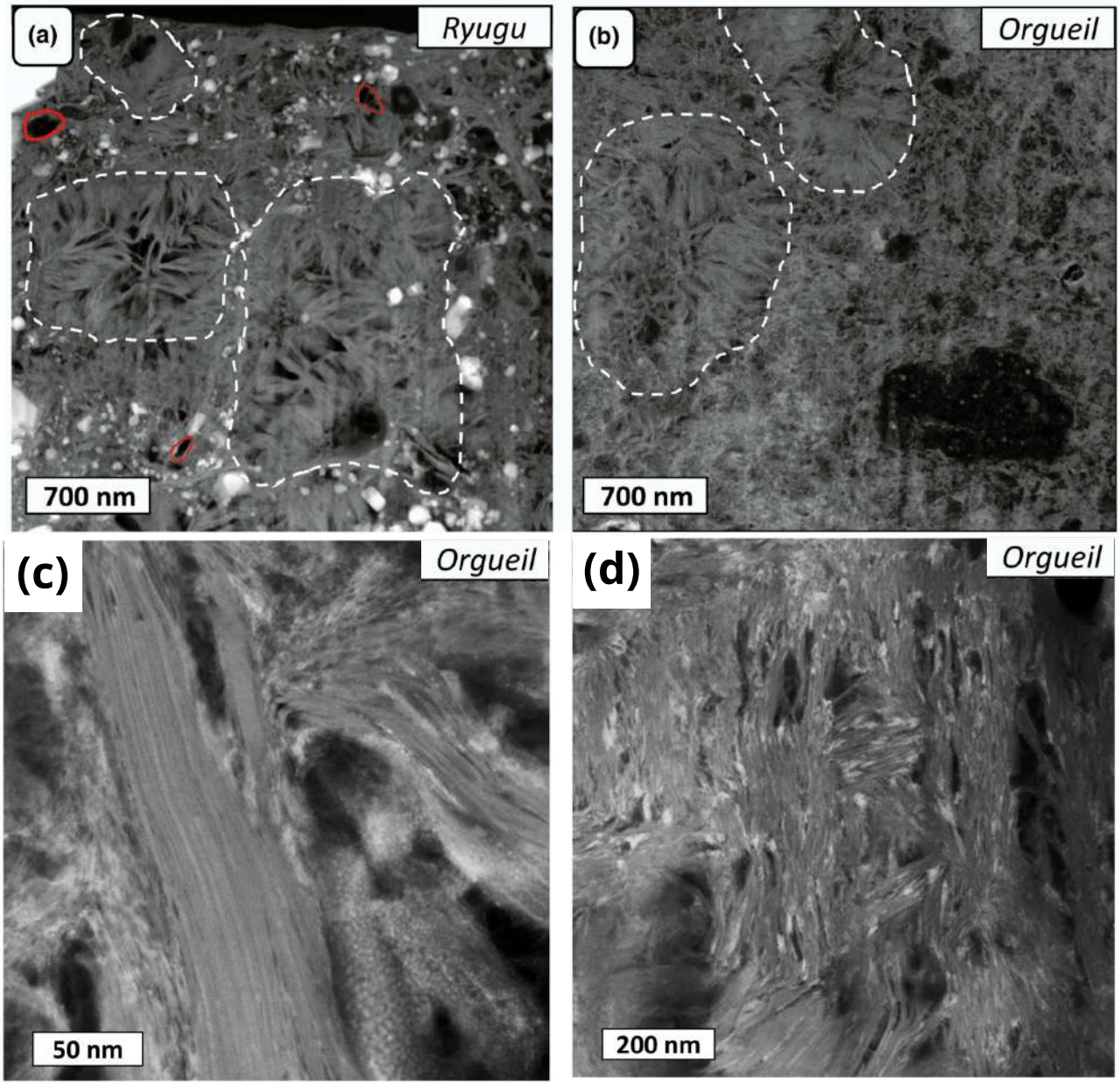

Figure 1.10: An overview of typical CI chondrite STEM-HAADF (High-Angle Annular Dark Field) images featuring phyllosilicate matrices with varying textures. These images typically show regions with a mix of fine and coarser grains, where inclusions like iron sulfides (In Ryugu) or iron oxydes (In Orgueil) may be less abundant or absent in the coarser areas. The transition between these different regions is often relevant, providing a clear distinction in the texture and composition within the chondritic material. Nanometer-scale organic matter is highlighted in Red. Ferrihydrite appears in (c) as bright areas within the fine-grained phyllosilicate matrix, while in (d), Fe-rich layers are interstratified within the phyllosilicates. Adapted from Leroux et al. (2023)

In summary, the matrix material in CI chondrites primarily consists of fine-grained minerals resulting from aqueous alteration processes, with a notable abundance of phyllosilicate minerals like serpentine and smectite clays. These minerals are indicative of extensive aqueous alteration on the meteorites' parent bodies. CI chondrites also contain anhydrous components such as olivine and pyroxenes, offering valuable clues about the original material present in the solar

nebula. The matrix hosts organic matter, including complex carbon compounds and amino acids. Sulfides are also abundant within the matrix, as well as carbonates and sulfates, the latter being generally a terrestrial weathering product.

4 Asteroidal Observations and Sample Return Missions

Sample return missions, such as *OSIRIS-REx* and *Hayabusa2*, play a vital role in advancing our understanding of the Solar System's formation and the fundamental materials that contributed to earth's development. Asteroidal samples offer unique insights that are unattainable through the study of meteorites found on earth. For instance, meteorites often lack the necessary context of their origin and sampling site, making it challenging to interpret their significance accurately. Moreover, meteorites are often influenced by terrestrial weathering processes, which can alter their composition and properties over time. In contrast, samples returned from asteroids remain relatively pristine, preserving their original state and providing a more accurate representation of the early Solar System. Sample return missions not only retrieve samples but also characterize the asteroids themselves, providing essential context for the collected materials. For example, the unexpected discovery of multiple lithologies on Bennu's surface by NASA's OSIRIS-REx space mission underscored the importance of understanding the context of the returned samples, a level of detail impossible to attain with meteorites whose parent bodies are unknown (Lauretta et al. 2019). Furthermore, these missions intentionally target asteroids believed to preserve some of the most primitive Solar System materials, such as carbonaceous chondrites. These materials may play an essential role in furthering our understanding of the Solar System formation as well as the potential role they might have played in delivering volatiles like water to Earth.

4.1 Hayabusa2 Space Mission

Launched in December 2014 as the successor to the original Hayabusa mission by the Japanese Aerospace Exploration Agency (JAXA), Hayabusa2 employs a unique hovering approach, matching the orbit of its target asteroid, 162173 Ryugu, rather than orbiting around it unlike many other space missions.

The main objective of Hayabusa2 space mission is sample collection. However, Hayabusa2 spacecraft also carries a suite of instruments for remote sensing and sampling, and contains

four deployable rovers to investigate the asteroid's surface. Key instruments include Optical Navigation Cameras (ONCs) for navigation and proximity operations, as well as a LIght Detection And Ranging (LIDAR) altimeter, which measures the distance between the spacecraft and the asteroid's surface. These tools collectively offer comprehensive data about Ryugu's dimensions and shape (Tsuda et al. 2013).

Hayabusa2 deployed several payloads during the mission. Rover-1A (HIBOU) and Rover-1B (OWL) successfully landed on the asteroid's surface in September 2018, capturing photographs. The Mobile Asteroid Surface Scout (MASCOT), landed in October 2018, carrying instruments to study the regolith structure. In April 2019, the Small Carry-on Impactor (SCI) excavated a crater to retrieve subsurface materials. A deployable camera (DCAM3) observed the crater and ejected particles (Tsuda et al. 2013).

The first sample retrieval operation took place in February 2019, with a 5 g metal bullet fired into the surface. On July 2019, Hayabusa2 conducted its second touchdown on Ryugu's surface, creating a crater approximately 20 meters in diameter and about 1.7 meters deep. This second touchdown aimed to collect samples that had not been exposed to space weathering. After this second collection, the spacecraft resumed its journey towards Earth, where it would release a capsule containing the 5.4 grams of asteroid samples collected from Ryugu's surface on December 6, 2020. The capsule containing the samples collected has landed in Australia, from where it has been transported to Japan for an initial analysis phase.

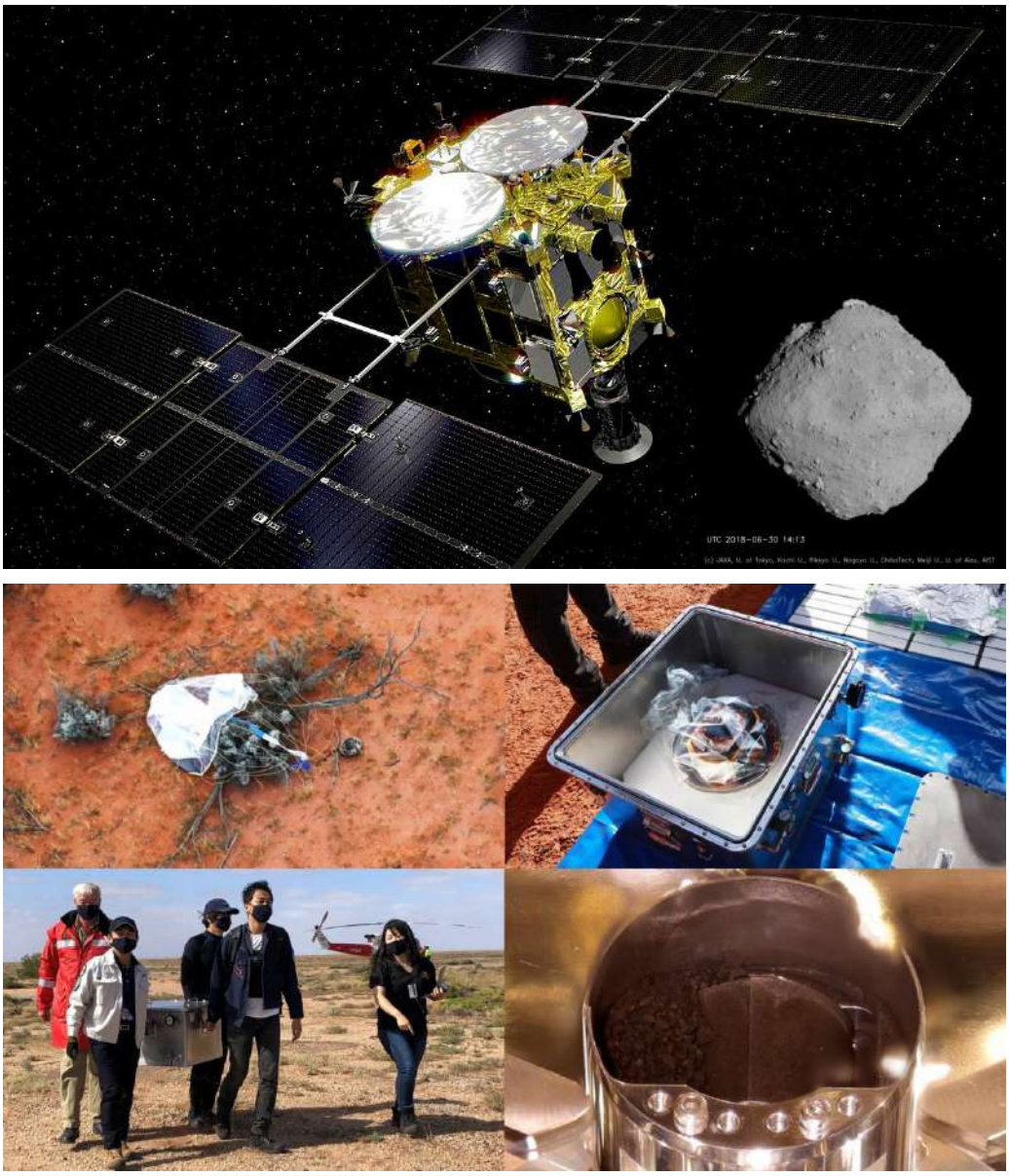

Figure 1.11: Hayabusa2 probe and Ryugu asteroid sample retrieval: Top: An artistic rendering of the Hayabusa2 probe with Ryugu asteroid in the inset image. Bottom: The initial images capturing the retrieval of the capsule containing the samples collected from Ryugu and one of the sample collection chambers. From JAXA's website

4.2 Early Discoveries and Initial Analyses of Asteroid Ryugu by Hayabusa2

Terrestrial observations of the asteroid (162173) Ryugu provided valuable informations about its properties before the Hayabusa2 space mission. Ryugu is roughly spherical with a diameter of approximately 875 meters, resembling a spinning top or diamond in shape. It has a slow rotation period of *7.63* hours and exhibits a low albedo of 0.0476, making it one of the darkest objects observed in the Solar System.

The initial observations of Hayabusa2's remote sensing instruments have been documented in the works of Kitazato et al.; Watanabe et al. (2019; 2019) and Sugita et al. (2019). Watanabe et al. (2019) provided measurements of Ryugu's mass, shape, and density, revealing its composition as an aggregate of loosely bound rocks, resulting in its distinctive spinning-top shape, which was likely shaped during a previous period of rapid rotation. Additionally, this study identified potential landing sites suitable for sample collection.

An important observation regarding the mineralogical properties of Ryugu was made using data acquired with the Near-Infrared Spectrometer (NIRS3) on Hayabusa2. In their work, Kitazato et al. (2019) highlighted the presence of a distinctive absorption feature at 2.72 μm, indicating the probable presence of OH attached to a cation, most likely magnesium (Mg), within a comparatively uniform phyllosilicate composition similar to the Mg-rich phyllosilicates observed in chondrites. Although there exist no meteorite samples so far which reflectance spectra match those of Ryugu samples at visible to NIR wavelengths, spectra from thermally metamorphosed CI chondrites and shocked CM chondrites (Fig.1.12) closely resemble the brightness and shape of Ryugu at near-infrared wavelengths. Additionally, it is observed that spectra of heated Ivuna meteorite samples and MET 01072 are darker, flat, and retain a weak 2.72 μm feature compared to unaltered carbonaceous chondrites.

Sugita et al. (2019) extensively described the geological features and surface colors of Ryugu. Combining their findings with those from the aforementioned papers, they provided some insights into the asteroid's formation process.

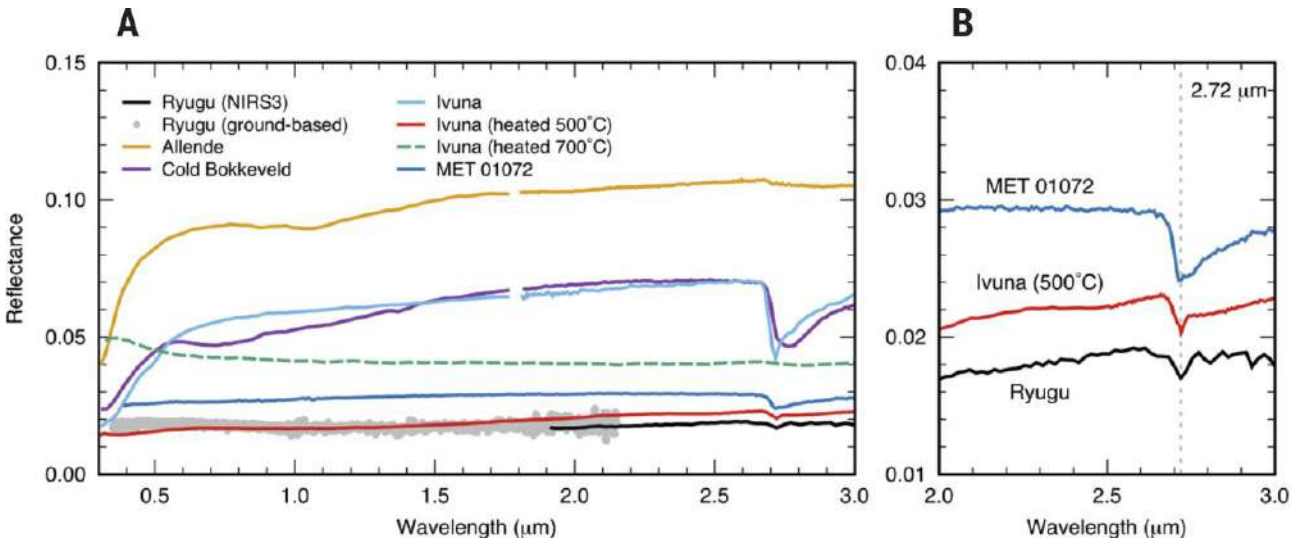

Figure 1.12: Comparison of Ryugu with meteorite spectra. (A) Globally averaged NIRS3 spectrum of Ryugu compared with laboratory spectra of meteorite samples: Ivuna (CI1), Cold Bokkeveld (CM2), MET 01072 (shocked CM2), and Allende (CV3). Details and references for the meteorite spectra are listed in table S1. A ground-based visible and NIR spectrum of Ryugu (6) is also plotted. (B) Enlargement of the NIRS3 wavelength range in (A). Adapted from Kitazato et al. (2019)

Upon their return to Earth in December 2020, an initial non-destructive phase 1 characterization of the particles in a dedicated, contamination-free and pure-nitrogen-filled chamber at the JAXA curation facility was conducted and are outlined in the works of Ito et al.; Yada et al.; T. Nakamura et al. (2022; 2022; 2022) and Yokoyama et al. (2022). All of their results further confirm that Ryugu particles closely resemble CI chondrites but exhibit a higher degree of chemical pristine nature, rendering them the best available match to the chemical composition of the Sun's photosphere. Ito et al. (2022) conducted a comprehensive bulk and micro-analytical study of Ryugu particles, revealing an intricate spatial relationship between aliphatic-rich organics and phyllosilicates, indicative of maximum aqueous alteration temperatures of approximately $\sim$ 30°C. In terms of mineralogy, Ryugu features rich phyllosilicates and carbonates formed through low-temperature and high-pH aqueous alteration processes. In contrast, less altered fragments comprise olivine, pyroxene, amorphous silicates, calcite, and phosphide, with notably low abundances of materials formed at high temperatures, such as chondrules and Ca-Al-rich Inclusions (T. Nakamura et al. 2022). Numerical simulations, based on the mineralogical and physical properties of the samples, suggest that the parent body of Ryugu formed nearly 2 million years after the beginning of Solar System formation.

5 Conclusion and Problem statement

This introductory chapter has provided a comprehensive overview of asteroids and meteorites, with a specific focus on the significance of CI chondrites in understanding the formation and evolution of the Solar System. By exploring the processes involved in the formation of meteorites and asteroids, as well as the secondary processes shaping their mineralogy and chemistry, we have gained valuable insights into the early stages of planetary formation. The discussion of CI chondrites, their unique characteristics, and their role as primitive remnants of the early Solar System has underscored their importance as key objects for scientific investigation. Furthermore, the examination of asteroidal observations and sample return missions has highlighted the importance of direct exploration and analysis of celestial bodies in advancing our understanding of planetary evolution.

Transmission electron microscopy (TEM) has emerged as a powerful tool for unraveling the mineralogical and petrographical properties of meteoritic samples. At varying scales, TEM techniques facilitate the observation and analysis of diverse matrix constituents, from providing an overview of different components in a single image through low-magnification imaging TEM and scanning transmission electron microscopy-high angle annular dark field (STEM-HAADF) imaging, to discerning complex fine-scale mixtures such as serpentine and smectite as well as atomic resolution imaging of coarse grained material via high-resolution TEM.

TEM has been instrumental in numerous studies on chondrites, particularly in elucidating the nature of phyllosilicates through imaging and diffraction, while advanced scanning transmission electron microscopy techniques, such as energy dispersive X-ray spectroscopy (STEM-EDXS), enabled multifaceted analyses, including segmentation of elemental maps into distinct mineral phases within samples and compositional field analyses.

However, the series of structural and chemical transformations that the primitive material of the solar system has undergone are still not well understood. For instance, the debate persists regarding the formation of phyllosilicates—whether through alteration of amorphous material or anhydrous silicates. Studies have demonstrated that amorphous silicates can undergo rapid transformation into phyllosilicates when exposed to aqueous fluids, while other findings suggest that phyllosilicates are the result of alteration on olivine and/or pyroxene. The formation

mechanisms of amorphous silicates themselves are still subject to debate. Hypotheses include their origin as "primordial" dust inherited from the molecular cloud, their formation through the condensation of high-temperature gas associated with chondrule formation, or their creation through the alteration of a crystalline precursor.

Acquiring more comprehensive mineralogical and structural insights into phyllosilicates and the associated minerals can provide more constraints on potential precursor identities and the environmental conditions under which they and the matrix minerals were formed.

Although phyllosilicates in chondrites may hold insights into these different questions, conventional TEM and STEM methods face limitations in analyzing these intricate phases due to factors such as the poor crystallinity in phyllosilicates and the fine-scale mixing of their constituents such as serpentine and smectite, as well as their beam sensitive nature.

Recent advances in electron detection technologies, notably direct electron detectors (DEDs), have revolutionized characterization techniques. These detectors facilitate faster scanning electron diffraction experiments, essential for structural characterization and high-resolution STEM imaging. Among the array of characterization techniques enabled by DEDs, four-dimensional scanning transmission electron microscopy (4D-STEM) has overcome many challenges faced by conventional TEM techniques. Unlike selected area electron diffraction, where electron diffraction patterns are obtained from specific regions of $\sim 100\ nm$ sizes and which is constrained by the fine-grained nature and thickness changes of individual crystallites, 4D-STEM, as will be described in the next chapter, enables spatially representative structural analysis with minimal irradiation damage by acquiring full two-dimensional diffraction patterns across the entire illuminated area of a specimen at each position of the converged electron probe, making it suitable for the structural investigation of beam-sensitive and poorly crystallized materials such as phyllosilicates at various scales.

In this thesis, we aim to gain insights into the intricate structural characteristics of phyllosilicates using 4D-STEM, particularly focusing on serpentine and its interactions with smectites and other constituents. The spatial representativity of 4D-STEM empowers a comprehensive characterization of phyllosilicates at a fine-scale level, capturing intricate local information and overall patterns within field of views comparable to those employed in STEM-EDXS. By exploring the mineralogy of Hayabusa2's Ryugu samples and Orgueil carbonaceous chondrite samples

with 4D-STEM, we aim to delve into the nature of serpentine and smectite in these materials and the subsequent consequences on the evolutionary history of Ryugu and Orgueil. Moreover, we seek to assess the different structural features of smectites, including the variability in their interlayer spacing in chondritic samples, which is still subject to debate. Through these endeavors, we aim to contribute to a deeper understanding of the mineralogical and evolutionary dynamics of these extraterrestrial objects.

Chapter 2

Experimental Methods and Data Analysis

1 General Setup of a Transmission Electron Microscope (TEM)

The concept of transmission electron microscopy was first demonstrated by Knoll and Ruska (1932). The setup of a Transmission Electron Microscope (TEM) can be summarized as an electron emitting gun, an electrons accelerating system, a condenser system of electromagnetic lenses to control beam intensity and focusability, a specimen holder for positioning samples, and an objective lens that transmits electrons through the specimen. Additionally, in scanning transmission electron microscopy (STEM) mode (STEM mode will be presented in a dedicated section), a scanning system is also used to shifting a focused probe across the investigated sample. Finally, TEMs are generally equipped with a set of systems allowing for different types of imaging and analysis.

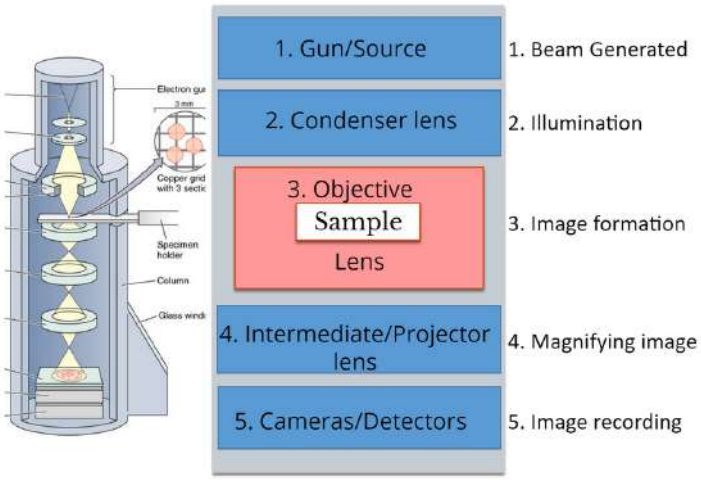

Figure 2.1: Typical Transmission Electron Microscope column: In addition to the elements outlined in the present figure, most TEMs can also work in STEM mode. Adapted from Alberta NanoFab 2024

1.1 Conventional and High Resolution TEM

When using a collimated broad electron illumination on electron-transparent samples, the TEM is said to operate in its conventional mode. Upon transmission through the specimen, the electron wave in this mode is detectable in both diffraction and real spaces, leading to a wide range of signals corresponding to different informations. The short wavelength of electrons in TEM systems operating at acceleration voltages of few hundred kilovolts theoretically ensures picometer resolutions assuming the diffraction limit (Fig. 2.2). However, achieving this is generally not possible due to unavoidable imaging errors, such as spherical and chromatic aberrations. These errors originate from the electromagnetic lenses used to focus the electron beam. Scherzer (1936) theorem outlines these aberrations, proving the positive nature of spherical aberration regardless of lens design and nature (electrostatic or magnetic). These inherent limitations have led to the development of advanced correction techniques and innovative imaging approaches, such as aberration-corrected TEM and phase-contrast imaging striving to push the boundaries of achievable resolution in electron microscopy. These are considered as major breakthroughs in high-resolution TEM (Eg. Haider et al. 1998; Shibata et al. 2019).

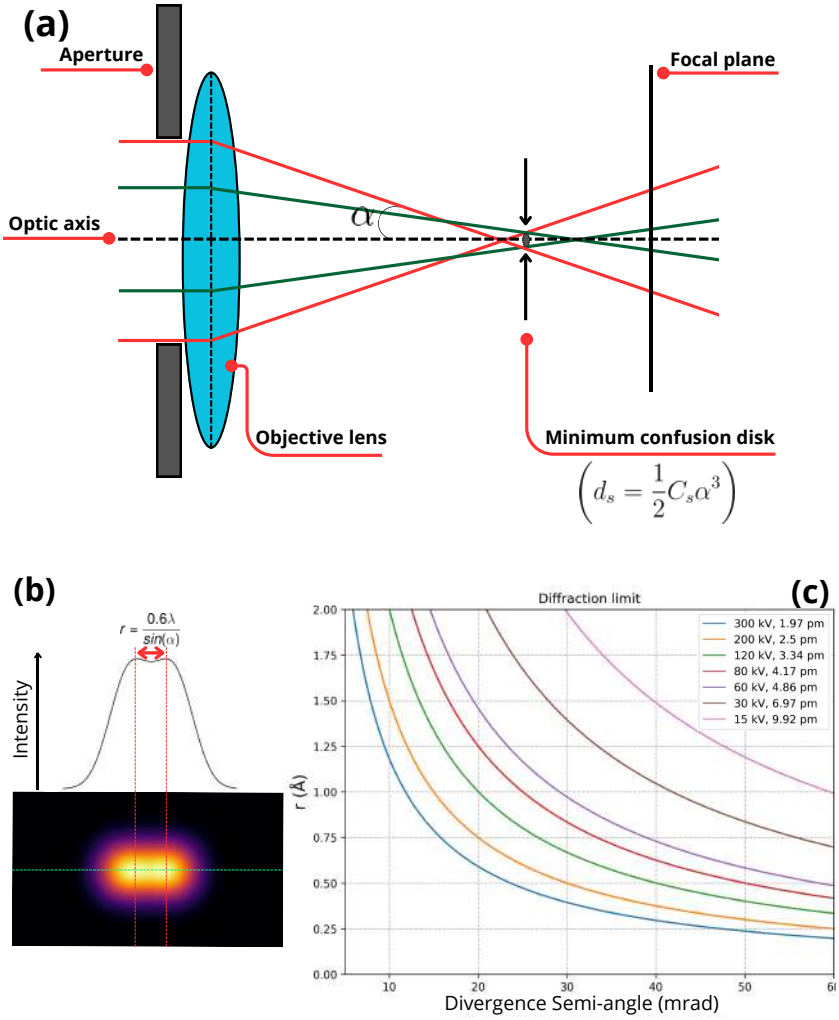

Figure 2.2: Effect of spherical aberration and diffraction limit on the resolution in electron microscopy. (a) Schematic diagram depicting the spread of electron beams due to the spherical aberrations of the objective lens. Due to these aberrations, a point is imaged as a spot and the smallest such spot that a lens can produce is a *disk of least confusion* of diameter $d_s = \frac{1}{2}C_s\alpha^3$. (b) Two spatially close points are blurred by diffraction, hence limiting the resolution. The smallest resolvable distance between two points with any optical technique is limited by $r = \frac{0.6\lambda}{sin(\alpha)}$. (c) The resolution r as a function of divergence semi-angle for multiple accelerating voltages. Increasing the divergence angle enhances resolution, yet it also enlarges the disk of least confusion because of spherical aberrations resulting in a blurred image. Therefore, it is crucial to minimize spherical aberrations and find a balance between divergence angle and aberrations to achieve optimal resolution.

2 Scanning Transmission Electron Microscopy (STEM)

In STEM mode, the electron beam is focused into a fine probe using a combination of condenser lenses and apertures (Fig. 2.3). The focused probe is then scanned across the specimen in a raster pattern using scanning coils or deflectors. The focusability of an electron microscope in STEM mode is further improved by probe-forming aberration correctors (Krivanek et al. 1999). During a STEM acquisition, a multitude of sample-material interaction channels

can be read and used for different analytical purposes simultaneously. For instance, elastically scattered electrons can be used for imaging and diffraction purposes. Indeed, different collection angle ranges lead to different STEM imaging techniques such as bright-field (BF), annular dark-field (ADF), and high-angle annular dark-field (HAADF), each utilizing dedicated detectors. Furthermore, diffraction patterns produced by electrons interacting with the sample can be recorded using dedicated detectors and used for structural analysis. Inelastic scattering also occurs where incident electrons transfer energy to the specimen hence resulting in an energy loss. This phenomenon leads to the generation of various signals including, for instance, electron energy-loss spectroscopy (EELS) signals which provide information about the sample's electronic structure and composition. Other types of signals are also encountered, such as X-ray emission, where incident electrons interact with the sample material, inducing the emission of characteristic X-rays. These X-rays are analyzed by energy-dispersive X-ray spectroscopy (EDS) to determine the sample's elemental composition. Other types of signals are also encountered, such as cathodoluminescence, plasmon and phonon excitations and many others (Williams and Carter 2008), each offering distinct informations about the sample's characteristics and behavior. Table 2.1 summarizes the most widely used STEM signals.

Table 2.1: Some relevant STEM signals dimensions: (x, y) represent the probe position in real space. E_{EL} represents the energy loss in EELS. E_{Xrays} represents the X-rays energy detected in EDX, and (k_x, k_y) are the coordinates of the reciprocal space in 4D-STEM.

Signals generated in STEM	**Signal dimensions**
Imaging (BF, DF, HAADF, HR-STEM)	(x, y)
Electron Energy Loss Spectroscopy (EELS)	$(x, y \mid E_{EL})$
Energy-Dispersive X-ray Spectroscopy (EDX)	$(x, y \mid E_{Xrays})$
Four-dimensional Scanning Transmission Electron Microscopy (4D-STEM)	$(x, y \mid k_x, k_y)$

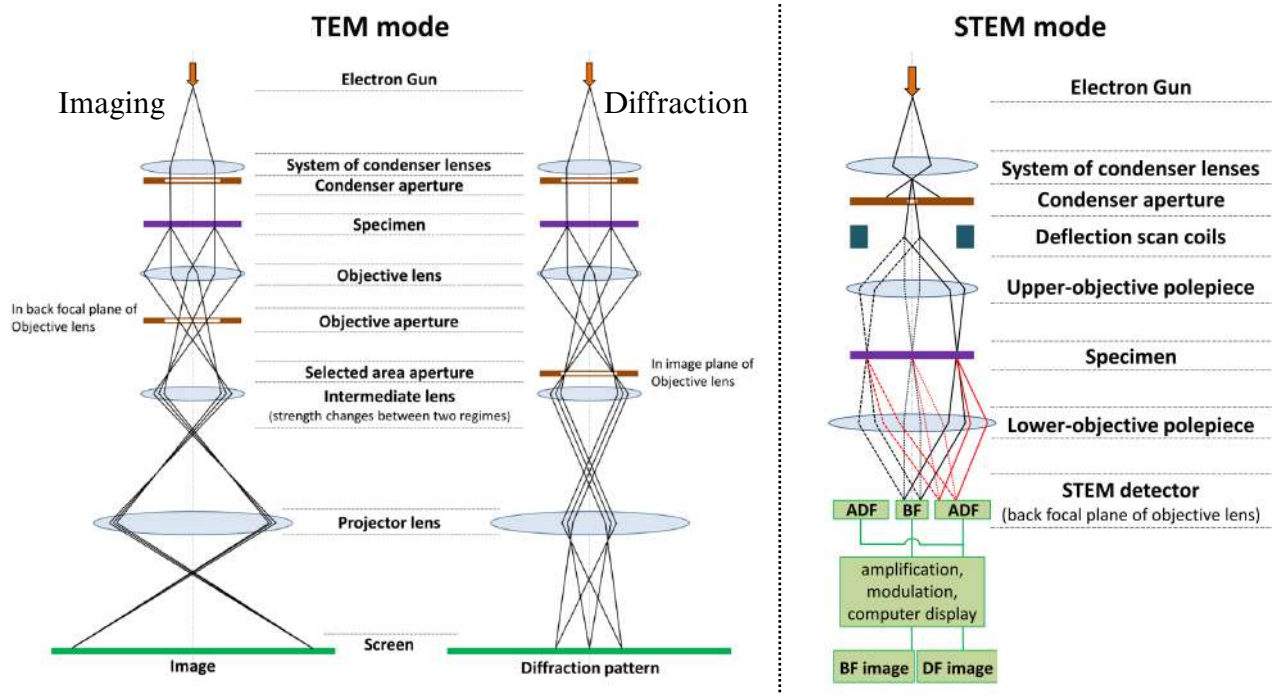

Figure 2.3: TEM vs STEM modes: In the left panel, TEM operational mode is depicted for both imaging and diffraction lens configurations. Here, the necessity to toggle between diffraction and real space imaging is necessary to obtain relevant informations from both spaces. In contrast, the right panel illustrates the STEM mode in which simultaneous acquisition of imaging and diffraction information, as well as multiple other signals through different dedicated detectors, is possible. Adapted from Williams and Carter (2008)

2.1 High-Angle Annular Dark Field Imaging (HAADF)

High-angle annular dark field (HAADF) is a STEM imaging technique in which electrons scattered at sufficiently high angles are recorded in a dedicated annular detector to form an image. High-angle scattering involves electrons experiencing the full nuclear charge, leading to a scattering cross-section approaching that of Rutherford scattering ($\propto \mathbf{Z}^2$). However, due to electron screening, the scattering cross section is slightly modified and is nearly proportional to $\mathbf{Z}^n$ with $n \in [1.1, 1.8]$ (Williams and Carter 2008). A direct consequence of requiring high scattering angles to be involved in this Z-contrast imaging technique is that the atoms, in this case, behave like independent scatterers. Consequently, when passing a STEM probe over an array of them, each atom will scatter independently and proportionally to the local probe intensity it sees. This is exactly what the action of convolution between a probe and an object is and the image in this case is given by:

$$I(\mathbf{R}) = O(\mathbf{R}) \otimes |P(\mathbf{R})|^2 \tag{2.1}$$

Where $O(\mathbf{R})$ is the object function which represents, in this case, the array of scatterers (atoms) and $|P(\mathbf{R})|^2$ is the probe intensity profile.

The image, in this configuration, is hence a representation of the object blurred by the size of the probe which is referred to as *incoherent imaging*. Therefore, unlike coherent imaging where contrast may form due to interference processes, HAADF images are easily interpreted in terms of material composition and its resolution is almost determined by the incident probe diameter on the specimen (Kirkland 2020; Williams and Carter 2008).

2.2 Energy Dispersive X-ray Spectroscopy (EDX)

When a high energy electron beam penetrate through the outer valence band and interacts with the inner-shell electrons of an atom, characteristic X-rays can be produced. Indeed, when an inner-shell electron absorbs an excessive amount of energy, it breaks free from the nucleus' pull, leaving a hole within the inner shell. The ionized atom eventually returns to its ground state by filling the hole left by another electron from an outer shell. This transition is accompanied with the emission of characteristic X-rays which energies are measured with dedicated X-ray spectrometers. The specific energies of the emitted X-rays carry information about the elemental composition of the sample being analyzed. Their intensity however can vary based on different factors such as sample thickness, depth of the electron beam penetration, and the atomic number of the element. An approach to mitigate these effects for a robust *EDX* quantification is using the Cliff-Lorimer method (Cliff and Lorimer 2011). For the scope of this thesis, no *EDX* quantification is required and the only focus is on qualitative analysis in which the goal is to identify the elements present in our samples by matching the observed X-ray lines with X-ray lines of known elements.

3 Four-dimensional Scanning Transmission Electron Microscopy (4D-STEM)

Four-dimensional Scanning Transmission Electron Microscopy (4D-STEM) is an advanced electron microscopy technique that enables the simultaneous acquisition of both spatial and diffraction information at the nanoscale. In 4D-STEM, a finely focused electron probe is scanned across a two-dimensional (2D) grid of positions on the sample surface. At each position, a full two-dimensional diffraction pattern is acquired (See Fig. 2.4), resulting in a dataset with two spatial dimensions (x and y) and two reciprocal space dimensions (k_x and k_y). This dataset can be visualized and analyzed to extract a wide range of informations about the sample, including crystallographic orientation, strain distribution, local atomic arrangement and medium and short range order in poorly crystalline materials. Unlike conventional TEM, where diffraction and imaging are typically performed separately or early STEM imaging where images are acquired simultaneously but on separate detectors, 4D-STEM offers a holistic approach by combining imaging and diffraction into a single measurement. This allows for rapid and comprehensive characterization of complex materials and nanostructures, making 4D-STEM a powerful tool for investigating the properties and behavior of materials down to the atomic scale.

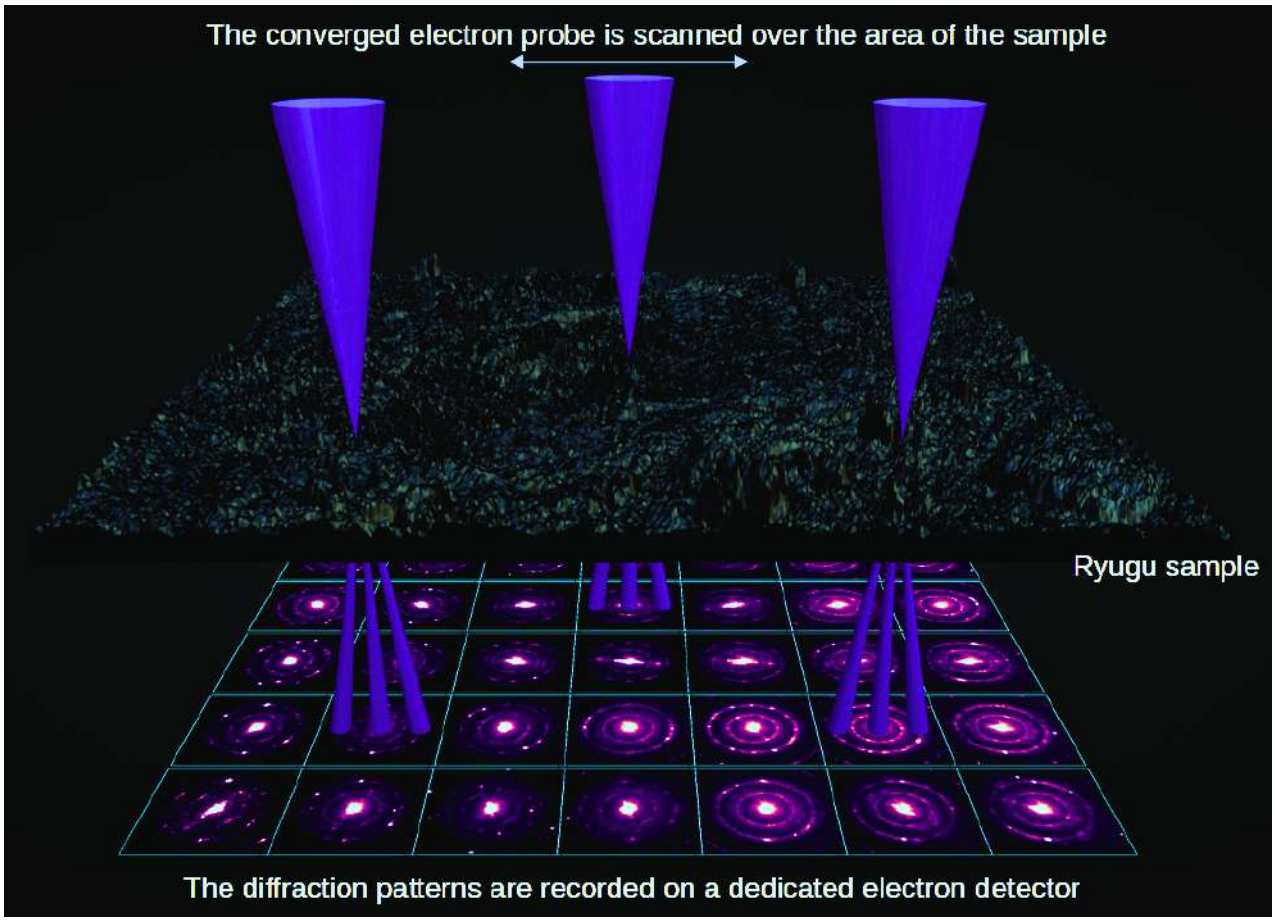

Figure 2.4: Schematic of a typical 4D-STEM experiment. The cones in blue represent the STEM electron probe being rastered over the sample area. Each diffraction pattern in the figure is an average of 9×9 experimental diffraction patterns recorded on a Medipix3 pixelated detector.

Although 4D-STEM has gained a lot of popularity due to advancements in high-performance electron detection technology (Yang et al. 2016; Krajnak et al. 2016; Yang et al. 2017; Ophus 2019; Pennycook et al. 2019; Savitzky et al. 2021; Ophus et al. 2022), some first measurements that can be also regarded as 4D-STEM were performed in the early 2000s by Zaluzec (2002). Others have also performed 4D-STEM for different purposes, although using different terms sometimes instead of "4D-STEM" including Clément et al.; E. Rauch and Dupuy; E. Rauch and Dupuy; Tao et al.; A. Hirata et al.; Liu et al.; E. Rauch and Véron; Ozdol et al.; Gallagher-Jones et al. (2004; 2005; 2006; 2009; 2010; 2013; 2014; 2015; 2019) and Hachtel et al. (2018), the latter, alongside Muller et al. (2016) being among the first to have introduced the term "universal detectors" to describe virtual imaging in 4D-STEM experiments.

An overview of the basic principles of diffraction pattern formation is provided in annex A.

3.1 Example Applications of 4D-STEM

3.1.1 Virtual Imaging

The most obvious, yet fundamental, use of 4D-STEM is diffraction contrast imaging, usually referred to, in the context of 4D-STEM, as "virtual imaging", since "virtual" detectors are used to form an image. Indeed, by adding together subsets of pixels in the diffraction patterns at each probe position, not only can we mimic various imaging modes that traditionally require different physical detectors, but we can also reconstruct virtual images using arbitrarily shaped virtual detectors that are impossible to physically implement in STEM. For instance, when adding together the subset of pixels in diffraction space corresponding to the transmitted beam, we form a "virtual bright field (VBF)"image. Conversely, when doing so in any other subset besides the transmitted beam, this results in a "virtual dark field (VDF)" image. Furthermore, virtual diffraction patterns can be reconstructed by adding together subsets of pixels in the real space. This flexibility allows for different types of materials characterization without the need to physically changing the experimental setup.

This form of imaging is well explained in Gammer et al. (2015), highlighting its use in the analysis of an Fe–Al–Ni–Cr alloy. The concept is well illustrated in Figure 2.5a, wherein virtual detectors in real space are used for extracting representative virtual diffraction patterns over arbitrarily shaped regions of interest (ROIs). These ROIs may be referred to as *real space virtual detectors*. Simultaneously, virtual detectors in diffraction space (Figure 2.5b) are employed for extracting virtual dark field images representative of the corresponding diffraction signatures, achieved through combinations of multiple ROIs in diffraction space.

Figure 2.5c, from Shukla et al. (2016), illustrates the use of virtual detectors to assess the existence of three ordering variants within a battery cathode material. This example underscores two significant advantages of 4D-STEM. Firstly, with a single selected area electron diffraction pattern covering the entire particle, it would not be possible to differentiate between the variants since the fundamental reflections in the diffraction patterns are common among them. However, 4D-STEM enables the separation of these variants using virtual apertures. Secondly, this example illustrates how 4D-STEM can in some cases yield comparable information to atomic-resolution HRTEM or conventional STEM images but over a considerably larger

field of view (FOV), providing a broader perspective for analysis. Finally, in Figure 2.5d, an atomic resolution imaging of $DyScO_3$ example illustrates the possible implementation of virtual annular detectors (Hachtel et al. 2018).

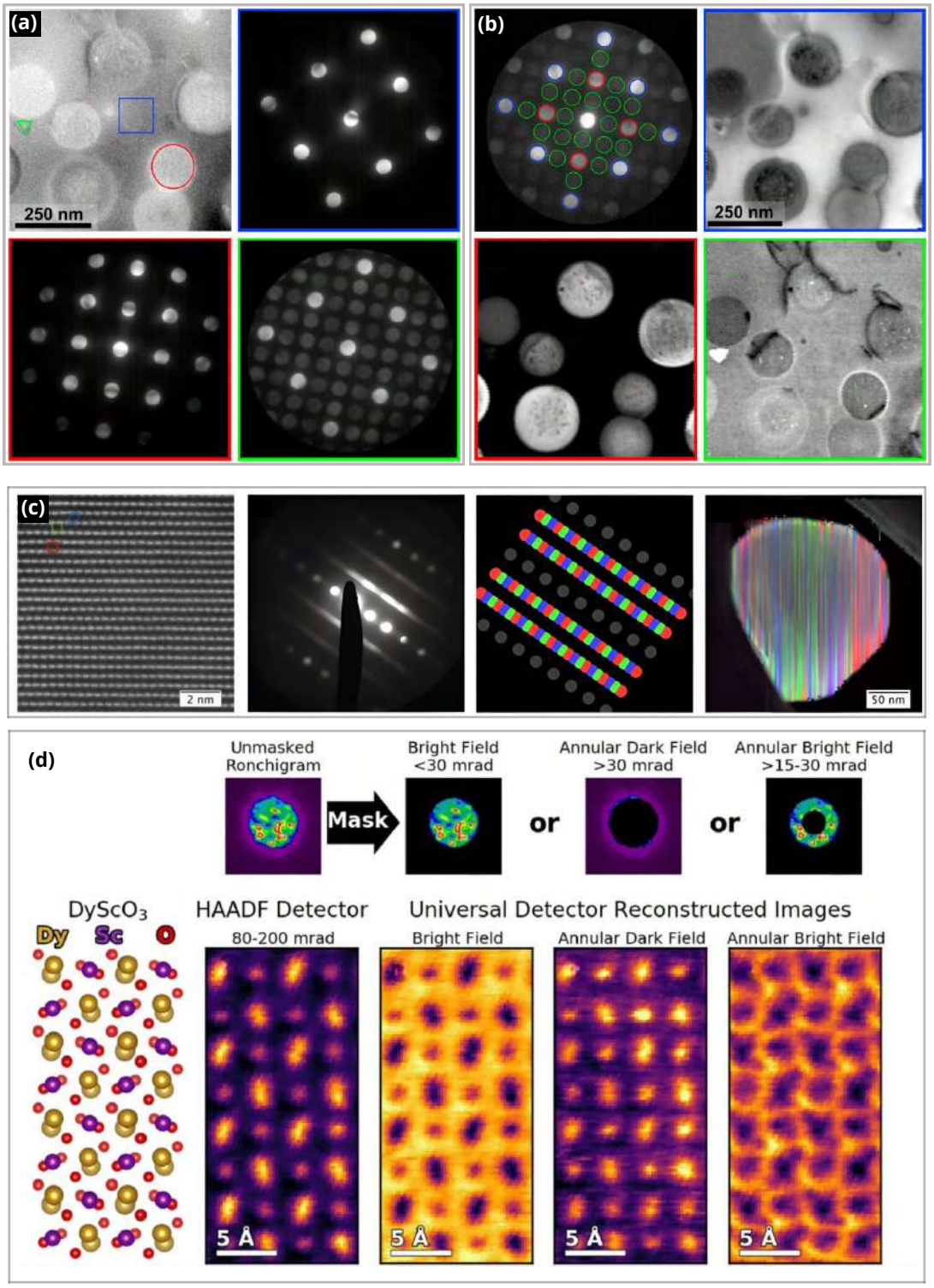

Figure 2.5: 4D-STEM virtual imaging use cases: (a) shows mean diffraction patterns from ROIs in real space, while (b) highlights virtual images generated from ROIs in diffraction space from Gammer et al. (2015). (c) HAADF-STEM image capturing a *LRTMO* cathode particle, alongside the summed virtual pattern derived from the 4D-STEM dataset and the location and shape of virtual apertures (color-coded) corresponding to the three monoclinic variants. A reconstructed RGB virtual dark field image is also displayed, highlighting domains corresponding to the three variants (From Shukla et al. (2016)). (d) Example of Virtual annular detectors for atomic resolution imaging for a $DyScO_3$ sample from Hachtel et al. (2018).

3.1.2 Phase and Orientation Mapping

Significant advances in structural characterization of materials with 4D-STEM predate its recent surge in popularity. Early contributions, such as those by E. Rauch and Dupuy; E. Rauch and Veron (2005; 2005) and E. Rauch and Véron (2014), laid the foundation for "template matching" based automated crystal orientation mapping, culminating in the development of the *ASTAR system* (Véron and E. Rauch 2011; Veron and E. Rauch 2012a). This system, now compatible with most commercial TEMs, has been successfully employed across multiple disciplinary fields. Noteworthy applications include its utilization in metallurgy and plasticity studies such as in E. Rauch; Descartes et al. (2008; 2011), in mineralogical investigations (Eg. Verezhak et al. 2016; Roqué Rosell et al. 2018), in virtual dark field imaging (Boulay et al. 2014; E. Rauch and Véron 2014b; Guo et al. 2018), and in-situ strain mapping (Veron and E. Rauch 2012b; Kobler et al. 2013; Mompiou et al. 2013; Armstrong et al. 2021), among many others.

For orientation mapping, diffraction patterns are pre-computed for each orientation of a given material, and then, a correlation score is computed for each experimental pattern. As outlined previously, this method can be fully automated and can also generate an estimate of the measurement confidence using the maximum correlation score (E. F. Rauch et al. 2010; E. Rauch and Véron 2014b).

An example of orientation mapping over a twisted polycrystalline $AuAgPd$ nanowires sample is shown in Figure (2.6a-e). This example, from Ophus et al. (2022), features the use of a "bullseye" patterned probe (shown in the inset of the HAADF-STEM image 2.6a) for improved detection precision of the Bragg disks, showcasing innovative developments in acquisition methodologies. Using a correlation intensity threshold of 0.5 that was arbitrarily chosen as a lower bound for a potential match, the number of matching patterns is shown in Figure 2.6c. Two matches to a single diffraction pattern are also shown in 2.6d. Finally, the orientations, in the three different direction (x, y, z), for all probe positions, with only the two best matches shown are outlined in 2.6e.

Figure 2.6f shows the possibility of simultaneous phase and orientation mapping, which is showcased for a $LiFePO_4$ sample, from an experiment performed by Brunetti et al. (2011) using Precession electron diffraction (PED) and the ASTAR system. These experiments were

used to determine the correct transformation pathway model for this material.

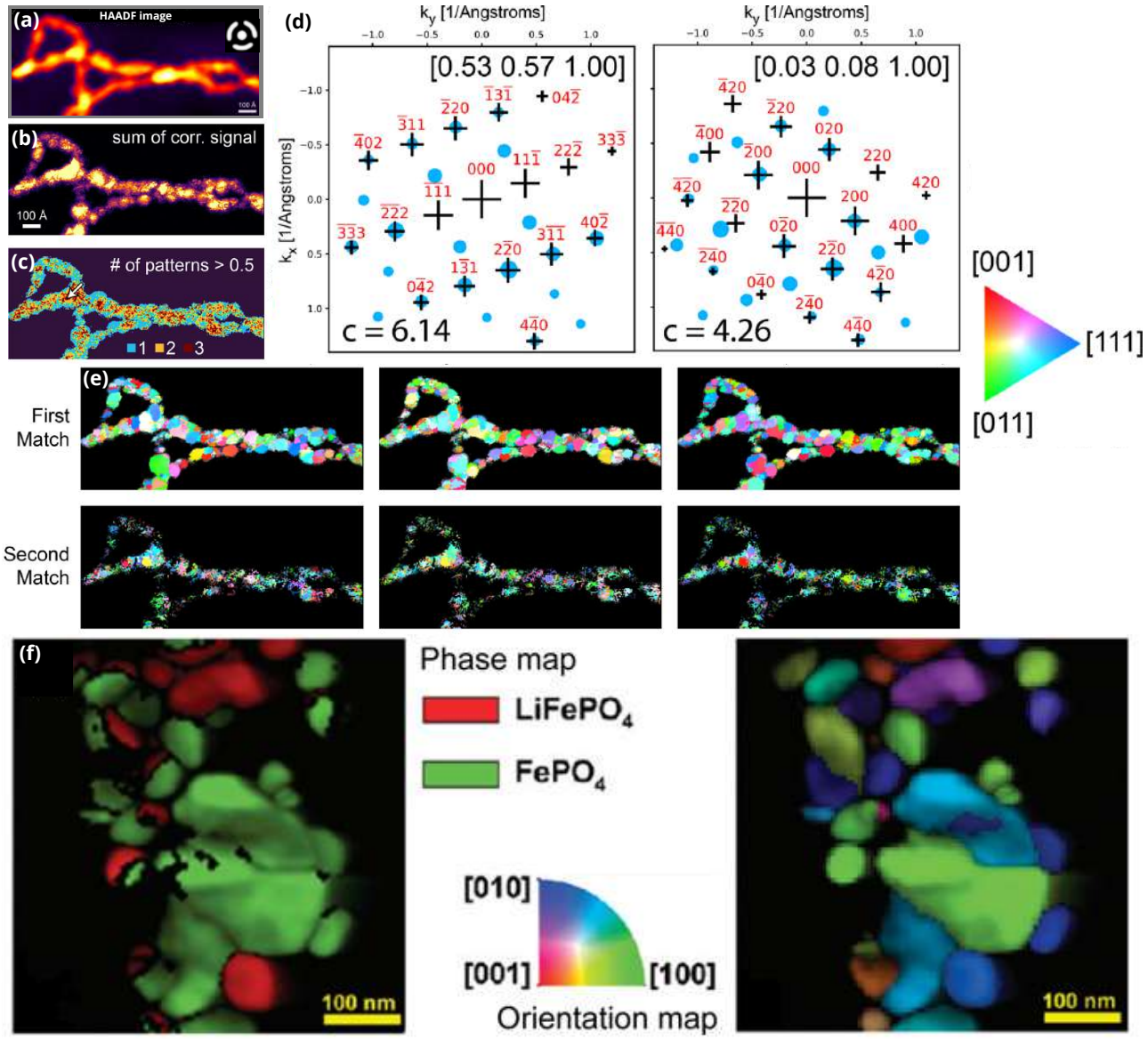

Figure 2.6: 4D-STEM phase and orientation mapping examples: For a (a) polycrystalline $AuAgPd$ nanowires sample from Ophus et al. (2022), (b) shows the total measured correlation signal for each probe position, along with (c) the estimated number of patterns indexed for each probe position. An example of two orientations indexed from a single diffraction pattern, collected at the position indicated by the arrow, is shown in (d). (e) represents the final orientation maps obtained for the two highest correlation signals for each probe position. An example of simultaneous phase and orientation determination for a $LiFePO_4$ sample is shown in (f) from Brunetti et al. (2011).

3.1.3 4D-STEM of Beam Sensitive Samples

Characterizing beam-sensitive materials presents a significant challenge in materials science, primarily due to the inherent limitations of conventional characterization methodologies. Traditional techniques in TEM and STEM often result in sample damage or alteration of the material under investigation. Additionally, these methods may lack the spatial resolution or sensitivity required to fully capture the intricate features of beam-sensitive samples. However, in 4D-STEM experiments, the total fluence of incident electrons can be effectively controlled through various approaches. These may include careful use of the beam blanker, steering of the localized electron dose, sample cooling, or minimizing the fluence in the convergent beam, thus potentially minimizing beam-induced damage (Bustillo et al. 2021). This technique is suitable for a wide range of beam sensitive materials with different structural characteristics. A common example is the case of the π-π stacking of polymer chains encountered in covalent organic frameworks (COFs) and many other organic materials (Eg. Zheng et al. 2022). These stackings are often characterized by weak and/or diffuse diffraction spots at separations on the order of 3.4-4.2 Å. With 4D-STEM, we are able to map these stacking and their orientations, but also the degree of stacking as well as the stacking domain sizes. An example application on covalent organic frameworks (*COFs*) from Salaün et al. (2023) is summarized in Figure 2.7. In their innovative study, focusing on utilizing polymers to control the growth of *COFs* in specific directions, Salaün et al. (2023) used a combination of HRTEM imaging and 4D-STEM to decipher the unique atomic structure and the π-π stacking nature. The approximate domain size of this stacking can be deducted from the VDF image in (2.7d). Furthermore, the corresponding orientation of the π-π stacking can be obtained as shown in (2.7e). Figures 2.7(f-i) show the differences in the π-π stacking orientation in two different types of *COFs* which hasn't been previously seen for this type of particles providing yet another avenue currently under exploration.

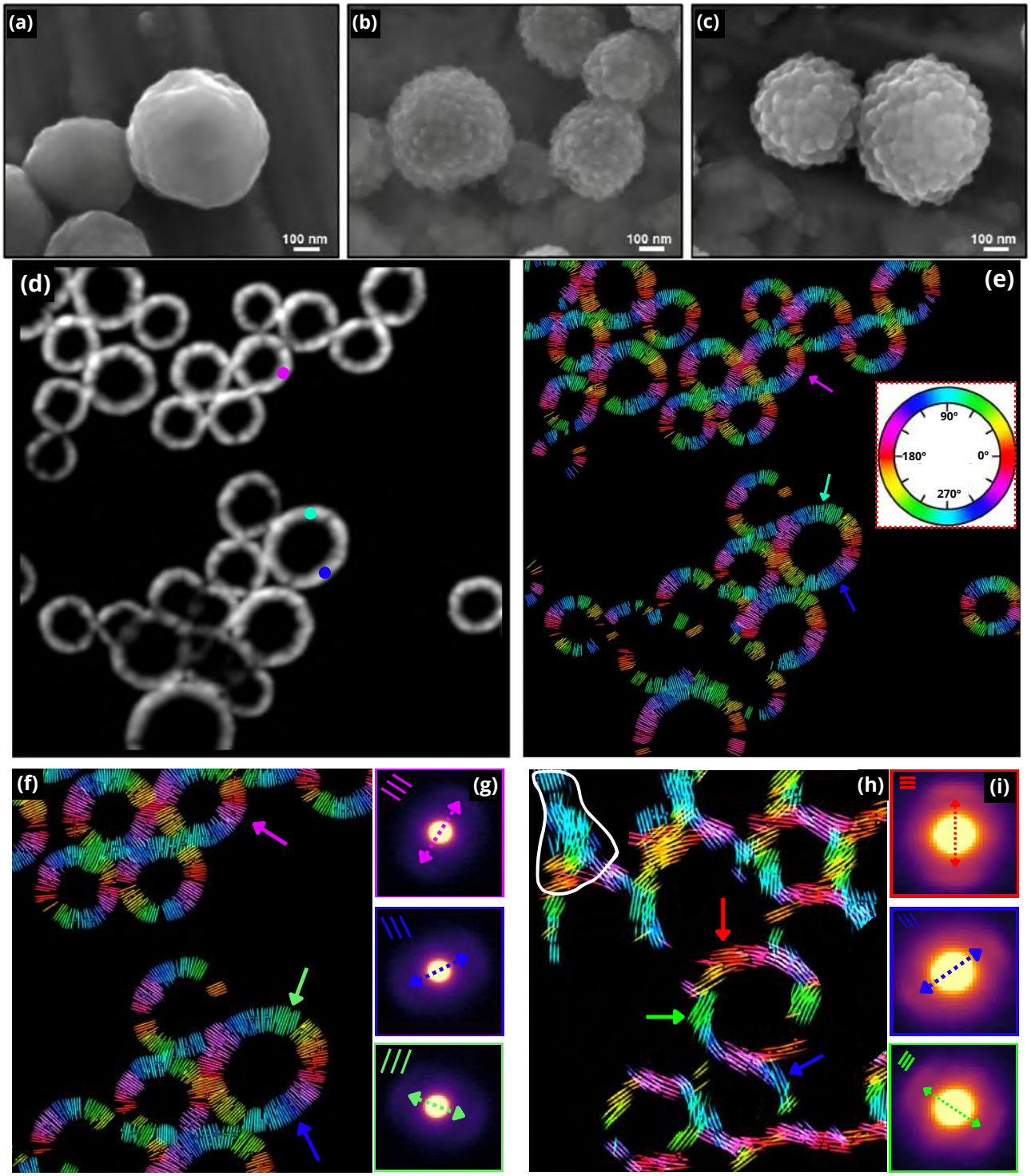

Figure 2.7: π-π stacking nature in different COF particles revealed by 4D-STEM: Scanning electron microscope (SEM) images of (a) COF-catechol-PNIPAm$_{25}$ particles, (b) COF-catechol-PNIPAm$_{50}$ particles, (c) COF-catechol-PNIPAm$_{100}$ particles. (d) shows a virtual dark-field reconstruction over an area of a $COF-5$ sample along with (e) a flowline map featuring a radial π-π stacking of the polymer chains. The orientation of the π-π stacking was found different comparing two types of COF particles. While (f,g) COF-5 particles feature a radial π-π stacking direction ($\sim$ 3.75 Å stacking separation), (h,i) COF-10 particles feature a tangential π-π stacking direction ($\sim$ 3.9 Å stacking separation). Note that the top left inset in the diffraction patterns shows the stacking direction (perpendicular to the Bragg spots direction). Adapted from Salaün et al. (2023). Part of the results here are yet to be submitted.

3.1.4 Other Applications

A diverse array of other applications is possible using 4D-STEM. For instance, 4D-STEM allows for strain mapping, which utilizes nanoscale precision to measure deformations in materials, valuable in understanding mechanical properties and material behavior under stress. As for amorphous and glassy materials, 4D-STEM allows for fluctuation electron microscopy (FEM) and pair distribution function (PDF) analyses to be performed which are used to study short- and medium-range order in these materials. Beyond structural analysis, 4D-STEM also allows for different imaging modalities. For instance, differential phase contrast (DPC) in 4D-STEM enables the imaging of electric and magnetic fields at the nanoscale, providing a powerful tool for studying nanoscale electromagnetic properties in materials. Moreover, a 4D-STEM dataset made of CBED patterns adequately collected over a grid of probe positions can be processed in electron ptychography to reconstruct high-resolution images, offering enhanced sensitivity and resolution beyond conventional imaging techniques. FEM and PDF as well as electron Ptychography will be revisited as part of the future prospects of this thesis work.

4 Used Experimental Setup and Data Analysis Softwares

The experimental setup used throughout this study is part of the "Plateforme de Microscopie Électronique de Lille (PMEL)" at Michel-Eugène Chevreul Institute, University of Lille. These include:

- TEM/STEM: Thermo-Fisher Titan Themis S/TEM $60 - 300\ keV$ equipped with a high brightness Schottky field emission gun and a monochromator.
- EDXS: Thermo-Fisher super-X windowless 4 quadrants silicon drift detection (SDD).
- 4D-STEM: Medipix3 Merlin hybrid-pixel DED installed in a Gatan post-column energy filter (GIF) (Quantum ERS/966) for energy-filtered 4D-STEM.

As exciting as the possibilities that 4D-STEM may offer in materials science research, it also introduces a layer of complexity to both the raw experimental data and the computational processing needed for meaningful analysis. To fully leverage the potential of this advanced STEM technique in structural characterization research, it is imperative that the computational

methods facilitating the diverse characterization modalities within 4D-STEM are accessible to a wide range of researchers. Luckily, a surge in the development of open-source software tools tailored for electron scattering experiments is actively being developed with the most prominent of all being *HyperSpy* (De la Peña et al. 2022). Other software packages include *py4DSTEM*, *pyXem*, *liberTEM*, *AtomAI*, among others (Savitzky et al. 2021; Cautaerts et al. 2022; Clausen et al. 2020; Ziatdinov et al. 2022). These tools not only democratize access to 4D-STEM data analysis but also foster collaboration and innovation within the scientific community by offering flexible and user-friendly solutions. In this thesis, the software analysis tools utilized include *Py4DSTEM*, *Hyperspy* and *PyXem*.

Chapter 3

4D-STEM Analysis of Ryugu Asteroid Samples

Preamble

This chapter of the thesis includes material previously published in the paper titled "Four-dimensional-STEM analysis of the phyllosilicate-rich matrix of Ryugu samples" in *Meteoritics and Planetary Sciences (MAPS)* and can be found in Mouloud et al. (2024). The content presented here has been adapted to fit within the context of this thesis.

1 Introduction

In December 2020, the Hayabusa2 space mission, led by the Japanese Aerospace Exploration Agency (JAXA), successfully returned samples from the C-type (carbonaceous) asteroid 162173 Ryugu to Earth. Extensive studies of these samples were conducted in the framework of preliminary analyses led by several research groups. T. Nakamura et al. (2022) suggested that Ryugu's formation likely occurred in the outer reaches of the solar system, supported by evidence of carbon dioxide (CO_2)-bearing water within iron-nickel (Fe-Ni) sulfide crystals. Equally significant is the detection of remanent magnetization, implying that the solar nebula may have still existed when magnetite crystals formed on the parent body.

In terms of composition and mineralogy, Ryugu samples closely resemble CI chondrites, with shared abundances of elements like C, N, Na, and Mg. Furthermore, isotope signatures, including chromium-titanium isotopes (Cr-Ti) and volatile element abundances, closely align with CI chondrites. Isotopic dating indicated aqueous alteration occurring approximately 4.6 mil-

lion years after the formation of the solar system (T. Nakamura et al. 2022). Ryugu samples contain minerals such as magnetite, breunnerite, dolomite, and pyrrhotite, within a matrix of serpentine and smectite, resembling CI meteorites. Oxygen isotopes in the samples also match with those found in CI chondrites. This prevalent mineralogy, reminiscent of CI chondrites, indicates widespread aqueous alteration on the parent body (T. Nakamura et al. 2022, Ito et al. 2022, Yokoyama et al. 2022). However, other results reported the presence of few anhydrous silicates, amorphous silicates, and other minor phases indicative of varying degrees of aqueous alteration (Yokoyama et al. 2022).

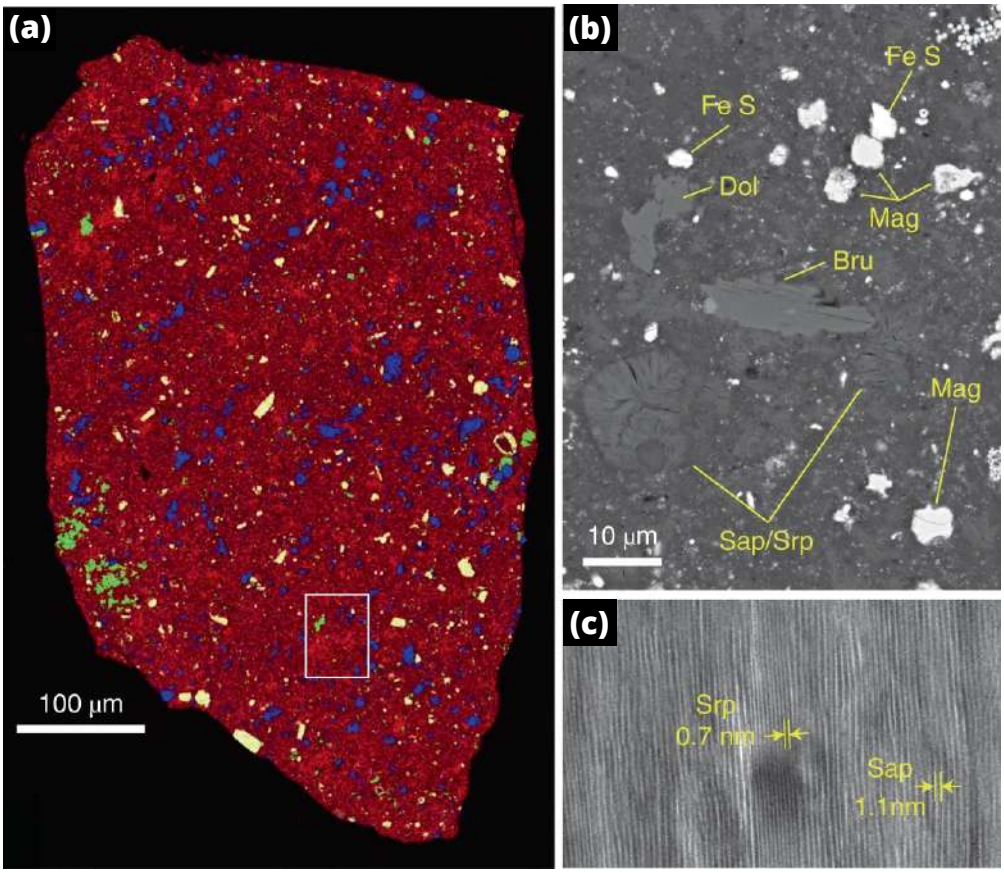

Figure 3.1: Petrography of a Ryugu fragment. (a) Combined X-ray map composed of Mg Kα (red), Ca Kα (green), Fe Kα (blue), and S Kα (yellow) of a dry-polished section of a Ryugu grain (Grain *C*0068 of chamber C). The section consists of phyllosilicate (red), carbonate (dolomite; light green), magnetite (blue) and sulfide (yellow). (b) Backscattered electron image of regions of outlined in a. Bru, breunnerite; Dol, dolomite; FeS, Iron sulfide; Mag, magnetite; Sap, saponite; Srp, serpentine. (c) High-resolution transmission electron microscopy (TEM) image of a typical saponite–serpentine intergrowth area showing 7Å and 11Å lattice fringes of serpentine and saponite, respectively. Adapted from Ito et al. (2022).

Regarding water content and its evolution, T. Nakamura et al. (2022) observed that phyllosilicate minerals within Ryugu samples hosted water, with structural water content similar to CI

chondrites. Notably, interlayer water was largely absent, suggesting its loss to space.

Ryugu grains have never witnessed terrestrial weathering effects, making them the most fresh and uncontaminated CI chondrites studied so far (eg. Yokoyama et al. 2022; Yada et al. 2022; Ito et al. 2022; T. Nakamura et al. 2022). This high level of preservation makes Ryugu samples particularly valuable for understanding the composition and evolution of the early solar system and the transformations of solid matter on small carbonaceous asteroids, as well as for developing new analytical techniques that can be applied to future sample return missions.

In this chapter, we use 4D-STEM in combination with a Medipix3 hybrid-pixel direct electron detector (DED) to explore some aspects of Ryugu's mineralogy, particularly in two distinct sample areas. With 4D-STEM having not been previously used for such case studies, our primary objective is to undertake an exploratory analysis. We seek to comprehend Ryugu's mineralogy using 4D-STEM, mapping the distribution of its diverse phases. Our specific focus will be on Ryugu's phyllosilicate-rich matrix, with a particular interest in discerning the characteristics of serpentine and smectite.

2 Acquisition and Data analysis

2.1 Sample Preparation and Data Acquisition

The fragment of Ryugu studied in this chapter comes from chamber A of the first touchdown site. The sample studied is labeled $A0104-00600303$ and was prepared using the focused ion beam (FIB) technique at Kyoto University (Helios NanoLab 3G, ThermoFisher Scientific). Two different $\sim 1\,\mu m \times 1\,\mu m$ areas of the FIB section, with a thickness of approximately 100 nm, were examined in this work using STEM-HAADF, STEM-EDXS, and 4D-STEM. Analyses were conducted on the ThermoFisher Titan Themis 300 S/TEM with an operational voltage of $200\,kV$. The 4D-STEM datasets were acquired using the Medipix3 Merlin hybrid pixel DED. Three datasets denoted R_1U, R_1F, and R_2U were acquired from the two examined areas. The first region was analyzed twice: first without energy filtering (R_1U) and then again with energy filtering (R_1F), both with a dwell time of $3.5\,ms$ per pixel. The second area was analyzed once without energy filtering (R_2U) with a dwell time of $20\,ms$ per pixel. In all acquisitions, an $20\,eV$ energy filter slit was used. A converged electron probe, with a convergence semi-angle of 0.1

mrad, was rastered on a 128×128 grid of pixels. The full-width half-maximum (FWHM) of the probe profile was approximately $\sim 7\,nm$. No beam damage was observed after the 4D-STEM acquisitions.

2.2 Analysis of 4D-STEM data

The acquired data were analysed using the open-source Python packages py4DSTEM (Savitzky et al. 2021) and HyperSpy (De la Peña et al. 2022). The analysis pipeline involves a number of common pre-processing steps followed by radial analysis and specific processing procedures for each case study.

Pre-processing: All the 4D-STEM data were pre-processed prior to further investigation as follows:

- *Dead pixel correction*: Dead pixels are malfunctioning pixels that do not respond to incoming electron signals or do not produce a measurable output. These pixels were corrected through linear interpolation with neighbouring pixels.

- *Diffraction stack alignment*: The method utilized is described in detail in Savitzky et al. (2021). The data were cropped to only retain the direct beam. The second diffraction pattern in the stack was cross-correlated with the first one to find its relative offset, and then the second pattern was shifted to align with the first one. The third pattern was then aligned with the second, and so on until all the diffraction patterns in the stack were properly aligned.

- *Vacuum probe and probe kernel*: The aim is to extract the shape of the electron probe for pattern matching. First, pixels corresponding to vacuum or very thin areas in the sample are identified, and the corresponding diffraction patterns are averaged to generate a two-dimensional image of the unscattered electron probe in diffraction space, which is referred to as the vacuum probe. A kernel for cross-correlative template matching is generated in two steps: The vacuum probe is centred and shifted to the origin to remove any offset in the measurements. Then, a wider Gaussian is subtracted from the probe, resulting in a negative intensity region around the probe to ensure that the total integrated intensity of the kernel is zero (Eg. Savitzky et al. (2021)).

Processing

- *Bragg spot registration*: In this step, diffraction spots are found by calculating the cross-correlation of the probe kernel generated in the pre-processing step with each individual diffraction pattern in the 4D-STEM stack, and then locating the correlation maxima. This results in a list of Bragg spots detected, where each spot is defined by the coordinates of the pixel containing the diffraction pattern from which they originate (a unique pair (x, y)), the coordinates of the different spots detected in the reciprocal space (qx, qy), and the intensity of each of these spots.

- *Mineralogical phase identification*: Several virtual diffraction patterns can be useful for identifying the mineralogical phases present in the surveyed area. An average diffraction pattern can be generated by summing up all the diffraction patterns in the 4D data stack, which can be regarded as equivalent to a selected area electron diffraction (SAED) pattern. This can then be azimuthally integrated to obtain an average radial profile over the surveyed area. However, the Bragg spots from minor phases may be obscured in the average diffraction pattern. Therefore, we mainly rely on the variance diffraction pattern (vDP) and the Bragg vector map (BVM) to obtain an overview of the mineralogy. The vDP is the variance intensity of every diffraction pixel across the entire dataset. The BVM is a reconstructed pattern obtained by merging all the diffraction peaks detected via the peak detection processing step previously described from every diffraction pattern in the 4D stack in a single image (for more details, see Savitzky et al. (2021)). We can then azimuthally average the BVM pattern and use the resulting 1D profile for X-ray diffraction-like mineral phase identification.

- *Virtual imaging and phase mapping*: By assigning each diffraction peak in the reconstructed BVM to a particular phase or orientation, virtual dark field images corresponding to these phases and orientations can be generated. This enables us to create a comprehensive map of the sample's mineralogical features, which can then be correlated with its chemical composition providing valuable insights into both the composition and microstructure of the sample.

- *Template matching*: Template matching involves comparing experimentally obtained diffraction patterns with simulated diffraction patterns generated from crystallographic information files (CIF) after the Bragg peaks finding procedure. The resulting correlation values are calculated to identify the crystal structure or orientation. A high correlation value indicates a good match, but the specific threshold for a "good match" value varies depending on the material

and quality of data. For more details on the template matching procedure and the underlying mathematical framework, readers are referred to Ophus et al. (2022).

3 Results

STEM-HAADF images from areas of the examined FIB section show typical heterogeneous mixtures of fine-grained matrix components (Fig. 3.2). The dominant component is the phyllosilicate matrix (PSM). It constitutes a groundmass for other minerals such as sulfides that are present in various proportions. The image in Figure 3.3a is a VBF reconstruction from the 4D-STEM dataset (R_1F), which corresponds to the STEM-HAADF image in Figure 3.2a. An average diffraction pattern over the whole surveyed area is shown in Figure 3.3b alongside a vDP in Figure 3.3c and a BVM in Figure 3.3d over the same area. The vDP and the BVM virtual diffraction patterns better emphasize weakly diffracting phases and/or diffraction spots from minor phases which can be obscured in the average diffraction pattern. Consequently, these maps provide additional information about the phases that are present and can be used to investigate deviations from the dominant phase. These differences can be better emphasized by azimuthally integrating these virtual patterns as shown in Figure 3.3(e,f).

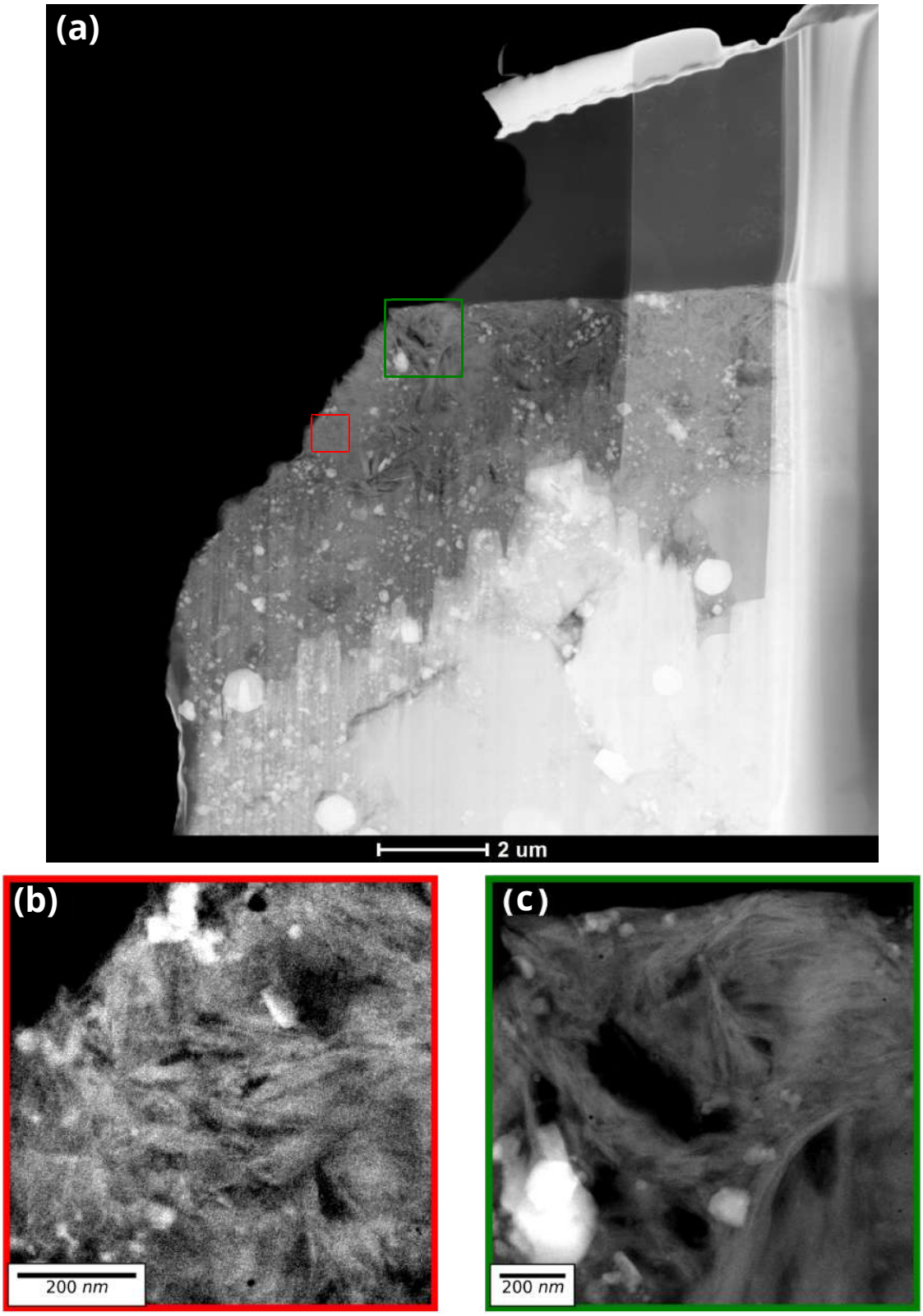

Figure 3.2: (a) A low magnification HAADF image of the sample $A0104 - 00600303$, with color-coded boxes overlayed to indicate the specific areas that were further examined by EDXS and 4D-STEM and for which the corresponding high magnification HAADF are shown in (b,c) Both areas examined are magnetite and carbonates free and the brighter regions correspond to Fe-bearing sulfides.

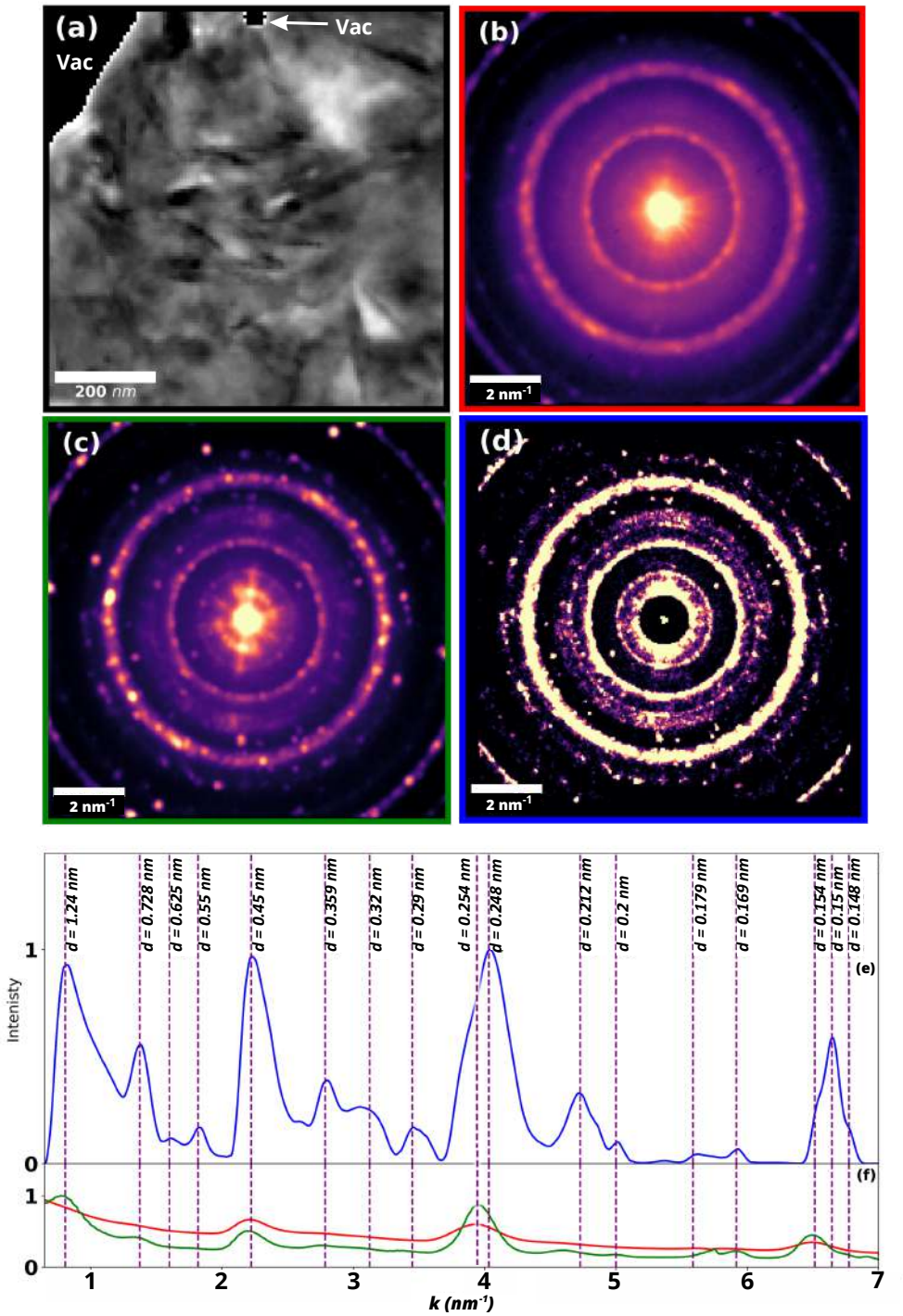

Figure 3.3: (a) Virtual Bright-Field (VBF) image of the area corresponding to the HAADF image in Fig 2a. Figures (b-d) correspond to the mean diffraction pattern, the variance diffraction pattern and the Bragg vector map of the whole 4D-STEM dataset (R_1F), respectively. Corresponding 1D radial profiles, obtained by azimuthally averaging diffraction patterns (b-d) are shown in (e,f) color coded to match the corresponding diffraction patterns. While the BVM-based radial profile show characteristic peaks of all the minerals present in the area that was investigated, the average radial profile captures mainly the *hk0* reflections of phyllosilicates while the variance radial profile captures the *001* reflections as well as the *hk0* reflections of phyllosilicates. The radial profile obtained by integrating the Bragg vector map can be used to describe the mineralogy of Ryugu asteroid.

3.1 General Description of Ryugu's Mineralogy

Different mineralogical phases present in Ryugu's matrix can be identified by analyzing and indexing the BVM-based radial profile of Figure 3.3e and correlating with VDF imaging to identify each diffraction peak in the profile. The BVM-based radial profile can be indexed by analogy to the XRD profile indexation of bulk Ryugu samples performed by Viennet et al. (2023) which can also be found in Figure 3.4. Viennet et al. (2023) identify serpentine, smectite and clays minerals where the latter refers to the $(hk0)$ reflections of phyllosilicates, as well as, pyrrhotite, pentlandite, magnetite and dolomite. This is in agreement with the major minerals identified in several studies of different Ryugu fragments from different collection chambers (Ito et al. 2022; T. Nakamura et al. 2022; Yokoyama et al. 2022).

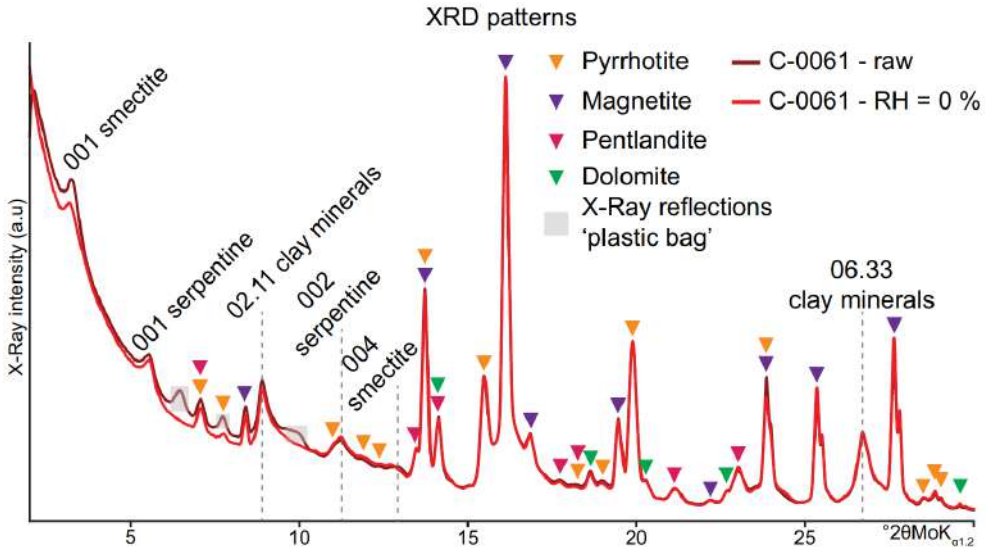

Figure 3.4: XRD measurements and the corresponding peak assignment of grain $C-0061$ under "raw" and 0% relative humidity conditions. (a) correspond to the *001* reflection of smectite while (b) correspond to the (004) reflection. Adapted from Viennet et al. (2023)

3.1.1 Sulfides

Iron and iron-nickel sulfides have characteristic peaks located at $\sim 0.55\,nm$, $\sim 0.29\,nm \sim 0.2\,nm$, $\sim 0.179\ nm$ and $\sim 0.169\ nm$. Taking all these peaks into account, a combined VDF image of sulfides distribution is shown in Figure 3.5a along with an EDXS map over the same area (Fig. 3.5b). A clear consistency between the two image reconstructions is observed. Figure 3.5(c-e) are diffraction patterns obtained from 4D-STEM data over the areas that are shown in Figure 3.5a. Template matching of pyrrhotite and pentlandite diffraction pattern libraries (calculated

respectively from the $P3_121$ space group (Rajamani and Prewitt 1975), and the $Fm-3m$ space group (Nakano et al. 1979)) with the sample diffraction patterns were performed using the automated crystal orientation mapping (ACOM) module of py4DSTEM (Ophus et al. 2022). These patterns were properly indexed as pyrrhotite as shown in Figure 3.5(f,g), while pentlandite did not match these diffraction patterns at all. This suggests that Ryugu may contain Ni-bearing pyrrhotite which is consistent with the findings of Harrison et al. (2022), Ito et al. (2022) and T. Nakamura et al. (2022). The gray areas of Figure 3.5a have corresponding diffraction patterns that lacked enough Bragg spots to be indexed, and hence, no structure information was retrieved to complement the chemical information. The interested reader can consult in-depth investigations on the formation of Ni-bearing pyrrhotite and pentlandite in CI-chondrites described in Berger et al. (2016) and Schrader et al. (2021).

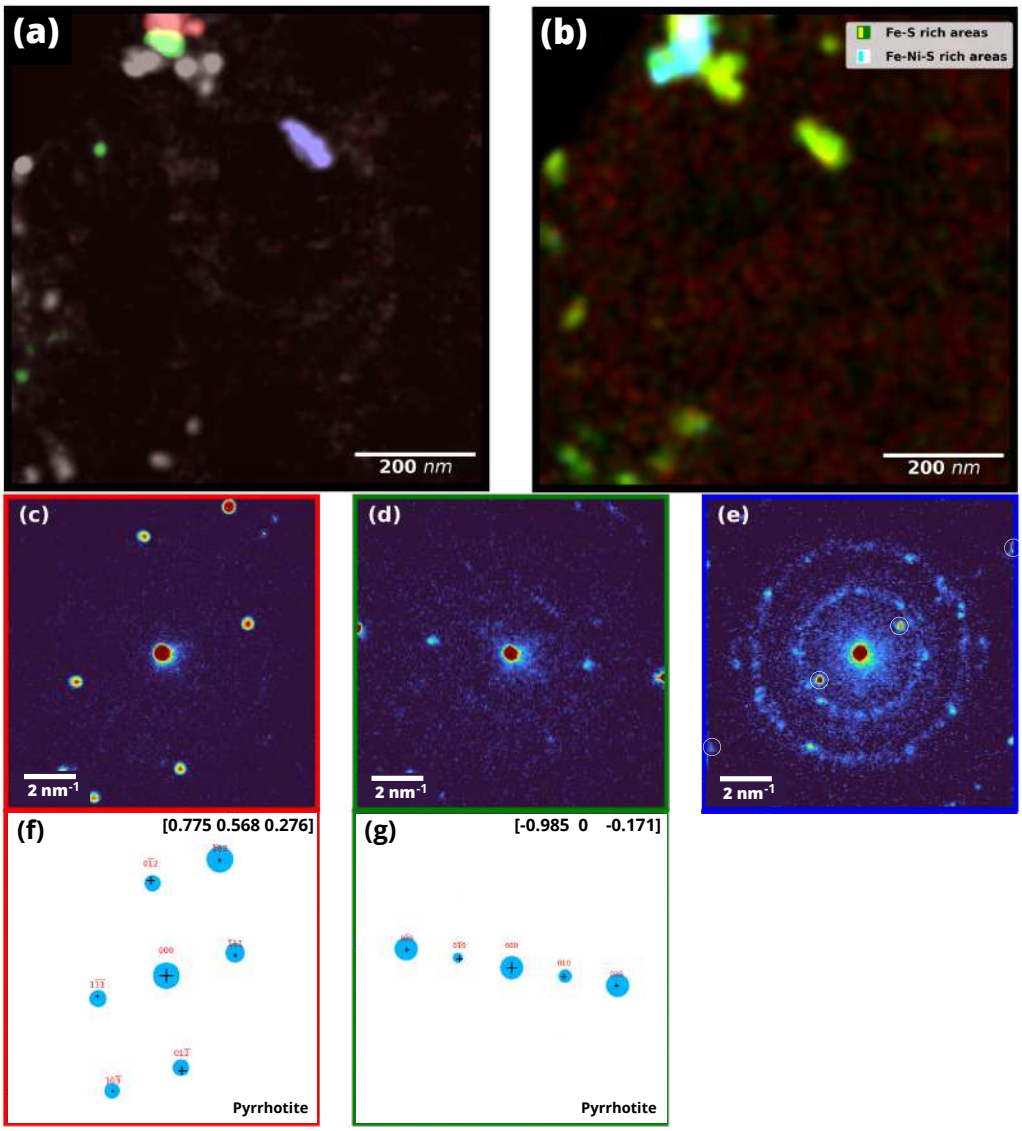

Figure 3.5: (a) A 4D-STEM combined virtual dark-field image showing Ni-free and Ni-bearing sulfides in the examined area along with (b) the corresponding STEM-EDXS maps. (c-e) are color-coded diffraction patterns corresponding to the different areas of equivalent color shown in (a). Grey areas in (a) correspond to sulfides that couldn't be indexed due to insufficient diffraction spots in the corresponding DPs. White circles in (e) indicate diffraction spots relevant to the corresponding iron-rich sulfide in (a). Indexing diffraction patterns of (c,d) shows that both the Ni-free and Ni-bearing sulfides are pyrrhotite (f,g).

3.1.2 Serpentine and Smectite

The radial profile in Figure 3.3e, corresponding to the mean diffraction pattern in Figure 3.3b, displays three relatively broad diffraction peaks at $\sim 0.45\,nm$, $\sim 0.254\,nm$, and $\sim 0.154\,nm$. Following Brown and Brindley (1980), these peaks have been attributed to reflection on $(2, 11, 0)$, $(13, 20, 0)$ and $(6, 33, 0)$ basal planes of phyllosilicates. This suggests that most of the pixels in the examined area are mainly made up of a fine mixture of smectite and Mg-rich serpentine (Tomeoka and Buseck 1988; King et al. 2015).

In agreement with Viennet et al. (2023), the peaks located at $\sim 0.728\ nm$ and $\sim 0.359\ nm$ in Figure 3.3e correspond to the serpentine *001* and *002* reflections, respectively, while the peak located at $\sim 0.212\ nm$ corresponds to the (*112*) reflection of serpentine. The intense peak around $\sim 1.24\ nm$ corresponds to the (*001*) reflection of smectite. A small contribution can also be seen from the (*002*) reflection of smectite at $\sim 0.625\ nm$ and a relatively broad peak located at $\sim 0.32\ nm$ is attributed to the (*004*) reflection of smectite.

In the area shown in Figure 3.6a, a virtual dark-field map of smectite and serpentine distribution in the phyllosilicate matrix was obtained. This was accomplished by integrating over the smectite and serpentine *001* diffraction rings and over the *(2,11,0)* phyllosilicate reflection. The boundaries of the diffraction rings used for the integration are determined by the width of the corresponding peaks in the 1D radial profiles. On this virtual dark-field, serpentine- and smectite-rich areas are respectively colored in green and red whereas mixed areas are colored in blue. An elemental map obtained by STEM-EDXS showing Si/Mg ratio is shown in Figure 3.6c. In favourable cases, serpentine and smectite can be distinguished through STEM-EDXS analysis. Without taking into account possible Al substitutions, Mg-rich serpentine exhibits a *Mg/Si* ratio of ~ 1.5, while smectite, possessing a permanent charge of 0.4, has a *Mg/Si* ratio of ~ 0.83. However, the mixing scale between both phases is often smaller than our pixel size in the EDXS maps, and, therefore, only the larger grains can be reliably identified in this way. Comparison of Figure 3.6b and Figure 3.6c indicates that, smectite-rich areas oriented with (*001*) planes edge-on are correlated with Si-rich areas in the corresponding elements map (both in red). Nevertheless, serpentine (*001*) area as well as smectite-serpentine rich areas (green and blue respectively) are both associated to Mg-rich areas (blue on the EDXS map). It shows that 4D-STEM identifies serpentine and smectite grains at a finer scale than EDXS when they are properly oriented with basal planes edge-on.

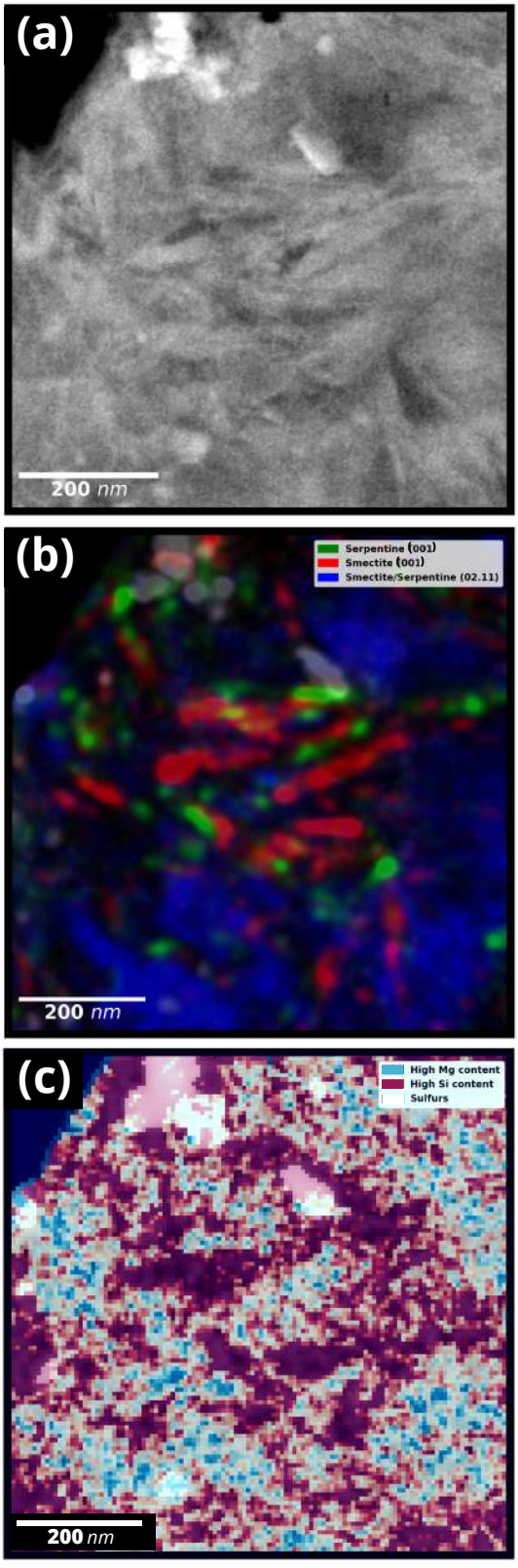

Figure 3.6: (a) STEM-HAADF image of the surveyed area (Same as Fig 2a). (b) A corresponding combined virtual dark field image made by 4D-STEM showing smectite/serpentine distribution in the matrix along with (c) Energy dispersive X-ray spectroscopy (EDXS) map made by scanning transmission electron microscopy (STEM) of Mg/Si ratio over the same area. Sulfides in (b) are imaged in light grey for a better localization of the different features observed in (a) and (c).

3.2 Serpentine in Ryugu

Serpentines are 1:1 tri-octahedral phyllosilicates. The three most common polymorphs of serpentine are lizardite, antigorite and chrysotile which are all Mg-rich. The ideal chemical formula of serpentines is $Mg_3Si_2O_5(OH)_4$. They only differ in terms of how their fundamental coordinating polyhedra are oriented with respect to each other. As outlined in Chapter 1, these form flat layers in the case of lizardite, wavy layers in antigorite and curled layers in chrysotile (Andreani et al. 2008; Mellini et al. 2013; Vance and Melwani Daswani 2020). Chrysotile is common in CM chondrites (MacKinnon 1980; Barber 1981) but rare in CI chondrites (Tomeoka and Buseck 1988) and is easily recognized by high resolution TEM because of its apparent tubular structure (Yada 1971). No previous investigations of Ryugu asteroid samples have indicated the presence of chrysotile; neither has the current study.

In order to identify the polymorph that can be most representative of serpentine in the PSM of Ryugu among lizardite and antigorite, a set of pixels (∼20 pixels) of serpentine that are close to Bragg conditions were chosen from the second area (R_2U) examined in this study (Fig.3.2b). This was accomplished by template matching of experimental diffraction patterns with simulated patterns of lizardite and antigorite using libraries from Marcello Mellini et al. (2010) for lizardite and Uehara (1998) for antigorite. We used the ACOM module of py4DSTEM to compare the experimental diffraction patterns in the 4D-stack to the template patterns, and retained only the pixels that showed correlation values higher than 0.5 for both cases. We selected this threshold value because we found it to be the minimum value that excluded diffraction patterns for which the corresponding simulated patterns were obviously different from the measured ones. Afterwards, the diffraction patterns of these pixels were summed and then azimuthally averaged to get the radial profile in Fig.3.7b. For clarity, diffraction patterns corresponding to only three different pixels are shown in Fig.3.7c1-c3.

From the template matching results, the correlation value between Ryugu's serpentine diffraction patterns and lizardite simulated diffraction patterns was consistently higher than that of antigorite as shown in Fig.3.7. This was observed in all the pixels that corresponded to serpentine close to the Bragg conditions. Furthermore, the simulated diffraction patterns of antigorite in Fig.3.7 suggest that certain spots in the corresponding experimental patterns should exhibit a perpendicular streaking, which is not observed here. Perpendicular streaking is also com-

monly observed SAED patterns of both antigorite and chrysotile (Zvyagin 1967), providing additional support for our assumption. This supports the interpretation that serpentine in the PSM of Ryugu is most likely present in the form of lizardite.

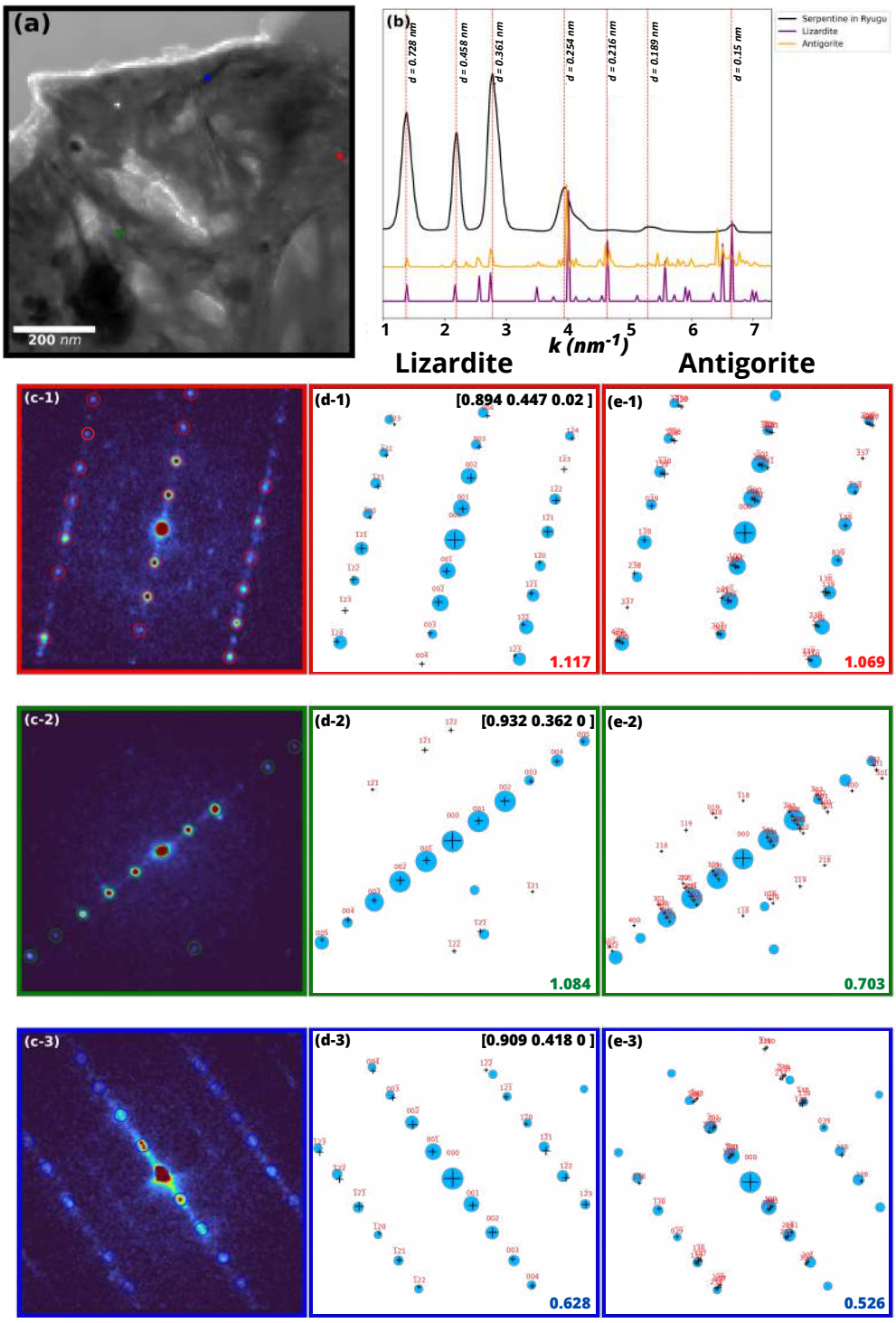

Figure 3.7: (a) A reconstructed VBF image of the area that was examined in 4D-STEM along with a corresponding average radial profile reconstructed from the diffraction patterns of the 4D data stack. The homogeneous light grey region in top is vaccum. (b) 1D histogram of scattering vectors from oriented serpentine (black) and simulated electron diffraction profiles of lizardite (purple) and antigorite (yellow) with serpentine's detected inverse plane spacings overlaid. (c1 - c3) are diffraction patterns from the three separate color coded areas of serpentine in (a) along with (d1 - d3) lizardite matches and (e1 - e3) antigorite matches of the respective diffraction patterns. Lizardite's and antigorite's correlation scores are shown in the bottom right of their respective matches showing that the correlation score for Lizardite is higher than that of antigorite. Best fit zone axes of lizardite are shown in the top right of their respective matches.

3.3 Smectite in Ryugu

Smectite minerals are a type of clay minerals that belongs to the phyllosilicate family and have a T-O-T structure. Isomorphic substitutions in variable amounts by lower charge cations in tetrahedral and/or octahedral sheets induce negatively charged 2:1 layers, the so-called "permanent charge". This permanent charge is in turn compensated by hydrated exchangeable cations in the interlayer space that are responsible for the hydration properties leading to the expansion of the layer-to-layer distance reflected by the position of the (*001*) reflection (Ferrage 2016). As a remainder from the Chapter 1, the layer-to-layer distance depends on the hydration state. Indeed, the tri-hydrated state of smectite, characterized by the presence of three water molecules between the layers, leads to a layer-to-layer distance of up to $\sim\ 19 - 21$ Å, while a dehydrated state can reduce the distance down to $\sim 0.93\ nm$. The radial profiles in Fig.3.3 for Ryugu samples indicate that smectites have a mean d-spacing of $\sim 1.24\ nm$ which is in agreement with findings by Viennet et al. (2023).

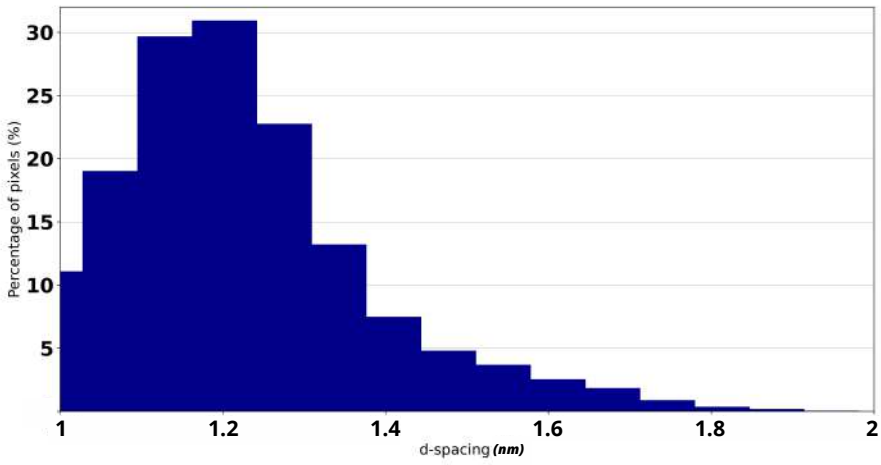

Figure 3.8: A histogram of the variability of d-spacings in the examined area of Ryugu showing, as a percentage, the frequency of smectite pixels in the map that correspond to a given d-spacing. Most d-spacings lie between $\sim 1.1\,nm$ and $\sim 1.4\,nm$ while some other pixels (less than 5%) display larger interlayer spacing values.

Using 4D-STEM, it is also possible to map the variation in the interlayer spacing of smectite by determining the d_{001}-spacing at each scan position. This was accomplished on the filtered data used in this study (R_1F) by first cropping each diffraction pattern to only retain a region of the reciprocal space up to a reciprocal space radius of 1.1 nm^{-1}. This selection restricts our

analysis to the *001* reflection areas of smectite, corresponding to a minimum observable real space distance of $\sim 0.9\ nm$. Afterwards, the peak finding procedure described in the previous section is used on this newly formed dataset to extract the positions of each pair of diffraction spots and measuring their spacing, and hence, the d_{001} of smectite. A histogram of the different smectite d-spacings identified by this procedure in the area examined by 4D-STEM is shown in Fig.3.8. It suggests that d-spacings are ranging from $\sim 1\ nm$ to $\sim 2\ nm$. Most d-spacings lie between $\sim 1\ nm$ to $\sim 1.4\ nm$ with a mean value that is around $\sim 1.24\ nm$ as previously emphasized by the radial profiles in Fig.(3.3e). The observed d-spacings range up to $\sim 1.9\ nm$ which is common for Tochilinite in Tochilinite-Cronstedtite Intergrowths (TCIs) present in CM chondrites (eg. Pignatelli et al. 2017; Vacher et al. 2019; Velbel and M. E. Zolensky 2021). However, despite the presence of diffraction peaks at similar d-spacings in some regions of the sample, no sulfide contribution has been identified from EDXS thereon, suggesting that TCIs are unlikely to be present in these areas. Notably, while tochilinite is commonly found in CM chondrites, its presence in other chondrite types is relatively uncommon. Interestingly, rare occurrences of tochilinite have been reported in CR chondrites by Le Guillou and Adrian Brearley (2014), Abreu et al. (2018), Abreu et al. (2018) and more recently, T. Nakamura et al. (2022) suggested its presence in the least altered areas of some Ryugu samples.

Figure 3.9a shows a VDF image reconstructed using the (*001*) reflection of smectite. At each smectite pixel in the surveyed area, we have a value for the interlayer spacing, which results in a map of the interlayer spacing of smectite that is shown in Figure 3.9b. The map displays a random distribution of d-spacing values without any discernible patterns or trends. Some representative diffraction patterns selected from a set of pixels in the smectite-rich area are displayed in Figure 3.9(c1-c6).

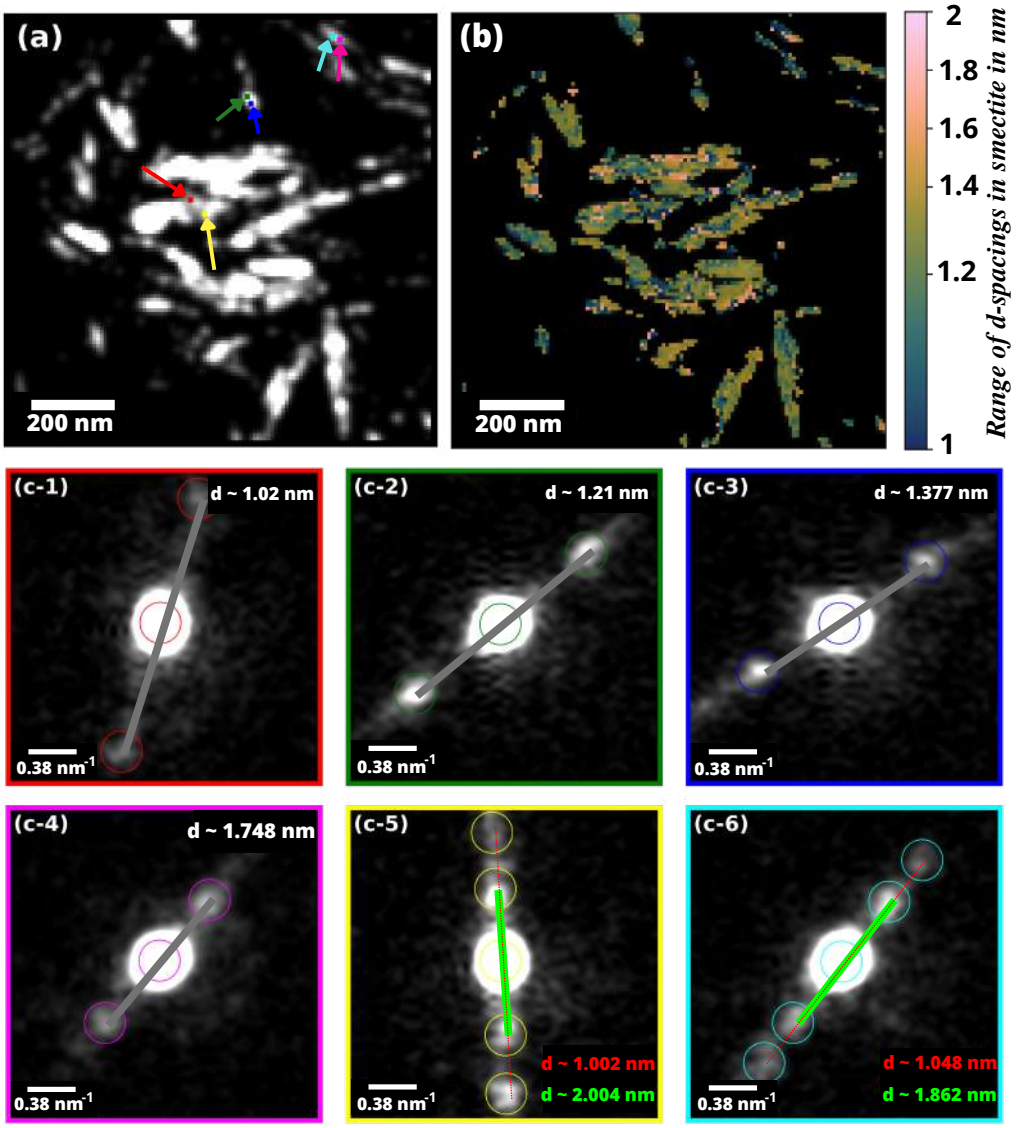

Figure 3.9: (a) VDF image of smectite-rich area in Ryugu reconstructed from the (*001*) reflection. Colored arrows indicate pixels from which a set of diffraction patterns are taken as a showcase. (b) A map of the distribution of the interlayer spacing in smectite over the same area shown in (a). (c1-c6) are diffraction patterns taken from the pixels color-coded in (a). A variety of d-spacings ranging from ~ 1 *nm* to ~ 2 *nm* were observed.

3.4 Effect of energy filtering

It is noteworthy that the 4D-STEM dataset we used for depicting the mineralogy of Ryugu (dataset R_1F) is acquired with zero-loss energy filtering. To illustrate the effect of filtering, we show in figures 3.10a and 3.10b two variance diffraction patterns that were reconstructed from two separate 4D-STEM datasets taken from the same area (HAADF image Fig. 3.2a). The first dataset was acquired without filtering (R_1U), while the second was acquired with filtering (R_1F). The energy filtering removes the inelastic scattering from the diffraction patterns (mainly plasmon scattering collection at low angles (Yi and Voyles 2011)), which can

cause broadening of the diffraction spots and decrease the contrast in the diffraction pattern (Fig. 3.10a). This results in a clearer diffraction pattern with sharper spots and reduced background. Figure 3.10c depicts the one-dimensional azimuthally averaged profiles of the two variance diffraction patterns, which are colour-coded for clarity. Notice that the smectite and serpentine reflections are hardly discernible in the unfiltered radial profile with a dwell time of $3.5\,ms$, but clearly visible in the radial profile obtained with energy filtering. In dataset (R_2U) we increase the dwell time to $20\,ms$ to improve the signal-to-noise (SNR) ratio to enable serpentine phase identification. While this enabled the detection of the *001* reflection of serpentine, it was not possible to detect the *001* reflection of smectite. As previously described, low-angle scattering features, such as smectite *001* d-spacings, can be resolved more effectively when using zero-loss energy filtering. Therefore, if energy filtering had been employed to acquire the dataset, it would likely have been possible to resolve the *001* reflection of smectite.

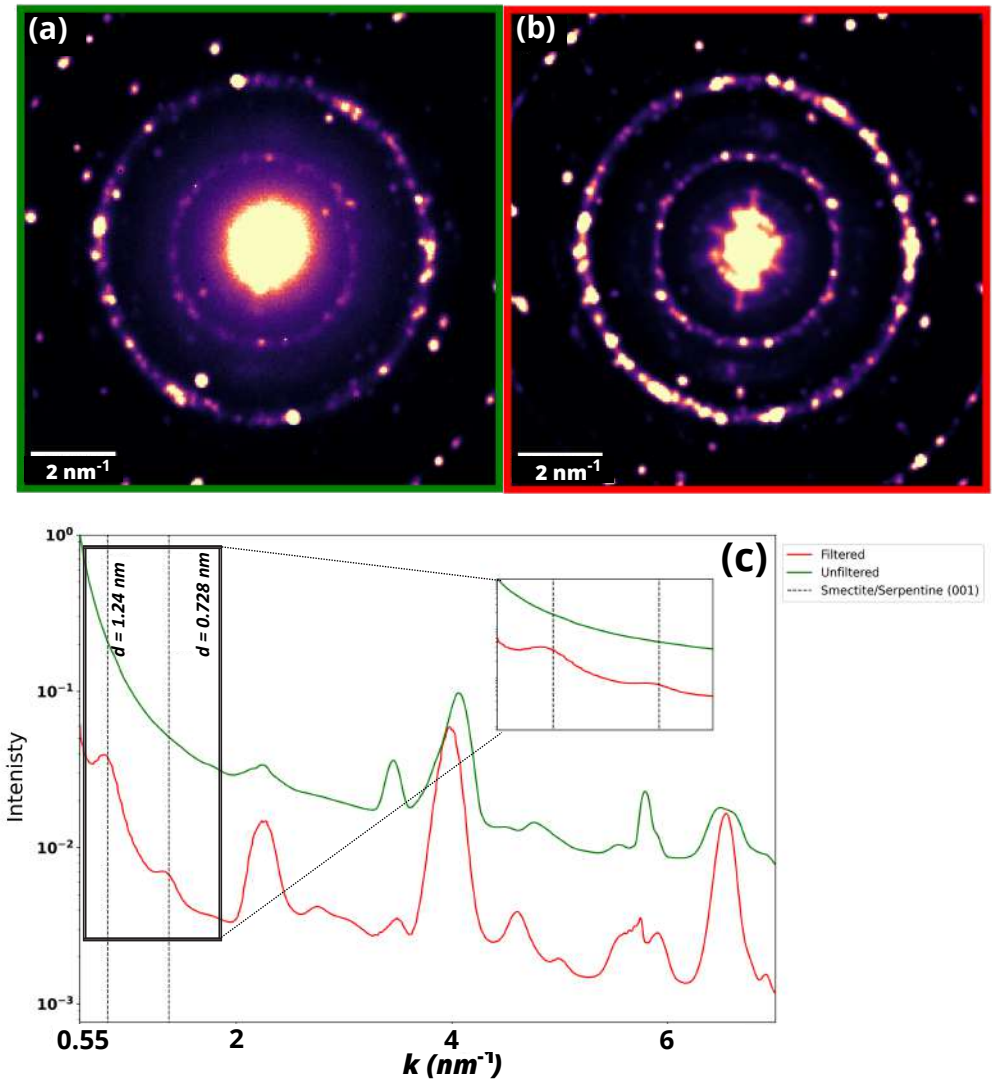

Figure 3.10: The effect of zero-loss energy filtering. A variance diffraction pattern over the area under investigation (a) without filtering and (b) with filtering. The corresponding azimuthally averaged one-dimensional profiles are shown in (c). We can clearly see that the intensity near the zero beam is higher without energy filtering which makes the diffraction signal of smectite and the *001* of serpentine near the direct beam very weak, hence, cannot be emphasized without energy filtering. We should note here than the unfiltered 4D-STEM dataset (R_1U) was acquired prior to the filtered one (R_1F).

4 Discussion

Using 4D-STEM we were able to accurately identify and map the different minerals present in Ryugu. The regions analyzed in this study did not include magnetite and carbonates, also present in Ryugu (Ito et al. 2022; Yada et al. 2022; T. Nakamura et al. 2022; Dobrică et al. 2023), as the focus was on phases of smaller grain size. Instead, our main focus was on the phyllosilicates, whose identification is strongly dependent on their crystallographic orientation conditions in the TEM.

4.1 Serpentine Polymorph Identification: Insights into Aqueous Alteration Processes in Ryugu

Several studies tried to address the identification of the serpentine polymorph in the phyllosilicate matrices of chondrites. For instance, Takir et al. (2013) used IR analysis on Ivuna CI-chondrites and detected the presence of both lizardite and chrysotile, but was unable to differentiate between them. Osawa et al. (2005) also reported, from IR spectra analysis, the signature of lizardite in Ivuna CI-chondrite, and that of chrysotile in CH and CB chondrites. TEM studies however have generally been able to distinguish serpentine polymorphs based on the appearance of basal lattice fringes. For instance, chrysotile has been identified in CM chondrites by HRTEM studies based on its tubular structure (Tomeoka and Buseck 1985). Additionally, the presence of polyhedral serpentine in Murchison, Mighei and Cold Bokkeveld CM chondrites was reported by Zega et al. (2006) using TEM imaging. They also proposed a possible pathway for its formation through alteration and oxidation of cronstedtite on the parent body. Determining the main serpentine polymorph in the matrix may provide clues about the conditions and processes that occurred during the formation and alteration of the parent body.

In this study, and by means of template matching over a selection of diffraction patterns close to exact Bragg conditions taken from serpentine areas, we have identified, the serpentine polymorph present in Ryugu to be lizardite. Investigating the conditions under which lizardite forms and the mechanisms that drive its formation will provide valuable information about the history and evolution of Ryugu. Serpentine minerals are known to form through a process called serpentinization, which involves the hydration of minerals that contain iron or magnesium, such as olivine (Bailey 1991). When olivine interacts with water, the crystal structure of the mineral breaks down, leading to the formation of lizardite with possibly magnetite and brucite (Bailey 1991). A work conducted by Wenner and Taylor (1971) measured ^{18}O-fractionations between coexisting serpentine and magnetite to give approximate temperatures of serpentinization of ultramafic rocks. They found that, at fluid pressures up to $\sim$ 4 kbar, different chrysotile-lizardite mixtures occur at temperatures ranging from 85°C to 185°C, while antigorite is stable at even higher temperatures. This is in agreement with other studies by O'Hanley et al. (1989) and O'Hanley and Wicks (1995), which investigated the stability of serpentine polymorphs

under different conditions. In these studies, they reported that, under fluid pressures up to ~ 4 kbar, the stability of serpentine polymorphs changed with increasing temperature. Specifically, lizardite was found to be the most stable phase at temperatures below 200°C, but as temperature increased, it was replaced by chrysotile. At even higher temperatures, the most stable serpentine polymorph was observed to be antigorite. A more recent study by Evans (2004) focused on the role of temperature and reported that lizardite is favored at lower temperatures. However, its stability diminishes as the temperature surpasses 290°C, and antigorite-brucite assemblage becomes stable. Schwartz et al. (2013) investigated phase transitions between the different polymorphs of serpentine and observed that below 300°C and 4 kbar, only lizardite is stable, while in the 320°C - 390°C range of temperatures, and for pressures greater than 9 kbar, antigorite progressively replaces lizardite. Since the present study suggests that lizardite is the predominant serpentine polymorph in Ryugu samples; it is likely that aqueous alteration occurred at low temperatures that are favourable for lizardite formation. This is consistent with recent studies of Ryugu grains. T. Nakamura et al. (2022) concluded, from the low abundance of Mg-chlorite, that aqueous alteration may have occured at temperatures below 100°C while Yamaguchi et al. (2023) reported that the alteration temperature doesn't exceed 210°C. Yet, the implications of lizardite formation discussed here might not be directly applicable to Ryugu and CI-chondrites meteorites because the precursor materials for the serpentine are still unknown. Indeed, our study did not find any evidence of amorphous, gel or glass like minerals in Ryugu from which a serpentine phase like lizardite could eventually be formed. However, as pointed out by Leroux et al. (2023) and T. Nakamura et al. (2022), a part of serpentine could have been formed from anhydrous silicate material such as Mg-rich olivine and pyroxene.

4.2 Variability in smectite d-spacing: Insights into organic matter intercalation and geochemical conditions

The detection of smectite in Ryugu grains is consistent with previous results on the mineralogy of Ryugu (Yokoyama et al. 2022; Ito et al. 2022; T. Nakamura et al. 2022; Leroux et al. 2023; T. Noguchi et al. 2023). Considering desorption of interlayer water molecules under vacuum conditions of the TEM, the expected value for the interlayer space should be around $\sim 1nm$. The 4D-STEM results reported here show that the average d-spacing of smectite in the examined

area is $\sim 1.24\,nm$. Common uncertainties on d-spacing values are generally less than 5%, which is far below the $\sim$ 20% dispersion (FWHM) of the distribution reported in Figure 3.8. So far, smectite's d-spacing had been inferred locally using HRTEM (T. Noguchi et al. 2023), and as a bulk value using XRD (T. Nakamura et al. 2022; Viennet et al. 2023; Yamaguchi et al. 2023). The average d-spacing value here measured is consistent with the study led by Viennet et al. (2023) through XRD experiments at both "raw" and 0% relative humidity conditions as shown in Figure.3.11.

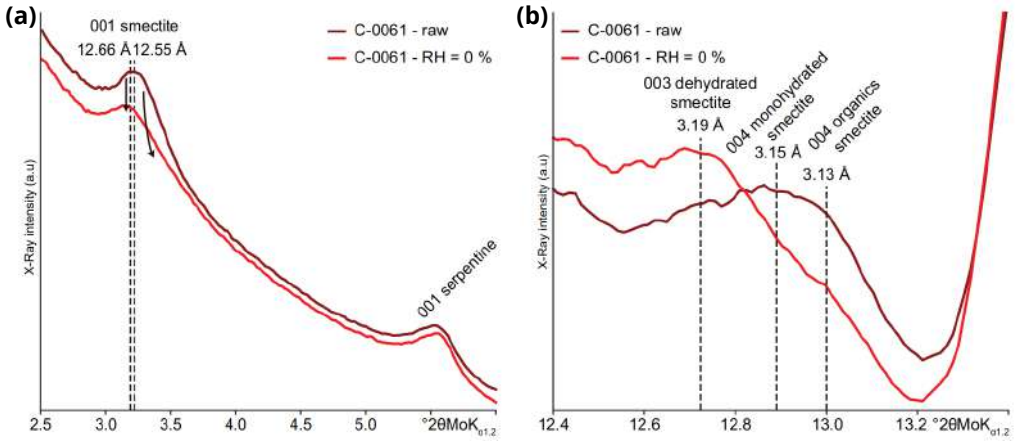

Figure 3.11: XRD measurements and the corresponding peak assignment of the (00l) reflections of the smectite layers of the grain $C-0061$ under "raw" and 0% relative humidity (RH) conditions. The arrows indicate the XRD behaviour of the two smectite phases after exposure to 0% RH. Similar behavior is observed from the 4D-STEM results confirming thus the observations of Viennet et al. (2023). Adapted from Viennet et al. (2023)

This, together with the high dispersion of the d-spacings distribution indicates that species other than water could be present within smectites' interlayer space, not volatile enough to be released under vacuum. One likely candidate is organic matter. Indeed, the presence of organic matter within the interlayer space of smectites would lock it at d-spacings $> 1\,nm$ under 0% RH or under vacuum. This behavior is long known in 2:1 phyllosilicates as organic intercalation (Lagaly and Beneke 1991; Lanson et al. 2022). More recently, experiments dedicated to the investigation of the interaction between organics and phyllosilicates in chondritic-like conditions revealed the same behavior (Viennet, Bernard, Le Guillou, et al. 2019; Viennet, Bernard, Le Guillou, et al. 2020; Viennet et al. 2021; Viennet et al. 2022; Viennet et al. 2023). Stroud et al. (2023) studied Ryugu's organic matter and its relationship to minerals at the micrometer to nanometer scale. Yabuta et al. (2023) investigated the abundant organic matter within Ryugu grains, composed of aromatic and aliphatic carbons, ketones and carboxyles. They

also discussed the interaction between minerals and organics based on the presence of diffuse organic matter, supporting the possibility of organic matter's involvement in the interlayer space of smectites. In our study, the ratios of K/Si, Na/Si, and Ca/Si over smectite-rich areas identified with 4D-STEM VDF imaging were below our detection limits (< 0.01 not shown) to be responsible for charge compensation in the interlayers of smectite, indicating that, apart for possible residual water molecules, organic matter could be the main species compensating the permanent charge of smectite layers.

While XRD provides a bulk scale d-spacing value (Viennet et al. 2023), 4D-STEM is a powerful complementary source of information. Indeed, our 4D STEM results indicate a considerable degree of heterogeneity among the smectite d-spacings at a scale of $\sim 80\,nm$, with values ranging from $\sim 1\,nm$ to $\sim 2\,nm$. This heterogeneity can have different interpretations. Distinct organic molecules, with different carbon chain lengths for instance, may be present within the interlayer space (Lanson et al. 2022). Alternatively, it could be possible for the same organic molecules to exhibit different spatial arrangements or configurations. Since the d-spacing heterogeneity cannot be attributed to one specific cause, it is difficult to determine its origin. However, one possible explanation for the observed variability is the influence of local geochemical conditions, which can be related to the nature of organic matter and its interactions within the smectite layers. Furthermore, if such heterogeneity is related to variations in the crystal chemistry of smectite layers, such differences could be attributed to local variations in geochemical conditions and/or smectite precursors. The d-spacing map shows that the variability occurs within each particle but does not seem to be totally random. Pixel clusters of several tens of nanometers display relatively similar d-spacing values (Fig 3.9b). It may suggest that the process controlling the d-spacing was variable at the same spatial scale and that heterogeneously localized environmental conditions affected either the crystal chemistry, the organic matter nature, or their interactions.

5 Conclusion

This chapter focuses on the 4D-STEM characterization of the phyllosilicates in Ryugu asteroid samples. Using a specific analysis protocol relying on an XRD-like description of the integrated Bragg vector maps and virtual dark field imaging, we characterized the mineralogy of Ryugu

asteroid samples and identified the main minerals that are present. Our study identified the presence of Ni-bearing pyrrhotite in Ryugu, consistent with previous findings. Furthermore, we were able to identify lizardite as the primary serpentine polymorph in Ryugu's matrix, suggesting that, if lizardite formed by the alteration of olivine, this alteration may have occurred at low temperatures. We have also observed that the main smectite reflection is located at an average distance of $\sim 1.24\ nm$ suggesting the presence of organic matter trapped within the interlayer space of smectite in addition to possible residual water molecules. Furthermore, the spatial mapping of the interlayer spacing of smectite highlights the sub-microscale heterogeneity of Ryugu and shows the close association of organics with smectite-type clay minerals. Our findings highlights the importance of continued investigation into the mineralogical, chemical and structural properties of asteroidal and chondritic samples, and the significant role that advanced electron microscopy techniques such as 4D-STEM can play in enhancing our understanding of such objects.

Chapter 4

4D-STEM Analysis of Orgueil Carbonaceous Chondrite Samples

1 Introduction

In the previous chapter, an extensive 4D-STEM analysis was carried out on two distinct regions of a Ryugu asteroid sample. The main aim of this investigation was to uncover the mineralogical features of phyllosilicates within the asteroidal sample, with the objective of establishing a connection to the geological history of Ryugu asteroid. However, due to a lack of sufficient diffraction signal, direct automated crystal orientation mapping (ACOM) on the 4D-STEM data was not possible, leading us to develop an alternative data analysis approach. This approach involved initial extraction of all diffraction information into a Bragg vector map (BVM). Subsequently, an azimuthal average of the resulting BVM was obtained to generate an X-ray diffraction (XRD)-like spectrum which contained both phase and orientation information. This spectrum was then interpreted in the same manner as an XRD profile which allowed for accurate mapping of the different mineralogical phases present in the sample area. These insights were subsequently leveraged to investigate more in-depth characteristics, such as the arrangement of smectites with different interlayer spacings, as well as the nature of the iron-sulfides and serpentine polymorph.

Ryugu samples exhibit similarities to Ivuna-type (CI) carbonaceous group of chondrites, which include the Orgueil meteorite samples (Ito et al. 2022). Therefore, it would be interesting to explore the phyllosilicate matrix characteristics of Orgueil meteoritic samples in comparison to

Ryugu samples using transmission electron microscopy (TEM).

A very illuminating TEM comparative study between Orgueil and Ryugu's phyllosilicates' mineralogy was recently undertaken by Leroux et al. (2023). Their investigation found that the Ryugu dominant lithology of the phyllosilicate matrix closely resembled that of Orgueil CI chondrite, exhibiting a mixture of serpentine and smectite fibers with varying textures at the nanometer and micrometer scales. Fine-grained regions in both materials were rich in smectite, but in Ryugu, they contained numerous (Fe,Ni) nanosulfides, while Orgueil had S- and Ni-rich ferrihydrite (Tomeoka and Buseck 1988). Iron valency in Orgueil's phyllosilicates was notably higher and more homogeneous compared to Ryugu. These observations suggested that aqueous alteration processes, including pseudomorphic replacement of submicrometric components and the potential involvement of GEMS (glass with embedded metal and sulfides) objects, played a crucial role in shaping the phyllosilicate textures in both materials. However, the presence of (Fe,Ni) sulfides in Ryugu and higher iron valency of phyllosilicates in Orgueil hinted at distinct evolutionary pathways, possibly influenced by terrestrial weathering or varying hydrothermal conditions on their respective parent bodies.

The initial goal of the present study was to expand upon the work of Leroux et al. (2023) by conducting a comparative 4D-STEM analysis of the fine-scale characteristics of smectites in both Orgueil and Ryugu, specifically focusing on smectite grains, their nature, degree of intercalation, and the resulting consequences. However, it was found that no smectite was present in the analyzed FIB sections of Orgueil and varying levels of FIB damage was also observed. Consequently, the primary purpose of this chapter changed to initially depict the mineralogical characteristics of the investigated FIB section of Orgueil, which can be more challenging to discern than those of Ryugu from a diffraction perspective due to the possible presence of additional mineralogical phases originating from terrestrial weathering. This chapter also aims to make a comparison with existing literature to highlight the insights that 4D-STEM can provide for a deeper understanding of Orgueil's mineralogy.

2 Acquisition Conditions and Data Analysis Approach

2.1 Sample preparation and data acquisition

The Orgueil sample section used in the present study was prepared by D. Troadec at *Institut d'Electronique, de Microélectronique et de Nanotechnologie* (IEMN) of the university of Lille by focused ion beam (FIB) using a Zeiss Crossbeam 550L. Two areas of the FIB section, of thickness $\sim 100\,nm$ were examined in this work using STEM-HAADF, STEM-EDS and 4D-STEM. The 4D-STEM datasets were acquired with energy-filtering with a slit of $20\,eV$. The convergence semi-angle, as obtained in the micro-probe mode, was 0.1 mrad. The full-width half-maximum (FWHM) of the probe profile was $\sim 7\,nm$. The datasets were acquired on a Medipix3 detector with a dwell time per pixel of $20\,ms$ and a camera length of $630\,mm$. The two areas will be denoted respectively as *Area1* and *Area2* corresponding to (a) and (b) in Figure 4.1, respectively.

2.2 Data analysis

The data analysis steps were outlined and detailed in the previous chapter. Here is a brief recapitulation:

1. **Preprocessing**:

   (a) **Dead pixel correction**: malfunctioning pixels are corrected using neighboring pixel interpolation.

   (b) **Diffraction stack alignment**: Data is cropped to retain the direct beam, then cross-correlating each diffraction pattern with the previous one is performed to find their relative offset. Patterns are then shifted accordingly until all patterns in the stack become properly aligned.

   (c) **Vacuum probe and probe kernel**: Electron probe shape is extracted which is then used to generate a probe kernel for pattern matching.

   (d) **Magnetite segmentation and removal**: Since we only care about the phyllosilicate matrix, Magnetite is removed from the investigated areas prior to further analysis.

This is done by first locating the diffraction peaks corresponding to magnetite from the 4D-STEM data, use them to reconstruct a virtual dark field image of magnetite, and then using the *Felzenszwalb* (Felzenszwalb and Pedro 2004) segmentation method to properly segment and isolate Magnetite.

(e) **Data storage**: The data is stored in a *hspy* file format which is based on the $HDF5$ open standard (De la Peña et al. 2022).

2. **Processing**:

(a) **Bragg spot registration**: Diffraction spots are located by cross-correlating the probe kernel with each diffraction pattern in the 4D-STEM stack. The result is a list of Bragg spots with pixel coordinates, reciprocal space coordinates, and intensity of the spots.

(b) **Mineralogical phase identification**: A Bragg vector map (BVM) is generated by merging diffraction peaks from all patterns in the stack. X-ray diffraction-like mineral phase identification is based on azimuthally averaged BVM patterns.

(c) **Virtual imaging and phase mapping**: After associating each peak in the radial profile with specific orientations of individual phases, the peaks are then clustered based on their phase belonging, and virtual dark field images are constructed by summing the contributions from peaks belonging to the same phase.

3 Results

High-angle annular dark field (HAADF) images of the areas investigated are shown in Figure 4.1(a,b). The observed regions exhibit the simultaneous presence of both coarse and fine-grained matrix constituents. The predominant matrix component is the phyllosilicate matrix, distinguishable by its gray contrast. The larger grains exhibiting a brighter contrast correspond to magnetite grains, which have been excluded from subsequent analyses as our primary focus is on the phyllosilicate matrix. In addition to these distinctions, both regions exhibit a significant presence of organic matter, possible silica-rich pockets and a low level of porosity. Figures 4.1(c,d) show high-angle annular dark-field (HAADF) images with high-magnification of some selected phyllosilicate-rich regions within the same focused ion beam (FIB) section. These images reveal some FIB-induced damage artifacts, as evidenced by the relatively smoother

texture within the phyllosilicate-rich areas and the presence of bubble-like artifacts dispersed across both regions.

Following the pre-processing steps described in the previous section, relevant mineralogical informations can be extracted from the 4D-STEM data. *Area1* is the first to be considered in the analysis. Figure (4.2a) is a field-of-view (FOV) of the area under investigation, excluding the magnetite grain situated in the top left. Subsequently, Figure (4.2b) showcases a BVM representative of this area, which is subjected to azimuthal averaging in Figure (4.2c). It is noteworthy that this particular region of the sample has endured significant Focused Ion Beam (FIB) damage. Evidently, the diffraction peak intensities in Figure (4.2c) appear notably weaker in comparison to the maximum peak intensity, signaling a pronounced level of structural degradation. Furthermore, upon examination of the diffraction patterns extracted from the boxes overlaid onto Figure (4.2a) and displayed in Figure (4.2d), it becomes apparent that the degree of damage within the area is substantial. This is evident from the amorphization of the phyllosilicates which is characterized by the presence of diffuse halos at approximately ~ 2.5 Å.

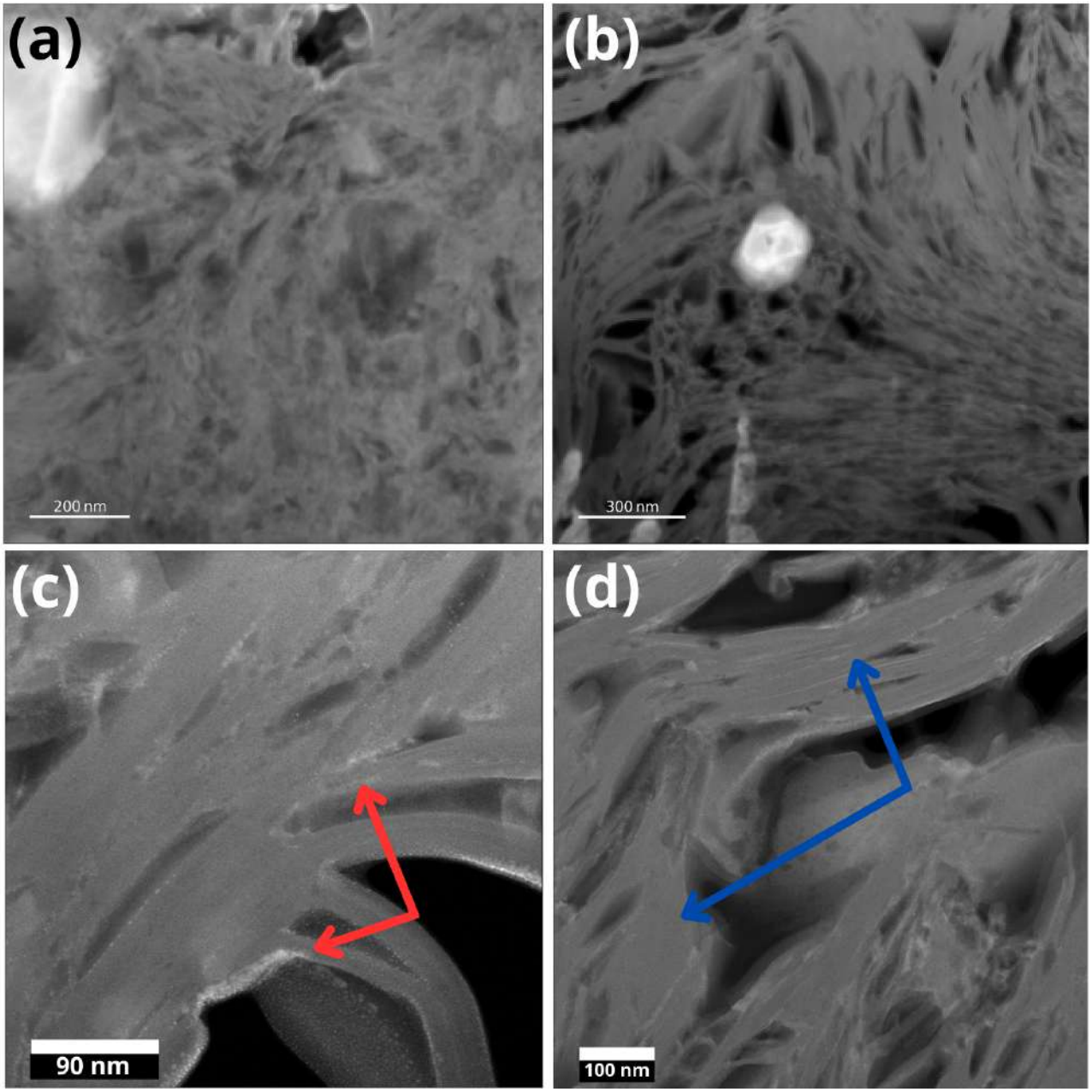

Figure 4.1: STEM-HAADF images from areas of Orgueil sample FIB section. (a) Depicts an area (*Area1*) with a prominent magnetite grain (The large bright grain in the top left). (b) Shows a different area (*Area2*) with another substantial magnetite inclusion in the middle. Both regions appear phyllosilicate-rich, with a smooth texture indicative of potential damage. (c) and (d) are high-magnification STEM-HAADF images highlighting possible FIB-induced damage artifacts. These artifacts manifest as very smooth phyllosilicate textures (indicated by blue arrows) and the presence of bubble-like features (indicated by red arrows), ultimately resulting in phyllosilicate amorphization.

Despite these notable damage observations, the reconstruction of virtual dark field images (VDF) remains feasible. This process involves the integration of 4D-STEM data over each diffraction ring, as emphasized in the radial profile. In Figure 4.3, a set of VDF images corresponding to distinct diffraction peaks observed in the radial profile of Figure (4.2c) is presented.

Notably, a distinctive pattern emerges within the VDF images. Upon close examination of the VDF images associated with peaks at approximately $\sim$ 4.4 Å, $\sim$ 3.45 Å, $\sim$ 2.48 Å, and $\sim$ 1.5 Å for phyllosilicates, and $\sim$ 7.1 Å for serpentine. A clear absence of discernible texture and the presence of noisy-looking distributions of these phases is evident. Indeed, when phyllosilicates are finely distributed (fine-grained phyllosilicates), the texture of the phyllosilicates lamellae is usually evident from VDF images, while coarse phyllosilicates tend to appear as large packets with a rather homogeneous intensity (coarse phyllosilicates).

This relevant, potentially FIB-induced, degradation of *Area1* makes the interpretation of our results extremely challenging in terms of mineralogy and accurate mapping of the various mineralogical phases within this area of the sample will be misleading.

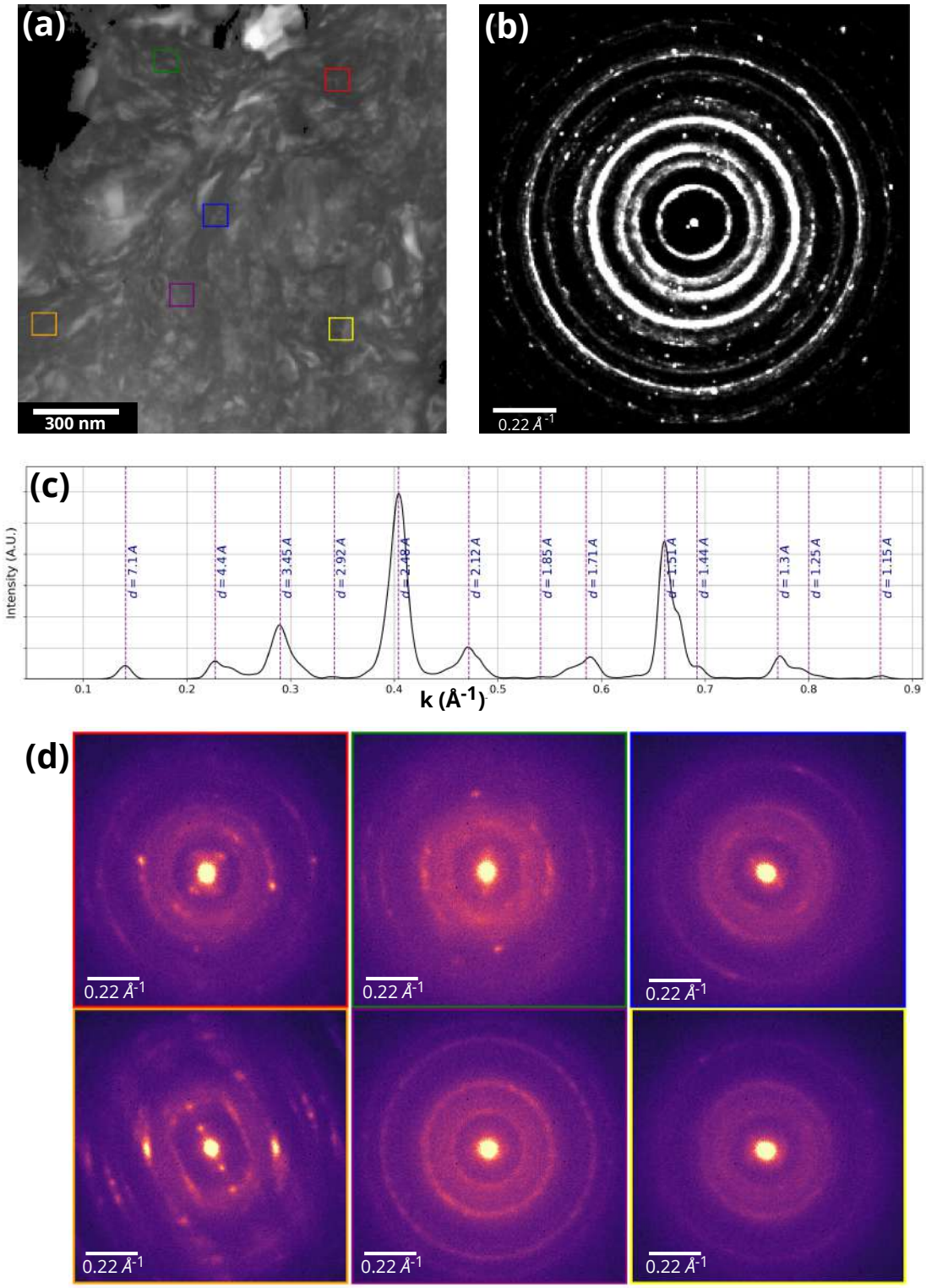

Figure 4.2: 4D-STEM analysis results of the first area in the FIB section corresponding to image (a) in figure 4.1. (a) is a field of view of the analyzed region, excluding the large magnetite grain in the top left. (b) Presents a Bragg vector map (BVM) covering the entire area. (c) Depicts the radial profile derived from azimuthal averaging of the BVM. Both the BVM and the radial profile collectively indicate severe crystalline degradation and amorphization of phyllosilicates. (d) Displays diffraction patterns from various phyllosilicate regions within the area, revealing diffuse halos around ~ 2.5 Å, consistent with the amorphous state of the phyllosilicates.

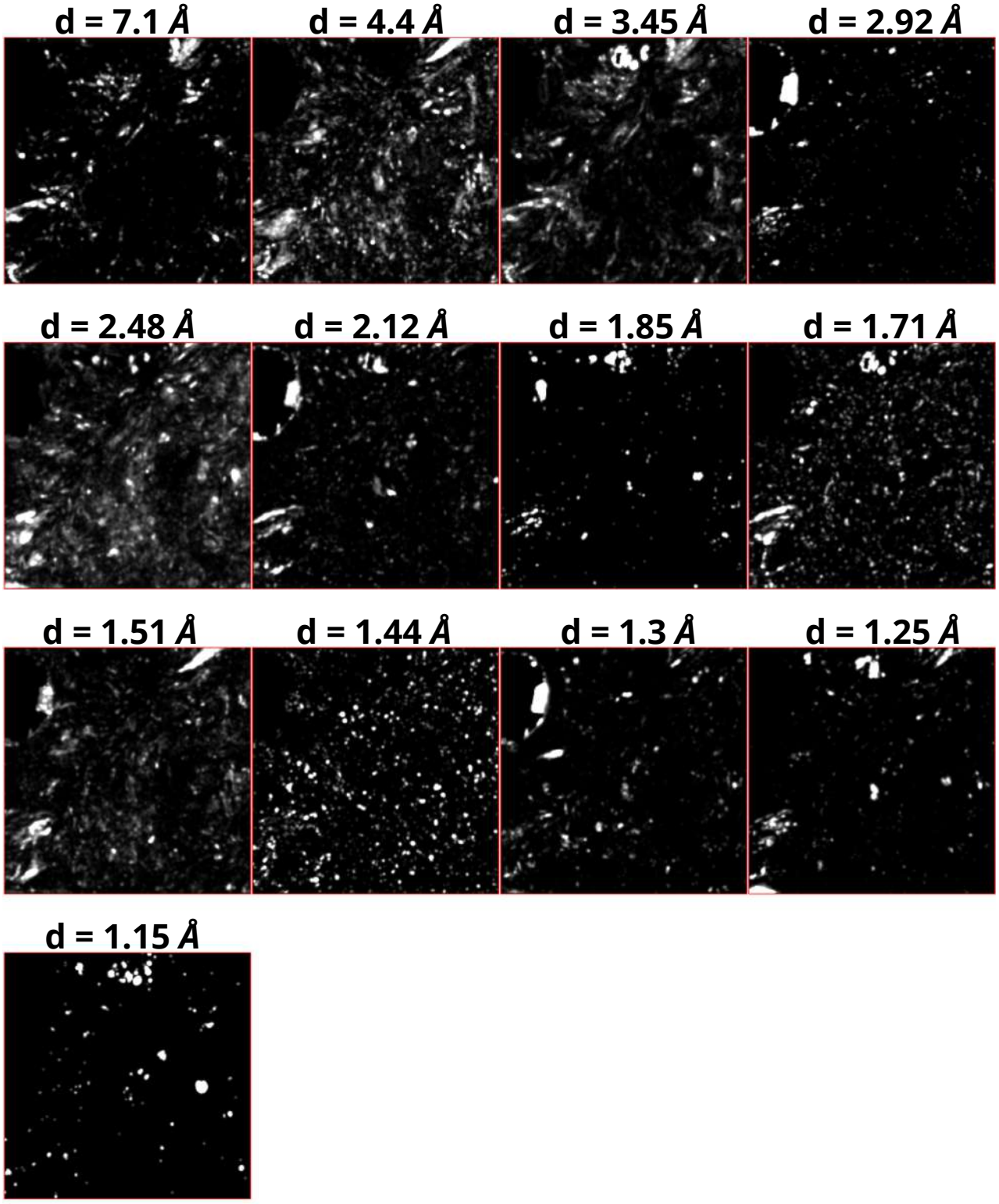

Figure 4.3: 4D-STEM analysis results from the first area in the FIB section corresponding to image (a) in figure 4.1. Integrating the 4D-STEM data over each diffraction ring emphasized in the radial profile results in a series of virtual dark field (VDF) images. Each VDF image is annotated with its respective characteristic d-spacing. The VDF images collectively highlight the pronounced crystalline degradation, potentially attributed to FIB-induced damage.

In contrast, *Area2* exhibits a noticeably lower level of degradation, as evidenced by a comparison

of the Bragg vector maps characteristic of both areas in the sample in Figure 4.2(b,c) and their respective radial profiles in Figure 4.4(b,c), respectively. *Area2* demonstrates a significantly higher count of detected diffraction spots when compared to *Area1*, and its radial profile exhibits more pronounced diffraction peak intensities relative to the maximum intensity, distinguishing it from the latter.

Moreover, an analysis of the individual diffraction patterns displayed in Figure 4.2d reveals that finer phyllosilicates in *Area2* have incurred some degree of damage, although it is notably less severe than what was previously observed in *Area1* resulting in a higher amount of diffraction signal. This makes the 4D-STEM data from *Area2* sufficiently rich in diffraction information to provide an accurate characterization of the area's mineralogy from a 4D-STEM perspective. Figure 4.5 presents a set of VDF images generated by integrating the intensity of each diffraction ring, guided by the peak positions and widths (~ 0.03 Å) outlined in Figure 4.4c and shown in the BVM in Figure 4.4b. Notably, when examining the VDF corresponding to the ~ 2.48 Å d-spacing relevant to phyllosilicates for instance, it becomes apparent that the textural features of phyllosilicates, as well as the typical intensity distribution in regions with coarser phyllosilicates, are distinct. This contrast becomes particularly evident when compared to the observations made in *Area1* which makes this 4D-STEM dataset suitable for further processing to extract relevant mineralogical features of the area.

3.1 Phase Mapping

Upon closer examination of the VDF images presented in Figure 4.5, it becomes apparent that certain images exhibit correlations indicative of their belonging to the same phase or sharing similar orientation conditions. This observation motivates the exploration of an image correlation-based metric like the Pearson correlation coefficient, with the aim of using correlations among the VDF images to perform phase segmentation.

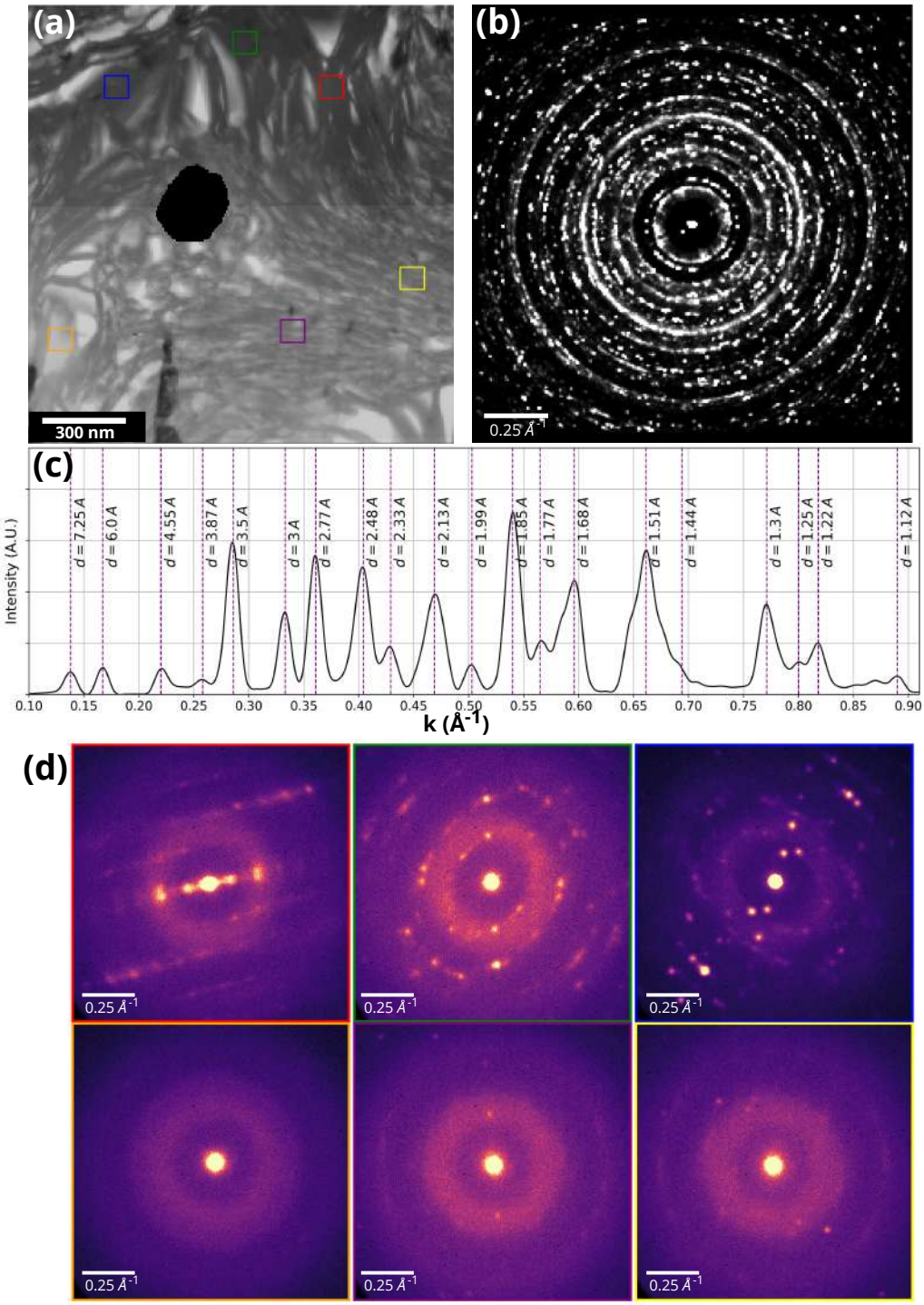

Figure 4.4: 4D-STEM analysis results from the second area in the FIB section corresponding to image (b) in Figure 4.1. (a) Provides a field of view of the analyzed region, excluding the large magnetite grain in the middle of the Figure (b) Presents a BVM covering the entire area. (c) Depicts the radial profile derived from azimuthal averaging of the BVM. While the radial profile and the BVM do not indicate severe degradation of the area, some level of degradation is still present, as evidenced by the relative smoothness in the phyllosilicates of the HAADF images. This is also indicated by (d) diffraction patterns retrieved from various phyllosilicate regions within the area, revealing diffuse halos around ~ 2.5 Å, suggesting a certain degree of amorphization in the phyllosilicates, although not as severe as in the *Area1*.

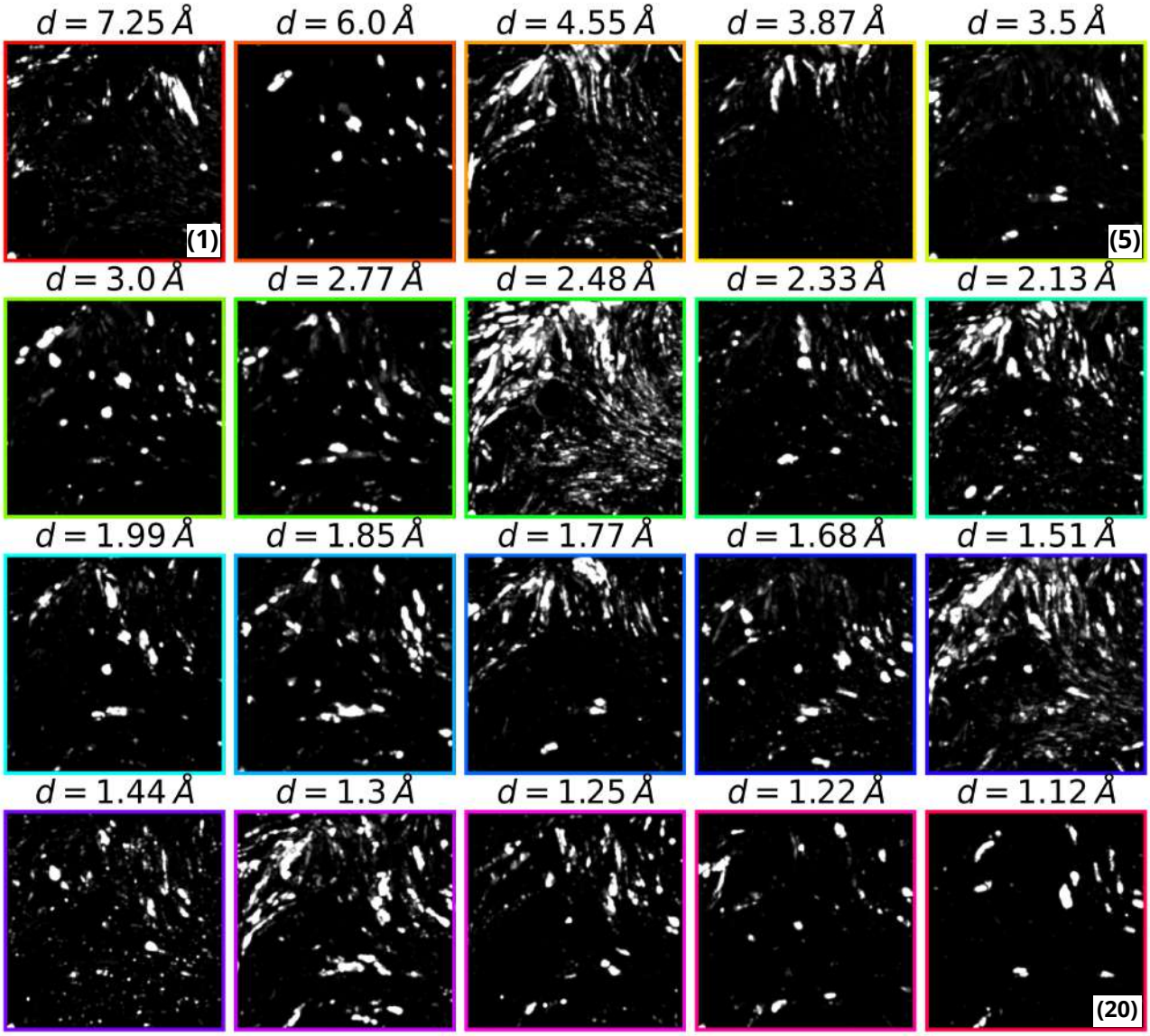

Figure 4.5: 4D-STEM analysis results of the second area in the FIB section corresponding to image (b) in figure 4.1. Integrating the 4D-STEM data over each diffraction ring observed in the radial profile results in a series of virtual dark field (VDF) images. Each VDF image is annotated with its respective characteristic d-spacing.

The Pearson correlation coefficient, when applied to images, measures the linear relationship between the pixel intensities of two images, indicating how well the intensities in one image can be "predicted" from those in another through a linear relationship. This coefficient ranges from -1 to +1. A value of 0 suggests no linear relationship, a negative value suggests an inverse linear relationship, and a positive value implies a direct linear relationship. In the context of VDF images, a high positive correlation signifies similar and coordinated pixel intensity changes, while a high negative correlation suggests opposite changes. A correlation coefficient of 1 or -1 indicates a perfect linear relationship.

Given two images represented as matrices A and B. The Pearson correlation coefficient can be formulated as follows:

$$corr(A, B) = \frac{cov(A, B)}{\sigma_A \sigma_B} \tag{4.1}$$

$$cov(A, B) = \frac{(A_{ij} - \bar{A})(B_{ij} - \bar{B})}{N} \tag{4.2}$$

$$\sigma_X = \sqrt{\frac{\sum_{ij} \left(X_{ij} - \bar{X}\right)^2}{N}} \tag{4.3}$$

Where:

- Each element A_{ij} or B_{ij} in these matrices correspond to the intensity of a pixel at position (i, j) in the respective images.
- $\bar{A}$ and $\bar{B}$ are the means of the pixel intensities of images A and B, respectively. N is the total number of pixels in the images.
- $cov(A, B)$ is the covariance matrix between matrices A and B.
- X = (A, B)

Figure 4.6 depicts the Pearson correlation coefficients matrix, quantifying the correlations among the various VDF images as presented in Figure 4.5. For instance, the second VDF image (Index 1 in Figure 4.6) demonstrates a correlation score of 90% with the sixth VDF image (Index 5 in Figure 4.6), and a correlation score of 60% with the eleventh (Index 10 in Figure 4.6) VDF image. This suggests a notably strong correlation between VDF images 1, 5, and 10, with the order determined by decreasing d-spacing values in Figure 4.5. This implies that these VDF images may be representative of the same mineralogical phase. However, it is essential to note that while this correlation-based approach may provide valuable insights, it fails to achieve complete phase segmentation. High correlation indices in this context are only achieved when the involved VDF images exhibit substantial similarities. While this can be useful in depicting orientation relationships across different mineralogical phases for example, it may not provide accurate results when the aim is to segment the area into different mineralogical phases especially when these exhibit very distinct orientation conditions.

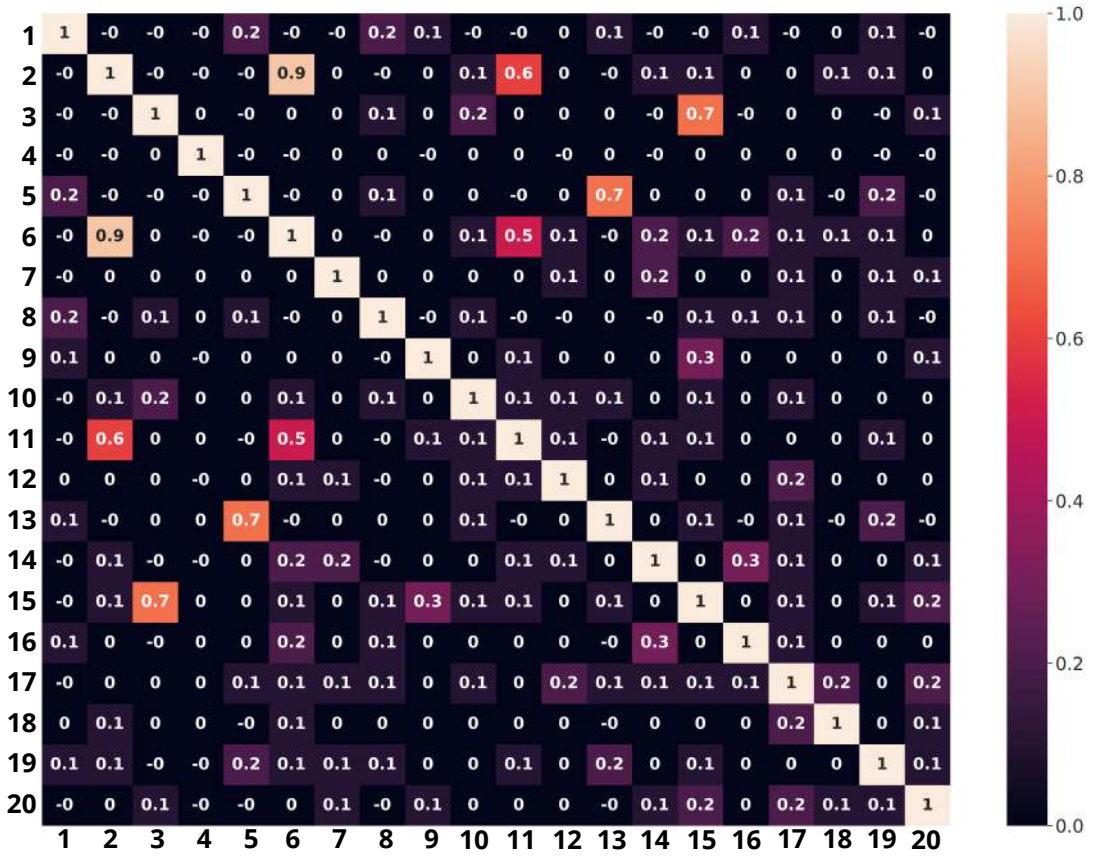

Figure 4.6: Clustering Analysis of the VDF images. A Pearson correlation coefficient map reveals relationships among the VDF images, with correlations (in absolute value) above 0.05 considered. Correlation values, rounded to the nearest tenth, are indicated.

To address this limitation, it becomes crucial to back our 4D-STEM data with energy dispersive X-ray spectroscopy (EDS) data for elemental mapping which can be used to guide the mineralogical phase segmentation. EDS results are outlined in Figure 4.7. Figure 4.7(a,b) shows the elemental distributions of Ca and S, while Figure 4.7c illustrates the elemental distribution map for (Mg,Si), overlaid with the elemental distributions of (Ca,S). Within the chemical segmentation, the darker regions primarily correspond to amorphous, carbon-rich, material distribution and/or porosity, with the exception of the prominent dark region in the center, which represents the magnetite grain, removed in the pre-processing steps.

In addition to amorphous material, this segmentation suggests that *Area2* predominantly consists of phyllosilicates and sulfates, providing a reliable starting point for the 4D-STEM phase mapping.

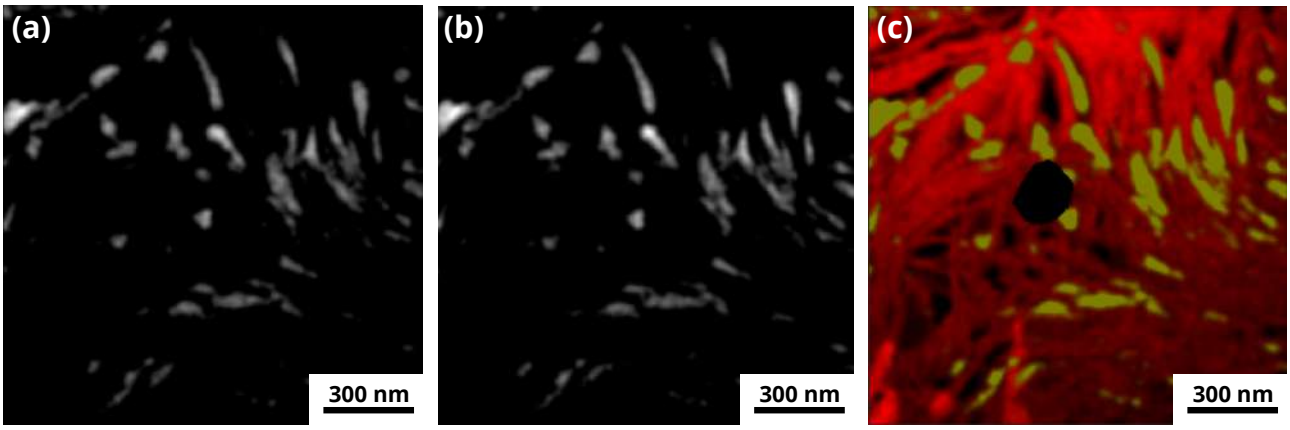

Figure 4.7: Energy dispersive X-ray spectroscopy (STEM-EDS) mapping of *Area2*. (a) Calcium element distribution within *Area2*. (b) Sulfur element distribution within *Area2*. (c) Segmentation result of the (Ca,S) map superimposed onto the (Mg,Si) map, showing the spatial distribution of sulfates in the phyllosilicate-matrix.

In Figure 4.8a, Four instances of the overall radial profile are reported to which are overlayed simulated profiles of lizardite, smectite, ferrihydrite, and the three possible (Ca,S) sulfates which are anhydrite, bassanite, and gypsum. Notably, these sulfates differ in their water content within their chemical structures, with anhydrite being anhydrous ($CaSO_4$), bassanite containing one water molecule per every two calcium sulfate molecules ($CaSO_4 + 0.5H_2O$), and gypsum having two water molecules for each calcium sulfate molecule ($CaSO_4 + 2H_2O$). Comparing the simulated profiles of sulfates with the original BVM-based radial profile of our data, a strong correlation between the simulated profiles and the BVM-based profile exists for sulfate structures with low water content, specifically anhydrite and bassanite.

Combining informations from the simulated profiles in Figure 4.8a, the VDF images in Figure 4.5, and the EDS segmentation in Figure 4.7, phase assignment becomes feasible. Figure 4.8b illustrates the fully indexed BVM-based radial profile highlighting the different mineralogical phases in different colors with peaks associated with at least two different phases highlighted in gray (anhydrite/serpentine) and cyan (anhydrite/phyllosilicates). Notably, both bassanite and anhydrite peaks closely align with BVM-based radial profile peaks. A discussion about the Ca-sulfate that is possibly present in the area investigated will be discussed in a dedicated section.

It is important to note that a complexity emerged in identifying calcium sulfates without EDS data, as some of the d-spacings associated with Ca-sulfates also align with d-spacing from Apatite and Hydroxyapatite. This highlights a challenge in relying solely on 4D-STEM

for accurate mineral phase identification in meteoritic samples and the crucial need for the additional informations provided by EDX analysis.

The serpentine structure in this profile exhibits d-spacings of $\sim$ 7.25 Å, $\sim$ 3.5 Å, and $\sim$ 1.77 Å corresponding to the (001), (002) and (133) crystallographic planes, respectively. Anhydrite exhibits d-spacings of $\sim$ 6 Å, $\sim$ 3.5 Å, $\sim$ 3 Å, $\sim$ 2.77 Å, $\sim$ 2.33 Å, $\sim$ 1.99 Å, $\sim$ 1.85 Å, $\sim$ 1.68 Å and $\sim$ 1.12 Å corresponding to the (010), (200), (020), (102), (022), (130), (212), (032), and $(42\bar{1})$ crystallographic planes, respectively, with the $\sim$ 3.5 Å d-spacing being common to serpentine (002) crystallographic plane. Phyllosilicates peaks, in this particular context refer to diffraction peaks associated with possible serpentine/smectite mixtures which cannot be discerned from the radial profile nor from the VDF images. These are the peaks at d-spacings of $\sim$ 4.55 Å, $\sim$ 3.87 Å, $\sim$ 2.48 Å, $\sim$ 2.13 Å and $\sim$ 1.51 Å . The peaks at $\sim$ 1.3 Å, $\sim$ 1.25 Å and $\sim$ 1.22 Å are common to phyllosilicates and anhydrite crystallographic planes. The crystallographic information files (CIF) used in the indexation process of lizardite, anhydrite, bassanite, gypsum and ferrihyrdite originate respectively from Laurora et al.; Hawthorne and Ferguson; Ballirano et al.; Comodi et al.; Jansen et al. (2011; 1975; 2001; 2008; 2002) which were arbitrarily chosen while that of smectite originates from Tsipursky and Drits (1984) which was the only one we found available.

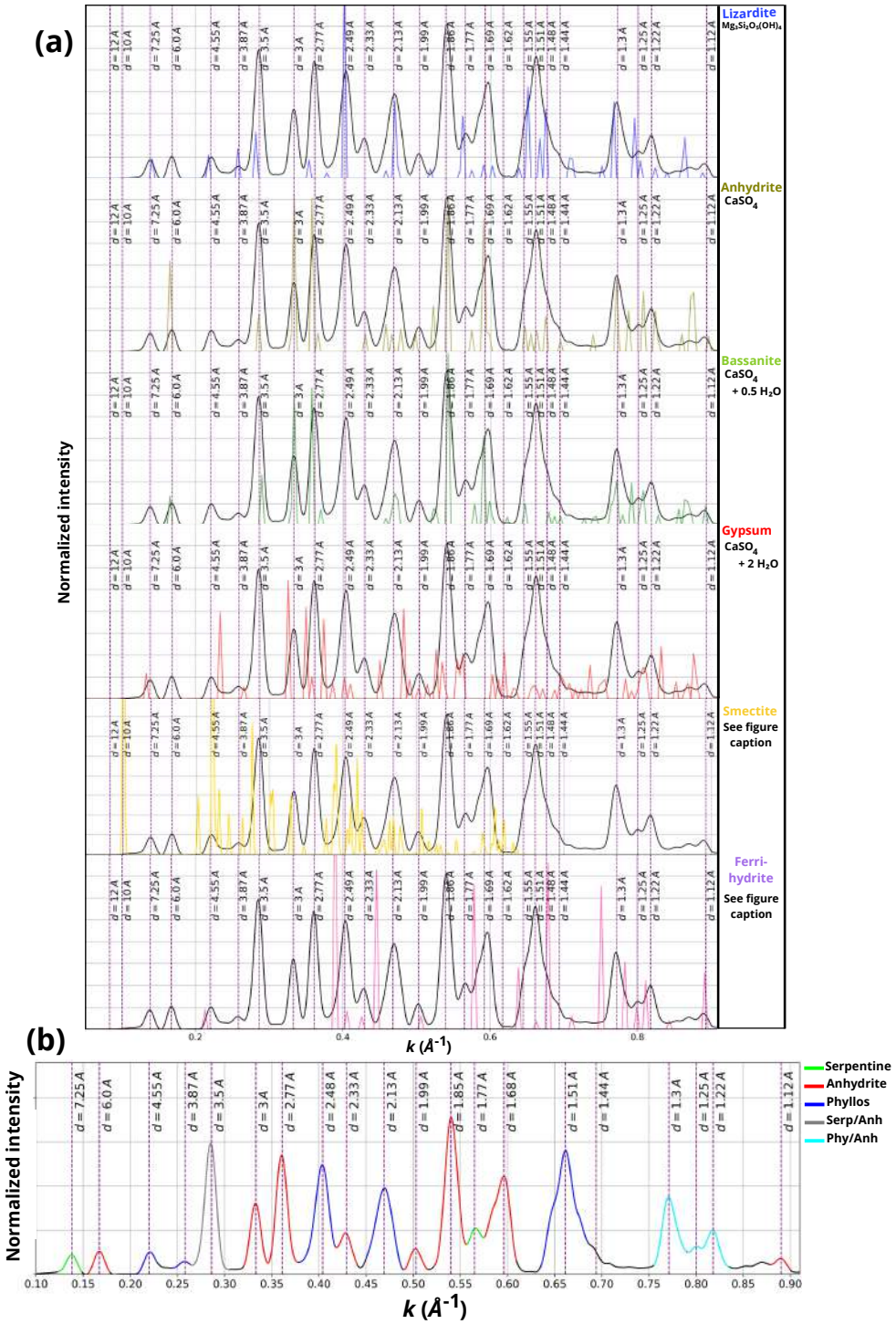

Figure 4.8: Diffraction peaks assignment and phase identification in *Area2*. This figure combines informations from radial profiles, simulated profiles, virtual dark field (VDF) imaging, and Energy Dispersive X-ray Spectroscopy (EDS) segmentation to facilitate phase assignment. (a) Four instances of the overall radial profile are presented, each overlaid with color-coded simulated profiles for distinct phases (lizardite, anhydrite, bassanite, gypsum, smectite and ferrihydrite). In this example, an electron diffraction pattern of a smectite of chemical formula $(Ca_{0.06}Na_{0.21}K_{0.27})(Al_{1.64}Fe_{0.06}Mg_{0.31})(Al_{0.29}Si_{3.71}O_{10}(OH)_2)$ from Tsipursky and Drits (1984) has been used, while the chemical formula for ferrihydrite was $5Fe_2O_3 \cdot 9H_2O$ from Jansen et al. (2002). (b) A fully indexed overall radial profile highlights mineralogical phases through color-coded peaks, with gray and cyan peaks indicating common features shared by two different phases (legend provided).

Integrating the 4D-STEM data over the diffraction peaks that are uniquely associated with serpentine, anhydrite and phyllosilicates, VDF images associated with each of these individual mineralogical phase are obtained. The 4D-STEM VDF imaging results are presented in Figure 4.9. The green areas are representative of serpentine, the red areas are representative of anhydrite while the blue areas are representative of phyllosilicates distribution. Without taking into account the big magnetite grain removed during pre-processing, black areas are attributed mostly to organic matter and porosity while it is not inconceivable that some of these areas might also correspond to regions whom mineral grains are oriented such as Bragg conditions are simply not satisfied, and hence a phase assignment was not possible.

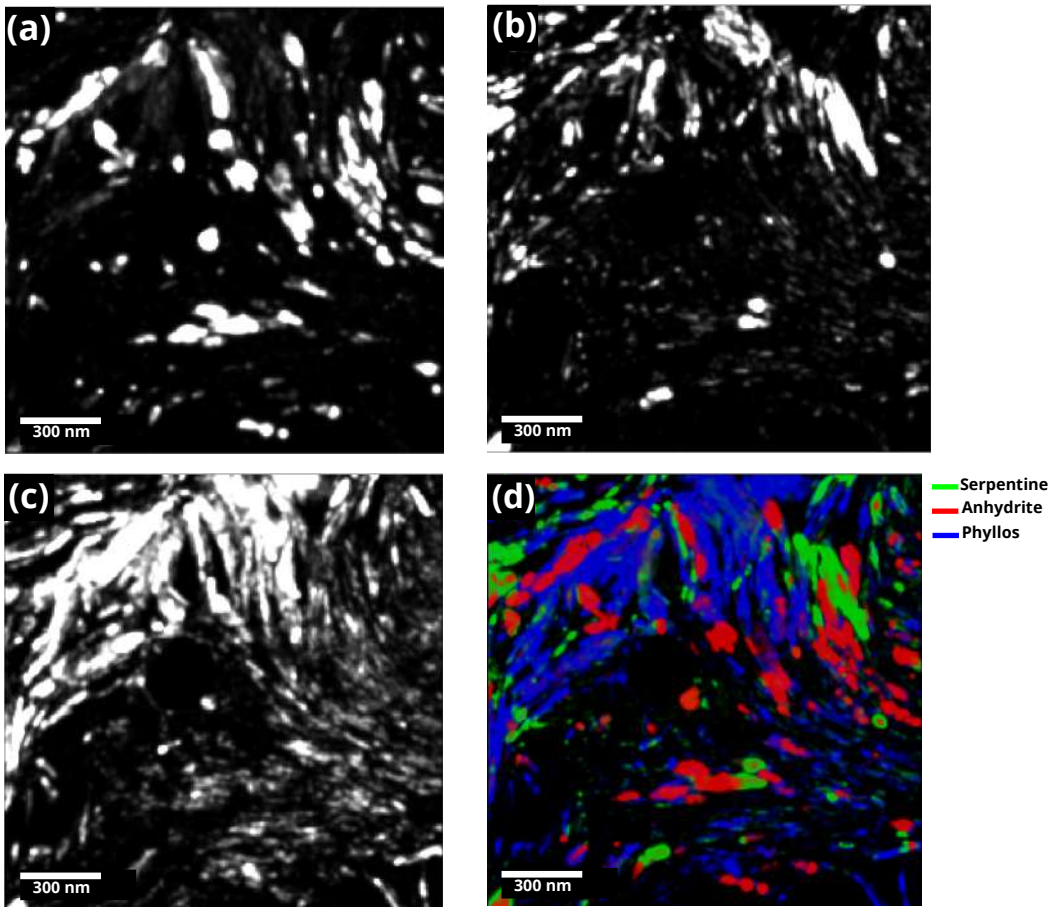

Figure 4.9: VDF phase mapping with 4D-STEM of *Area2*. (a) VDF image, reconstructed by integrating 4D-STEM data over each diffraction ring corresponding to the anhydrite phase. (b) VDF image, created by integrating 4D-STEM data over each diffraction ring corresponding to pure serpentine reflections. (c) VDF image displaying the distribution of phyllosilicates in *Area2* reconstructed by integrating 4D-STEM data over each diffraction ring of phyllosilicates. (d) A combined VDF image showing a segmentation of phyllosilicates, serpentine, and anhydrite distributions in *Area2*

.

4 Discussion

4D-STEM analysis of *Area2* have shown the presence of phyllosilicates and Ca-sulfates aligning with the typical mineralogy of Orgueil (Tomeoka and Buseck 1988; Brearley 2006). The focus was primarily on crystalline phases, and the study of amorphous regions, seen as dark areas in the HAADF image in Figure 4.1b, was beyond the main scope of this study.

4.1 Phyllosilicates in Orgueil

Phyllosilicates in Orgueil are a mixture of serpentine and smectite with the coarser areas usually enriched in serpentine while finer phyllosilicates are seldom enriched in smectites (Leroux et al. 2023; Tomeoka and Buseck 1988). No diffraction signature from pure smectite in its 00ℓ orientation was detected in the current 4D-STEM study. In addition to the $\sim$ 100 nm thickness of the sample, it is conceivable that smectite grains absence in these areas occurred coincidentally or that the orientation conditions of the smectite grains with respect to the electron beam do not enable the detection of the 00ℓ reflections of smectite which is the only possible way smectite can be unambiguously identified in 4D-STEM conditions. Otherwise, it is always found in intimate, fine mixing with serpentine which makes an exact segmentation in the current experimental conditions very challenging.

4.2 Ferrihydrite

Ferrihydrite is a major constituent in Orgueil meteorite. It occurs as S,Ni-rich particles dispersed in Orgueil's phyllosilicate matrix. Ferrihydrite aggregates usually occur as bright areas within the fine-grained phyllosilicate matrix. Their SAED signature is usually in the form of two broad rings at $\sim$2.58 Å and $\sim$1.50 Å with a diffuse background (Tomeoka and Buseck 1988). Ferrihydrite occurrence was first explained by Tomeoka and Buseck (1988) by the replacement of Fe-(Ni) sulfides and the aqueous alteration effect on coarse phyllosilicates which ultimately produces intimate mixtures with the finer phyllosilicates. However, this hypothesis was re-examined by recent findings from studies on Ryugu samples (Ito et al. 2022; T. Nakamura et al. 2022; Yamaguchi et al. 2023; Yokoyama et al. 2022). T. Noguchi et al. (2023) highlighted that the absence of ferrihydrite and sulfates in Ryugu samples, akin to CI chon-

drites, suggests that these minerals in Orgueil might be terrestrial weathering products, not intrinsic to the original composition. Additionally, their observations propose that ferrihydrite in CI chondrites might have emerged as an alteration product of tiny Fe-Ni sulfide grains due to terrestrial weathering, indicating a potential alternative pathway for the formation of these minerals in Orgueil, which is in agreement with Leroux et al. (2023). In the present study, ferrihydrite presence in *Area2* cannot be confirmed. Typically, ferrihydrite in Orgueil is intimately mixed with fine-grained phyllosilicates, but, as it can be seen from the radial profiles in Figure 4.8, ferrihydrite diffraction peaks can be very closely associated with peaks from other matrix constituents, in which case, ferrihydrite cannot be independently segmented to a VDF image.

4.3 Calcium Sulfates

Gounelle and M. Zolensky (2001) have reinterpreted the origin and formation mechanisms of sulfates within CI chondrites, revisiting and expanding upon their earlier assertions outlined in M. Zolensky et al. (1993). Initially, M. Zolensky et al. (1993) posited that the presence of abundant sulfates in certain CI chondrites, such as Orgueil, Ivuna, Alais, and Tonk, could be attributed to late-stage oxidizing conditions on their parent bodies. However, this viewpoint was reassessed in Gounelle and M. Zolensky (2001), which introduced a nuanced perspective. The reinterpretation suggests a plausible scenario in which sulfate veins may have formed through terrestrial oxidation processes. Earth's weathering mechanisms are implicated in the transformation of nanosulfides into ferrihydrite, thereby contributing to the creation of calcium sulfates (eg. Harries et al. 2013; Belzile et al. 2004; Janzen et al. 2000).

This process involves the dissolution of pyrrhotite to ferrous ions (Fe^{2+}) when exposed to water and high oxygen levels, with subsequent oxidation to ferric ions (Fe^{3+}) in the presence of oxygen. The precipitation of ferric hydroxide ($Fe(OH)_3$) follows, giving rise to ferrihydrite. The sulfuric acid produced in this process may react with dissolved elements like Ca^{2+}, resulting in the formation of calcium sulfates (Leroux et al. 2023).

The observed close spatial relationship between calcium sulfate and pure serpentine areas in VDF images (Figure 4.9a,b) reveals a distinct superposition of sulfate and serpentine grains. The porous nature of serpentine masses, as indicated by their corresponding VDF images, may facilitate the migration and precipitation of sulfate phases within these regions. Given the

relative solubility of calcium sulfate phases, dissolution near weathered sulfides and subsequent precipitation in other areas is plausible. This interpretation aligns with the suggestion that the observed association of anhydrite-serpentine lacks paragenetic meaning, emphasizing a compatibility with an alteration process on Earth. If co-precipitation of serpentine-sulfate grains is ruled out, the proposed explanation posits that the high porosity of serpentine areas facilitated the concentration of a sulfate-rich fluid, ultimately resulting in the precipitation of calcium sulfate upon evaporation or sublimation of the aqueous sulfate solution.

Interestingly, T. Nakamura et al. (2022) observed the formation of sodium and calcium sulfates in Ryugu samples shortly after their preparation for analysis. These findings were attributed to a reaction believed to occur between calcite and sulfuric acid, the latter generated from the oxidation of pyrrhotite grains in samples exposed to Earth's atmospheric conditions. Furthermore, recent studies on the Winchcombe CM chondrite have concluded that the sulfates (gypsum, bassanite, and anhydrite) observed on the edges of the CM chondritic sample were attributed to the damp fall environment, likely resulting from sulfide-derived H_2S reacting with calcite within the meteorite after its entry into the Earth's atmosphere (Jenkins et al. 2023).

4.3.1 Which Ca-sulfate in Orgueil ?

Our 4D-STEM investigation of Orgueil chondrite yielded crucial insights into the nature of Ca-sulfates present in the sample. The results indicate that the Ca-sulfate phase is weakly hydrated, pointing towards the likelihood of it being either bassanite or anhydrite. This finding aligns with recent research by Phan et al. (2022), where the analysis of Orgueil based on infrared (IR) signatures identified sulfate as the second most frequent signature after phyllosilicates. The study suggests that the Mg-rich and Ca-rich sulfates in Orgueil could be respectively epsomite and bassanite, possibly originating from the decomposition of primary iron sulfide during aqueous alteration on the parent body. In contrast, Tomeoka and Buseck (1988) and Fredriksson and Kerridge (1988) propose Ca-sulfates in Orgueil as likely gypsum which was also detected in XRD measurements in Viennet et al. (2023). Our 4D-STEM results support the presence of bassanite as a weakly hydrated Ca-sulfate phase and highlight the improbability of gypsum representing the Ca-sulfate phase in the studied area. However, the possibility of anhydrite as the most likely Ca-sulfate phase present in the area under investigation is also indicated.

Indeed, it is not unlikely to encounter anhydrite in the Orgueil sample, even if we consider the possibility of sulfates forming on Earth as a secondary product of aqueous alteration. The initial phase likely formed at lower temperatures as gypsum, which is stable at temperatures below 40-50°C. However, considering the gypsum-anhydrite transition, particularly if the temperature exceeds 40°C and/or the relative humidity is below the gypsum-anhydrite transition threshold as outlined in Charola et al. (2007), there is a plausible scenario in which gypsum crystals could transform into anhydrite. Conversely, the presence of bassanite is deemed highly unlikely in Orgueil, given its metastable nature under typical Earth surface conditions. This is supported by the tendency of this metastable phase to decompose into a mixture of gypsum and anhydrite at temperatures below 97°C over time (Kelley et al. 1941; Charola et al. 2007). Consequently, it is proposed from our work that anhydrite is also probably present in Orgueil.

5 Conclusion

The 4D-STEM analysis of *Area2* in the Orgueil CI chondrite unveils the existence of phyllosilicates and Ca-sulfates, aligning with earlier investigations. Notably, the lack of diffraction signatures from pure smectite may be attributed to orientations outside Bragg conditions, and the absence of ferrihydrite could be attributed to its extensive mixing with the fine phyllosilicates. The study aligns with the previously proposed scenario of calcium sulfate formation, emphasizing that our results provide further confirmation rather than introducing a new hypothesis. The close spatial relationship, as revealed by the 4D-STEM VDF images, between calcium sulfate and pure serpentine areas implies complex dissolution and precipitation processes. However, it should be noted that, while many studies detect the presence of gypsum and few mention the presence of bassanite, our 4D-STEM study reveal that the Ca-sulfates are present, at least in the particular area investigated, in the form of anhydrite.

This study also underscores the significance of integrating 4D-STEM data with EDX data to ensure accurate interpretations. However, it is crucial to acknowledge the challenges inherent in the proposed procedure. The reliance on a Bragg vector map (BVM), which offers a summarized virtual diffraction pattern of all diffraction events during sample beam interactions, poses difficulties in indexation. The process requires careful examination of VDF images, elemental composition, and a comprehensive understanding of the potential sample mineralogy. Direct

indexation of 4D-STEM data is restrained by the fact that individual grain orientations often do not meet Bragg conditions. In contrast, 4-dimensional scanning precession electron diffraction experiments can address effectively this limitation. However, the high beam sensitivity of the sample and the fine mixing between different mineralogical phases present ongoing challenges in overcoming these complexities.

One potential strategy to keep experiments as simple as possible while further streamlining the analysis involves leveraging machine learning approaches such as non-negative matrix factorization (NNMF). These techniques can be employed to segment 4D-STEM data into a condensed set of representative VDF images and their corresponding diffraction signatures. The goal is to map the outcomes of these unsupervised learning approaches to the mineralogy of the sample, which will be the focus of investigation in the next chapter.

Chapter 5

4D-STEM Phase and Orientation Mapping Using a Non-Negative Matrix Factorization Approach: Application to Chondritic Samples

1 Introduction

In the previous two chapters, a comprehensive analysis of 4D-STEM data based on an Bragg vector map (BVM)-based approach obtained from Ryugu and Orgueil samples was conducted, revealing the intricate structural features of their mineralogical constituents. While this provided valuable informations, some limitations were recognized in our approach that needed to be addressed.

One major concern was the semi-manual identification and mapping of different phases from the 4D-STEM data, which can introduce subjectivity and tediousness in the process. Additionally, when some phases present similar or relatively close interplanar spacings, these cannot be accurately unmixed from the BVM-based description, which limits, in this case, the accuracy of mineral phase identification.

In contrast, automated crystal orientation mapping (ACOM) on 4D-STEM datasets (E. Rauch and Dupuy 2005; Ophus et al. 2022) is an optimal way to accurately determine the orientation of all crystalline grains that exhibit sufficient diffraction signal and can also be used to identify the different phases that are potentially present in the sample area. This method is generally more efficient when combined to precession electron diffraction (PED). In the latter,

the converged electron beam is continuously rotated around a cone at each grid position. A diffraction pattern is thus formed by integrating over a collection of diffraction conditions excited by the rotating electron beam generating a quasi-kinematical diffraction pattern which facilitates direct comparison with kinematical simulations for accurate determination of crystal phase and/or orientation (Brunetti et al. 2011; Eggeman et al. 2015; Nalin et al. 2020).

Despite the considerable success of ACOM in various studies that involve phase and/or orientation mapping, it has not been successful in our case studies for several reasons. Primarily, the main focus of our analyses was on the phyllosilicate-rich matrix which exhibit a nanometer-scale mixture between fine-grained constituents, leading to overlapping diffraction patterns of different phases and/or orientations. Additionally, the sample's thickness, typically around 100 nm further complicates this overlapping, increasing the challenges of accurate phase identification. Various attempts, mainly relying on machine learning, have been utilized to address the above limitations or simplify the processing of extensive data generated in a 4D-STEM experiment. Uesugi et al. (2021) applied singular value decomposition (SVD) and non-negative matrix factorization (NNMF) directly on raw data to reconstruct sparse diffraction patterns from a 4D-STEM dataset of Titanium Oxide nanosheets, consisting of 100×100 diffraction patterns. Their goal was to resolve two overlapping diffraction patterns of $Ti_{0.87}O_2$ and Ti_2O_3 nanosheets. They demonstrated that NNMF based on alternating least-square multivariate curve resolution (ALS-MCR) successfully resolved the two patterns, while SVD was used to provide an initial estimate of the maximum number of resolvable components.

Allen et al. (2021) introduced another NNMF-based approach. The method initially performed Bragg spots registration and reduction, converting each diffraction spot into a single point representing the spot's center, with all spot intensity concentrated in it. This process yields a new 4D-STEM sparse dataset as all spots are concentrated as single points with background and/or amorphous signal significantly reduced in the process. Subsequently, NNMF was applied to this newly generated 4D-STEM dataset and proved successful in mapping individual grains in a gold-palladium nanoparticle catalyst.

Bruefach et al. (2022) presented a pipeline for developing 4D-STEM feature representations suitable for unsupervised clustering using NNMF. They evaluated each feature with NNMF and discussed the results for both simulated and experimental data. The research highlighted certain

feature representations exhibiting enhanced performance in identifying overlapping grains with greater reliability and used real space refinement to identify spatially distinct sample regions, which allowed grain size and shape analysis. Building on their previous work, Bruefach et al. (2023) further improved their approach by implementing consensus clustering.

Machine learning have also been used in several studies to elucidate intriguing material properties from 4D-STEM data in particular (Shi et al. 2022; Nalin et al. 2020) and in scanning transmission electron microscopy in general (Kalinin et al. 2022).

Although these different approaches have shown significant success in unraveling the specific challenges addressed in the respective papers, it is important to note that they have not been extensively tested on more complex samples or applied to broader materials which present heterogeneous mixtures of numerous phases with multiple orientations.

In this chapter, we attempt to adapt the approach used in Allen et al. (2021) to our case study on meteoritic samples. Our aim is to leverage this approach to effectively segment our 4D-STEM data into distinct mineralogical phases and their corresponding diffraction signatures. We will initially assess the effectiveness of this method using a basic MgO nanocubes dataset from Bergh et al. (2020) as a benchmark. This comparison will highlight the efficiency differences between the pre-processing pipeline used in Allen et al. (2021) before applying NNMF, and the direct application of NNMF on raw data with minimal pre-processing, as demonstrated in Bergh et al. (2020). Afterwards, the performance of this approach will be tested on Ryugu and Orgueil 4D-STEM data, where reliable phase identification and mapping have been previously established in Chapters 3 and 4 through the BVM-based analysis procedure. Relative advantages and limitations of this strategy are discussed. Lastly, an improved approach including an additional azimuthal averaging step to the pre-processing pipeline outlined in Allen et al. (2021) will be introduced and its outcome on the 4D-STEM data of interest will be discussed.

2 Theory of Singular Value Decomposition and Non-Negative Matrix Factorization

Decomposition techniques, such as Singular Value Decomposition (SVD) and Non-Negative Matrix Factorization (NNMF), are widely used unsupervised learning approaches. SVD iden-

tifies significant features by reducing dimensionality, facilitating data compression and noise reduction while NNMF breaks down complex data into non-negative components, aiding in pattern recognition and source separation. Both techniques enable clearer insights and improved understanding of complex data structures. In this section, the theoretical background behind SVD and NNMF decomposition methods will be briefly introduced.

2.1 Singular Value Decomposition

The Singular Value Decomposition (SVD) is essentially a matrix factorization method that decomposes any matrix A into three constituent matrices: U, containing left singular vectors; S, with singular values; and V^T, comprising right singular vectors. SVD finds application in diverse areas such as data compression, image processing, and machine learning (Golub and Van Loan 1996; Jolliffe and Cadima 2016).

Given $A \in \mathbb{R}^{m\times n}$, there exist orthogonal matrices $U \in \mathbb{R}^{m\times m}$ and $V \in \mathbb{R}^{n\times n}$ with columns $\{u_i\}_{i=1}^m$ and $\{v_i\}_{i=1}^m$ along with a diagonal matrix $S \in \mathbb{R}^{m\times n}$ ($\sigma_i \equiv S_{i,i}$) satisfying $\sigma_1 \geq \sigma_2 \geq \cdots \geq \sigma_{\min(m,n)} \geq 0$ such that:

$$A = USV^T \tag{5.1}$$

We call the columns of U the left singular vectors of A and the columns of V the right singular vectors of A. The σ_i's are the singular values of A. Collectively, the matrices U, S, and V are referred to as the SVD of A.

Several fundamental properties are characteristic to SVD. Firstly, it involves orthogonal matrices U and V, whose columns form orthonormal bases. Secondly, the singular values are arranged in descending order along the diagonal, facilitating rank determination of the original matrix A. Moreover, SVD offers compact representation by retaining significant singular values and their corresponding vectors, allowing for efficient data compression and dimensionality reduction.

2.1.1 Truncated Singular Value Decomposition and Eckart-Young Theorem

Truncated SVD involves selecting an optimal number of components to retain, typically determined through the analysis of what is referred to as the scree plot showcased in Figure 5.1. It

is generated by plotting the ratio of the singular values $\frac{\sigma_i}{\sum \sigma_i}$ against their corresponding indices i. We shall frequently refer to it simply as the singular value ratio here but we note that is also usually referred to as the explained variance ratio in the literature.

The decay pattern of the singular values visually indicates the rate at which information is captured by each component. Typically, the plot exhibits an initial rapid decrease followed by a more gradual decline. The point of inflection in the plot, where the slope begins to level off, often serves as a heuristic for selecting the optimal number of components to retain in the truncated SVD. This point represents the balance between retaining significant information and reducing dimensionality, as further components beyond this point contribute minimally to the overall information captured. Thus, by examining the scree plot, we can make informed decisions regarding the truncation level for dimensionality reduction.

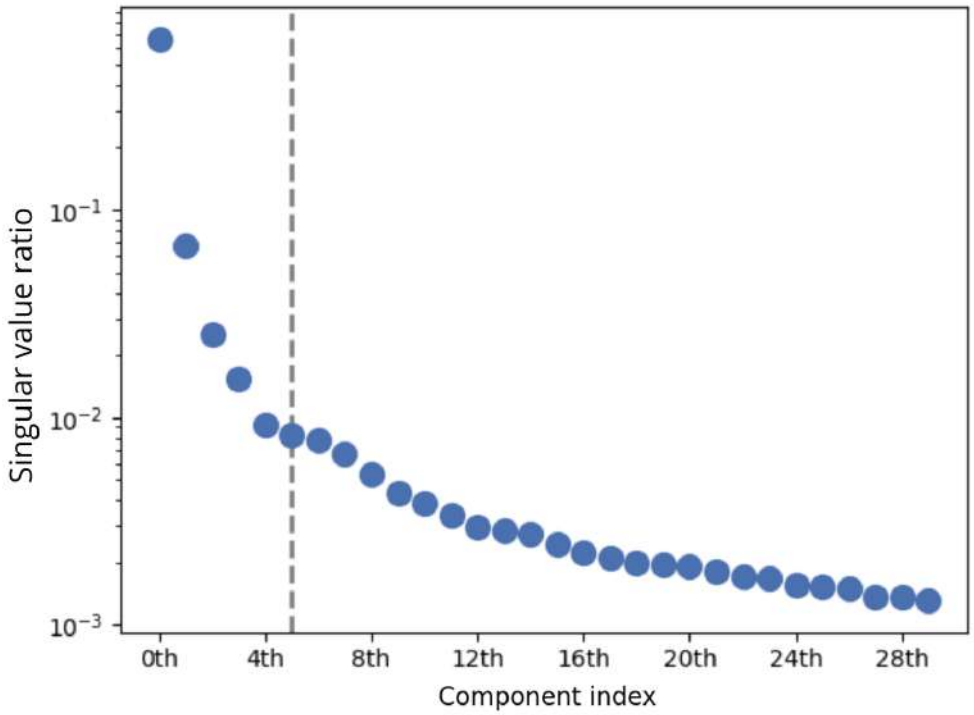

Figure 5.1: Example of a scree plot with the "elbow" position suggesting an estimate of the truncated number of components that best approximates the input data (Adapted from HyperSpy Documentation).

The reason why SVD is very suitable for dimensionality reduction lies in the Eckart-Young theorem (Eckart and Young 1936).

Let us consider the SVD of A in 5.1 which can also be reformulated as,

$$A = \sum_{i=1}^{n} \sigma_i u_i v_i^\top = \sum_{i=1}^{r} \sigma_i u_i v_i^\top \tag{5.2}$$

where $\{\sigma_i\}_{i=1}^{r}$ are the nonzero singular values of A up to r. Let us define an approximation A_p to A as:

$$A_p = \sum_{i=1}^{p} \sigma_i u_i v_i^\top \qquad (p \leq r) \tag{5.3}$$

Eckart-Young theorem states that (Eckart and Young 1936), for $A, B \in \mathbb{R}^{m \times n}$ and $\text{rank}(B) = p \leq \text{rank}(A) = r$, we have:

$$\min_{\text{rank}(B)=p} \|A - B\|_2 = \|A - A_p\|_2 = \sqrt{\sum_{i=p+1}^{p} \sigma_i^2} \tag{5.4}$$

In other terms, A_p is the best possible rank p approximation to the original matrix A in the euclidean norm (L^2) sense.

For the remainder of this thesis, SVD will be solely used for determining the optimal number of components to be used in the NNMF decomposition.

2.2 Non-Negative Matrix factorization

Non-Negative Matrix Factorization (NNMF), introduced by Paatero and Tapper (1994), stands out as an unsupervised learning algorithm employed for decomposing multivariate data into a more manageable and interpretable form. Similarly to SVD, NNMF decomposes the observed data matrix A into two matrices denoted here as W and H such that:

$$A_{m,n} \approx W_{m,p}\, H_{p,n} \qquad \textit{with } p < r \quad \textit{and} \quad W, H > 0 \tag{5.5}$$

W and H are called the basis and coefficients matrices, respectively, while p is the truncated number of components to be used in the NNMF procedure. The factorization in NNMF is iterative and the goal is to minimize the residual between A and WH.

NNMF, known for its interpretability, decomposes data into non-negative components, facilitating comprehension of underlying structures. The non-negativity constraint particularly suits diffraction data, as negative values lack meaningful interpretations. Additionally, NNMF

excels in feature extraction from high-dimensional datasets, offering a robust approach that withstands outliers and noise.

3 An Approach for Diffraction Signal Unmixing in 4D-STEM Data

To compare the efficacy of different NNMF-based procedures, we will adopt the pre-processing methodology outlined by Allen et al. (2021) and evaluate it against another NNMF-based approach used by Bergh et al. (2020) in the subsequent section. In the following, the approach used Allen et al. (2021) will be described.

3.1 Data Pre-processing

Prior to applying NNMF, Allen et al. (2021) undertake some necessary pre-processing steps. These are summarized in Figure 5.2. The first pre-processing step involves Bragg peaks registration, aiming to automatically identify and locate all the Bragg spots present within the dataset. For this, the direct beam is first cropped from the diffraction pattern of a vaccum or very thin area, and used to create a template. Diffraction spots are then identified by computing the cross-correlation between the probe template and individual diffraction patterns within the 4D-STEM stack (Savitzky et al. 2021). The third step in the pre-processing pipeline involves the reduction of each detected Bragg spot into a single pixel point containing all the intensity of the original diffraction spot. Next, all detected Bragg peaks are plotted in a single image, creating a BVM. The BVM is subsequently employed to center the 4D-STEM data and correct for elliptical distortions. This is done by, first, computing the center of mass of opposite peak clusters and then re-center all the diffraction patterns to $(k_x, k_y) = (0, 0)$. For the correction of elliptical distortions, an annulus is fitted to a clearly defined diffraction ring within the BVM. This annulus serves as a reference, allowing us to gauge and subsequently correct distortions present in the diffraction rings. The derived fit parameters are then utilized to accurately mitigate distortions in the diffraction patterns. Consequently, a new corrected 4D-STEM dataset is obtained, ideally devoid of any diffraction background, and with all diffraction spots transformed into points.

The resulting output is a centered, elliptically corrected 4D-STEM data stack, where the original peaks have been transformed into points. This 4D-STEM data stack can be rebinned by a specified binning factor if it aligns with the data's characteristics, potentially reducing computational demands and processing time for the decomposition process. Afterwards, The 4D data is flattened and reshaped into a 2D matrix format, as required for matrix decomposition algorithms such as *NNMF*, resulting in dimensions of ($N_x \times N_y$, $N_{k_x} \times N_{k_y}$) where (N_x, N_y) are the spatial dimensions and (N_{k_x}, N_{k_y}) are the diffraction space dimensions.

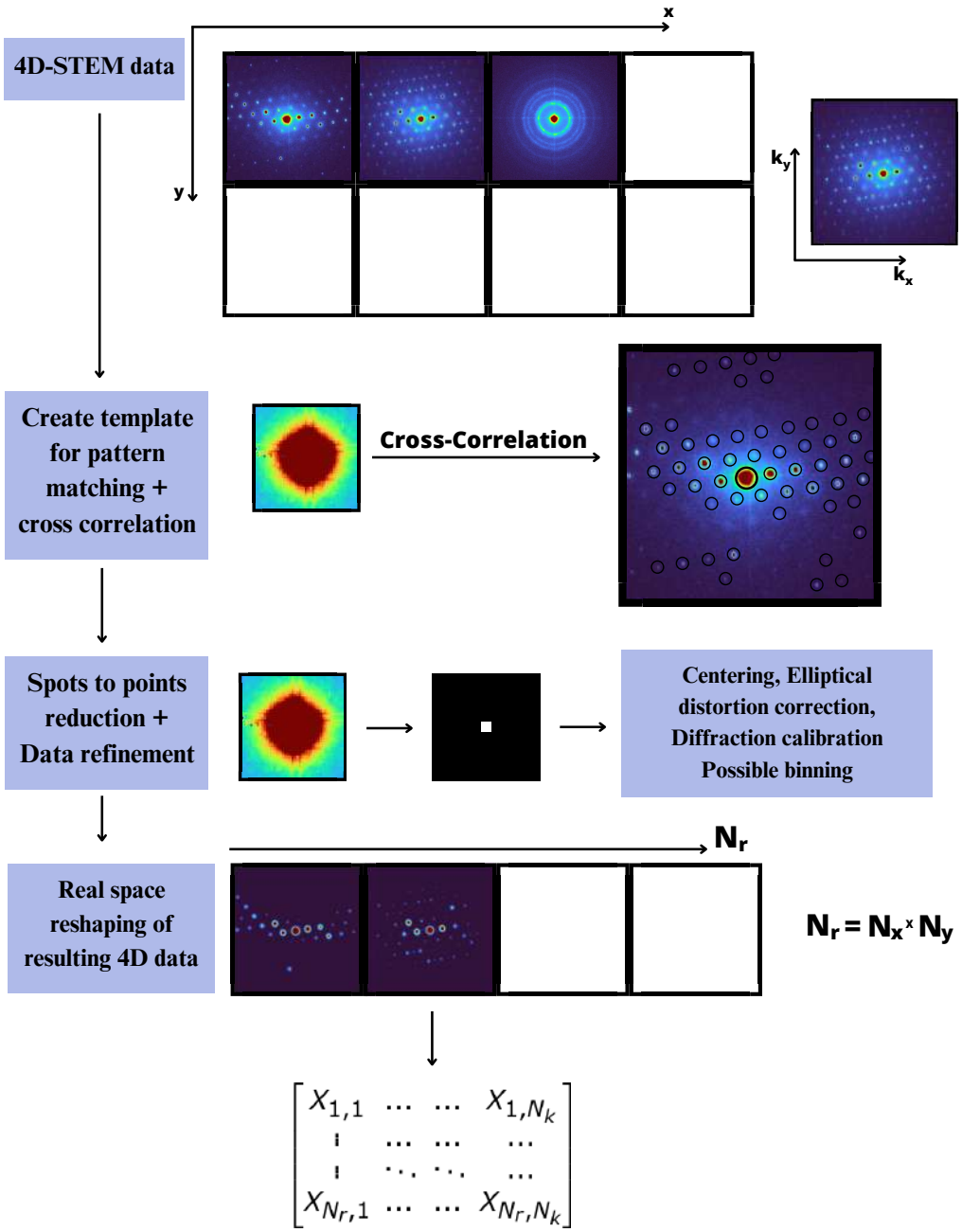

Figure 5.2: 4D-STEM data preparation for NNMF decomposition. First a template is created for cross-correlative Bragg spots registration, and data refinement is performed on the detected Bragg spots. The resulting 4D data are reshaped into a 2D matrix of shape (N_r, N_k), where $N_r = N_x \times N_y$ and $N_k = N_{k_x} \times N_{k_y}$ are the real space, and diffraction space sizes in pixels, respectively.

3.2 Diffraction Signal Unmixing Using NNMF

The resulting data from the pre-processing step is a 2D matrix of shape (N_r, N_k) with $N_r = N_x \times N_y$ and $N_k = N_{k_x} \times N_{k_y}$. This matrix is very sparse because only the diffraction spots are retained, and the background noise is significantly reduced. To address this sparsity, a small constant value is typically added to the data. This ensures that no divergences are encountered

in the decomposition processes.

A Non-negative matrix factorization of a 2D matrix A can be written as:

$$A_{N_r,N_k} \approx W_{N_r,p}\, H_{p,N_k} \qquad with \quad \begin{cases} p < min(N_r, N_k) \\ W, H > 0 \end{cases} \tag{5.6}$$

Where;

- A is the input 2D diffraction matrix.
- W is the basis matrix (factors).
- H is the coefficients matrix (loadings).
- p is the truncated number of components which we'll estimate by SVD.

It is evident that, in NNMF, the basis matrix holds the representative spatial components derived from the original data, whereas the representative diffraction components are encapsulated in the coefficients matrix. Thus, by appropriately reshaping these matrices, both the direct space and the corresponding diffraction space informations can be reconstructed. In the context of NNMF decomposition, the basis matrix W with dimensions (N_r, p) can be reshaped into (N_x, N_y, p) and the coefficients matrix can be reshaped from (N_k, p) to (N_{k_x}, N_{k_y}, p). This implies that each identified component holds one *factor map* of shape (N_x, N_y) and a corresponding *loading pattern* of shape (N_{k_x}, N_{k_y}).

4 A Case Study of a Sample MgO Nanocubes 4D-STEM Dataset

The performance of the NNMF algorithm posterior to the pre-processing step will be evaluated using a 4D-STEM dataset featuring MgO nanocubes from Bergh et al. (2020). In addition to some amorphous and vacuum areas, the sample area contains multiple distinct orientations of the MgO nanoparticles. A demonstration of the potential generation of comprehensive orientation maps using ACOM following the NNMF-based approach will be conducted. Subsequently, the evaluation of the NNMF algorithm against the procedure in Bergh et al. (2020) will be performed.

4.1 Sample Overview and Acquisition Conditions

In their investigation, partly overlapping MgO nanoparticles were formed by burning Mg in air using a gas torch. Afterwards, these nanoparticles were deposited onto carbon-coated TEM grids.

Scanning precession electron diffraction (SPED) was used to acquire the 4D-STEM data from the MgO nanoparticles sample. The dataset consists of diffraction patterns measuring 256×256 pixels, with a spatial grid size of 105×105 pixels. This was performed using a JEOL JEM-2100F equipped with a Nanomegas ASTAR system. PED patterns were captured through an externally mounted Stingray optical camera, imaging the microscope's phosphor viewing screen. The microscope operated at $200\,kV$ with a $1.0\,mrad$ convergence semi-angle and $16\,mrad$ precession angle. The precession frequency was 100 Hz, and the dwell time per pixel was 10 ms. To have a quick overview of the data, a VDF image of the area under investigation was reconstructed by summing over all the available diffraction signal along with a mean diffraction pattern of the whole 4D-STEM dataset in Figure 5.3(a,b) respectively.

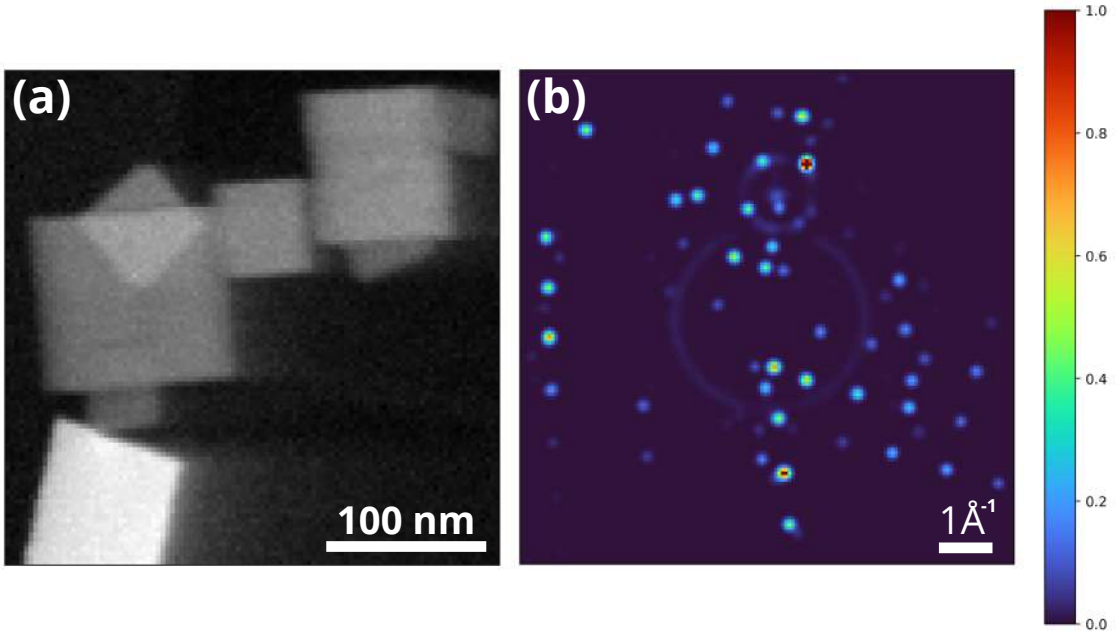

Figure 5.3: Overview of the MgO nanoparticles 4D-STEM data. (a) VDF image and (b) average virtual diffraction pattern from MgO nanocubes 4D-STEM dataset. The diffraction pattern shows a central, ring shaped, halo corresponding to amorphous material originating from the carbon grid, and another donut shaped halo on top of it which is an acquisition artefact.

4.2 Data Analysis

In Bergh et al. (2020), Data analysis was performed using Hyperspy and Pyxem. The aim was to perform nanocrystal segmentation (see Figure 5.4) for which two different approaches were applied, the first being a VDF imaging based method while the second was an NNMF-based approach. The MgO model system contained crystals that excited the same diffraction conditions and emphasized situations where neither of the methods distinguished all orientations through NNMF alone. Therefore, a watershed segmentation routine, generally used for segmenting regions based on gradients or intensity changes, was included in both methods to overcome this issue. For the remainder of this section, only the NNMF-based approach will be considered.

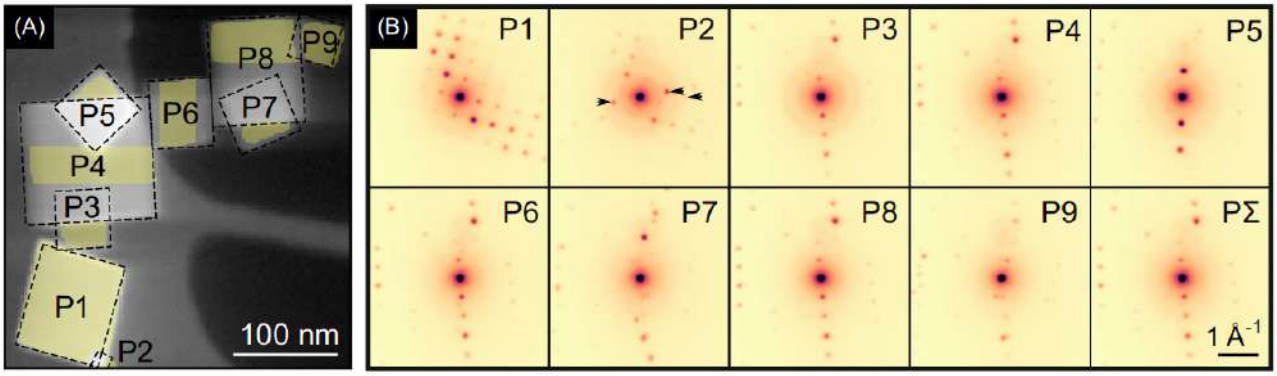

Figure 5.4: MgO nanoparticles and Summed PED Patterns: (A) Annular virtual dark-field (VDF) image showing nine magnesium oxide (MgO) particles (grey), labelled P1–P9, lying on top of a holey amorphous carbon film (dark grey) or over vacuum (black). The outlines of the MgO particles are indicated by dashed rectangles. (B) Sum of PED patterns within the yellow areas in (A). The detected diffraction vectors of P2 are marked by black arrows. PΣ is the sum of P3, P4, P6 and P8. From Bergh et al. (2020)

The NNMF-based nanocrystal segmentation workflow they used is illustrated in Figure 5.5. The pre-processing steps before NNMF decomposition included diffraction patterns alignment, direct beam masking and binning. Subsequently, NNMF was applied to generate component patterns (C_P) and loadings (C_L) from the resulting dataset (D). Further processing involved correlating component patterns and loadings, leading to the derivation of correlated patterns (C_{CP}) and correlated loadings (C_{CL}). Watershed segmentation is then performed on correlated loadings, producing loading segments (C_{SL}) alongside corresponding patterns (C_{SP}).

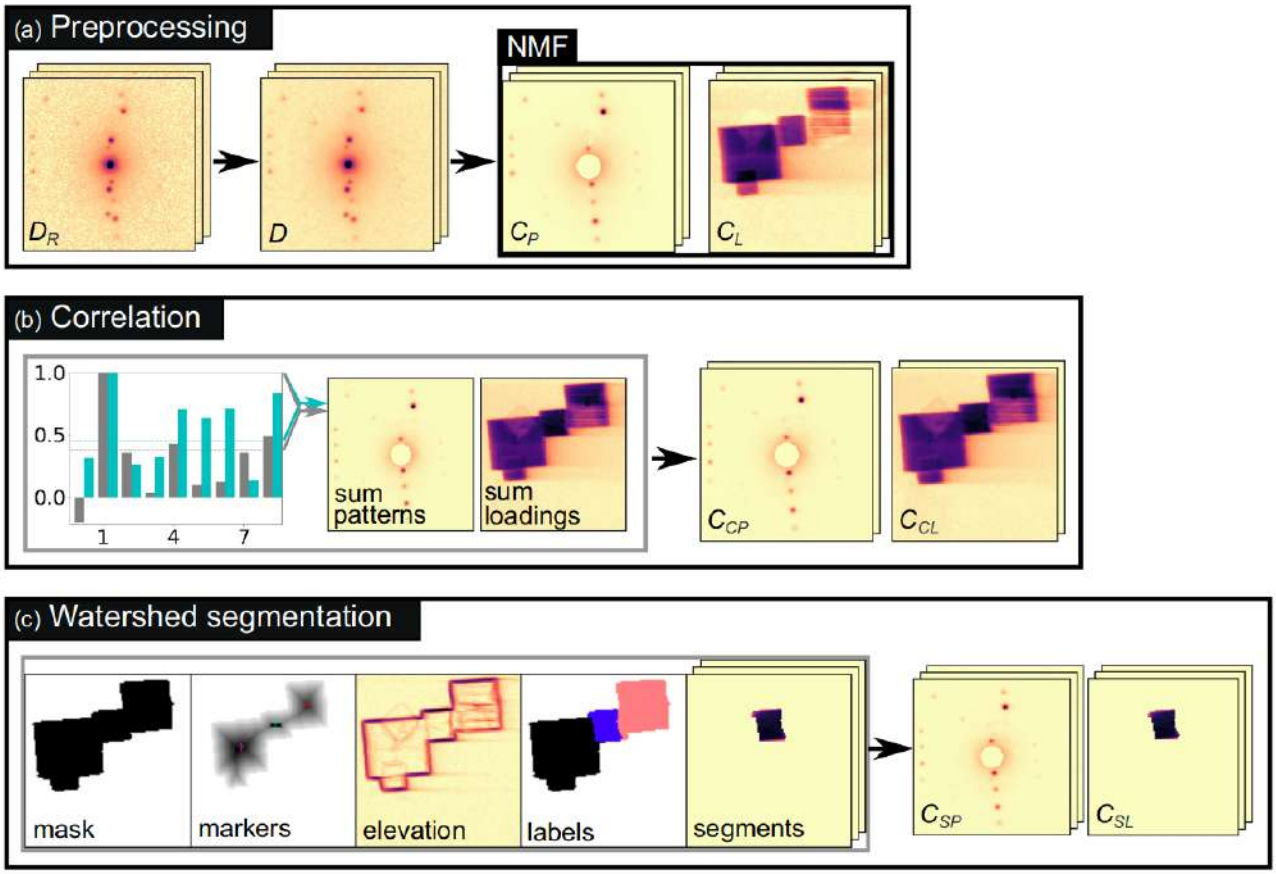

Figure 5.5: NNMF-based segmentation workflow from Bergh et al. (2020). (A) Raw data (D_R) is binned and aligned, then the direct beam is masked yielding a new dataset denoted (D). NNMF is performed on D yielding component patterns (C_P) and loadings (C_L). (B) Correlation of the component patterns and loadings, where components are summed if the correlations of both patterns and factors exceed threshold values, leading to correlated patterns (C_{CP}) and loadings (C_{CL}). (C) Watershed segmentation is performed on each correlated loading to yield loading segments (C_{SL}) with corresponding patterns (C_{SP}). For each loading, a mask is formed, markers are determined and watershed segmentation is performed on the elevation image, leading to labelled regions that are used to define segments.

The result of the NNMF-based procedure introduced in Bergh et al. (2020) is shown in Figure 5.6. Bergh et al. (2020) used SVD scree plot to estimate the number of components to use in the NNMF decomposition process which was set to 11. The outcome of the NNMF decomposition process is shown in Figure 5.6B. Clearly, the components patterns and corresponding loadings maps that were obtained don't align neither with the different orientations of the MgO nanocubes nor with the individual crystals present within the sampled area.

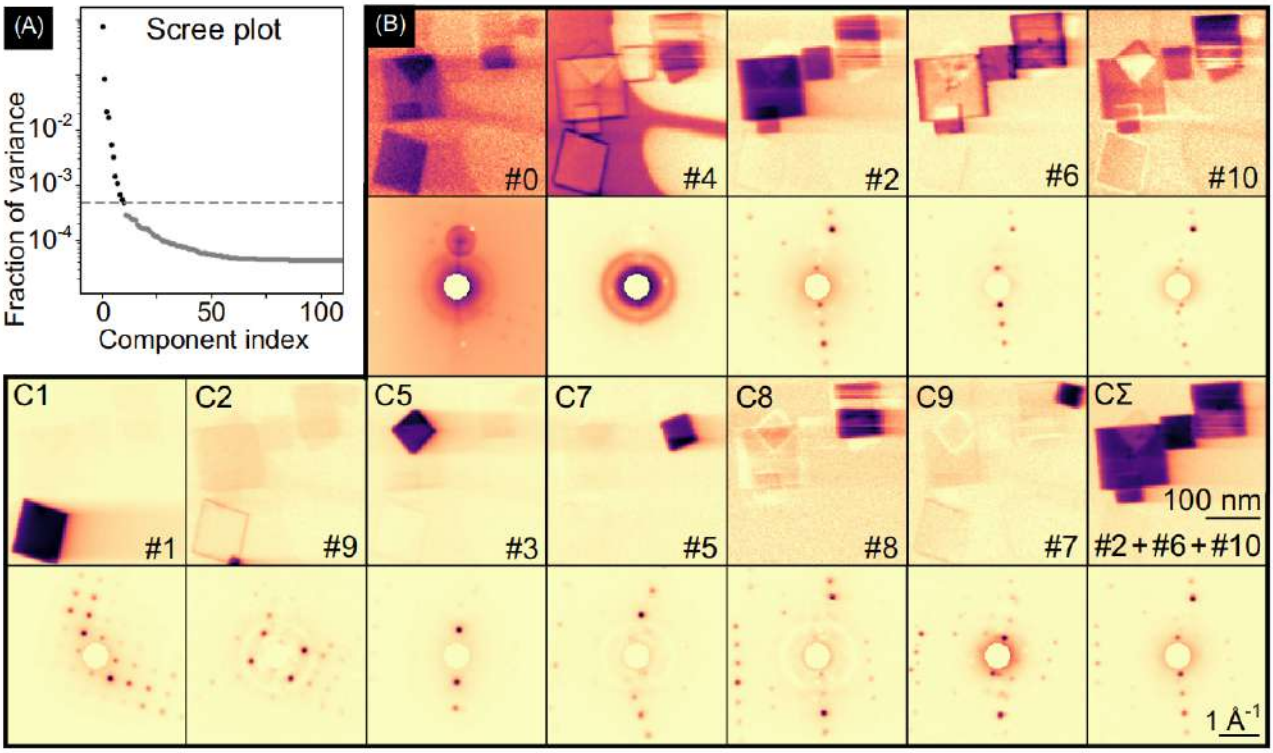

Figure 5.6: NNMF results from Bergh et al. (2020). Non-negative matrix factorization (NNMF) results. (A) Singular value decomposition (SVD) scree plot showing the fraction of total variance that each component accounted for. The dashed horizontal line indicates that a number of 11 components was used for NNMF. (B) Loading maps (top) and corresponding component patterns (bottom) obtained by NNMF, labelled #0-#10. The component patterns and loadings after correlation are labelled C1–C9, according to the particle labelling in Figure 3, and $C\Sigma$ is the sum of components #2, #6 and #10.

4.3 Comparative Analysis and Performance Evaluation

An attempt to achieve accurate orientation mapping of the MgO nanocubes sample using the approach in Allen et al. (2021) will be outlined. The particularity of their method lies in the use of a meticulous pre-processing pipeline, delineated in Figure 5.2, prior to applying NNMF. In the case of MgO samples, we have binned the diffraction patterns by a factor of 3. Additionally, the SVD scree plot presented in Figure 5.7 suggests selecting a truncated number of components of seven to be used in the NNMF decomposition process.

The NNMF decomposition components, comprising seven loading maps and corresponding component patterns are showcased in Figure 5.8. Remarkably, The seven components obtained align well with the different phases and orientations of the MgO sample here studied. Among these, five components capture distinct orientations of the MgO nanocubes (components 1,2,4,5 and 6), while the remaining two (components 3 and 7) represent amorphous regions and vac-

uum, respectively, as discerned from Figures 5.8(a1-a7) and Figures 5.8(b1-b7). It is important to mention that incorporating a tolerance for "false positives" during peak registration ensures the detection of as many Bragg spots as possible. This however unavoidably leads to maintaining the visibility of non-crystalline signal which is detected in two separate NNMF components. Also, it's worth noting that, in the Bragg peak detection algorithm, a same diffraction spot across multiple diffraction patterns can be identified at slightly different positions, potentially leading to Bragg spot shifts that weren't present in the original dataset.

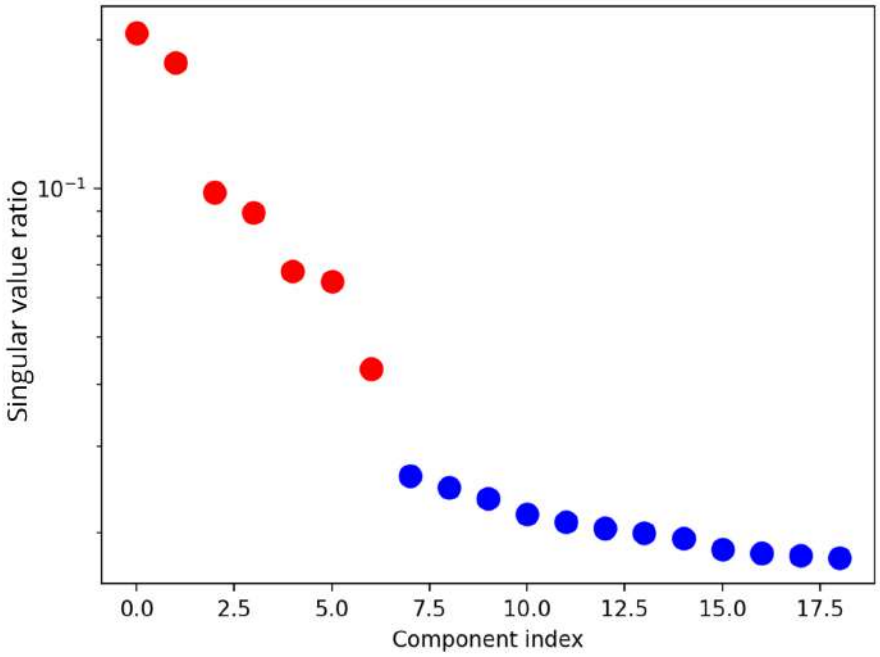

Figure 5.7: SVD scree plot depicting singular value ratio attributed to each individual component posterior to the pre-processing pipeline. 7 components shall be used as initial estimate for the NNMF decomposition algorithm.

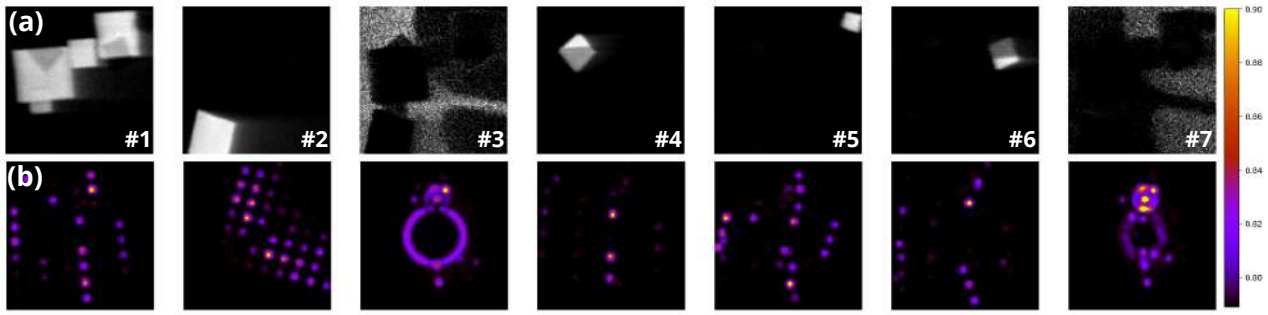

Figure 5.8: NNMF decomposition of 4D-STEM data of the MgO nanoparticles system. (a) shows individual loading maps resulting from the two decomposition approaches along with (c) corresponding component patterns.

Comparing our findings to those of Bergh et al. (2020) reveals significant disparities. Initially, SVD scree plot converge on seven primary components, aligning precisely with the count of orientations, vacuum, and amorphous components. However, in Bergh et al. (2020), eleven components were initially needed. This forced them to use a correlation-based strategy for merging components with identical orientations.

Additionally, the NNMF approach in Bergh et al. (2020) faces challenges in effectively separating the different orientations, vacuum and amorphous contributions, as observed in Figure 5.6B, contrary to our study's approach which forced them to use a correlation based method. However, their methodology still struggled to entirely separate crystalline orientations, as indicated by the persistent MgO grain edges across all reconstructed loading maps in Figures 5.6(C1 - CΣ).

These discrepancies highlight the superior ability of applying NNMF procedure as described in Allen et al. (2021) to efficiently capture essential data features more concisely.

Following the successful NNMF decomposition, ACOM can be performed on the component patterns. A composite map of the different crystal orientations depicted by the NNMF decomposition approach is shown in Figure 5.9a. Alongside it, in Figure 5.9b, is an orientation map reconstructed by indexing each component pattern generated by NNMF and an orientation map generated directly from the raw data with the conventional ACOM procedure Figure 5.9c. Comparing the orientation map obtained posterior to NNMF decomposition and the raw orientation map obtained by ACOM, it becomes evident that the NNMF decomposition followed by ACOM yields accurate orientation mapping.

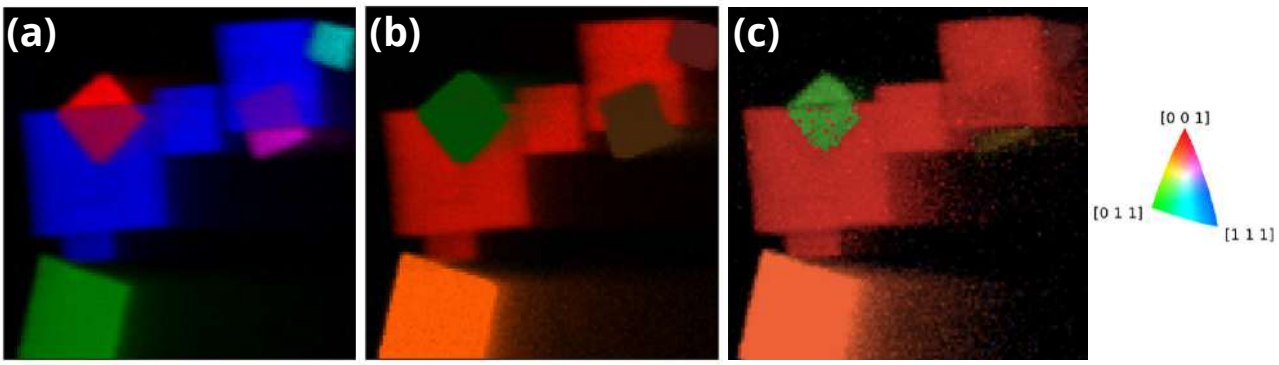

Figure 5.9: NNMF reconstruction and orientation mapping of the MgO nanoparticles system. (a) NNMF segmented map of the MgO nanocrystals reconstructed from the five relevant components of the NNMF decomposition in Figure 5.8 (Colors are arbitrary). (b) a corresponding orientation map reconstructed solely from the component patterns generated from NNMF. (c) An ACOM orientation map reconstructed directly from the raw data.

In the present study, the whole processing of the 4D-STEM data (including pre-processing), the NNMF decomposition, as well as the ACOM orientation mapping posterior to the NNMF decomposition may take up to ~ 3 minutes, while the ACOM procedure alone on the raw data took ~ 10 minutes. The processing was performed using a **Dell Inc. Intel Xeon(R) CPU @ 4.10 GHz $\times$ 8 | 64 GB RAM**. It is important to mention that the SVD and NNMF computations alone took ~ 5 seconds to complete. The size of the raw 4D-STEM data set was 104 MB while that of the 2D matrix data after the pre-processing pipeline was 7.3 MB.

5 Application on Meteoritic Samples

In the following section, the same NNMF-based approach will be used on Ryugu and Orgueil samples' 4D-STEM data, but before going much further, it is worth recalling that, in the MgO case outlined in the previous section, the data was acquired using a conventional optical camera rather than a direct electron detection technology, and in SPED mode which allows more diffraction conditions to be excited, producing a better signal-to-noise ratio, and hence making the 4D-STEM data suitable for accurate ACOM either on raw data or the NNMF-factorized data. However, unlike the MgO nanocubes data, ACOM on raw 4D-STEM datasets from chondritic samples did not yield accurate results. With the NNMF-based approach outlined previously, it should be possible to, first, factorize the 4D-STEM data into simpler components and perform the phase identification on the individual components afterwards. In the next section, we shall

investigate the use of the NNMF-based procedure posterior to the pre-processing pipeline on Ryugu samples' 4D-STEM data previously introduced in Chapter 3.

5.1 Application on Ryugu's 4D-STEM Data

In Chapter 3, an extensive analysis was conducted on a 4D-STEM dataset of Ryugu. Initially, a Bragg Vector Map (BVM) of the area under investigation was produced after several pre-processing steps. Then, by azimuthally averaging this BVM, an overall radial profile of the area was generated as shown in Figure 5.10 (Extracted from Figure 3.3 - Chapter 3).

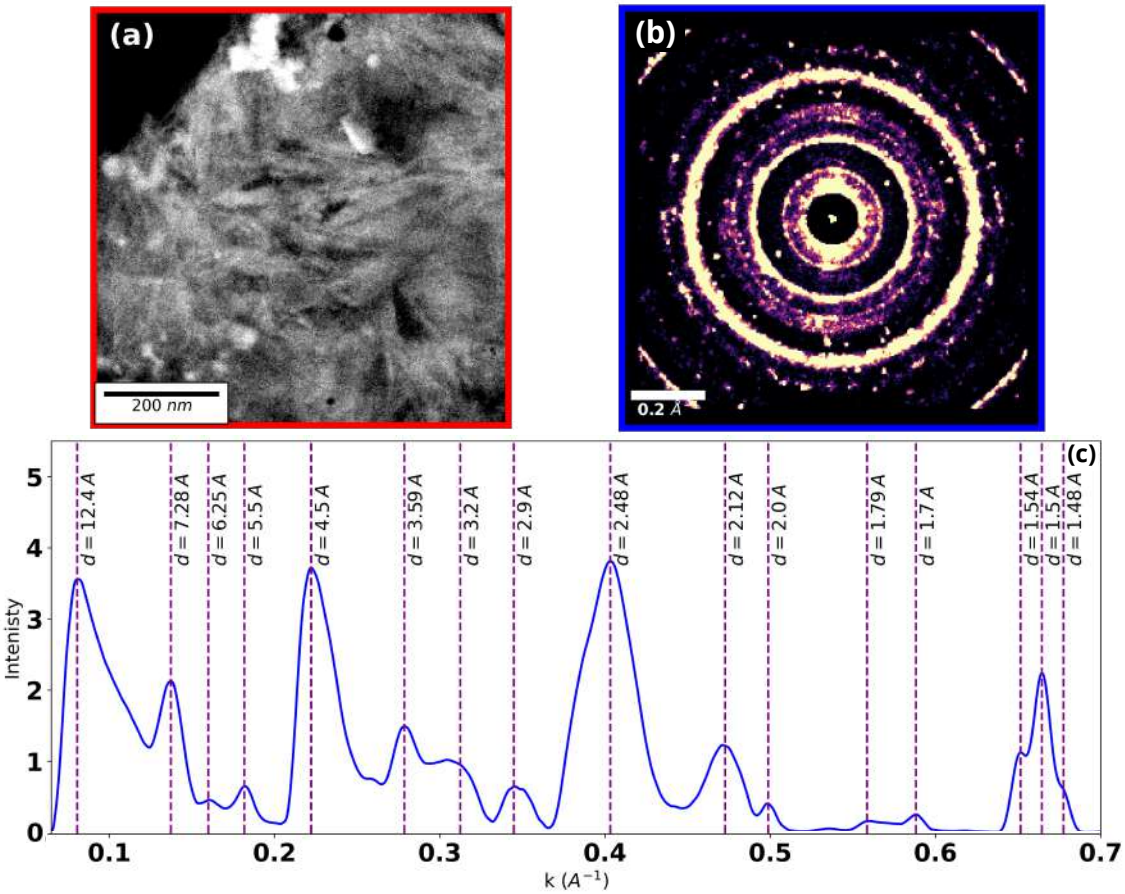

Figure 5.10: Summary of the BVM-based analysis of Ryugu 4D-STEM data. (a) HAADF image of the area. Brighter areas correspond to iron-sulfides while the remainder are phyllosilicate-rich areas. (b) A BVM and (c) the corresponding radial profile of the area under investigation.

The various peaks within the overall radial profile are indicative of distinct mineralogical phases and/or orientations. Leveraging this knowledge, we successfully segmented the virtual dark field images, obtained by integrating the subset of pixels in the diffraction space associated with each peak, into their respective mineralogical phases. For instance, by leveraging unique

peaks related to iron-sulfides and phyllosilicates, virtual dark field imaging accurately produced distribution maps of these constituents in the sampled area of Ryugu. The combination of these segmented phase maps resulted in a comprehensive composite phase map, as illustrated in Figure 5.11 (Extracted from Figure 3.5 - Chapter 3).

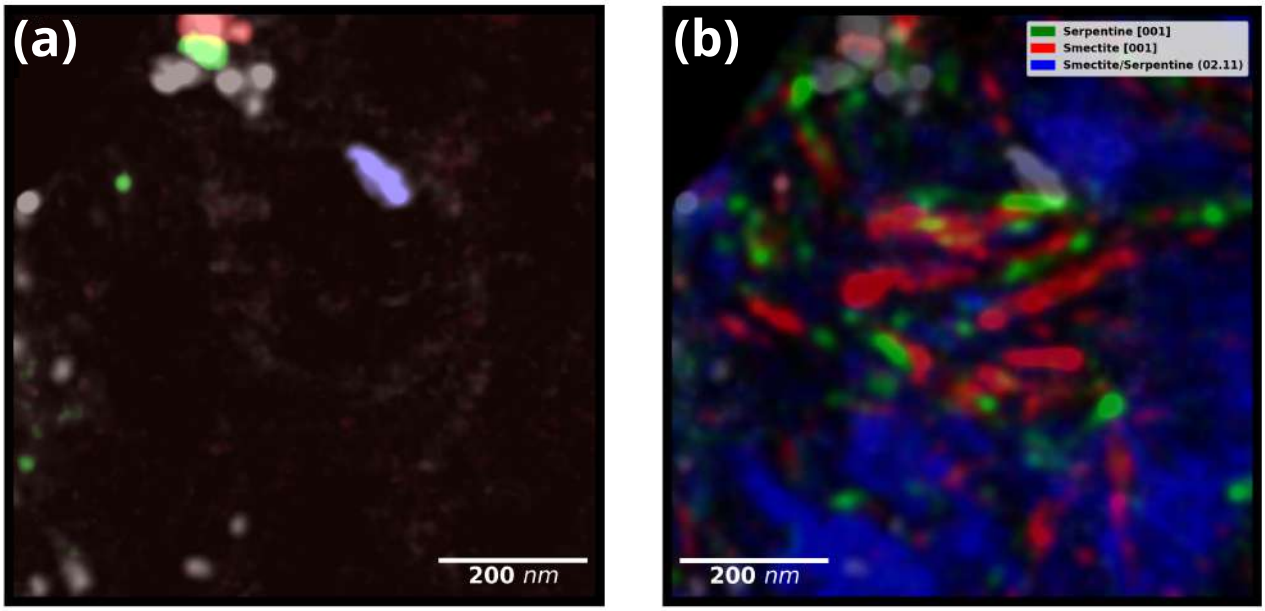

Figure 5.11: Phase mapping of iron-sulfides and phyllosilicates from Ryugu's 4D-STEM data. (a) Iron-sulfides distribution map and (b) Serpentine, smectite and Mg-rich serpentine/smectite mixture areas combined map. These maps have been obtained by first indexing the BVM-reconstructed radial profile and performing virtual dark field imaging afterwards.

With the NNMF-based approach, we must be able to decompose the 4D-STEM data of Ryugu into a finite number of loadings maps and corresponding component patterns, an then link these maps and patterns to the corresponding mineralogical phases and diffraction signatures in the sampled area of Ryugu.

We shall follow the same pre-processing protocol introduced by Allen et al. (2021) and previously described in Section 3.1. Diffraction patterns are rebinned by a factor of 3. Notably, By examining the SVD scree plot in Figure 5.12, it is not clear how many components should be employed in NNMF in order to approximately reconstruct the original data.

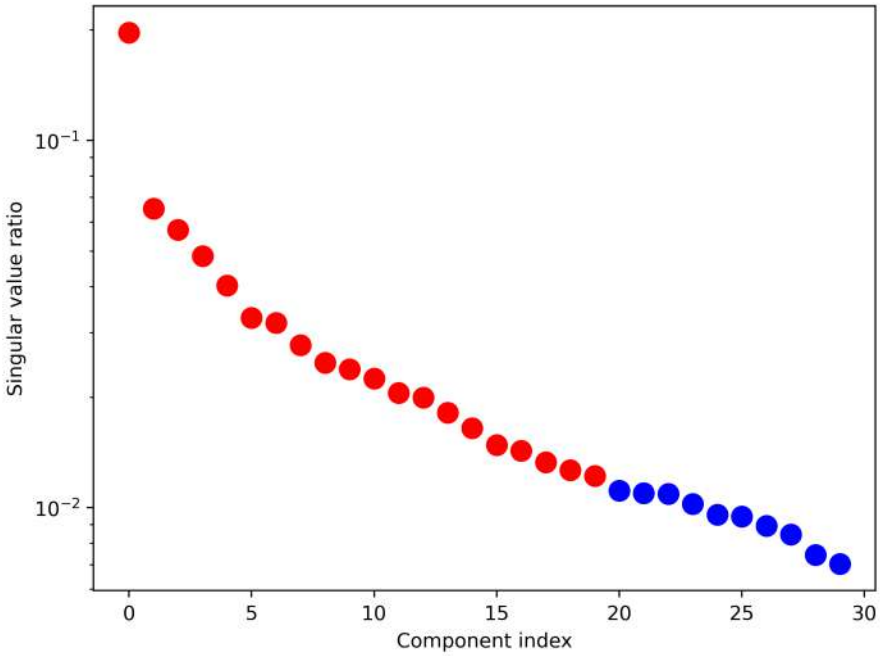

Figure 5.12: SVD scree plot depicting singular value ratio attributed to each individual component posterior to the 4D pre-processing pipeline for Ryugu samples' data. The first 20 components are highlighted in red. These are used as an initial estimate for the NNMF decomposition algorithm but only the first 10 components will be subsequently displayed.

Figure 5.13 shows the outcome of the first 10 components of the NNMF decomposition. Figure 5.13a features the basis vectors, essentially the loading maps obtained following the NNMF decomposition, while the right column features the coefficients (Figure 5.13b), denoting the component patterns associated with each loading map.

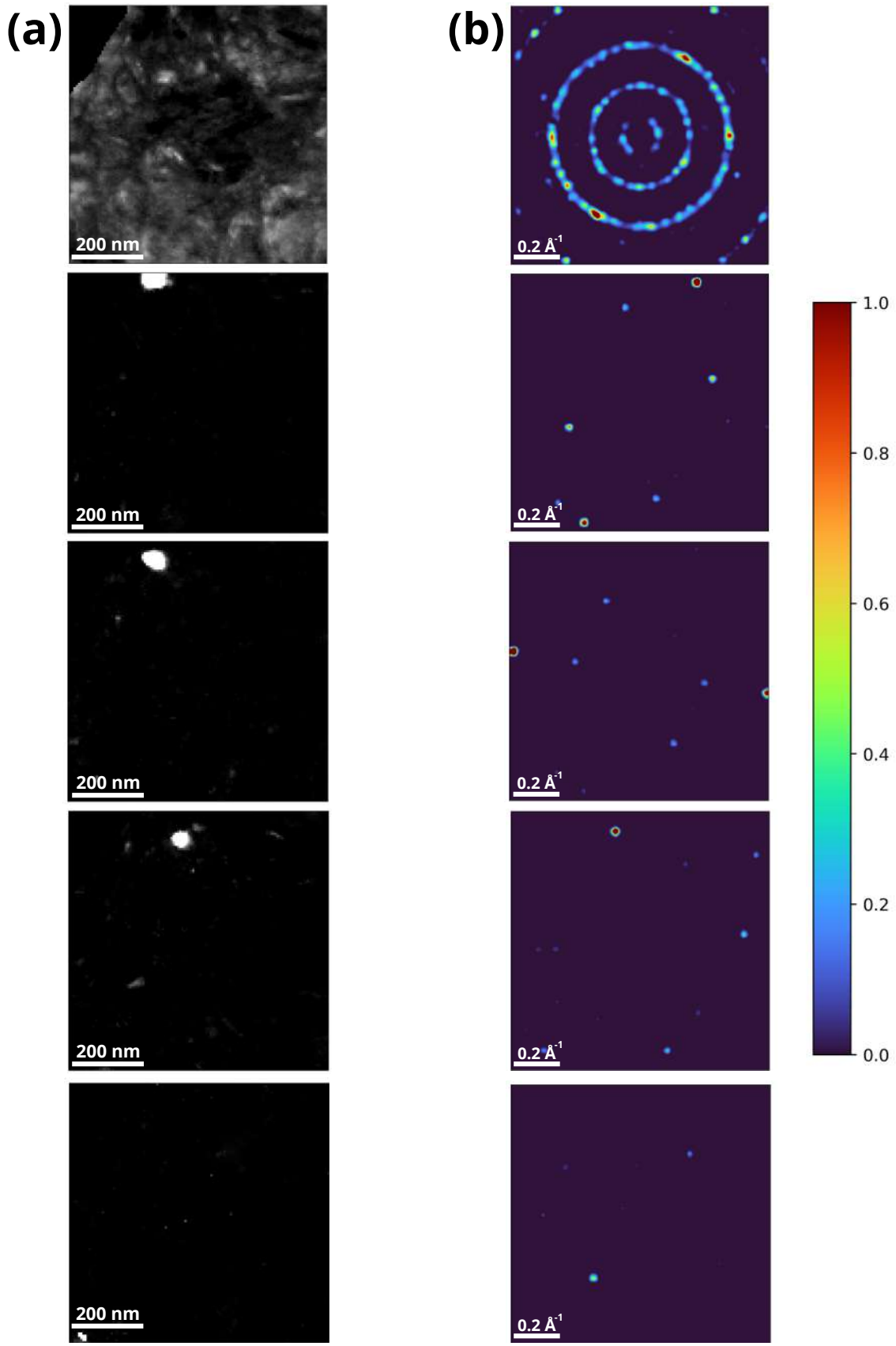
(a)
(b)
200 nm
0.2 Å^{-1}
1.0
0.8
0.6
0.4
0.2
0.0

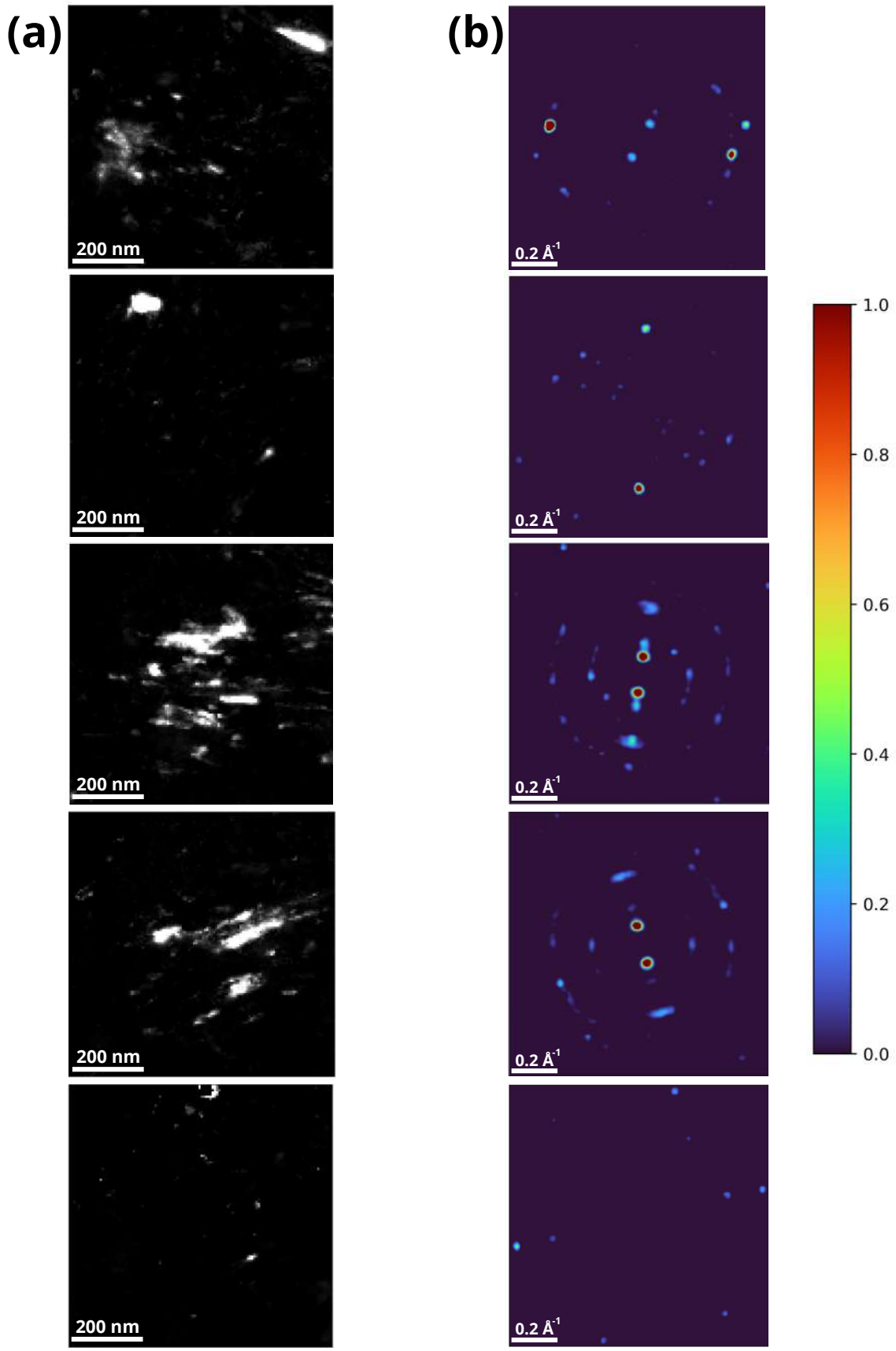

Figure 5.13: NNMF decomposition of Ryugu's data after the pre-processing pipeline. Column (a) displays individual loading maps obtained from the NNMF decomposition, while column (b) features the corresponding representative component patterns associated with each loading map in a row-wise manner.

Remarkably, the segmentation of iron-sulfides demonstrates notable proficiency, with the corresponding component patterns effectively capturing their distinctive diffraction signal, as evidenced in Figure 5.14. However, it is noteworthy that one iron sulfide entity is absent from the segmentation and is lost within the components representative of phyllosilicates (Components 1 and 8). In parallel, the unmixing of serpentine and smectite proves to be very challenging as many components indicative of phyllosilicates, remain inadequately disentangled through the NNMF procedure. These observations underscore the limitations of the approach outlined in Allen et al. (2021) for this type of samples.

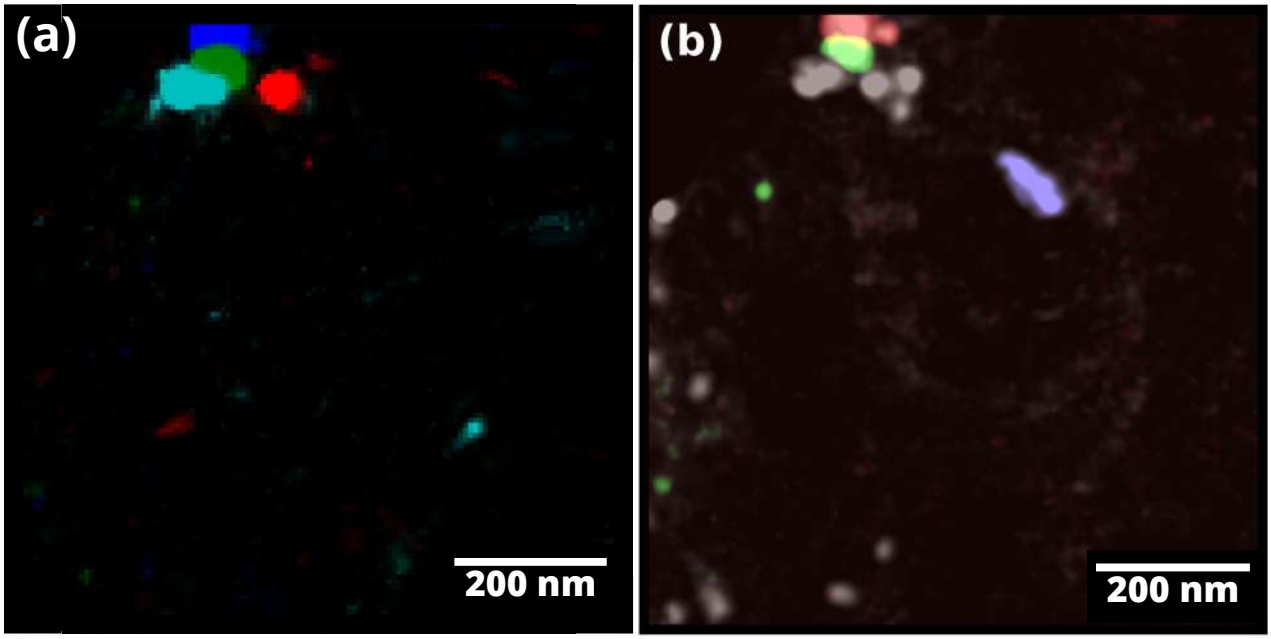

Figure 5.14: Iron sulfides segmentation from the NNMF approach versus the classical segmentation method. (a) NNMF-segmentation of iron sulfides from the NNMF approach combining components (2,3,4,7) in Figure 5.13. (b) BVM-based segmentation performed by combining virtual dark field relevant to iron-sulfides.

The ineffectiveness of NNMF in this scenario can be attributed to the unique characteristics of Ryugu's 4D-STEM data. While the MgO nanocubes data featured substantial grain sizes and a limited number of orientations, the BVM of Figure 5.10 unveils a distinctive powder-like diffraction pattern which suggests a fine mixture of tiny grains with a large number of possible orientations across each phase present within the sampled area.

Under such intricate conditions, automated crystal orientation mapping directly on the 4D-STEM data proved unsuccessful, as did the application of NNMF subsequent to preprocessing steps. Instead, as demonstrated in preceding chapters, we successfully segmented different

phases within the sampled regions by indexing the azimuthally-averaged BVM. This approach involved associating each peak in the resultant averaged profile with a specific mineralogical phase or orientation.

Hence, a promising avenue for further exploration could involve applying NNMF to 3D-STEM data composed of azimuthally averaged diffraction patterns rather than full two-dimensional diffraction patterns. Such an approach may offer greater potential for resolving the complexities inherent in Ryugu's data and could lead to more robust and insightful analyses.

5.1.1 An Alternative Approach for Improved NNMF Using 3D-STEM Data

Instead of using the complete 4D-STEM dataset, which is transformed into a 2D matrix during pre-processing, 3D data will be employed instead. A schematic depicting the modified pre-processing pipeline is illustrated in Figure 5.15. In this alternative approach, azimuthal averaging of the diffraction patterns is conducted subsequent to the data refinement step in the pre-processing pipeline.

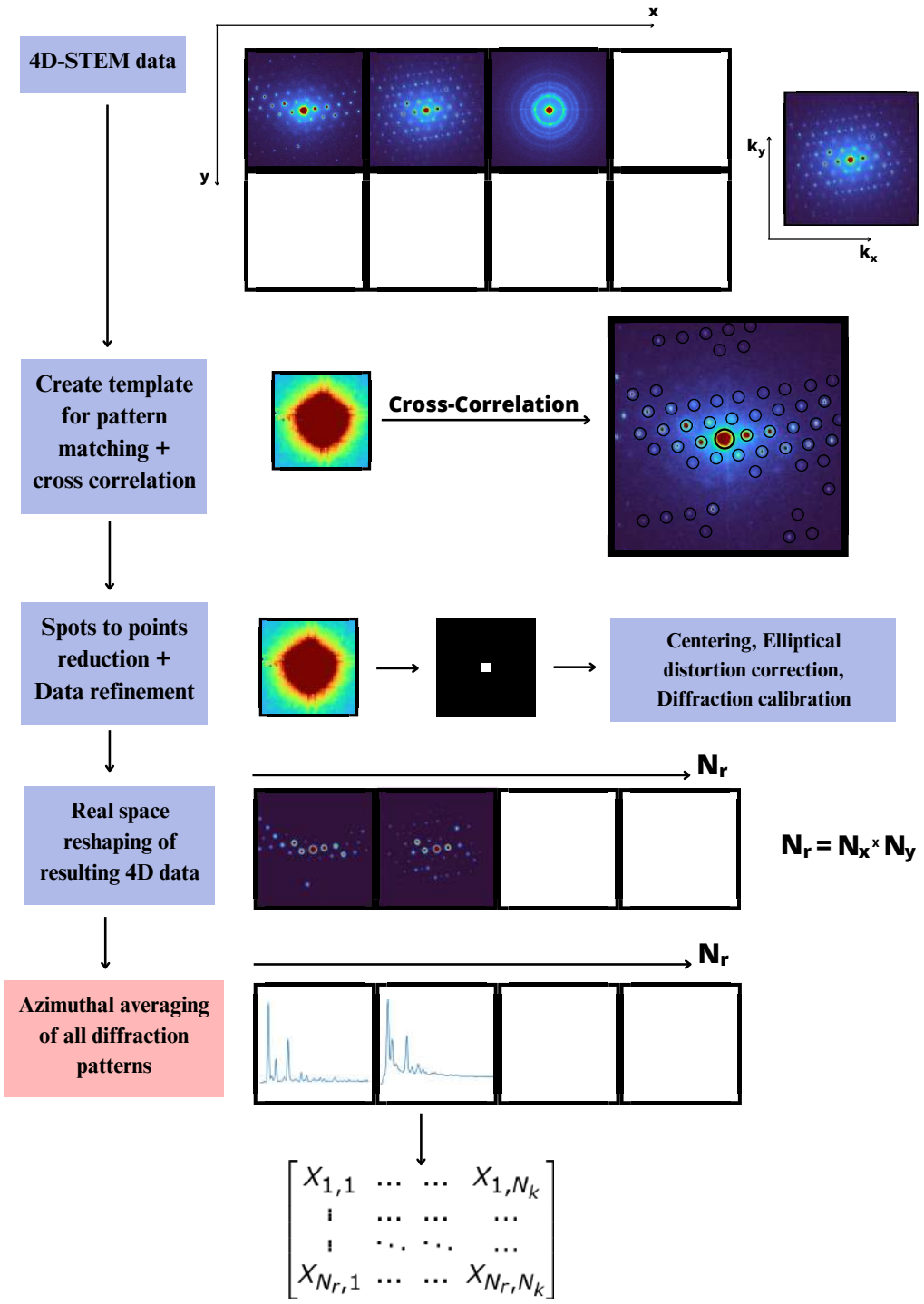

Figure 5.15: 4D-STEM data pre-processing and azimuthal averaging pipeline prior to NNMF decomposition. First a template is created for cross-correlative Bragg spots registration, and data refinement is performed on the detected Bragg spots. The resulting 4D data are then reshaped into 3D data (N_r, N_{k_x}, N_{k_y}) of diffraction patterns, then each of these patterns is azimuthally averaged yielding (N_r, N_k), where $N_r = N_x \times N_y$ is the real space size and N_k is the number of bins used in the azimuthal angle range.

Similarly to the previous approach, the estimated truncated number of components will be obtained from the SVD decomposition. However, in contrast to the previous approach where full 2D diffraction patterns were used, no binning is required since the size of the data will be

significantly reduced after the azimuthal averaging step which already reduces computational demands and time constraints by a significant amount.

In contrast to the straightforward determination of the "elbow" position in the previous example involving MgO nanocubes, identifying this position on the SVD scree plot in Figure 5.16 is less evident. Therefore, in addition to the scree plot, we inspect the individual factors and loadings to judge if they contain physically relevant information. Using this criterion, we determine that we need a minimum of 8 components to accurately describe the data. The NNMF decomposition on Ryugu's dataset is subsequently performed.

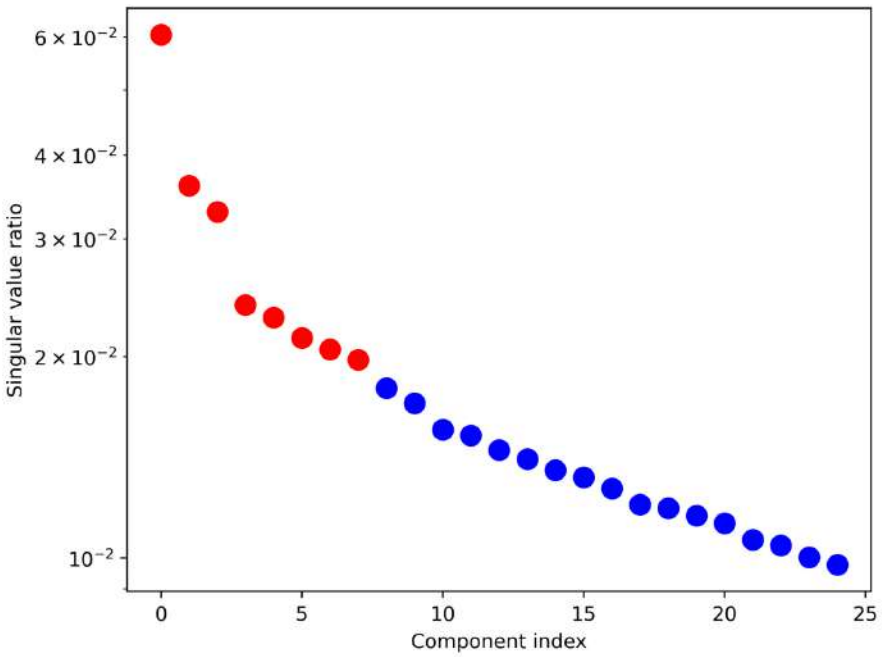

Figure 5.16: SVD scree plot depicting singular value ratio attributed to each individual component posterior to the 3D pre-processing pipeline for Ryugu samples' data. 8 components shall be used as initial estimate for the NNMF decomposition algorithm.

The outcome of the NNMF decomposition is depicted in Figure 5.17. This visualization encompasses both the NNMF loading maps, shown in Figure 5.17a, and their corresponding component profile, illustrated in Figure 5.17b. Each loading map is color-coded to align with its respective component profile.

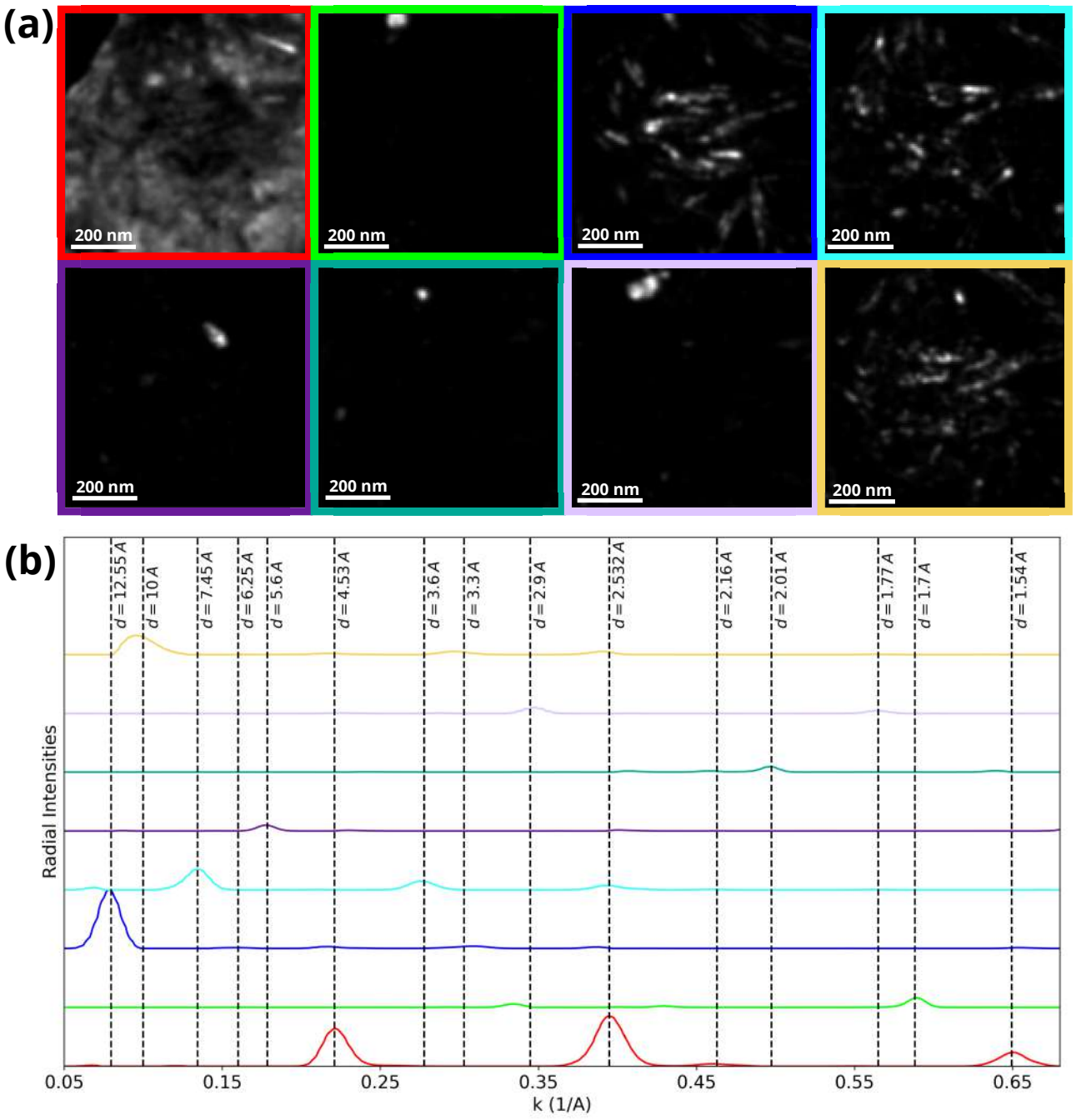

Figure 5.17: NNMF decomposition of Ryugu's data after the 3D pre-processing pipeline. Figure (a) showcases, from left to right, the individual loading maps resulting from the NNMF decomposition, while (b) presents, from bottom to top, the corresponding component profiles derived from the NNMF procedure. The loading maps are color-coded to align with their corresponding component profiles.

The segmentation results obtained using the BVM-based approach outlined in Chapter 3 are displayed in Figure 5.11. These serve as a basis for comparative analysis with the outcomes of the NNMF procedure. From Figure 5.17, we can see, first, that the dominant presence of serpentine/smectite mixtures ($hk0$) reflections is largely depicted by the first component, as evidenced by their characteristic peaks at 4.53 Å, 2.53 Å, 2.16 Å, and 1.54 Å in the correspond-

ing radial profile (Bottom (1^{st}) radial profile) which is consistent with the results outlined in Chapter 3.

Similarly, the smectite-rich regions, exhibiting (00ℓ) reflections, are effectively captured by components 3 and 8 of the NNMF decomposition. These components highlight smectite's (001) reflection around ~ 12.5 Å associated with grains exhibiting different degrees of organic matter intercalation, the (001) reflection of smectite at 10 Å suggestive of collapsed smectite grains, as well as its (004) reflection at 3.3 Å (Profiles 3 and 8).

Furthermore, the presence of serpentine and its characteristic (00ℓ) reflections are distinctly illustrated by the fourth component. This is evident through the characteristic peaks at 7.45 Å (001) and 3.6 Å (002) in the radial profile (Profile 4).

Finally, the iron sulfide reflections are effectively depicted by the combined contributions of components 2, 5, 6, and 7. These reflections are indicated by their characteristic peaks located at 1.7 Å, 1.77 Å, 2.01 Å, 2.9 Å, and 5.6 Å in the respective radial profiles.

The loading maps generated by NNMF and their corresponding component profiles can be merged together into distinct mineral phase maps and corresponding radial profiles. For instance, the iron sulfide components (2, 5, 6, 7) are merged to create a comprehensive composite map illustrating the distribution of iron sulfides within the phyllosilicate matrix. Similarly, components 3 and 8, both associated with smectite but with differing interlayer arrangements, are merged to create a unified composite map revealing the distribution of smectite within the phyllosilicate matrix. A comprehensive depiction of the distribution of ($hk0$) reflections of phyllosilicates, (00ℓ) reflections of serpentine as well as the (00ℓ) smectite reflections within the phyllosilicate matrix is shown in a composite map in Figure 5.18 along with the corresponding radial profiles after merging the relevant components.

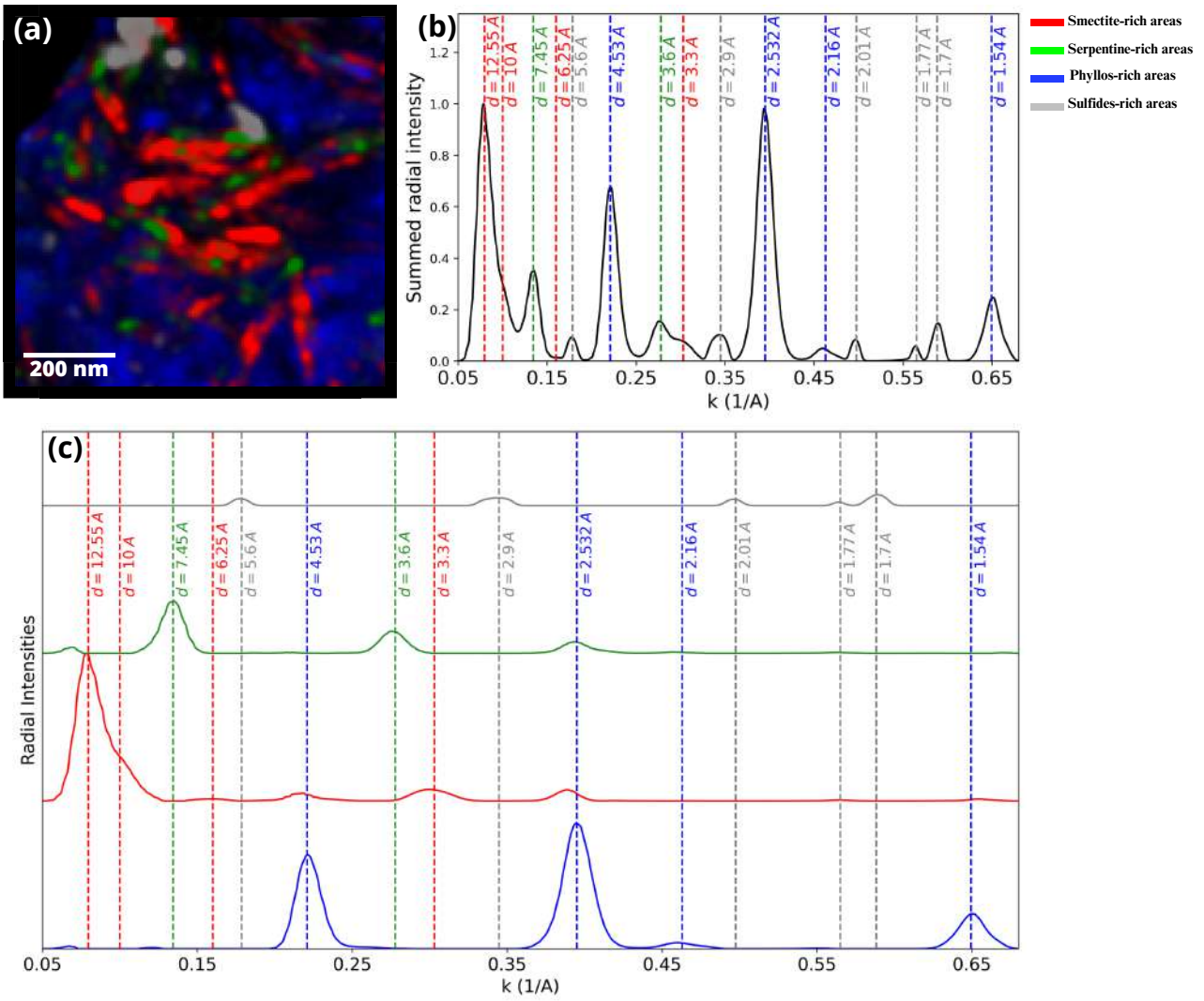

Figure 5.18: NNMF results summary after the 3D data pre-processing pipeline. (a) Mineralogical phases segmentation of the phyllosilicate matrix in Ryugu's sample 4D-STEM data using the NNMF-based approach. (b) Normalized average of all NNMF coefficients. (c) Summed NNMF coefficients by class: Smectite, Serpentine, Sulfides and serpentine/smectite mixtures.

These results highlight the effectiveness of the 3D-NNMF approach illustrated in Figure 5.15 in accurately unraveling the distribution of mineralogical phases from 4D-STEM data, as compared to the 4D-NNMF procedure in Figure 5.2.

5.2 Application on Orgueil's 4D-STEM Data

As elucidated in Chapter 4, Orgueil's mineralogy present more complexities than that of Ryugu due to the intricate presence of mineralogical phases resulting from terrestrial weathering, such as sulfates and ferrihydrites. Consequently, employing a BVM-based approach on such sample data may become more time-consuming and requiring careful investigation.

Following the same pre-processing steps outlined in Figure 5.15, NNMF is applied to Orgueil samples' data used in Chapter 4 and a comparison with the BVM-based approach used in the previous chapter will be discussed.

Similarly to the previous case on Ryugu, estimating the right number of components from the SVD scree plot shown in Figure 5.19 is not straightforward and an arbitrary choice of 7 components has been made. While this count exceeds the anticipated number of phases in the examined area, the NNMF-based approach is still applied for 7 components as previously demonstrated for Ryugu samples.

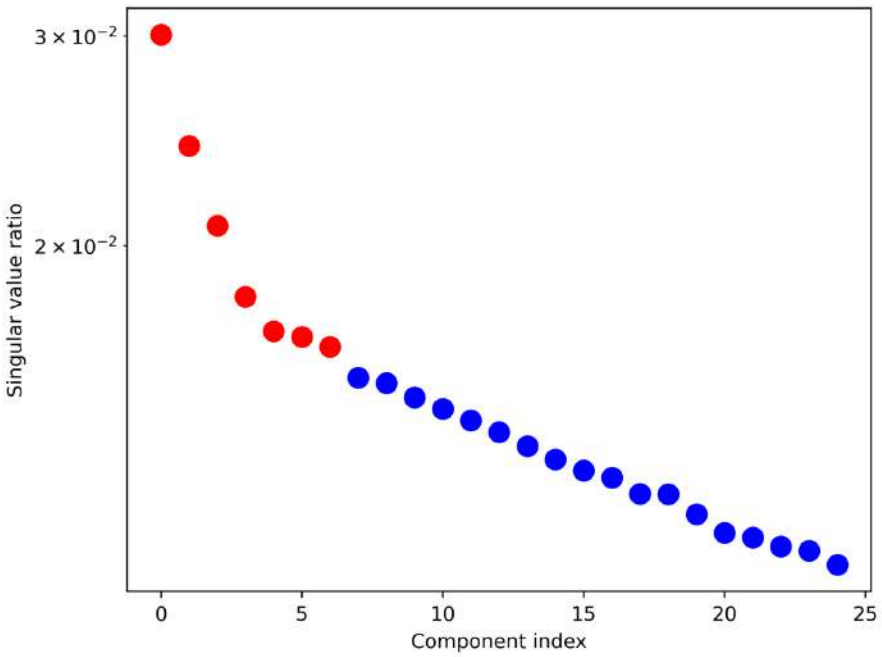

Figure 5.19: SVD scree plot depicting singular value ratio attributed to each individual component posterior to the 3D pre-processing pipeline for Orgueil samples' data. 7 components shall be used as initial estimate for the NNMF decomposition algorithm.

Subsequently, the output components corresponding to identical mineralogical phases are found by indexing each component's profile and then merged. This results in only three components for the studied sample area of Orgueil, as depicted in Figure 5.20.

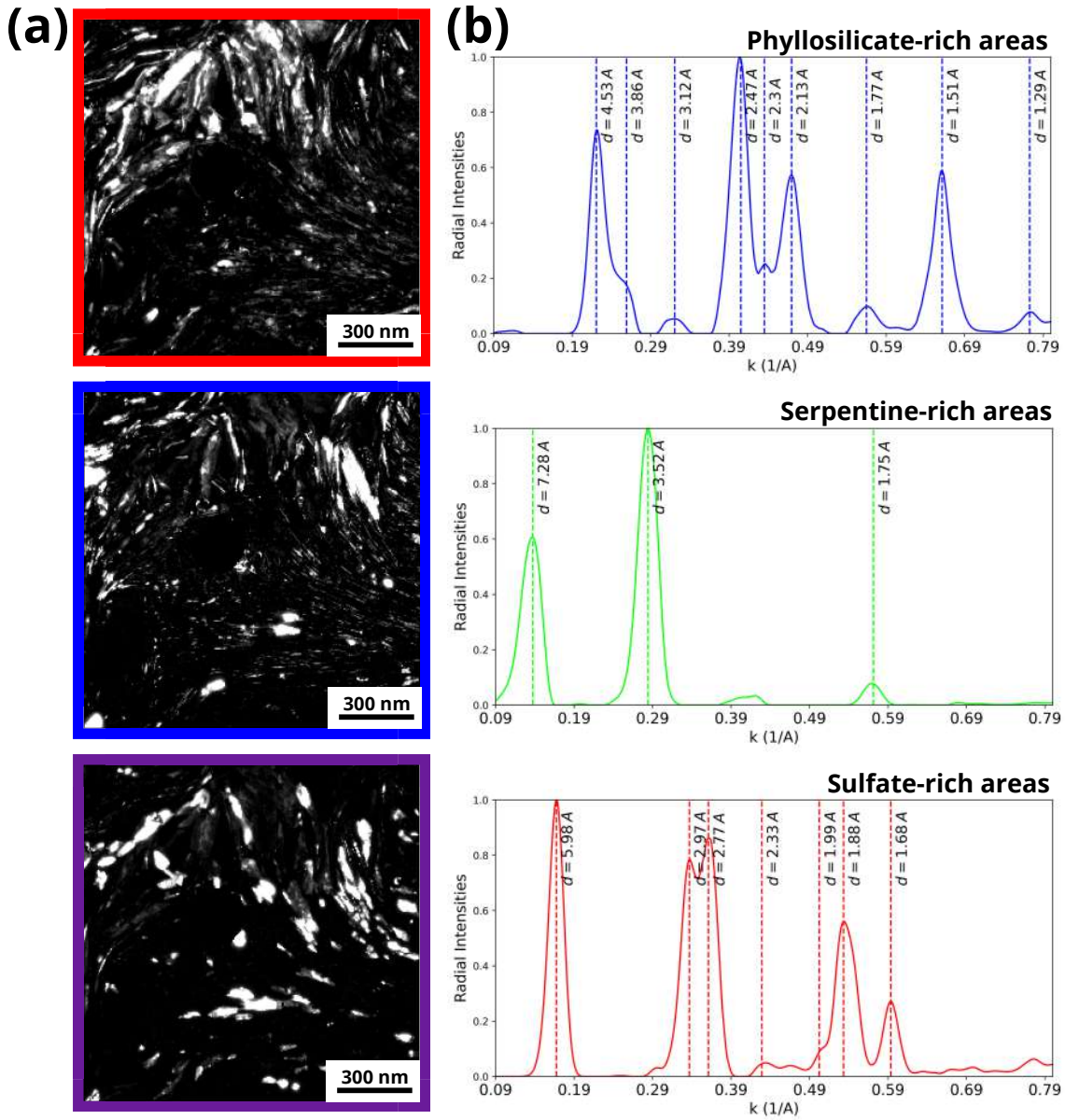

Figure 5.20: NNMF decomposition results of Orgueil's data after the 3D pre-processing pipeline. Column (a) displays the individual loading maps resulting from the NNMF decomposition, while column (b) contains the corresponding component profiles.

The NNMF decomposition results of Orgueil's data are shown in Figure 5.20. Figure 5.20a displays the individual loading maps resulting from the NNMF decomposition, while Figure 5.20b contains the corresponding component profiles. The simulated radial profiles for Ca-sulfates (anhydrite) and serpentine (lizardite) match well with the component profiles derived from the NNMF decomposition. This agreement is clearly demonstrated in Figure 5.21, which juxtaposes these simulated profiles against those from Figure 5.20b. The crystallographic information files (CIFs) for serpentine (specifically Lizardite) and anhydrite were sourced from Laurora et al.; Hawthorne and Ferguson (2011; 1975), respectively. Notably, no available data

exists for comparing with the serpentine/smectite mixtures.

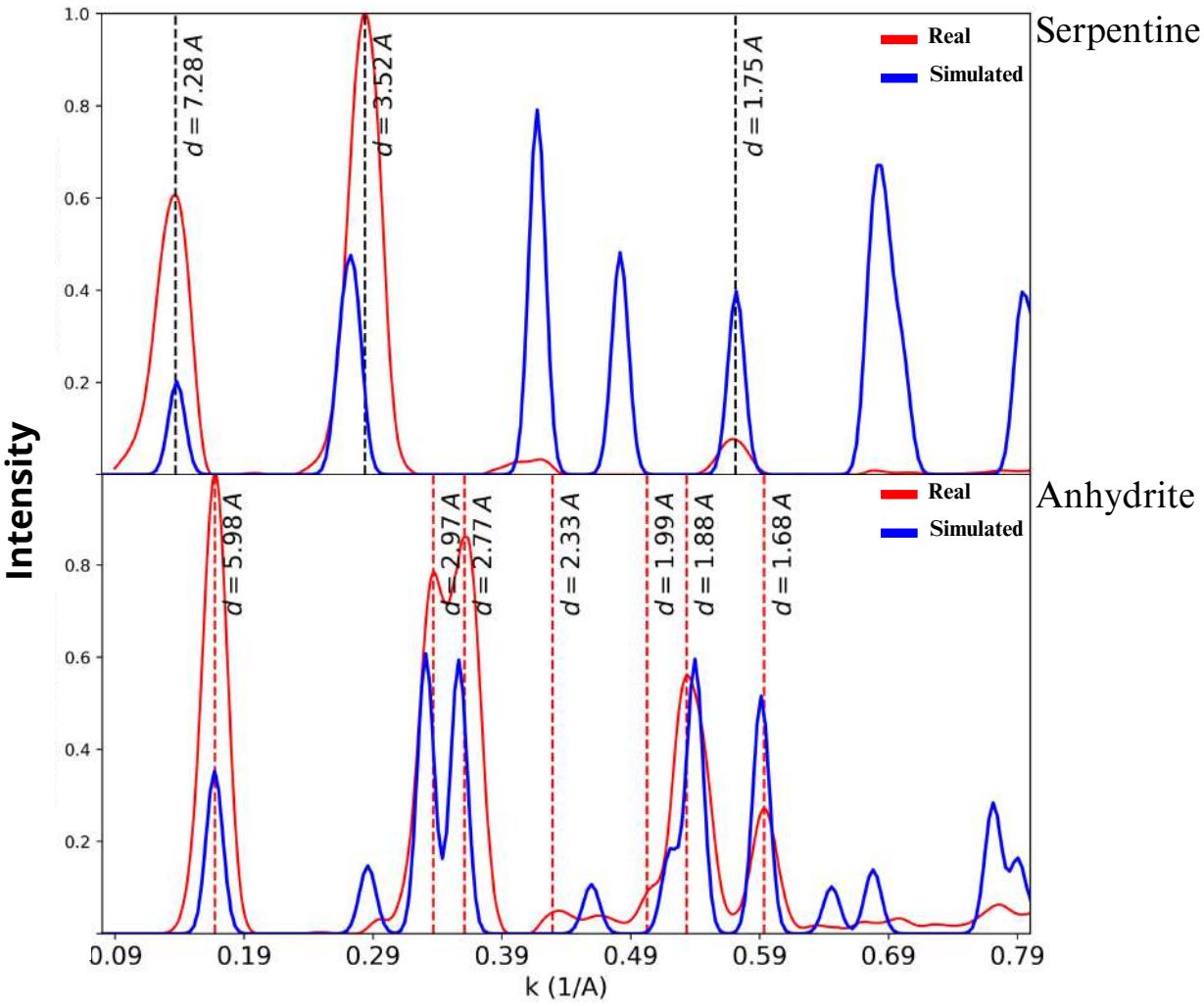

Figure 5.21: NNMF component profiles versus simulated profiles of Anhydrite and Serpentine phases. The upper panel corresponds to serpentine, while the lower panel corresponds to Anhydrite, with intensities normalized to unity.

Comparing each NNMF-reconstructed mineralogical phase map (top panel in Figure 5.22) to its equivalent obtained through the BVM-based approach (lower panel in Figure 5.22) from Chapter 4 reveals a remarkable concordance. The mean squared errors for the corresponding image pairs are quantified as (a : 0.17, b : 0.14, c : 0.08) respectively, underscoring a high level of agreement between the two reconstruction methods across the assessed mineralogical phases.

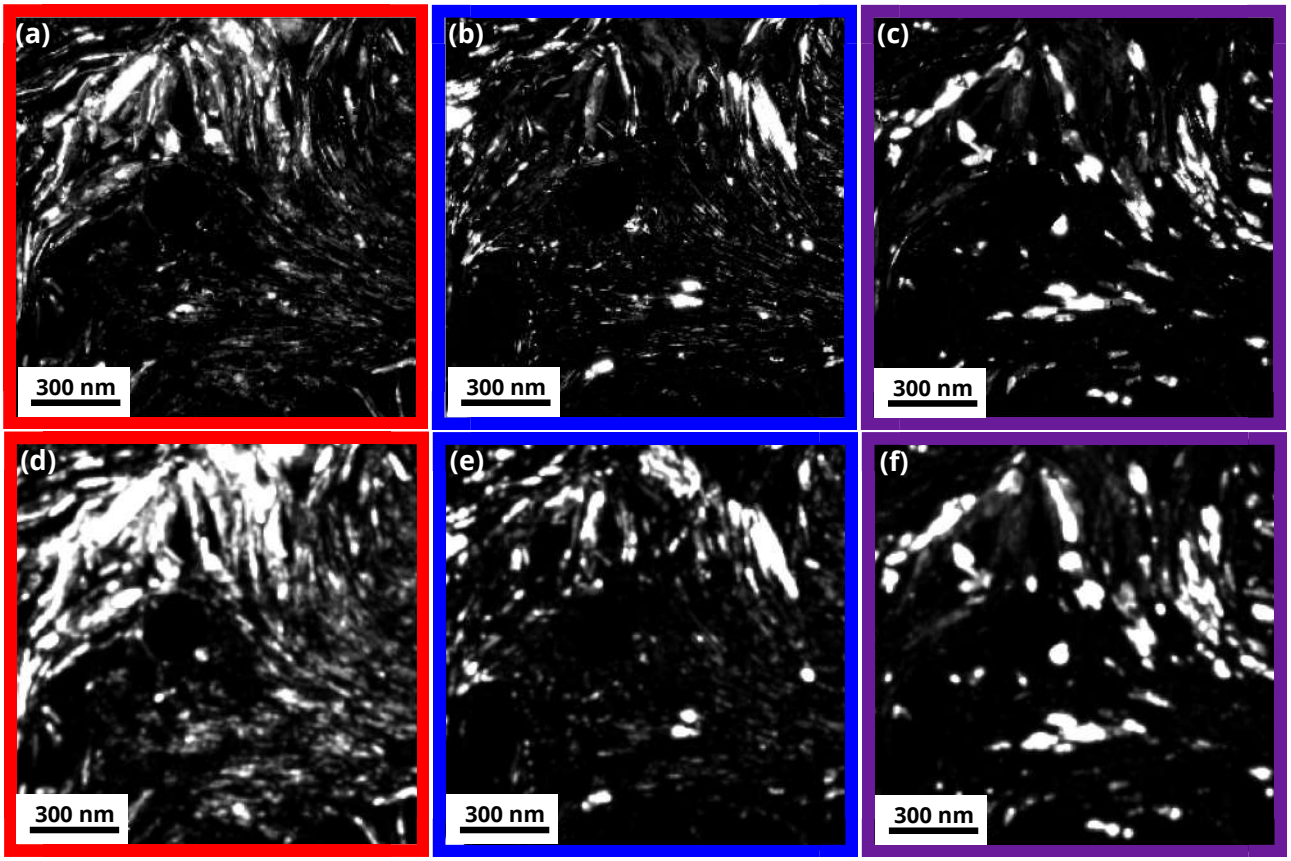

Figure 5.22: Comparison of NNMF-reconstructed VDF images and BVM-Based approach VDF images for phyllosilicates, serpentine, and Anhydrite (Top: a, b, c) and BVM-Based approach VDF images (Bottom: d, e, f) for phyllosilicates (a, d), serpentine (b, e), and anhydrite (c, f). Mean squared errors (0.17, 0.14, 0.08) respectively for phyllosilicates, serpentine and anhydrite indicate close agreement between both the BVM-based and the NNMF-based reconstruction methods across mineralogical compositions.

The final outcome derived from the NNMF analysis subsequent to the application of the 3D data pre-processing pipeline on the Orgueil sample is summarized in Figure 5.23. Figure 5.23a shows a loading map highlighting the distribution of serpentine, anhydrite, and serpentine/smectite mixtures within the phyllosilicate matrix of the Orgueil sample. This mineralogical phase distribution map aligns well with the EDX chemical maps and 4D-STEM reconstructed map presented in the previous chapter. Figure 5.23b shows an average of all NNMF-reconstructed component profiles, encompassing the totality of the diffraction informations obtained from the NNMF procedure. This reconstruction also demonstrates strong concordance with the BVM-reconstructed radial profile, ensuring that no diffraction information was lost during the reconstruction process.

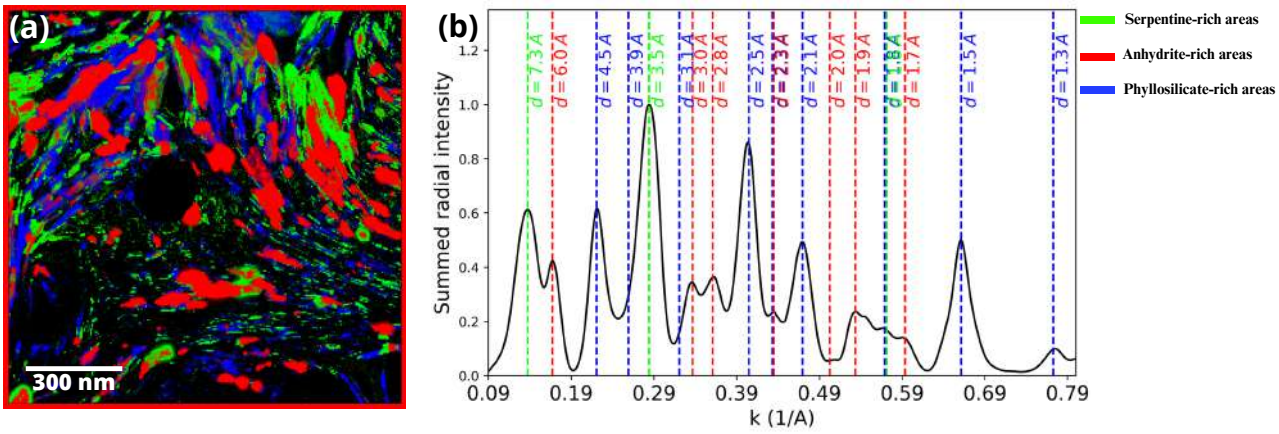

Figure 5.23: NNMF results summary after the 3D data pre-processing pipeline of Orgueil sample. (a) Segmented NNMF-based real space map of the phyllosilicate matrix of Orgueil sample, depicting the distribution of serpentine, anhydrite, and serpentine/smectite (Phyllosilicates) mixtures. (b) Normalized average of all NNMF coefficients capturing all the diffraction peaks identified through the previously used BVM-based approach.

6 Summary and Conclusion

In this chapter, we have explored the effectiveness of NNMF-based decomposition methods for segmenting mineralogical phases in chondritic samples using 4D-STEM.

First, an existing approach detailed in Allen et al. (2021) was benchmarked against another NNMF-based method described in Bergh et al. (2020), utilizing a simple MgO nanocubes sample 4D-STEM dataset. The method from Allen et al. (2021) involved a comprehensive pre-processing pipeline prior to NNMF decomposition, which demonstrated greater effectiveness in identifying the distinct orientations of the MgO nanocubes compared to the approach of Bergh et al. (2020). In the latter, NNMF decomposition was applied directly to the raw data with minimal pre-processing.

Afterwards, the methodology outlined by Allen et al. (2021) was applied to Ryugu's 4D-STEM data to explore its efficacy in segmenting complex mineralogical phases. Contrasting this with the BVM-based approach detailed in Chapter 3 revealed a significant shortfall; *Allen*'s method did not yield accurate segmentation of the different constituents within the phyllosilicate-rich matrix of Ryugu. This discrepancy can be attributed to the inherent complexity of Ryugu's and similar samples' 4D-STEM data. Unlike the MgO nanocubes samples, which displayed no more than five distinct orientations, the phyllosilicate-rich matrix of Ryugu, due to its fine-grained nature, features a myriad of distinct orientations. This results in an overall Bragg vector map

that closely resembles a powder diffraction pattern.

Inspired by the success in accurately segmenting distinct mineral phases in Ryugu and Orgueil in previous chapters through indexing an overall radial profile, a novel approach was developed. This method combines the pre-processing pipeline from Allen et al. (2021) —though excluding the binning step— and incorporates an additional step where the full 2D diffraction patterns are azimuthally averaged to produce radial profiles, thus generating a 3D-STEM dataset. This dataset is subsequently subjected to NNMF decomposition.

This approach proved to be efficient for both Ryugu and Orgueil 4D-STEM data. It has successfully produced a limited number of loading maps alongside corresponding component profiles which were then merged based on their mineralogical phase belonging by manually indexing the distinct component profiles obtained. This methodology not only overcame the challenges posed by the complex nature of the samples' 4D-STEM data but also established a new benchmark for segmenting mineralogical phases in such intricate datasets.

Summary and Future Work

In this last section, the results presented and discussed in the previous chapters will be summarized and an outlook on how future studies building on them could be undertaken will be given.

Developments in the Characterization of Fine Scale Mineral Assemblages in Astromaterials using 4D-STEM

In the quest to characterize mineral assemblages in chondritic samples, effectively mapping intricate assemblages within these samples poses a significant challenge. To tackle this issue, we devised a novel method based on Four-dimensional Scanning Transmission Electron Microscopy (4D-STEM), as detailed in Chapter 3. This method entails extracting diffraction information to construct a Bragg Vector Map (BVM) and generating an X-ray diffraction (XRD)-like spectrum to map different mineralogical phases. This approach notably enhanced the characterization process by offering a comprehensive overview of crystallographic phases in samples from Ryugu and Orgueil. Compared to conventional methods employed, such as automated crystal orientation mapping, our technique requires less processing time and proves more efficient, particularly considering the extremely fine-grained nature of the phyllosilicates.

Although our method is time-efficient and provides accurate mapping of the different mineralogical phases in such samples, it introduces a level of tediousness due to the semi-manual identification and mapping of phases. This process involved manual indexing of the differ-

ent mineralogical phases from an overall radial profile reconstructed from the BVM, which is prone to subjectivity, especially when dealing with phases with close interplanar spacings. This became particularly apparent in analyzing Orgueil samples' 4D-STEM data where phase assignment required meticulous attention during the peak assignment process.

In response to this challenge, we explored alternative techniques and found a promising solution in the application of Non-Negative Matrix Factorization (NNMF) on 3D radial profiles. By implementing a strict pre-processing pipeline to generate a 3D-STEM dataset, this approach proved highly effective in transforming raw data into unique virtual dark field images and corresponding radial profiles, jointly representing the mineral phases that are present within the sampled areas. Indexing this finite set of radial profiles was subsequently performed which allowed for segmenting the different components into unique phase maps of the different mineralogical phases.

The advantage of the NNMF-based method compared to the BVM-based method lies in its ability to reduce data into a minimal set of components. These components contain radial profiles already representative of specific mineral phases, simplifying interpretation and peak assignment. In contrast, the BVM-based method requires indexing the overall radial profile, which can be more cumbersome and prone to inaccuracies. Additionally, NNMF utilizes unique radial profiles from every position of the probe, preserving distinct diffraction signatures of each phase. This stands in contrast to the BVM approach, where all diffraction information is integrated into a single overall radial profile, potentially leading to inaccuracies in peak assignment, especially for phases with close interplanar spacings.

We believe that the ability to map different mineralogical phases from 4D-STEM data will significantly enhance our capacity for in-depth structural investigations of these individual phases. Such detailed analyses can provide invaluable insights into the evolutionary processes of the solar system since structural transformations within mineral phases stand as vital markers

of the evolution of solar system constituents.

Constraining the History of Ryugu Evolution and Insights into Orgueil from a 4D-STEM Perspective

The 4D-STEM developments that have been made throughout this work have enabled several observations from the meteoritic samples here studied. Being used for the first time on such intricate samples, the ability to unambiguously identify all the mineralogical phases present within the studied samples was a crucial step before delving into more in-depth analyses. This has been achieved through the developments outlined in the previous section in which two different approaches are proposed to identify and map all the mineral phases present in the phyllosilicate-rich matrices of Ryugu and Orgueil samples. This has enabled an in-depth exploration of the predominant phyllosilicate matrix constituents, namely serpentine and smectite, in Ryugu asteroid samples.

The results on Ryugu samples indicate that lizardite is the primary serpentine polymorph present, implying that aqueous alteration likely occurred at low temperatures suitable for lizardite formation. This discovery adds an additional constraint to our understanding of Ryugu's aqueous alteration history. Moreover, the variation in smectite interlayer spacing, mapped by measuring the (001) d-spacings across all the smectite-rich area, offers insights into the potential distribution and characteristics of organic matter which is believed to predominantly constitute the interlayer material in smectite grains. The observed heterogeneity suggests that localized environmental conditions may have influenced the crystal chemistry of smectite layers, thereby impacting the composition and interactions of organic matter within these minerals.

Transitioning to the study of Orgueil samples, which underlined the challenges posed by beam damage, 4D-STEM has nonetheless provided an accurate identification and mapping of the

minerals present within the sampled areas. While serpentine was commonly found, pure smectite orientations were not detected, nor was Ferrihydrite, both of which are common to Orgueil specifically and CI-chondrites in general. Therefore, to gain more insights into these samples, more areas on fresh uncontaminated samples should be investigated. Additionally, the study suggested that calcium sulfates, products of terrestrial weathering processes, are possibly bassanite or anhydrite.

Our findings underscore the necessity for ongoing exploration into the mineralogical, chemical, and structural attributes of asteroidal and chondritic samples, emphasizing the substantial contribution that advanced electron microscopy techniques like 4D-STEM can make in advancing our comprehension of these objects.

Future work

Evolution of Amorphous Silicates in meteoritic samples

Amorphous silicates, prevalent in primitive solar system objects, are highly susceptible to aqueous alteration, potentially leading to secondary mineral products. Their abundance in chondrites serves as a qualitative estimate of aqueous alteration. In the protoplanetary disk, silicate dust particles lack defined structure, but as they collide and aggregate, they become more susceptible to aqueous alteration processes. This leads to gradual reorganization, initially hydrating amorphous silicates and eventually forming proto-phyllosilicates. Understanding the initial stages of aqueous alteration and the conditions under which they occur, including the water-to-rock ratio, transport mechanisms, fugacities, and pH levels from fine scale investigations of the degree of structural organization in the amorphous silicate is therefore essential for having more insights into the intricate processes involved in aqueous alteration. Combining 4D-STEM with fluctuation electron microscopy (FEM) may be a suitable avenue for this

exploration.

Indeed, FEM is a technique used to measure the degree of medium-range order (MRO) in glassy materials. It involves focusing an electron probe to roughly the same length scale as the atomic ordering length of the sample, causing ”speckles” to appear in the diffraction pattern. By measuring the intensity variance as a function of scattering angle and probe size, FEM can provide information about the degree of MRO and the length scales where it is present in a sample. Combining 4D-STEM and FEM allows for a complete mapping of the MRO in amorphous silicates providing crucial clues about their evolution during aqueous alteration processes.

Subsequently, more refined approaches can be also investigated in 4D-STEM to delve more in to the intricacies of these medium range order areas in amorphous silicates. For instance, a pair distribution function (PDF) analysis can be done once MRO areas are discovered and 4D-STEM data on these MRO areas are acquired. The PDF essentially describes the probability of finding two atoms separated by a certain distance in the material under investigation, which can give insights into the atomic arrangements inside these MRO domains with a high spatial resolution.

Understanding Mineral Interstratifications through Electron Ptychography

Mixed-layering, a frequent occurrence in phyllosilicates, refers to the presence of multiple structurally and often chemically distinct layers or interlayers within a single crystal. This phenomenon is also known as interstratification which can be either random or regular as shown in Figure 5.24. In CI-type chondrites, interstratification can be very frequent, not only between phyllosilicates (such as serpentine/smectite) but also between phyllosilicates and hydroxy-sulfides (such as tochilinite). Being able to observe these interstratifications without

beam-induced damage at the scale of individual layers would thus enhance our understanding of precipitation sequences and associated physico-chemical conditions, offering additional constraints on the formation processes of these minerals within chondritic environments. While conventional High resolution STEM imaging techniques might potentially induce beam damage due to the high electron dose that can be involved, alternative approaches such as electron ptychography can be explored.

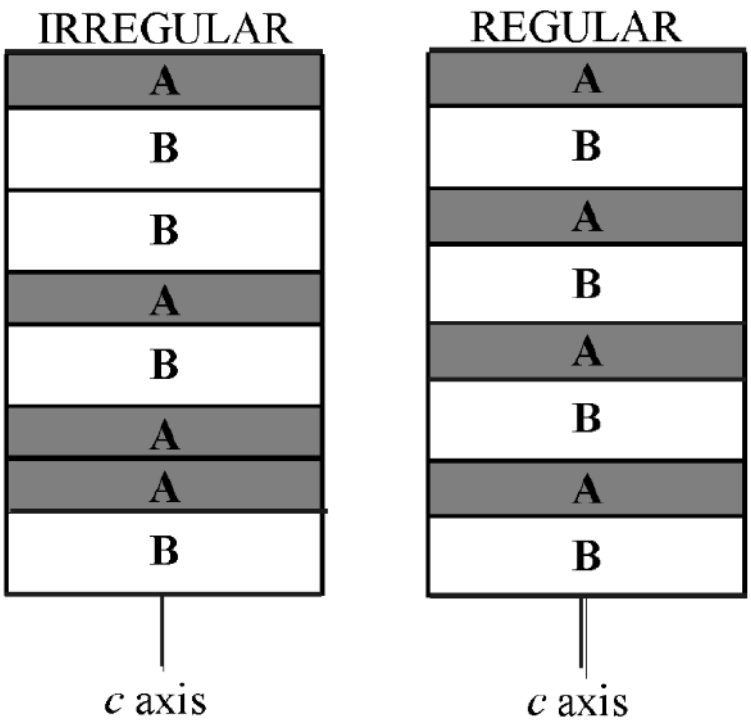

Figure 5.24: Examples of two different types of interstratifications of phyllosilicates: irregular (random) and regular (R = 1 ordered). **A** can be e.g. a 10 Å and **B** a 15 Å clay mineral. Adapted from Konta (2009)

Indeed, electron ptychography is a technique used in 4D-STEM for High resolution STEM imaging. The goal is to extract the extra phase added to the electron beam's wave at each scan point of the 4D-STEM data. This phase is seen as the overall sample potential at that point, multiplied by a constant value encompassing the strength of electron-charge interaction. Phase retrieval is achieved by analyzing overlapping regions of electron beams. By employing a large convergence angle, the central electron beam overlaps with other Bragg disks, allowing coherent addition of phases. This method enables reconstruction of phase information by

analyzing variations in interference patterns as the electron beam scans the specimen (Ophus 2019; Savitzky et al. 2021; Jiang et al. 2018).

We believe that electron ptychography can offer a promising avenue for observing interstratifications, such as mixed-layering in phyllosilicates within chondritic environments, with more accuracy and with a lower electron dose.

Annex A: Diffraction Pattern Formation

Kinematical Diffraction

Crystals are composed of atoms or molecules arranged in a highly ordered and repeating pattern, known as a crystal lattice. This regular arrangement results in particular symmetry and periodicity properties. The diffraction of waves by such crystal lattices is governed by **Bragg's Law**. This law describes in a simple geometric way the relationship between the angles of incidence, the spacing of crystal planes, and the resulting constructive interference of waves, whether they are X-rays, electrons, or other forms of electromagnetic radiations (See Fig. 5.25). It states that the angles at which waves are diffracted by a crystal lattice are related to the spacing of atomic planes within the crystal and the wavelength of the waves through:

$$2d\sin(\theta_B) = n\lambda \tag{5.7}$$

Where n is an integer representing the order of the diffraction peak, λ is the wavelength of the incident waves, d is the spacing between atomic planes, and θ_B is the Bragg angle which is the angle of incidence for which the incident waves reflected from parallel planes in a crystal lattice interfere constructively.
The constructive interference of the waves described by Bragg's Law results in a diffraction pattern. In electron microscopy, this diffraction pattern is formed in the back focal plane of the objective lens (See Fig. 2.3) and then magnified and projected onto dedicated detectors by an electromagnetic lens system.
Diffraction patterns provide information about the spacing and orientation of atomic planes in the crystal, and this relationship is mathematically expressed through the concept of the reciprocal lattice (See Figure 5.25b). This latter is characterized by its translation vector $\vec{g}$ that can be written in the reciprocal space basis, $(\vec{a}^*, \vec{b}^*, \vec{c}^*)$, corresponding to the direct space basis $(\vec{a}, \vec{b}, \vec{c})$ as:

$$\vec{g}_{hkl} = h\vec{a}^* + k\vec{b}^* + l\vec{c}^* \tag{5.8}$$

in which case, the interplanar spacing is defined as:

$$d_{hkl} = \frac{1}{|\vec{g}_{hkl}|} \tag{5.9}$$

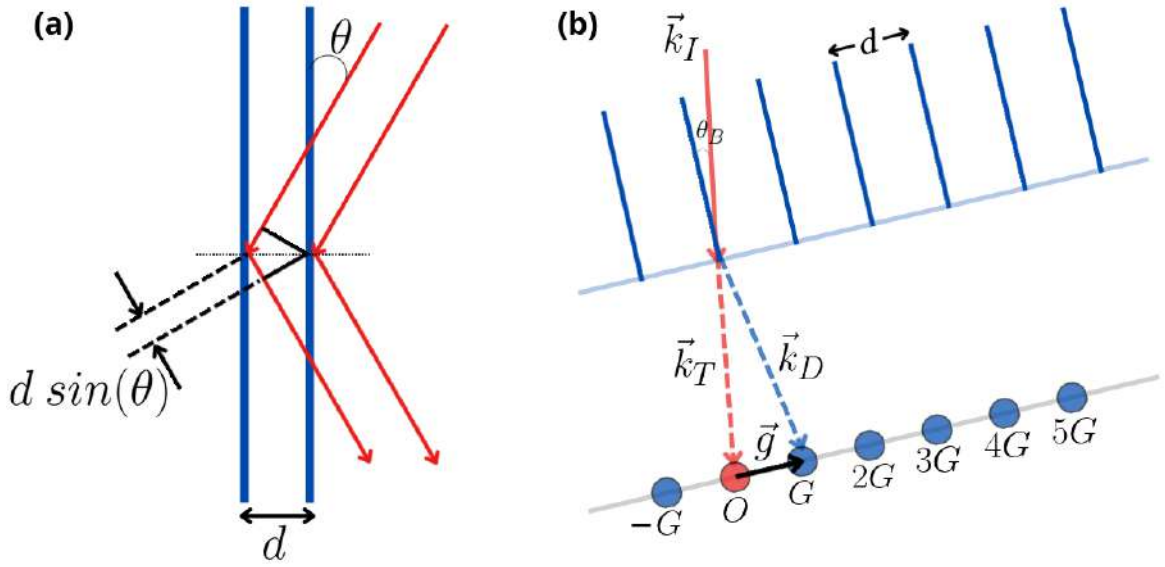

Figure 5.25: Bragg's Law: (a) Bragg diffraction involves waves reflecting off atoms in a crystal with a separation distance d between lattice planes. Bragg law, expressed as $2d\sin(\theta_B) = n\lambda$, dictates the condition for waves to stay in phase, leading to constructive interference, while angles corresponding to fractional n result in destructive interference. (b) A set of planes with a characteristic spacing d and oriented in Bragg diffraction conditions with respect to the electron beam result in diffraction spots. The reciprocal lattice vector $\vec{g}$ (defined in this case from the origin to the first diffraction spot encountered), is normal to the diffraction plane and has units of reciprocal length.

Equally significant in kinematical diffraction is the concept of the **Ewald sphere**. It provides a geometric representation of the reciprocal lattice points intersected by the incident wave. Indeed, when examining the diffraction pattern from a set of planes, and provided the "elastic" nature of scattering leading to diffraction, where the magnitudes of the incident ($\vec{k}_I$), transmitted ($\vec{k}_T$), and diffracted ($\vec{k}_D$) wavevectors are equal $\left(k = \left|\vec{k}_I\right| = \left|\vec{k}_T\right| = \left|\vec{k}_D\right|\right)$, it becomes evident that Bragg's Law holds true only for the reciprocal lattice points falling within a sphere centered at the position of the specimen (O) and which radius is $k = \frac{1}{\lambda}$. In this case, Bragg's Law can be rewritten as:

$$\vec{k}_D - \vec{k}_I = \vec{g}_{hkl} \tag{5.10}$$

The particularity of electron diffraction w.r.t to other diffraction techniques such as X-ray or neutron diffraction can be understood through Ewald sphere construction. For a simplistic view, let's consider the case when a high symmetry $[uvw]$ lattice row of the crystal is set parallel to the incident electron beam. In this specific scenario, this lattice row is referred to as a **zone axis**. The electron beam in this case effectively "sees" the reciprocal layers arranged in parallel and equidistant $(uvw)^*$ layers, as illustrated in Figure 5.26a. Assuming a hypothetical X-ray Ewald sphere with a CuK_α X-ray wavelength, the X-ray Ewald sphere nearly intersects three reciprocal lattice nodes, whereas the TEM Ewald sphere intersects a multitude of reciprocal lattice nodes, as depicted in Figure 5.26(b,c), owing to the small wavelength of electrons and hence the higher Ewald sphere radius. This explains the necessity in X-ray diffraction to either powdered or rotated specimen to ensure the excitation of a broad range of Bragg conditions which is not the case in TEM diffraction.

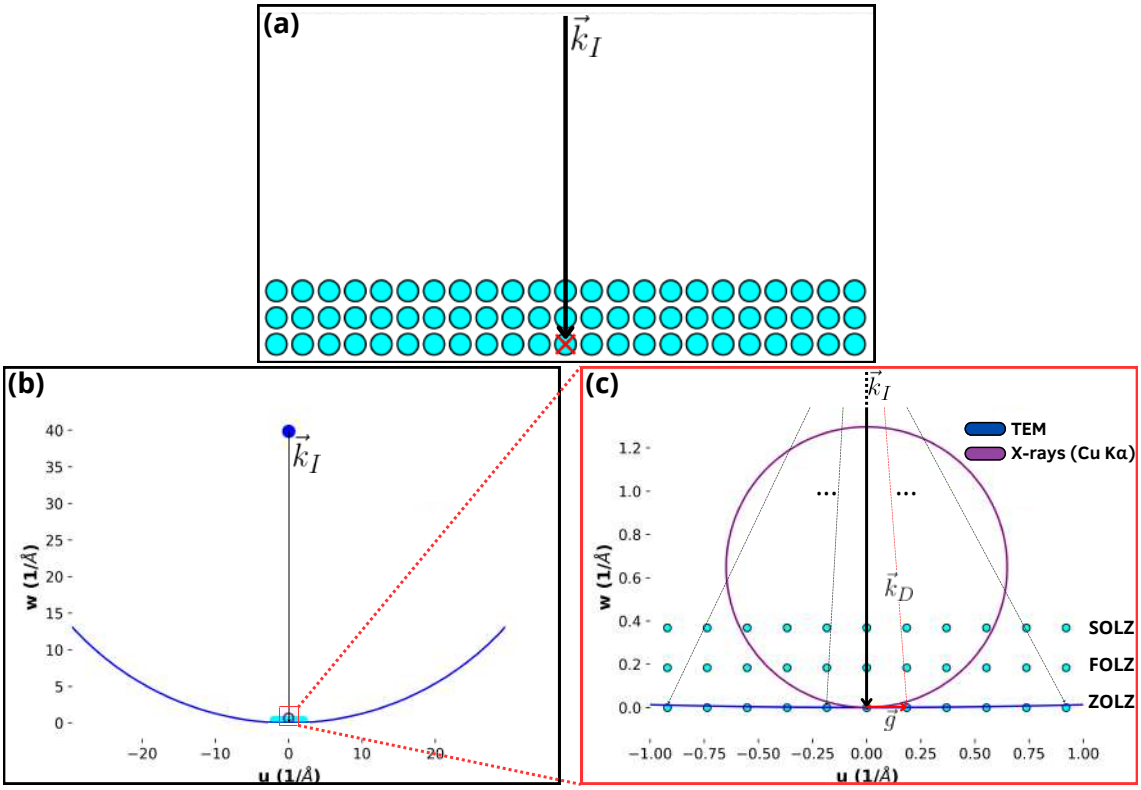

Figure 5.26: Ewald Sphere Construction for a zone-axis parallel to the incident electron beam: (a) Illustration of the $0th$ (Zeroth-order Laue Zone), $1st$ (First-order Laue Zone), and $2nd$ (Second-order Laue Zone) reciprocal layers in a cubic Silicon crystal system ($a \approx 5.4$ Å) with incident wavevector $\vec{k}_I$. Reciprocal lattice nodes are arranged in parallel and equidistant layers when a zone axis is set parallel to the incident electron beam. (b) Comparative Ewald sphere constructions for TEM and X-ray diffraction. The X-ray Ewald sphere, with its short radius, is nearly visible, while the TEM Ewald sphere is significantly larger. (c) Close-up of reciprocal lattice nodes surrounding the X-ray Ewald sphere. This zoomed depiction highlights the limited excitation of Bragg conditions because of the high curvature of the X-ray Ewald sphere, in contrast to the TEM Ewald sphere where the apparent flattening facilitates the excitation of numerous Bragg conditions simultaneously.

Another distinctive feature in TEM diffraction arises from what is known as the "excitation error" originating from the finite thickness of samples commonly encountered in transmission electron microscopy and the dynamical scattering generally occurring for sufficiently thick samples which we'll briefly outline in the next section. Indeed, TEM samples typically exhibit a thickness on the order of $\sim 100\ nm$, whereas, for instance, a TEM sample can easily have surface dimensions typically extending to over a few microns. This finite thickness relative to the surface causes reciprocal lattice nodes to deviate from their perfectly round shape to a more "relrod"-like configuration as shown in Figure 5.27. This distinctive feature can be explained through the Fourier transformation. The Fourier transformation of a disk of a finite thickness exhibits a relrod shape as shown in the inset of Figure 5.27. Under these conditions, sufficiently long relrods can intersect the Ewald sphere even if the Bragg conditions are not exactly met. This doesn't affect the position of the resulting diffraction spots but modifies their intensity. Taking this effect into account, Bragg's Law can be reformulated as:

$$\vec{k}_D - \vec{k}_I = \vec{g}_{hkl} + \vec{S}_g \tag{5.11}$$

Where $\vec{S}_g$ represents the excitation error.

These relrods are perpendicular to the sample and is the major contribution to the *excitation error*.

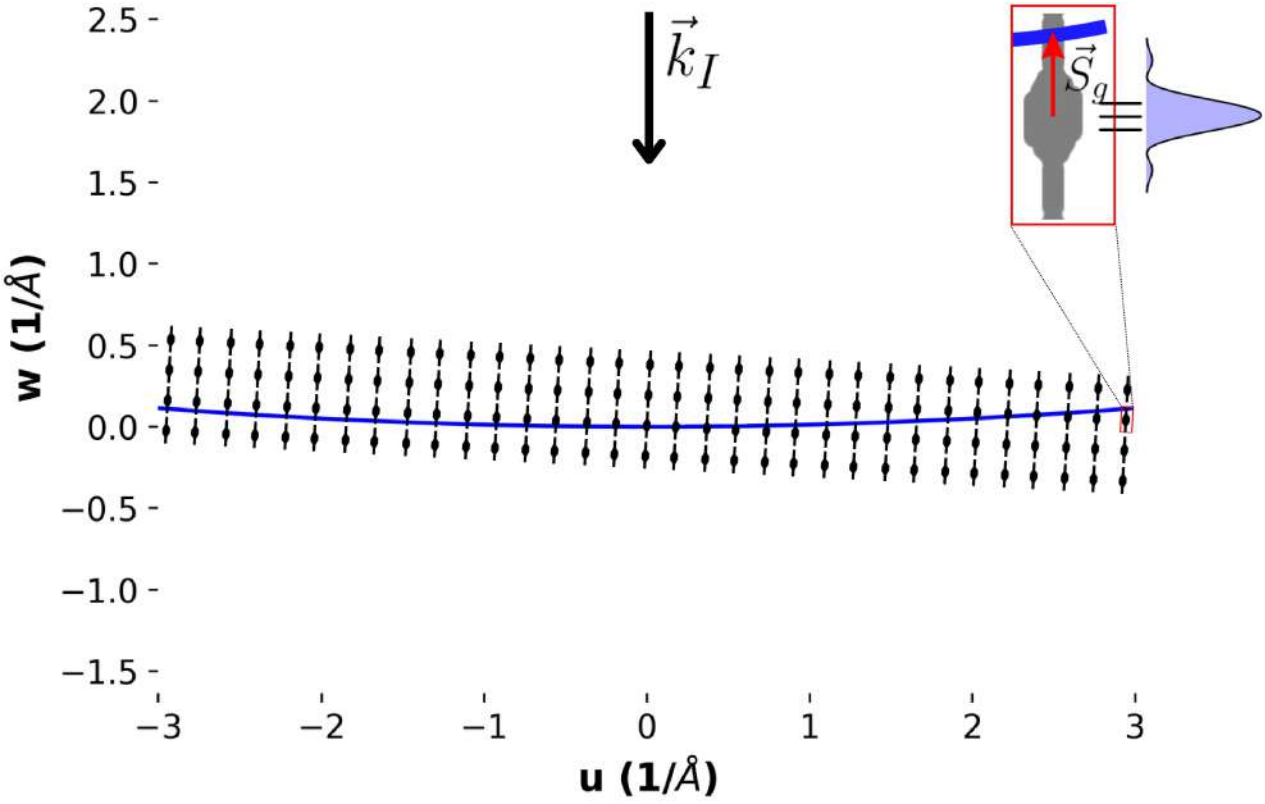

Figure 5.27: Ewald sphere construction for a random orientation of the sample w.r.t the incident electron beam: The reciprocal lattice layers are in this case randomly oriented w.r.t to the incident wavevector. The reciprocal lattice nodes exhibit the shape of "relrods" reflecting the finite dimensions of the sample. Due to this feature, more Bragg spots than predicted by infinite crystal conditions can be observed in the diffraction pattern.

Structure factors and Atomic Scattering Factors

So far, only the geometrical aspects of electron diffraction were considered. An essential aspect lies in understanding the factors governing the intensity of diffraction peaks. These factors are encapsulated in what is referred to as *structure factors* and *atomic scattering factors*, which play a crucial role in shaping the observed diffraction pattern.

Structure Factors:
The structure factors, denoted as $F(hkl)$, embodies the contribution of each lattice point to the intensity of a diffraction peak. It encompasses both the amplitude and phase information regarding the scattering process. It can be mathematically expressed as the sum over all atoms within the unit cell, each weighted by its respective atomic scattering factor and phase factor:

$$F(hkl) = \sum_j f_j e^{2\pi i(hx_j + ky_j + lz_j)} \tag{5.12}$$

where f_j represents the atomic scattering factor of the j-th atom, and (x_j, y_j, z_j) denotes its fractional coordinates within the unit cell. The phase factor accounts for the spatial arrangement of atoms within the crystal lattice. Example structure factors for a Silicon lattice are shown in Figure 5.28a.

Atomic scattering factors:
Atomic scattering factors describe how individual atoms within a crystal scatter radiation. These are derived from the atomic electrostatic potential when interacting with electrons. It is denoted as $f(\theta)$ and characterizes the scattering strength as a function of the scattering angle θ. The atomic scattering factor incorporates both elastic and inelastic scattering contributions, as it represents the combined effect of the electron distribution within the atom on the scattered radiation. Example of atomic scattering factors for multiple atoms are shown in Figure 5.28b.

Intensity of a diffracted beam:
The observed intensity of a diffracted beam, emerges from the interplay of structure factors, atomic scattering factors, and the geometry of the scattering process and is proportional to the scattering factor in kinematical diffraction.

$$I_{obs} \propto |F(hkl)|^2 \tag{5.13}$$

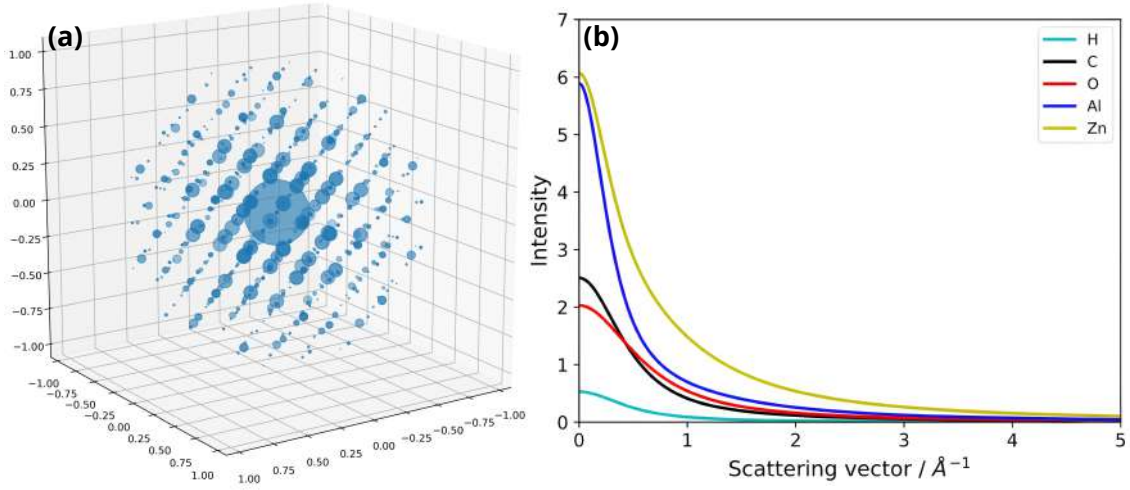

Figure 5.28: Example of structure factors and atomic scattering factors: (a) Structure factors for a Si lattice. (b) Atomic scattering factors for multiple atoms.

Dynamical Diffraction

Apart from the broadening of reciprocal lattice nodes due to the finite nature of TEM samples, another equally important effect arises known as dynamical scattering.
Dynamical scattering occurs when the incident electrons penetrate deeply into the sample, interacting with multiple atomic planes, before exiting the specimen. This results in complex interference patterns that can significantly alter the intensity and distribution of diffraction spots compared to what would be expected from kinematic scattering alone.
Essentially, while kinematic scattering assumes a single scattering event at each atomic plane, dynamical scattering accounts for the multiple interactions of electrons within the crystal lattice. As a result, dynamical scattering can lead to phenomena such where certain diffraction spots can be weakened or entirely suppressed, and changes in spots' intensity distribution (See Fig. 5.29).
Understanding and accounting for dynamical scattering effects are crucial for accurately interpreting TEM diffraction patterns. Advanced modeling techniques, such as multislice simulations (Lobato and Van Dyck 2015; Pryor et al. 2017; Ophus 2017; Rangel DaCosta et al. 2021;

Madsen and Susi 2021), are often employed to simulate dynamical scattering effects and improve the fidelity of TEM data interpretation through multislice or Bloch wave simulations. Furthermore, Precession electron diffraction (PED) is generally used to mitigate dynamical effects. In PED, the incident electron beam is tilted around the central axis of the microscope allowing for the integration over a collection of diffraction conditions leading to a quasi-kinematical diffraction pattern. These patterns are much more suitable as input into algorithms employed for phase/orientation mapping.
Notably, all "non-kinematical" effects, including dynamical scattering, are accounted for in the excitation error previously introduced.

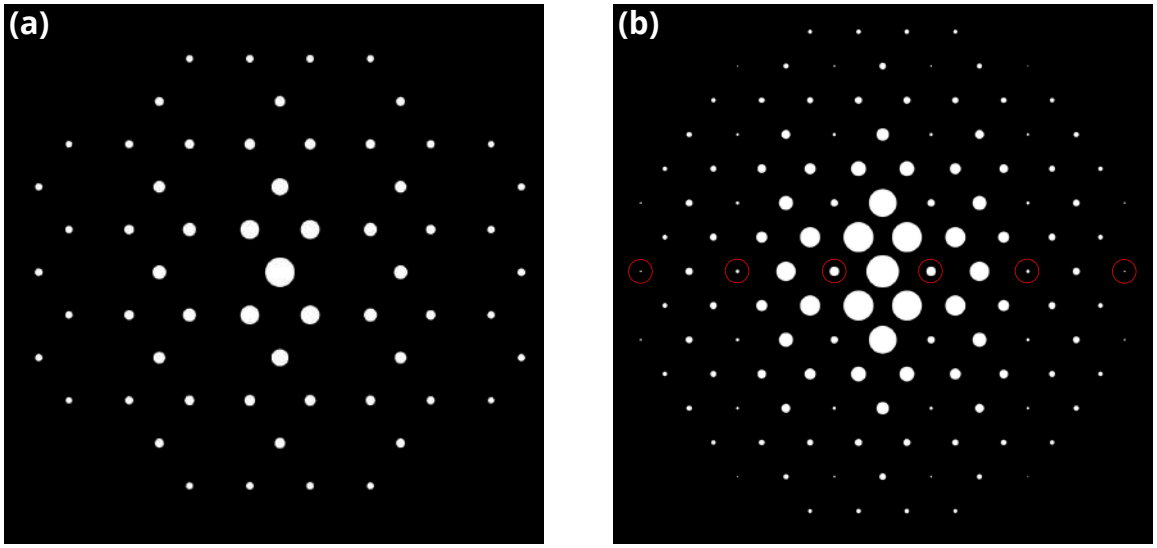

Figure 5.29: Simulated diffraction patterns of silicon in a $[0, 1, 1]$ zone axis orientation: (a) illustrates the kinematical diffraction pattern, characterized by uniformly distributed intensities across the spots, consistent with single scattering events. (b) shows the dynamical diffraction pattern, which displays varying intensities among the spots, including some with significant brightness, and double diffraction phenomena (highlighted by the red circles). This is indicative of multiple scattering events in the silicon specimen, simulated here at a thickness of 100 Å.

Effect of the Convergence Semi-Angle on Electron Diffraction Patterns

The convergence semi-angle in STEM refers to the half-angle within which the electron beam converges onto the specimen as shown in Figure 5.30(a-c). This semi-angle directly affects the diameter of the transmitted and diffracted beams.
For small semi-angles, typically less than 1 *mrad*, micro-diffraction patterns are observed, featuring well-defined spots representing individual diffracted beams. As the semi-angle increases to a moderate range, typically between 1-10 *mrad*, the resulting patterns are called convergent beam electron diffraction (CBED) patterns. These exhibit overlapping but still distinguishable diffraction spots. CBED analysis allows for comprehensive characterization of crystal structures, enabling the determination of properties such as specimen thickness, lattice parameter, crystal symmetry, and characteristics of lattice defects. Lastly, Large-Angle Convergent-Beam Electron Diffraction (LACBED) conditions, where semi-angle typically exceeds 10 *mrad*, offer enhanced ways for identifying lattice defects and accurately determining strains, including those

at interfaces of multi-layer materials, with high precision (Williams and Carter 2008; Morniroli 2004).
All the work presented in this thesis was conducted in micro-diffraction conditions using small semi-convergence angles ($\sim 0.1\,mrad$) and quasi-parallel illumination resulting in spot diffraction patterns.

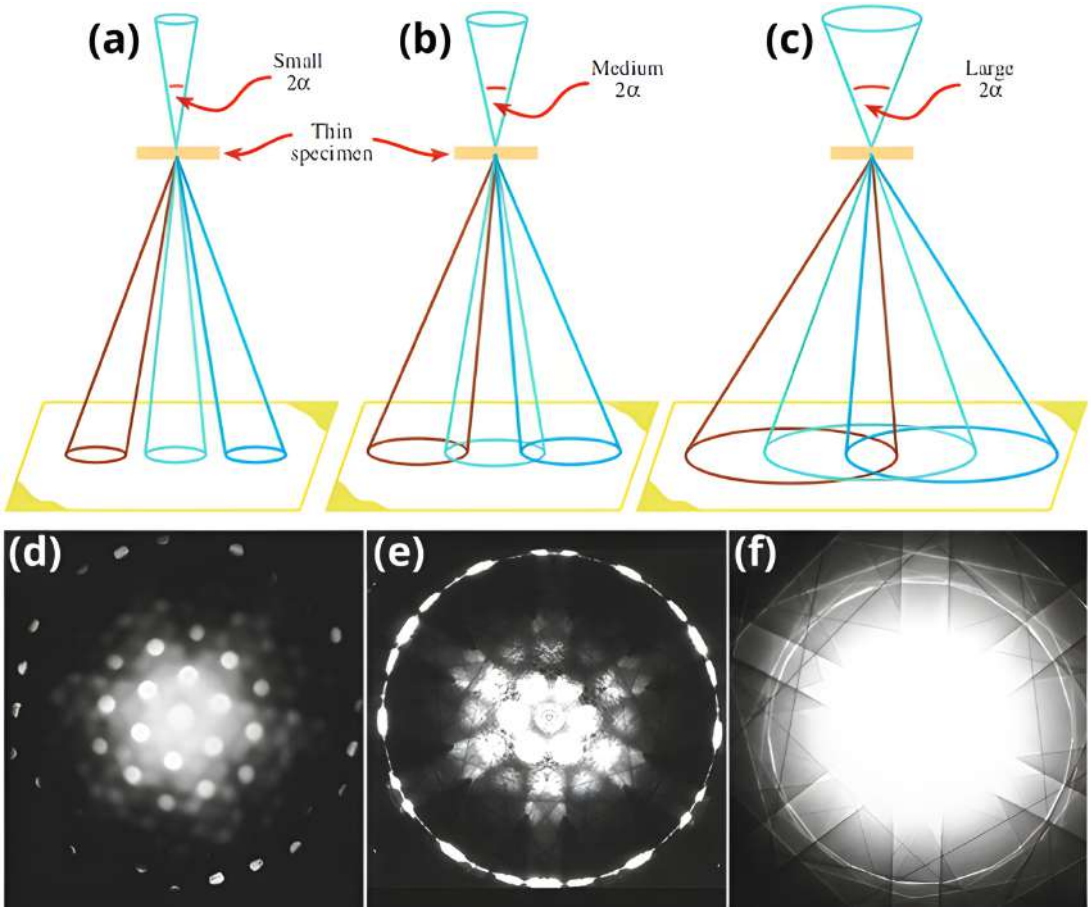

Figure 5.30: Effect of the convergence semi-angle on electron diffraction patterns: (a–c) Diagrams illustrating the impact of enlarging the convergence semi-angle (α) on the resulting diffraction pattern transitioning from resolving individual and separate disks (small α) to overlapping diffraction disks (large α). (d–f) Example experimental diffraction patterns under the respective (a-c) conditions. Adapted from Williams and Carter (2008).

Bibliography

Abreu, N. M. et al. (2018a). "Elephant Moraine (EET) 83226: A Clastic, Type 2 Carbonaceous Chondrite with Affinities to the CO Chondrites". In: *49th Annual Lunar and Planetary Science Conference*. Lunar and Planetary Science Conference, p. 2451.

Abreu, N. M. et al. (2018b). "Understanding the Effects of Antarctic Weathering on the Petrologic and Spectral Characteristics of Pristine CR Carbonaceous Chondrites". In: *49th Annual Lunar and Planetary Science Conference*. Lunar and Planetary Science Conference, p. 1297.

Alberta NanoFab, University of (2024). *JEOL ARM Instrumentation and Applications Overview*. URL: https://confluence.nanofab.ualberta.ca/display/EQ/JEOL+ARM+Instrumentation+and+Applications+Overview.

Alexander, C. M. O'D. et al. (2012). "The Provenances of Asteroids, and Their Contributions to the Volatile Inventories of the Terrestrial Planets". In: *Science* 337.6095, pp. 721–723. DOI: 10.1126/science.1223474.

Alexander, Conel et al. (2017). "Measuring the level of interstellar inheritance in the solar protoplanetary disk". In: *Meteoritics & Planetary Science* 52.9, pp. 1797–1821.

Alexander, Conel M.O'D. et al. (2013). "The classification of CM and CR chondrites using bulk H, C and N abundances and isotopic compositions". In: *Geochimica et Cosmochimica Acta* 123, pp. 244–260. DOI: https://doi.org/10.1016/j.gca.2013.05.019.

Allen, Frances et al. (2021). "Fast Grain Mapping with Sub-Nanometer Resolution Using 4D-STEM with Grain Classification by Principal Component Analysis and Non-Negative Matrix Factorization". In: *Microscopy and Microanalysis* 27, pp. 1–10. DOI: 10.1017/S1431927621011946.

Anders, Edward (1968). "Chemical processes in the early solar system, as inferred from meteorites". In: *Accounts of Chemical Research* 1.10, pp. 289–298. DOI: 10.1021/ar50010a001.

Andreani, Muriel et al. (2008). "Occurrence, composition and growth of polyhedral serpentine". In: *European Journal of Mineralogy* 20.2, pp. 159–171. DOI: 10.1127/0935-1221/2008/0020-1801.

Armstrong, N. et al. (2021). "Bayesian analysis reveals the impact of load partitioning on microstructural evolution in Ti-6Al-4V during in-situ tensile loading". In: *Materialia* 15. DOI: 10.1016/j.mtla.2020.100993.

Asplund, Martin et al. (2009). "The Chemical Composition of the Sun". In: 47.1, pp. 481–522. DOI: 10.1146/annurev.astro.46.060407.145222.

Bailey, S. W, ed. (1991). *Hydrous phyllosilicates: exclusive of micas*. en. 2. print. Reviews in mineralogy 19. Washington, D. C: Mineralogical Society of America, pp. 91–167.

Ballirano, Paolo et al. (2001). "The monoclinic I2 structure of bassanite, calcium sulphate hemihydrate (CaSO4 · 0.5H2O)". In: *European Journal of Mineralogy* 13.5, pp. 985–993. DOI: 10.1127/0935-1221/2001/0013-0985.

Barber, D.J. (1981). "Matrix phyllosilicates and associated minerals in C2M carbonaceous chondrites". In: *Geochimica et Cosmochimica Acta* 45.6, pp. 945–970. DOI: https://doi.org/10.1016/0016-7037(81)90120-4.

Barton, C.D. and A.D. Karathanasis (2002). "Clay Minerals". In: *Encyclopedia of Soil Science*. Ed. by R. Lal. New York, USA: Marcel Dekker, pp. 187–192.

Beck, P. et al. (2014). "Transmission infrared spectra (2-25um) of carbonaceous chondrites (CI, CM, CV-CK, CR, C2 ungrouped): Mineralogy, water, and asteroidal processes". In: *Icarus* 229, pp. 263–277. DOI: 10.1016/j.icarus.2013.10.019.

Belzile, Nelson et al. (2004). "A review on pyrrhotite oxidation". In: *Journal of Geochemical Exploration* 84.2, pp. 65–76. DOI: https://doi.org/10.1016/j.gexplo.2004.03.003.

Berger, Eve L. et al. (2016). "Heterogeneous histories of Ni-bearing pyrrhotite and pentlandite grains in the CI chondrites Orgueil and Alais". en. In: *Meteoritics & Planetary Science* 51.10, pp. 1813–1829. DOI: 10.1111/maps.12721.

Bergh, T. et al. (2020). "Nanocrystal segmentation in scanning precession electron diffraction data". In: *Journal of Microscopy* 279.3, pp. 158–167. DOI: https://doi.org/10.1111/jmi.12850.

Boulay, E. et al. (2014). "Influence of amorphous phase separation on the crystallization behavior of glass-ceramics in the BaO–TiO2–SiO2 system". In: *Journal of Non-Crystalline Solids* 384, pp. 61–72. DOI: 10.1016/j.jnoncrysol.2013.06.023.

Brearley, A and R Jones (1998). "Chondritic meteorites". In: *Reviews in Mineralogy and Geochemistry* 36.1, pp. 3-01-3–398.

Brearley, A. J. (2006). "The Action of Water". In: *Meteorites and the Early Solar System II*. Ed. by Dante S. Lauretta and Harry Y. McSween, pp. 584–624.

Brearley, Adrian (1992). "Mineralogy of Fine-Grained Matrix in the Ivuna CI Carbonaceous Chondrite". In: *Lunar Planet. Sci.* 23, p. 153.

Brigatti, M.F. et al. (2013). "Structure and Mineralogy of Clay Minerals". In: *Handbook of Clay Science*. Elsevier, pp. 21–81. DOI: 10.1016/b978-0-08-098258-8.00002-x.

Brown, G. and G. W. Brindley (1980). "X-ray Diffraction Procedures for Clay Mineral Identification". In: *Crystal Structures of Clay Minerals and their X-Ray Identification*, pp. 305–360. DOI: 10.1180/mono-5.5.

Bruefach, Alexandra et al. (2022). "Analysis of Interpretable Data Representations for 4D-STEM Using Unsupervised Learning". In: *Microscopy and Microanalysis* 28, pp. 1–11. DOI: 10.1017/S1431927622012259.

Bruefach, Alexandra et al. (2023). "Robust design of semi-automated clustering models for 4D-STEM datasets". In: *APL Machine Learning* 1. DOI: 10.1063/5.0130546.

Brunetti, G. et al. (2011). "Confirmation of the Domino-Cascade Model by LiFePO4/FePO4 Precession Electron Diffraction". In: *Chemistry of Materials* 23. DOI: 10.1021/cm201783z.

Bustillo, Karen C. et al. (2021). "4D-STEM of Beam-Sensitive Materials". In: *Accounts of Chemical Research* 54 (11), pp. 2543–2551. DOI: 10.1021/acs.accounts.1c00073.

Campbell, A. et al. (2005). "Origin and Thermal History of Fe-Ni Metal in Primitive Chondrites". In: *Chondrites and the protoplanetary disk* 341, p. 407.

Caroli, Emmanuel (2000). *Météorites et formation du système solaire*.

Cautaerts, Niels et al. (2022). "Free, flexible and fast: Orientation mapping using the multi-core and GPU-accelerated template matching capabilities in the python-based open source 4D-STEM analysis toolbox Pyxem". In: *Ultramicroscopy*. DOI: 10.1016/j.ultramic.2022.113517.

Charola, A. Elena et al. (2007). "Gypsum: a review of its role in the deterioration of building materials". en. In: *Environmental Geology* 52.2, pp. 339–352. DOI: 10.1007/s00254-006-0566-9.

Clausen, Alexander et al. (2020). "LiberTEM: Software platform for scalable multidimensional data processing in transmission electron microscopy". In: *Journal of Open Source Software* 5.50, p. 2006. DOI: 10.21105/joss.02006.

Clayton, Robert N., Lawrence Grossman, et al. (1973). "A Component of Primitive Nuclear Composition in Carbonaceous Meteorites". In: *Science* 182.4111, pp. 485–488. DOI: 10.1126/science.182.4111.485.

Clayton, Robert N. and Toshiko K. Mayeda (1996). "Oxygen isotope studies of achondrites". In: *Geochimica et Cosmochimica Acta* 60.11, pp. 1999–2017. DOI: https://doi.org/10.1016/0016-7037(96)00074-9.

— (1999). "Oxygen isotope studies of carbonaceous chondrites". In: *Geochimica et Cosmochimica Acta* 63.13, pp. 2089–2104. DOI: 10.1016/S0016-7037(99)00090-3.

Clayton, Robert N., Toshiko K. Mayeda, et al. (1991). "Oxygen isotope studies of ordinary chondrites". In: *Geochimica et Cosmochimica Acta* 55.8, pp. 2317–2337. DOI: 10.1016/0016-7037(91)90107-G.

Clément, L. et al. (2004). "Strain measurements by convergent-beam electron diffraction: The importance of stress relaxation in lamella preparations". In: *Applied Physics Letters* 85.4, pp. 651–653. DOI: 10.1063/1.1774275.

Cliff, G. and G. Lorimer (2011). "The Quantitative Analysis of Thin Specimen". In: *Journal of Microscopy* 103, pp. 203–207. DOI: 10.1111/j.1365-2818.1975.tb03895.x.

Colten-Bradley, Virginia et al. (1987). *Role of Pressure in Smectite Dehydration–Effects on Geopressure and Smectite-to-Illite Transformation*.

Comodi, Paola et al. (2008). "High-pressure behavior of gypsum: A single-crystal X-ray study". In: *American Mineralogist* 93, pp. 1530–1537. DOI: 10.2138/am.2008.2917.

De la Peña, Francisco et al. (2022). *hyperspy/hyperspy: Release v1.7.1*. Version v1.7.1. DOI: 10.5281/zenodo.6659919.

Demichelis, Raffaella et al. (2016). "Serpentine polymorphism: a quantitative insight from first-principles calculations". In: *CrystEngComm* 18.23, pp. 4412–4419. DOI: 10.1039/c6ce00190d.

Descartes, S. et al. (2011). "Inhomogeneous microstructural evolution of pure iron during high-pressure torsion". In: *Materials Science and Engineering: A* 528.10–11, pp. 3666–3675. DOI: 10.1016/j.msea.2011.01.029.

Di Maio, C. and G. Scaringi (2016). "Shear displacements induced by decrease in pore solution concentration on a pre-existing slip surface". In: *Engineering Geology* 200, pp. 1–9. DOI: https://doi.org/10.1016/j.enggeo.2015.11.007.

Dobrică, Elena et al. (2023). "Nonequilibrium spherulitic magnetite in the Ryugu samples". en. In: *Geochimica et Cosmochimica Acta* 346, pp. 65–75. DOI: 10.1016/j.gca.2023.02.003.

Eckart, Carl and G. Marion Young (1936). "The approximation of one matrix by another of lower rank". In: *Psychometrika* 1, pp. 211–218.

Eggeman, Alexander et al. (2015). "Scanning precession electron tomography for three-dimensional nanoscale orientation imaging and crystallographic analysis". In: *Nature communications* 6, p. 7267. DOI: 10.1038/ncomms8267.

Endress, M. and A. Bischoff (1993). "Mineralogy, Degree of Brecciation, and Aqueous Alteration of CI Chondrites Orgueil, Ivuna, and Alais". In: *Meteoritics* 28.3, pp. 345–346.

Evans, Bernard W. (2004). "The Serpentinite Multisystem Revisited: Chrysotile Is Metastable". In: *International Geology Review* 46.6, pp. 479–506. DOI: 10.2747/0020-6814.46.6.479.

Felzenszwalb, F. and Huttenlocher Pedro P. (2004). "Efficient graph-based image segmentation". In: *Intl. journal of computer vision 59.2*, pp. 167–181.

Ferrage, Eric (2016). "Investigation of the interlayer organization of water and ions in smectite from the combined use of diffraction experiments and molecular simulations. a review of methodology, applications, and perspectives." In: *Clays and Clay Minerals* 64.4, pp. 348–373. DOI: 10.1346/CCMN.2016.0640401.

Fredriksson, Kurt and John F. Kerridge (1988). "Carbonates and Sulfates in CI Chondrites: Formation by Aqueous Activity on the Parent Body". en. In: *Meteoritics* 23.1, pp. 35–44. DOI: 10.1111/j.1945-5100.1988.tb00894.x.

Gallagher-Jones, Marcus et al. (2019). "Nanoscale mosaicity revealed in peptide microcrystals by scanning electron nanodiffraction". In: *Communications Biology* 2.1. DOI: 10.1038/s42003-018-0263-8.

Gammer, Christoph et al. (2015). "Diffraction contrast imaging using virtual apertures". In: *Ultramicroscopy* 155, pp. 1–10. DOI: https://doi.org/10.1016/j.ultramic.2015.03.015.

Golub, Gene H. and Charles F. Van Loan (1996). *Matrix Computations*. Third. The Johns Hopkins University Press.

Gounelle, Matthieu and Michael Zolensky (2001). "A terrestrial origin for sulfate veins in CI1 chondrites". In: *Meteoritics & Planetary Science* 36, pp. 1321–1329. DOI: 10.1111/j.1945-5100.2001.tb01827.x.

Guan, Yunbin et al. (2000). "Oxygen isotopes in calcium–aluminum-rich inclusions from enstatite chondrites: new evidence for a single CAI source in the solar nebula". In: *Earth and Planetary Science Letters* 181.3, pp. 271–277. DOI: https://doi.org/10.1016/S0012-821X(00)00218-1.

Guo, Wei et al. (2018). "Extremely hard amorphous-crystalline hybrid steel surface produced by deformation induced cementite amorphization". In: *Acta Materialia* 152, pp. 107–118. DOI: 10.1016/j.actamat.2018.04.013.

Hachtel, Jordan A. et al. (2018). "Sub-Ångstrom electric field measurements on a universal detector in a scanning transmission electron microscope". In: *Advanced Structural and Chemical Imaging* 4.1. DOI: 10.1186/s40679-018-0059-4.

Haider, Maximilian et al. (1998). "Electron microscopy image enhanced". In: *Nature* 392, pp. 768–769.

Harries, Dennis et al. (2013). "Oxidative dissolution of 4C- and NC-pyrrhotite: Intrinsic reactivity differences, pH dependence, and the effect of anisotropy". In: *Geochimica et Cosmochimica Acta* 102, pp. 23–44. DOI: https://doi.org/10.1016/j.gca.2012.10.021.

Harrison, C S et al. (2022). "FE-SULFIDES IN RYUGU PARTICLE C0025_01: A COMPARISON WITH CI AND CY CHONDRITES". en. In: *85th Annual Meeting of The Meteoritical Society 2022*.

Hawthorne, F. C. and R. B. Ferguson (1975). "Anhydrous sulphates; II, Refinement of the crystal structure of anhydrite". In: *The Canadian Mineralogist* 13.3, pp. 289–292.

Herd, Christopher D. K. et al. (2011). "Origin and Evolution of Prebiotic Organic Matter As Inferred from the Tagish Lake Meteorite". In: *Science* 332.6035, pp. 1304–1307. DOI: 10.1126/science.1203290.

Hirata, Akihiko et al. (2010). "Direct observation of local atomic order in a metallic glass". In: *Nature Materials* 10.1, pp. 28–33. DOI: 10.1038/nmat2897.

Hoppe, Peter et al. (2017). "The stardust abundance in the local interstellar cloud at the birth of the solar system". In: *Nature Astronomy* 1.9, pp. 617–620.

Howard, K. T. et al. (2011). "Modal mineralogy of CM chondrites by X-ray diffraction (PSD-XRD): Part 2. Degree, nature and settings of aqueous alteration". In: *Geochimica et Cosmochimica Acta* 75 (10), pp. 2735–2751. DOI: 10.1016/j.gca.2011.02.021.

Howard, K. T. et al. (2015). "Classification of hydrous meteorites (CR, CM and C2 ungrouped) by phyllosilicate fraction: PSD-XRD modal mineralogy and planetesimal environments". In: *Geochimica et Cosmochimica Acta* 149, pp. 206–222. DOI: 10.1016/j.gca.2014.10.025.

Howard, K.T. et al. (2009). "Modal mineralogy of CM2 chondrites by X-ray diffraction (PSD-XRD). Part 1: Total phyllosilicate abundance and the degree of aqueous alteration". In: *Geochimica et Cosmochimica Acta* 73.15, pp. 4576–4589. DOI: https://doi.org/10.1016/j.gca.2009.04.038.

Ishii, Hope A et al. (2018). "Multiple generations of grain aggregation in different environments preceded solar system body formation". In: *Proceedings of the National Academy of Sciences* 115.26, pp. 6608–6613.

Ito, Motoo et al. (2022). "A pristine record of outer Solar System materials from asteroid Ryugu's returned sample". In: *Nature Astronomy* 6 (10), pp. 1163–1171. DOI: 10.1038/s41550-022-01745-5.

Jansen, Eval et al. (2002). "The structure of six-line ferrihydrite". In: *Applied Physics A* 74. DOI: 10.1007/s003390101175.

Janzen, Michael P et al. (2000). "Pyrrhotite reaction kinetics: reaction rates for oxidation by oxygen, ferric iron, and for nonoxidative dissolution". In: *Geochimica et Cosmochimica Acta* 64.9, pp. 1511–1522. DOI: https://doi.org/10.1016/S0016-7037(99)00421-4.

Jenkins, Laura E. et al. (2023). "Winchcombe: An example of rapid terrestrial alteration of a CM chondrite". In: *Meteoritics & Planetary Science*. DOI: https://doi.org/10.1111/maps.13949.

Jiang, Yi et al. (2018). "Electron ptychography of 2D materials to deep sub-ångström resolution". In: *Nature* 559.7714, pp. 343–349. DOI: 10.1038/s41586-018-0298-5.

Jolliffe, Ian T. and Jorge Cadima (2016). "Principal component analysis: a review and recent developments". In: *Philosophical Transactions: Mathematical, Physical and Engineering Sciences* 374.2065, pp. 1–16.

Jones, AP et al. (2013). "The evolution of amorphous hydrocarbons in the ISM: dust modelling from a new vantage point". In: *Astronomy & Astrophysics* 558, A62.

Kalinin, Sergei et al. (2022). "Machine learning in scanning transmission electron microscopy". In: *Nature Reviews Methods Primers* 2, p. 11. DOI: 10.1038/s43586-022-00095-w.

Keil, K. et al. (1997). "Constraints on the role of impact heating and melting in asteroids". In: *Meteoritics & Planetary sciences* 32, pp. 349–363. DOI: 10.1111/j.1945-5100.1997.tb01278.x.

Kelley, K.K. et al. (1941). *Thermodynamic Properties of Gypsum and Its Dehydration Products. By K.K. Kelley, J.C. Southard, and C.T. Anderson*. U.S. Bureau of Mines. Technical Paper. no. 625. U.S. Government Printing Office.

Kemper, F, W Vriend, et al. (2004). "The absence of crystalline silicates in the diffuse interstellar medium". In: *The Astrophysical Journal* 609.2, p. 826.

Kemper, F, L Waters, et al. (2001). "Crystallinity versus mass-loss rate in asymptotic giant branch stars". In: *Astronomy & Astrophysics* 369.1, pp. 132–141.

King, A. J. et al. (2015). "Modal mineralogy of CI and CI-like chondrites by X-ray diffraction". In: *Geochimica et Cosmochimica Acta* 165, pp. 148–160. DOI: 10.1016/j.gca.2015.05.038.

Kirkland, Earl J. (2020). *Advanced Computing in Electron Microscopy*. en. Cham: Springer International Publishing. DOI: 10.1007/978-3-030-33260-0.

Kitazato, K et al. (2019). "The surface composition of asteroid 162173 Ryugu from Hayabusa2 near-infrared spectroscopy". In: *Science* 364.6437, pp. 272–275.

Knoll, M. and E. Ruska (1932). "Das Elektronenmikroskop". In: *Zeitschrift für Physik* 78.5-6, pp. 318–339.

Kobler, A et al. (2013). "Combination of in situ straining and ACOM TEM: A novel method for analysis of plastic deformation of nanocrystalline metals". In: *Ultramicroscopy* 128C, pp. 68–81. DOI: 10.1016/j.ultramic.2012.12.019.

Konta, Jiří (2009). "Phyllosilicates in the sediment-forming processes: Weathering, erosion, transportation, and deposition". In: *Acta Geodyn. Geomater* 6, pp. 13–43.

Krajnak, Matus et al. (2016). "Pixelated detectors and improved efficiency for magnetic imaging in STEM differential phase contrast". In: *Ultramicroscopy* 165, pp. 42–50. DOI: https://doi.org/10.1016/j.ultramic.2016.03.006.

Krivanek, O.L. et al. (1999). "Towards sub-Å electron beams". In: *Ultramicroscopy* 78.1, pp. 1–11. DOI: https://doi.org/10.1016/S0304-3991(99)00013-3.

Krot, A et al. (2009). "Origin and chronology of chondritic components: A review". In: *Geochimica et Cosmochimica Acta* 73.17, pp. 4963–4997. DOI: 10.1016/j.gca.2008.09.039.

Lagaly, G. and K. Beneke (1991). "Intercalation and exchange reactions of clay minerals and non-clay layer compounds". en. In: *Colloid and Polymer Science* 269.12, pp. 1198–1211. DOI: 10.1007/BF00652529.

Lanson, Bruno et al. (2022). "Determination of layer charge density in expandable phyllosilicates with alkylammonium ions: A combined experimental and theoretical assessment of the method". en. In: *Applied Clay Science* 229. DOI: 10.1016/j.clay.2022.106665.

Lauretta, D. S. et al. (2019). "The unexpected surface of asteroid (101955) Bennu". In: *Nature* 568.7750, pp. 55–60. DOI: 10.1038/s41586-019-1033-6.

Laurora, Angela et al. (2011). "The crystal chemistry of lizardite-1T from northern Apennines ophiolites near Modena, Italy". In: *Canadian Mineralogist* 49, pp. 1045–1054. DOI: 10.3749/canmin.49.4.1045.

Le Guillou, Corentin and Adrian Brearley (2014). "Relationships between organics, water and early stages of aqueous alteration in the pristine CR3.0 chondrite MET 00426". en. In: *Geochimica et Cosmochimica Acta* 131, pp. 344–367. DOI: 10.1016/j.gca.2013.10.024.

LeGuillou, C. et al. (2011). "Aqueous alteration of organic matter and amorphous silicate in pristine chondrites: A multiscale study". In: *Goldschmidt Conference* 1291.

Leroux, H et al. (2023). "Phyllosilicates with embedded Fe-based nanophases in Ryugu and Orgueil". In: *Meteoritics & Planetary Science* n/a.n/a. DOI: https://doi.org/10.1111/maps.14101.

Leroux, H. et al. (2015). "GEMS-like material in the matrix of the Paris meteorite and the early stages of alteration of CM chondrites". In: *Geochimica et Cosmochimica Acta* 170, pp. 247–265. DOI: 10.1016/j.gca.2015.09.019.

Liu, A. C. Y. et al. (2013). "Systematic mapping of icosahedral short-range order in a melt-spun $Zr_{36}Cu_{64}$ metallic glass". In: *Physical Review Letters* 110.20. DOI: 10.1103/physrevlett.110.205505.

Lobato, I. and D. Van Dyck (2015). "MULTEM: A new multislice program to perform accurate and fast electron diffraction and imaging simulations using Graphics Processing Units with CUDA". In: *Ultramicroscopy* 156, pp. 9–17. DOI: https://doi.org/10.1016/j.ultramic.2015.04.016.

Lodders, Katharina (2019). "Solar Elemental Abundances". In: *Oxford Research Encyclopedia of Planetary Science*.

MacKinnon, Ian D. R. (1980). "Structures and textures of the Murchison and Mighei carbonaceous chondrite matrices". In: *Lunar and Planetary Science Conference, 11th, Houston, TX, March 17-21, 1980, Proceedings.* 2, pp. 839–852.

Madsen, Jacob and Toma Susi (2021). "abTEM: Transmission Electron Microscopy from First Principles". In: *Open Research Europe* 1.24, p. 13015. DOI: 10.12688/openreseurope.13015.1.

Mason, Brian (1960). "The origin of meteorites". In: *Journal of Geophysical Research (1896-1977)* 65.9, pp. 2965–2970. DOI: https://doi.org/10.1029/JZ065i009p02965.

McSween, Harry Y. and Steven M. Richardson (1977). "The composition of carbonaceous chondrite matrix". In: *Geochimica et Cosmochimica Acta* 41.8, pp. 1145–1161. DOI: https://doi.org/10.1016/0016-7037(77)90110-7.

McSween Harry Y., Jr. et al. (1988). "Thermal metamorphism." In: *Meteorites and the Early Solar System*. Ed. by John F. Kerridge and Mildred Shapley Matthews, pp. 102–113.

Mellini, M et al. (2013). "Structure and microstructure of serpentine minerals. Minerals at the Nanoscale". In: *Mineralogical Society of Great Britain and Ireland*.

Mellini, Marcello et al. (2010). "The crystal structure of Mg end-member lizardite-1T forming polyhedral spheres from the Lizard, Cornwall". In: *Mineralogical Magazine* 74, pp. 277–284.
Messenger, Scott et al. (2003). "Samples of stars beyond the solar system: Silicate grains in interplanetary dust". In: *Science* 300.5616, pp. 105–108.
Molster, F and L Waters (2003). "The mineralogy of interstellar and circumstellar dust". In: *Astromineralogy*. Springer, pp. 121–170.
Mompiou, F. et al. (2013). "Inter- and intragranular plasticity mechanisms in ultrafine-grained Al thin films: An in situ TEM study". In: *Acta Materialia* 61.1, pp. 205–216. DOI: 10.1016/j.actamat.2012.09.051.
Morniroli, Jean (2004). *Large-Angle Convergent-Beam Electron Diffraction Applications to Crystal Defects*. DOI: 10.1201/9780367806361.
Mouloud, Bahae-eddine et al. (2024). "Four-dimensional-STEM analysis of the phyllosilicate-rich matrix of Ryugu samples". In: *Meteoritics & Planetary Science*. DOI: 10.1111/maps.14124.
Moyano, Bernardo et al. (2012). "Modeling compaction effects on the elastic properties of clay-water composites". In: *Geophysics* 77 (5). DOI: 10.1190/geo2011-0426.1.
Muller, David et al. (2016). "An Electron Microscope Pixel Array Detector as a Universal STEM Detector". In: vol. 22, pp. 478–479. DOI: 10.1017/S143192761600324X.
Nakamura, Eizo et al. (2022). "On the origin and evolution of the asteroid Ryugu: A comprehensive geochemical perspective". In: *Proceedings of the Japan Academy, Series B* 98.6, pp. 227–282. DOI: 10.2183/pjab.98.015.
Nakamura, T. et al. (2022). In: *Science*. DOI: 10.1126/science.abn8671.
Nakano, A. et al. (1979). "Refinement of 3C pyrrhotite, Fe7S8". In: *Acta Crystallographica Section B* 35.3, pp. 722–724. DOI: https://doi.org/10.1107/S0567740879004532.
Nalin Mehta, Ankit et al. (2020). "Unravelling stacking order in epitaxial bilayer MX2 using 4D-STEM with unsupervised learning". In: *Nanotechnology* 31. DOI: 10.1088/1361-6528/aba5b6.
Nguyen, Ann N et al. (2007). "Characterization of presolar silicate and oxide grains in primitive carbonaceous chondrites". In: *The Astrophysical Journal* 656.2, p. 1223.
Noguchi, Takaaki et al. (2023). "Mineralogy and petrology of fine-grained samples recovered from the asteroid (162173) Ryugu". In: *Meteoritics & Planetary Science* n/a.n/a. DOI: https://doi.org/10.1111/maps.14093.
O'Hanley, David S. and Frederick J. Wicks (1995). "Conditions of formation of lizardite, chrysotile and antigorite, Cassiar, British Columbia". In: *The Canadian Mineralogist* 33.4, pp. 753–773.
O'Hanley, David S. et al. (1989). "The stability of lizardite and chrysotile". In: *The Canadian Mineralogist* 27.3, pp. 483–493.
Ophus, Colin (2017). "A fast image simulation algorithm for scanning transmission electron microscopy". In: *Advanced Structural and Chemical Imaging* 3.1. DOI: 10.1186/s40679-017-0046-1.
— (2019). "Four-Dimensional Scanning Transmission Electron Microscopy (4D-STEM): From Scanning Nanodiffraction to Ptychography and Beyond". In: *Microscopy and Microanalysis* 2019, pp. 563–582. DOI: 10.1017/S1431927619000497.
Ophus, Colin et al. (2022). "Automated Crystal Orientation Mapping in py4DSTEM using Sparse Correlation Matching". In: *Microscopy and Microanalysis* 28.2, pp. 390–403. DOI: 10.1017/s1431927622000101.
Osawa, Takahito et al. (2005). "Infrared spectroscopic taxonomy for carbonaceous chondrites from speciation of hydrous components". In: *Meteoritics & Planetary Science* 40.1, pp. 71–86. DOI: https://doi.org/10.1111/j.1945-5100.2005.tb00365.x.

Ozdol, V. et al. (2015). "Strain mapping at nanometer resolution using advanced nano-beam electron diffraction". In: *Applied Physics Letters* 106. DOI: 10.1063/1.4922994.

Paatero, Pentti and Unto Tapper (1994). "Positive matrix factorization: A non-negative factor model with optimal utilization of error estimates of data values". In: *Environmetrics* 5.2, pp. 111–126. DOI: https://doi.org/10.1002/env.3170050203.

Patterson, Claire (1956). "Age of meteorites and the earth". In: *Geochimica et Cosmochimica Acta* 10.4, pp. 230–237. DOI: https://doi.org/10.1016/0016-7037(56)90036-9.

Pennycook, Timothy J. et al. (2019). "High dose efficiency atomic resolution imaging via electron ptychography". In: *Ultramicroscopy* 196, pp. 131–135. DOI: https://doi.org/10.1016/j.ultramic.2018.10.005.

Phan, Van T. H. et al. (2022). "Nanoscale mineralogy and organic structure in Orgueil (CI) and EET 92042 (CR) carbonaceous chondrites studied with AFM-IR spectroscopy". eng. In: *Meteoritics & planetary science* 57.1, pp. 3–21.

Pignatelli, Isabella et al. (2017). "Mineralogical, crystallographic and redox features of the earliest stages of fluid alteration in CM chondrites". en. In: *Geochimica et Cosmochimica Acta* 209, pp. 106–122. DOI: 10.1016/j.gca.2017.04.017.

Pizzarello, S. et al. (2006). "The Nature and Distribution of the Organic Material in Carbonaceous Chondrites and Interplanetary Dust Particles". In: *Meteorites and the Early Solar System II*.

Pryor, Alan et al. (2017). "A streaming multi-GPU implementation of image simulation algorithms for scanning transmission electron microscopy". In: *Advanced Structural and Chemical Imaging* 3.1. DOI: 10.1186/s40679-017-0048-z.

Quirico, E. et al. (2013). "Collisions-Induced Thermal Metamorphism in CM Chondrites as Revealed by Organic Matter". In: *Meteoritics and Planetary Science Supplement* 76, p. 5132.

Rajamani, V. and C. T. Prewitt (1975). "Thermal Expansion of the Pentlandite Structure". In: *American Mineralogist* 60.1-2, pp. 39–48.

Rangel DaCosta, Luis et al. (2021). "Prismatic 2.0 – Simulation software for scanning and high resolution transmission electron microscopy (STEM and HRTEM)". In: *Micron* 151, p. 103141. DOI: https://doi.org/10.1016/j.micron.2021.103141.

Rauch, E. (2008). "Plastic Behavior of Metals at Large Strains: Experimental Studies Involving Simple Shear". In: *Journal of Engineering Materials and Technology* 131.1. DOI: 10.1115/1.3030942.

Rauch, E. and L. Dupuy (2005). "Rapid Diffraction Patterns identification through template matching". In: *Archives of Metallurgy and Materials* 50, pp. 87–99.

— (2006). "Comments on 'On the reliability of fully automatic indexing of electron diffraction patterns obtained in a transmission electron microscope'". In: *Journal of Applied Crystallography* 39.1, pp. 104–105. DOI: 10.1107/s0021889805033157.

Rauch, E. and M. Veron (2005). "Coupled microstructural observations and local texture measurements with an automated crystallographic orientation mapping tool attached to a tem". en. In: *Materialwissenschaft und Werkstofftechnik* 36.10, pp. 552–556. DOI: 10.1002/mawe.200500923.

Rauch, E. and M. Véron (2014a). "Automated crystal orientation and phase mapping in TEM". en. In: *Materials Characterization* 98, pp. 1–9. DOI: 10.1016/j.matchar.2014.08.010.

— (2014b). "Virtual dark-field images reconstructed from electron diffraction patterns". en. In: *The European Physical Journal Applied Physics* 66.1, p. 10701. DOI: 10.1051/epjap/2014130556.

Rauch, Edgar F. et al. (2010). In: *Zeitschrift für Kristallographie* 225.2-3, pp. 103–109. DOI: doi:10.1524/zkri.2010.1205.

Remusat, L. et al. (2010). "Accretion and preservation of d-rich organic particles in carbonaceous chondrites: evidence for important transport in the early solar system nebula". In: *The Astrophysical Journal* 713.2, pp. 1048–1058. DOI: 10.1088/0004-637x/713/2/1048.

Roqué Rosell, Josep et al. (2018). "Au crystal growth on natural occurring Au—Ag aggregate elucidated by means of precession electron diffraction (PED)". In: *Journal of Crystal Growth* 483, pp. 228–235. DOI: 10.1016/j.jcrysgro.2017.11.031.

Salaün, Pauline et al. (2023). "Cooperative Synthesis of Raspberry-Like Covalent Organic Framework-Polymer Particles with a Radial Single-Crystal Grain Orientation". In: *Small* 19.49. DOI: https://doi.org/10.1002/smll.202303697.

Savitzky, Benjamin H. et al. (2021). "py4DSTEM: A Software Package for Four-Dimensional Scanning Transmission Electron Microscopy Data Analysis". In: *Microscopy and Microanalysis* 27 (4), pp. 712–743. DOI: 10.1017/S1431927621000477.

Sayers, Colin M. and Lennert D. den Boer (2016). "The elastic anisotropy of clay minerals". In: *Geophysics* 81 (5), pp. C193–C203. DOI: 10.1190/GEO2016-0005.1.

Scherzer, O (1936). "Über einige Fehler von Elektronenlinsen". In: *Eur. Phys. J. A* 101.9-10, pp. 593–603.

Schmus, Van and John Wood (1967). "A chemical-petrologic classification for the chondritic meteorites". In: *Geochimica et Cosmochimica Acta* 31.5, pp. 747–765. DOI: https://doi.org/10.1016/S0016-7037(67)80030-9.

Schrader, Devin L. et al. (2021). "The Fe/S ratio of pyrrhotite group sulfides in chondrites: An indicator of oxidation and implications for return samples from asteroids Ryugu and Bennu". In: *Geochimica et Cosmochimica Acta* 303, pp. 66–91. DOI: https://doi.org/10.1016/j.gca.2021.03.019.

Schwartz, Stéphane et al. (2013). "Pressure–temperature estimates of the lizardite / antigorite transition in high pressure serpentinites". en. In: *Lithos*. Serpentinites from mid-oceanic ridges to subduction 178. DOI: 10.1016/j.lithos.2012.11.023.

Scott, E and A Krot (2007). "1.07 - Chondrites and Their Components". In: *Treatise on Geochemistry*. Oxford: Pergamon, pp. 1–72. DOI: https://doi.org/10.1016/B0-08-043751-6/01145-2.

Scott, E. et al. (1992). "Shock metamorphism of carbonaceous chondrites". In: *Geochemica et Cosmochemica Acta* 56.12, pp. 4281–4293. DOI: 10.1016/0016-7037(92)90268-N.

Sears, Derek W. G. and Robert T. Dodd (1988). "Overview and classification of meteorites." In: *Meteorites and the Early Solar System*. Ed. by John F. Kerridge and Mildred Shapley Matthews, pp. 3–31.

Sephton, Mark A. (2002). "Organic compounds in carbonaceous meteorites". In: *Nat. Prod. Rep.* 19 (3), pp. 292–311. DOI: 10.1039/B103775G.

Shi, Chuqiao et al. (2022). "Uncovering material deformations via machine learning combined with four-dimensional scanning transmission electron microscopy". In: *npj Computational Materials* 8, p. 114. DOI: 10.1038/s41524-022-00793-9.

Shibata, Naoya et al. (2019). "Atomic resolution electron microscopy in a magnetic field free environment". In: *Nature Communications* 10, p. 2308. DOI: 10.1038/s41467-019-10281-2.

Shukla, Alpesh Khushalchand et al. (2016). "Study of Structure of Li- and Mn-rich Transition Metal Oxides Using 4D-STEM". In: *Microscopy and Microanalysis* 22.S3, pp. 494–495. DOI: 10.1017/S1431927616003329.

Simon, J.I. et al. (2018). "Particle size distributions in chondritic meteorites: Evidence for pre-planetesimal histories". In: *Earth and Planetary Science Letters* 494, pp. 69–82. DOI: https://doi.org/10.1016/j.epsl.2018.04.021.

Stroud, Rhonda M et al. (2023). "Electron microscopy observations of the diversity of Ryugu organic matter and its relationship to minerals at the micro-to-nanoscale". en. In: *Meteoritics & Planetary Science*. Submitted.

Sugita, Satoshi et al. (2019). "The geomorphology, color, and thermal properties of Ryugu: Implications for parent-body processes". In: *Science* 364.6437, eaaw0422.

Suttle, M.D. et al. (2021). "The aqueous alteration of CM chondrites, a review". In: *Geochimica et Cosmochimica Acta* 299, pp. 219–256. DOI: https://doi.org/10.1016/j.gca.2021.01.014.

Takir, Driss et al. (2013). "Nature and degree of aqueous alteration in CM and CI carbonaceous chondrites". en. In: *Meteoritics & Planetary Science* 48.9, pp. 1618–1637. DOI: 10.1111/maps.12171.

Tao, J. et al. (2009). "Direct Imaging of Nanoscale Phase Separation in $La_{0.55}Ca_{0.45}MnO_3$: Relationship to Colossal Magnetoresistance". In: *Phys. Rev. Lett.* 103 (9), p. 097202. DOI: 10.1103/PhysRevLett.103.097202.

Tomeoka, Kazushige and Peter R. Buseck (1985). "Indicators of aqueous alteration in CM carbonaceous chondrites: Microtextures of a layered mineral containing Fe, S, O and Ni". In: *Geochimica et Cosmochimica Acta* 49.10, pp. 2149–2163. DOI: https://doi.org/10.1016/0016-7037(85)90073-0.

— (1988). "Matrix mineralogy of the Orgueil CI carbonaceous chondrite". In: *Geochimica et Cosmochimica Acta* 52 (6), pp. 1627–1640. DOI: 10.1016/0016-7037(88)90231-1.

Tsipursky, S. I. and V. A. Drits (1984). "The distribution of octahedral cations in the 2:1 layers of dioctahedral smectites studied by oblique-texture electron diffraction". In: *Clay Minerals* 19.2, pp. 177–193. DOI: 10.1180/claymin.1984.019.2.05.

Tsuda, Yuichi et al. (2013). "System design of the Hayabusa 2—Asteroid sample return mission to 1999 JU3". In: *Acta Astronautica* 91, pp. 356–362. DOI: 10.1016/j.actaastro.2013.06.028.

Uehara, S. (1998). "TEM and XRD study of antigorite superstructures". In: *The Canadian Mineralogist* 36.6, pp. 1595–1605.

Uesugi, Fumihiko et al. (2021). "Non-negative matrix factorization for mining big data obtained using four-dimensional scanning transmission electron microscopy". In: *Ultramicroscopy* 221. DOI: 10.1016/j.ultramic.2020.113168.

Vacher, Lionel G. et al. (2019). "Deciphering the conditions of tochilinite and cronstedtite formation in CM chondrites from low temperature hydrothermal experiments". en. In: *Meteoritics & Planetary Science* 54.8, pp. 1870–1889. DOI: 10.1111/maps.13317.

Vance, S. D. and M. Melwani Daswani (2020). "Serpentinite and the search for life beyond Earth". In: *Philosophical Transactions of the Royal Society A: Mathematical, Physical and Engineering Sciences* 378.2165, p. 20180421. DOI: 10.1098/rsta.2018.0421.

Velbel, Michael A. and Michael E. Zolensky (2021). "Thermal metamorphism of CM chondrites: A dehydroxylation-based peak-temperature thermometer and implications for sample return from asteroids Ryugu and Bennu". In: *Meteoritics & Planetary Science* 56.3, pp. 546–585. DOI: https://doi.org/10.1111/maps.13636.

Verezhak, Mariana et al. (2016). *ACOM-TEM analysis of the effect of heating on the mineral nanocrystals in bone*. DOI: 10.1002/9783527808465.emc2016.6109.

Veron, M. and E. Rauch (2012a). "Introduction to ASTAR technique". In: *ASTAR Workshop*. France.

— (2012b). "TEM Deformation Maps : Microstructure & Mechanical Behavior". In: *TMS 2012, A symposium in Memory of Patrick Veyssière*. ORLANDO, Florida, United States.

Véron, M. and E. Rauch (2011). "TEM automated Orientation and Phase mapping." In: *Frontiers in electron microscopy in materials Science (FEMMS)*. Sonoma, Californie, United States.

Viennet, J. -C. et al. (2022). "Experimental investigation of Fe-clay/organic interactions under asteroidal conditions". en. In: *Geochimica et Cosmochimica Acta* 318, pp. 352–365. DOI: 10.1016/j.gca.2021.12.002.

Viennet, J.-C., S. Bernard, C. Le Guillou, et al. (2020). "Influence of the nature of the gas phase on the degradation of RNA during fossilization processes". In: *Applied Clay Science* 191, p. 105616. ISSN: 0169-1317. DOI: https://doi.org/10.1016/j.clay.2020.105616.

Viennet, J.-C., S. Bernard, Corentin Le Guillou, et al. (2019). "Experimental clues for detecting biosignatures on Mars". Anglais. In: Accepted: 2020-02-04T10:03:56Z Publisher: European Association of Geochemistry. DOI: 10.7185/geochemlet.1931.

Viennet, Jean Christophe et al. (2023). "Interaction between clay minerals and organics in asteroid Ryugu". In: *Geochemical Perspectives Letters* 25, pp. 8–12. DOI: 10.7185/geochemlet.2307.

Viennet, Jean-Christophe et al. (2021). "Martian Magmatic Clay Minerals Forming Vesicles: Perfect Niches for Emerging Life?" In: *Astrobiology* 21.5. Publisher: Mary Ann Liebert, Inc., publishers, pp. 605–612. DOI: 10.1089/ast.2020.2345.

Visser, Robbin et al. (2019). "Sulfur isotope study of sulfides in CI, CM, $C2_{ung}$ chondrites and volatile-rich clasts – Evidence for different generations and reservoirs of sulfide formation". In: *Geochimica et Cosmochimica Acta* 261, pp. 210–223. DOI: 10.1016/j.gca.2019.06.046.

Wang, Xiaoli and Hejing Wang (2021). "Structural Analysis of Interstratified Illite-Smectite by the Rietveld Method". In: *Crystals* 11.3, p. 244. DOI: 10.3390/cryst11030244.

Warren, Paul H. (2011). "Stable-isotopic anomalies and the accretionary assemblage of the Earth and Mars: A subordinate role for carbonaceous chondrites". In: *Earth and Planetary Science Letters* 311.1, pp. 93–100. DOI: 10.1016/j.epsl.2011.08.047.

Watanabe, Seiichiro et al. (2019). "Hayabusa2 arrives at the carbonaceous asteroid 162173 Ryugu—A spinning top–shaped rubble pile". In: *Science* 364.6437, pp. 268–272.

Weisberg, Michael K et al. (1993). "The CR (Renazzo-type) carbonaceous chondrite group and its implications". In: *Geochimica et Cosmochimica Acta* 57.7, pp. 1567–1586. DOI: https://doi.org/10.1016/0016-7037(93)90013-M.

Wenner, David B. and Hugh P. Taylor (1971). "Temperatures of serpentinization of ultramafic rocks based on O18/O16 fractionation between coexisting serpentine and magnetite". en. In: *Contributions to Mineralogy and Petrology* 32.3, pp. 165–185. DOI: 10.1007/BF00643332.

Williams, David B. and C. Barry Carter (2008). *Transmission electron microscopy: a textbook for materials science*. en. 2nd ed. New York: Springer.

Wood, John (2000). In: *Space Science Reviews* 92.1/2, pp. 87–93. DOI: 10.1023/a:1005249417716.

Yabuta, Hikaru et al. (2023). "Macromolecular organic matter in samples of the asteroid (162173) Ryugu". In: *Science* 379.6634, eabn9057. DOI: 10.1126/science.abn9057.

Yada, Keiji (1971). "Study of microstructure of chrysotile asbestos by high-resolution electron microscopy". In: *Acta Crystallographica Section A* 27, pp. 659–664.

Yada, Toru et al. (2022). "Preliminary analysis of the Hayabusa2 samples returned from C-type asteroid Ryugu". In: *Nature Astronomy* 6 (2), pp. 214–220. DOI: 10.1038/s41550-021-01550-6.

Yamaguchi, Akira et al. (2023). "Insight into multi-step geological evolution of C-type asteroids from Ryugu particles". In: *Nature Astronomy*. DOI: 10.1038/s41550-023-01925-x.

Yang, Hao et al. (2016). "Enhanced phase contrast transfer using ptychography combined with a pre-specimen phase plate in a scanning transmission electron microscope". In: *Ultramicroscopy* 171, pp. 117–125. DOI: https://doi.org/10.1016/j.ultramic.2016.09.002.

Yang, Hao et al. (2017). "Electron ptychographic phase imaging of light elements in crystalline materials using Wigner distribution deconvolution". In: *Ultramicroscopy* 180, pp. 173–179. DOI: https://doi.org/10.1016/j.ultramic.2017.02.006.

Yi, Feng and P. M. Voyles (2011). "Effect of sample thickness, energy filtering, and probe coherence on fluctuation electron microscopy experiments". en. In: *Ultramicroscopy* 111.8, pp. 1375–1380. DOI: 10.1016/j.ultramic.2011.05.004.

Yokoyama, Tetsuya et al. (2022). "Samples returned from the asteroid Ryugu are similar to Ivuna-type carbonaceous meteorites". In: *Science* 0.0, eabn7850. DOI: 10.1126/science.abn7850.

Zaluzec, Nestor J (Aug. 2002). "Quantitative Measurements of Magnetic Vortices using Position Resolved Diffraction in Lorentz Stem". In: *Microscopy and Microanalysis* 8.S02, pp. 376–377. ISSN: 1431-9276. DOI: 10.1017/S143192760210064X.

Zega, Thomas J. et al. (2006). "Polyhedral serpentine grains in CM chondrites". en. In: *Meteoritics & Planetary Science* 41.5, pp. 681–688. DOI: 10.1111/j.1945-5100.2006.tb00984.x.

Zheng, Qi et al. (2022). "A covalent organic framework onion structure". In: *Materials Today* 60, pp. 98–105. DOI: https://doi.org/10.1016/j.mattod.2022.09.002.

Zhukovska, Svitlana et al. (2008). "Evolution of interstellar dust and stardust in the solar neighbourhood". In: *Astronomy & Astrophysics* 479.2, pp. 453–480.

Ziatdinov, Maxim et al. (2022). "AtomAI framework for deep learning analysis of image and spectroscopy data in electron and scanning probe microscopy". In: *Nature Machine Intelligence* 4.12, pp. 1101–1112. DOI: 10.1038/s42256-022-00555-8.

Zolensky, Michael et al. (1993). "Mineralogy and composition of matrix and chondrule rims in carbonaceous chondrites". In: *Geochimica et Cosmochimica Acta* 57.13, pp. 3123–3148. DOI: https://doi.org/10.1016/0016-7037(93)90298-B.

Zvyagin, Boris Borisovich (1967). *Electron-Diffraction Analysis of Clay Mineral Structures*. en. Boston, MA: Springer US. DOI: 10.1007/978-1-4615-8612-8.